# Study of Long-Distance High-Temperature Superconductor Cables for HVDC Power Transmission

Lakshmana Geetha Pavan Kumar Chaganti

Department of Electronic and Electrical Engineering

University of Strathclyde

A thesis submitted for the degree of

*Doctor of Philosophy*

August 2024

Supervisor: Prof. Weijia Yuan, Prof. Min Zhang

# Copyright

# Acknowledgements

First and foremost, I express my sincere gratitude to my main supervisors, Prof. Weijia Yuan and my co-supervisor Prof. Min Zhang, for their valuable support and guidance throughout my PhD. Their experience and expertise in high-temperature superconductors played a crucial role in shaping my development as a researcher. I am deeply grateful for their patience and the opportunity they provided for me to pursue my PhD at the University of Strathclyde.

I would also like to extend my thanks to Prof. Lie Xu for his valuable support and guidance in the project, especially in my modelling work. I am very thankful to Supernode and ORE Catapult for supporting this research. I want to thank Eoin Hodge, Keith McCullough and Paul McKeever from Supernode and ORE Catapult for their industrial supervision, and the experience has helped me drive my PhD in an organised way.

I want to express my special thanks to my colleagues and friends at the Applied Superconductivity Laboratory for their support. The research fellows in the ASL are Ercan, Alexander, and Wakeel, who supported the lab experiments. My fellow students have always supported me during my stay at Strathclyde.

I also take this opportunity to express my heartfelt gratitude to my family and friends for their enduring support throughout this journey. Their love and encouragement have been my constant sources of inspiration during these challenging times. Finally, I owe a debt of gratitude to my wife and mother, who have been pillars of strength and support throughout this journey. Their persistent faith in me has given me the courage to persevere through tough times.

# Abstract

The carbon neutrality goal of achieving net zero by 2050 has sparked significant interest in offshore wind farms. With offshore wind farms being installed from short distances to long distances away from the seashore, a submarine power transmission infrastructure is a necessity. Considering power cable length and low net effective losses, a high-voltage direct-current (HVDC) system has been chosen over HVAC. HVDC cables are considered to be made out of high-temperature superconductor (HTS) material. HTS power cables hold immense potential for efficient, low-loss, high-current-density, and compact power transmission. But, unlike copper/aluminium, the HTS material has a sharp transient behaviour as a function of the operating current, temperature, and magnetic field. However, the susceptibility of HTS cables to faults in the grid, resulting in quenching or permanent damage due to joule heating, poses a critical challenge to their real-world resilience.

The main aim of this thesis is to study and evaluate the long-distance HTS subsea power cable for offshore to onshore power transmission along the radial and axial direction of the 2G HTS power cable in terms of electrical, thermal, hydraulic and quench characteristics during the normal and grid fault conditions. Prior to the installation of long-distance cable experiments and lab prototypes, modelling and simulation work is needed to predict cable behaviour. Furthermore, modelling the HTS power cable was necessary as part of enhancing cable performance and design. To tackle the problem described above, a computationally efficient high-fidelity model over the whole length of the cable was needed to understand HTS cable characteristics. The complex design of the superconductor power cable was modelled using Finite Element Method (FEM). However, for long-distance superconductor electrical-thermal-hydraulic studies, the FEM

simulation involves a computational burden and for the electrical network, it is not suitable.

Novel discretised electrical-thermal-hydraulic SIMSCAPE components with non-linear resistive behaviour dependent on current and temperature in MATLAB/SIMSCAPE software were modelled, partitioning the cable into discrete blocks to understand the temperature along the axial length and to determine the impact of transient conditions on a long-distance superconducting power cable in transmission. The model has the advantage of having the flexibility to change the fault location and cryocooler spacing length along the length of the cable, including the HTS and copper former and LN2 layers. The experiment measured the joint resistance of the tape incorporated into the model. This study is unique in that it is the first to look at 100 km long-distance HVDC subsea HTS for offshore to onshore grid use capable of transmitting more than 1 GW of power at 100 kV voltage and an ampacity of 10 kA. The primary technical challenges in modelling this long-distance HVDC subsea HTS cable are due to its non-linear resistive properties, which vary with temperature, current, and magnetic field. These variations result in the cable's electrical and thermal behaviour changes along its length, complicating accurate modelling. Distributed RLC network models are implemented using Simscape cable blocks to address these complexities. Each Simscape block includes thermal, electrical, and hydraulic parameters of respective cable layers, considering conduction, convection, radiation heat losses, non-linear resistance, critical current, and pressure drop and temperature. It allows the integration of cryocoolers at specific points along the cable.

For this study, an HVDC HTS power cable was considered and modelled both as a lumped element and as a distributed element model with 100 elements to compare and evaluate the cable parameters along the length. The parameters include temperature distribution, resistance, critical current, current, and losses at different spots throughout the length of the cable. To simulate the transient condition, a pole-to-ground (PG) fault is considered and the current distribution between the copper former and HTS tapes is studied. Using this cable model, the maximum temperature of the HTS and coolant both in the superconducting state and transient state has been evaluated and presented.

This research is the first to develop a 2D T-A of a subsea HTS cable with a 10-kA transport current to investigate the electromagnetic behaviour of the superconductor and the impact of the harmonics generated in the AC/DC converters on the cable. The cross-sectional area of the HTS cable was modelled in 2D using COMSOL Multiphysics to examine harmonic ripple losses in the cable. These findings were further validated through experimental investigations on the superconductor tapes.

This study underscores the benefits of integrating Superconducting Fault Current Limiters (SFCL) with HTS cables in the network, showcasing load sharing between the superconductor and copper former during steady and transient state operations, HTS quench and recovery time.

# Contents

# List of Figures

# List of Tables

# Abbreviations

| | | |
|---|---|---|
| 1G | - | 1$^{st}$ Generation |
| 2G | - | 2$^{nd}$ Generation |
| CD | - | Cross direction |
| CICC | - | Cable-in-Conduit Conductor |
| CIGRE | - | Council on Large Electric Systems |
| CORC | - | Conductor-on-Round-Core |
| DAQ | - | Data Acquisition |
| EHVDC | - | Extra- High Voltage Direct Current |
| FCL | - | Fault Current Limiter |
| FDTD | - | Finite-Difference Time-Domain |
| FEM | - | Finite Element Method |
| GW | - | Giga Watt |
| HVDC | - | high-voltage Direct-Current |
| HTS | - | High-Temperature Superconductor |
| IBAD | - | Ion-Beam-Assisted Deposition |
| LH$_2$ | - | Liquid Hydrogen |
| PG | - | Pole-to-Ground |
| LN2 | - | Liquid Nitrogen |
| LTS | - | Low-Temperature Superconductors |

| | | |
|---|---|---|
| MD | - | Machine direction |
| MRI | - | Magnetic resonance imaging |
| NI | - | National Instruments |
| NMR | - | Nuclear Magnetic Resonance |
| OWF | - | Offshore Wind Farms |
| PDE | - | Partial Differential Equations |
| PIT | - | Power in-the-Tube |
| PPLP | - | Polypropylene Laminated Paper |
| RACC | - | Roebel Assembled Coated Conductor |
| RABiTS | - | Rolling-Assisted Biaxially Textured Substrates |
| RANS | - | Reynolds Averaged Navier Stokes |
| REBCO | - | Rare-Earth Barium Copper Oxide |
| RTD | - | Resistance Temperature Detector |
| SFCL | - | Superconducting Fault Current Limiter |
| SDGs | - | Sustainable Development Goals |
| TNM | - | Thermal Network Model |
| TSTC | - | Twisted Stack Tape Cable |
| UHVDC | - | Ultra-High Voltage Direct Current |
| VE | - | Volume Element |
| VEM | - | Volume Element Method |
| YBCO | - | Yttrium Barium Copper Oxide |

# Symbols

| | | |
|---|---|---|
| A | - | Cross-sectional area of the corrugated pipe in m$^2$. |
| $A_{fe}$ | - | Effective area of the copper former (m$^2$) |
| $A_f$ | - | Area of the hydraulic path. |
| $B_o$ | - | Constant. |
| C | - | Capacitance |
| $C_p$ | - | Specific heat of the coolant in J/kg-K |
| $d_o$, and $d_i$ | - | Outer diameter of the pipe and the inner diameter of the hydraulic path. |
| D | - | former diameter |
| $D_h$ | - | hydraulic diameter |
| e | - | Electronic charge |
| E | - | Electric field |
| $E_0$ | - | Electric-field criterion of $1 \times 10^{-4}$ V/m |
| $E_c$ | - | Critical electric field |
| f | - | frequency |
| $f_f$ | - | friction factor |
| $f_\text{n}$ | - | Nominal frequency |
| $G_r$ | | Grashof number |

| | | |
|---|---|---|
| $H_c$ | - | Critical magnetic field value. |
| $H_o$ | - | External magnetic field with amplitude |
| $h$ | - | Planck's constant |
| $I_C$ | - | Critical current |
| $I_o$ | - | Transport current |
| $i_{hts}$ | - | Current in HTS layers |
| $i_{cu}$ | - | Current in the copper layer |
| J | - | Current density |
| $J_{co}(T)$ | - | Temperature-dependent current density at zero fields |
| $J_c$ | - | Critical current density |
| $K$ | | current vector potential |
| $l_{st}$ | - | Length of the single tape |
| $l_{tt}$ | - | The length of the twisted tape on the cable former |
| $l_{T,total}$ | - | Total length of $N_{T,i}$ tapes in the cable |
| $l$ | - | length of the cable (metres) |
| L | - | Inductance |
| $l_p$ | - | Pitch length of the tapes. |
| $L_{self\_hts}$ | - | Self-inductance of HTS |
| $L_{self\_cu}$ | - | Self-inductance of copper |
| M | - | Mutual inductance |

| | | |
|---|---|---|
| $\dot{m}$ | - | Mass flow rate (kg/s) |
| $N_{LA}$ | - | Number of layers. |
| $N_{T,i}$ | - | Number of tapes |
| $n$ | - | Exponential coefficient that differs from the HTS material |
| $\rho$ | - | Density of LN2 |
| $Pr$ | - | Prandtl number |
| $Pe$ | - | Peclet number |
| $\Delta P$ | - | Pressure change |
| $Q$ | - | Total losses in the superconductors. |
| $Q_v$ | - | Volumetric flow rate (m$^3$/s) |
| $Q_f$ | - | Friction losses |
| $R_e$ | - | Reynolds number |
| $R_s$ | - | Resistance across the shunt |
| $R_{hts}$ | - | Superconductor resistance |
| $R_{cu}, R_f$ | - | Copper stabiliser and former resistance |
| $R_{cable}$ | - | Cable resistance |
| $R_{hts,tape}$ | - | HTS tape resistance |
| r | - | Radius |
| $r_f$ | - | Copper former radius |

| | | |
|---|---|---|
| t | - | Thickness of the superconducting section |
| $T_i$ | - | $i^{\text{th}}$ layer temperature |
| T | - | Temperature. |
| $T_c$ | - | Critical Temperature |
| $\Delta T$ | - | Temperature change |
| $V_{hts}$ | - | Voltage across HTS |
| $V_{cu}$ | - | Voltage across copper |
| $v$ | - | Velocity of LN2 |
| $V_s$ | - | Voltage across shunt |
| w | - | Energy |
| $\alpha$ | - | Average winding angle |
| $\alpha t$ | - | Twisting angle |
| $\beta_i$ | - | Pitch angle |
| $\beta$ | - | Filling factor |
| $\varepsilon_0$ | - | The dielectric constant of the free space. |
| $\varepsilon_s$ | - | The dielectric constant of insulation material |
| $\xi$ | - | Coherence length |
| $\lambda$ | - | Penetration depth |
| $\mu_0$ | - | Permeability of the free space |
| $\mu_r$ | - | Relative permeability of copper |
| $\rho_{hts}$ | - | HTS resistivity |

| | | |
|---|---|---|
| $\rho_{cui}$ | - | Copper resistivity |
| $\eta$ | - | Viscosity of LN2 |
| $\varphi$ | - | Electrical scalar potential |
| $\delta_i$ | - | Skin depth |

# Chapter 1

# Introduction

## 1.1. Electrical grid modernisation

The energy sector is undergoing significant transformations as countries strive for carbon neutrality. This shift aims to reduce the level of greenhouse gas emissions, particularly carbon dioxide, resulting from burning coal, oil, and natural gas for electricity production. The push towards cleaner energy resources marks a new direction for the energy sector.

The growing environmental consciousness has also influenced transportation, leading to the adoption of electric vehicles and, consequently, increased electricity consumption. In 2015, the United Nations General Assembly officially endorsed the Sustainable Development Goals (SDGs). Among these, SDG 7 is dedicated to global energy objectives and sets three key targets: to double the worldwide energy efficiency by 2030, to enhance the proportion of energy derived from renewable sources, and to ensure economic and universal access to modern energy services [1].

The future energy pathways analysis shows that it can be achievable to get better energy access, energy security, and air quality while avoiding serious climate change. This can be attained by an alternative combination of energy resources, technology, and policies [2].

In particular, renewable energy sources like wind and solar power have led to numerous projects. The electricity demand has risen from previous years and will remain up for the next 20 to 30 years, it is necessary to meet this rising energy demand. The global energy

usage of data centres is estimated to be 1%, which is around 205 TWH as per 2018 predictions.

In the total energy supply, the share of renewable energy was 14% in 2015 and will rise to 63% in 2050. In the renewable energy sector, wind power has risen from 25% to 85% from 2015 to 2050 [1].

Governments have supported renewable energy initiatives by offering incentives and maintaining price caps on renewable energy. Technological advancements have also enhanced power generation capabilities, leading to more reliable and cleaner energy production. Many countries are setting targets to achieve 100% renewable energy generation.

Solar and wind energy are prominent competitors in the renewable energy market. Solar power generation is limited to daytime, while wind turbines can operate continuously depending on wind availability. The choice of renewable energy source often depends on geographical location and weather conditions. Offshore wind farms, for instance, benefit from the higher wind availability to generate multi-megawatts of electricity.

Advances in wind turbine technology have led to the development of variable-speed turbines and increased capacity, with modern turbines now reaching megawatt (MW) ranges. Both onshore and offshore wind turbines have distinct advantages and applications.

## 1.2. High-Voltage AC vs. DC Transmission

The high-voltage AC is suitable for use in a short to medium-range power transmission system. They have issues with long-distance transmission applications. The charging current generated by the cable capacitance leads to high losses. Additionally, controlling power flow is difficult. There is also an absence of asynchronous operation. Furthermore, the need for reactive power compensation makes it less suitable for long-distance

transmission compared to DC. The other key issues with AC are the skin effect and Ferranti effects [3].

The DC cable exhibits many superior characteristics compared to its AC counterpart. Unlike the AC system, which consists of three single phases separated by insulation in a coaxial cable, the DC cable is more compact. For instance, a 1 GW cable operating at 110 kV DC is less than half the diameter of a comparable 3-phase AC cable.

The advancement in this technology concerning wind power generation to reach GW at a particular site means that traditional copper cables are facing challenges carrying such a high level of power. To transmit power in the GW range using copper cables, the voltage must be stepped up to ultra-high voltage (UHV) or extra UHV levels to minimise $I^2R$ losses in the transmission system. This also increases the need for enhanced insulation in the cables. Figure 1.1 illustrates the electricity generation from offshore wind farms and the subsea cable links in Europe. The European Commission aims to expand offshore wind farm energy generation from 12 GW in 2020 to 300 GW by 2050, necessitating modernization of the electrical grid infrastructure.

Superconductors that have negligible resistance, high current density, and are compact compared with copper or aluminium material are the best option to replace it with. They can carry 5 to 6 times more current than copper and aluminium power cables. This study focuses on the feasibility of superconductor power cables and their reliability in the renewable energy sector.

The DC superconducting cable has almost negligible losses when operating below the critical current limit of the superconducting layer. There is no reactive power; hence, there are no losses in insulation. The primary sources of loss are heat leakage and coolant friction. However, DC cables have specific issues related to the accumulation of charge in the extruded cable insulation. Additionally, harmonic ripples generated by semiconductor devices in converters can lead to extra losses, which vary depending on the transferred power. Another significant concern in DC systems is associated with abrupt changes in load current, proportional to the rate of current change (di/dt). This can cause

flux jumps and the risk of thermal runaway. With proper cable system design these issues can be mitigated.
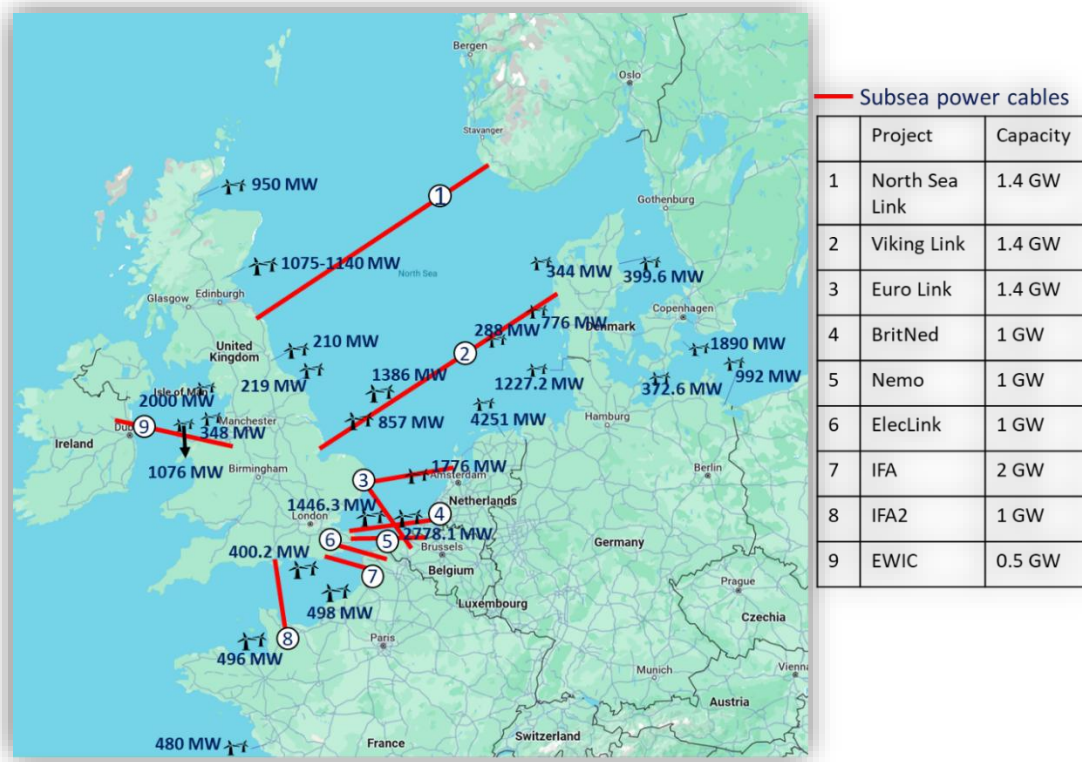


Figure 1.1 Offshore wind farms and the subsea cable links in Europe.

## 1.3. Superconductor power grids

Since the discovery of superconductors based on ceramic materials in the late 1980s, the application interest of superconductors in the power industry has increased and been revived. High-temperature superconductors (HTS) are now becoming more popular due to their low losses when compared with traditional cables, and the advantage of using liquid nitrogen as a coolant is that it is more economical and environmentally friendly [4], [5]. The growing power demand in metro cities is leading to challenges in power transmission due to the lack of land present to install the cables. Load density is going to impact the security and economy in major areas [6]. HTS cables are more compact, around 10 times than traditional cables, and can be applied to solve these issues [7]. The HTS

cable cost savings in terms of initial cost and operating cost are required to bring them into practical application. The practical cost can be reduced by the utilisation of a single cooling system for a long length of cable [8]. Over the last two decades, several projects using HTS cables have been tested and ongoing for the full application of HTS cables in the power grid. In 2000 (Milan), a warm dielectric HTS cable of 50 m length with a current carrying capacity of 1250 A was designed [9]. In 2007, at Long Island in the USA, a 600-metre long HTS cable was commissioned rated at 138 kV and 2400 amps [10]. In Hannover, Germany the ENDESA super cable was developed at a length of 30 metres with a 3200 A rated current. It was implemented with the scope of application being in a medium voltage grid of 25 kV with a transmission capacity of 138 MVA [11]. In Essen Germany, an AC HTS cable of 1 km in length was installed with a voltage of 10 kV and a current of 2.4 kA [12]. In Albany, in the real power grid, a 350 m HTS cable was installed with operating conditions of 34.5 kV and 800 A [13]. In Ishikari, Japan a 500 m and 1000 m DC HTS was installed [14]. In Gongyi, Henan a 360-metre-long DC HTS cable was installed at Zhongfu Industrial Co., Ltd, with a capacity of 10 kA and 1300 V. In St. Petersburg Russia, a DC HTS cable link was developed with a capacity of 2.5 kA, 20 kV, and 50 MW for a length of 2.5 km. Since 2015 in the KEPCO grid, a South Korean HVDC cable of 500MW/80 kV has been in operation [11], [12].

In 2017, a prototype of a 30 m long medium voltage 3-phase AC concentric HTS cable, rated at 10 kV/2.5 $kA_{rms}$ with a current capacity ($I_c$) of 6 kA per phase, was developed for electrical grid installation. Following a successful trial, Shenzhen Power Supply installed a 400-metre-long HTS cable at the Ping'an Financial Centre on September 28, 2021, which has been operating smoothly [13], [14]. A demo project consisting of a 1.2 km, 35 kV/2.2 kA Shanghai superconductor power cable began in 2019 and completed both prototype and commissioning test by November 2021 [15]. Another significant endeavour, supported by the New Energy Technology Development Organization (NEDO) and BASF Japan Ltd., showcased a 6 kV/3 kA triaxial HTS cable. This cable was specifically deployed in the chemical plant grid of BASF to bypass the need for substations [16]. In

August 2021, in Chicago, the AMSC's AC power cable of 200 metres was integrated into an electric grid with a capacity of 62 MW/12 kV/3 kA [17].

When it comes to designing HTS power lines, there are still some issues to work out. To make HTS applications competitive in terms of operational reliability compared to traditional applications, a significant amount of research effort must be put into understanding HTS's loss characteristics and mitigation measures. Only by having a thorough grasp of the HTS loss characteristics can appropriate cooling and auxiliary systems be devised to assure the HTS applications' long-term stability.

Nowadays, offshore wind farms are constructed more than 100 km away from the shore. DC is more suitable for transferring power than AC due to the low power loss and no limitation on the length of the cable [22] [23]. The current study available on the application of superconductors in the power grid is over short distances and MW power ratings. A simulation model of a 10 kV, 1 kA, 1 km-long tri-axial AC HTS cable was developed using MATLAB and Ansys to analyse cable performance under a 10-kA fault current lasting 10 ms [18]. Additionally, a 400 m, 2.5 kA, 10 kV tri-axial HTS AC cable was simulated using a finite element model in COMSOL software [19]. Another model represents a 30 m HTS cable system carrying a 3-kA current in both AC and DC forms, with cooling provided by cryogenic gaseous helium using the TNM [20].

The high energy transfer from renewable sources to loads and to achieve carbon neutrality can be achieved through the implementation of either point-to-point grids or a meshed or SuperGrid structure.

This report explores the use of subsea high-voltage direct current (HVDC) high-temperature superconductor (HTS) cables for linking offshore wind farms with the mainland power grid, as illustrated in Figure 1.2. It is crucial to analyse the thermal, hydraulic, and electrical characteristics of long-length HTS cables under various topologies and during transient conditions. The configuration of a meshed HVDC grid system is depicted in Figure 1.3.
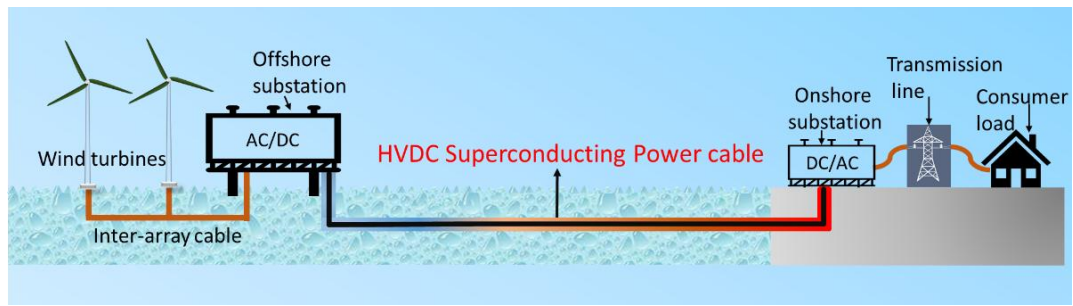
Figure 1.2 Point-to-point HVDC superconducting power cable in the offshore to onshore energy transmissions.
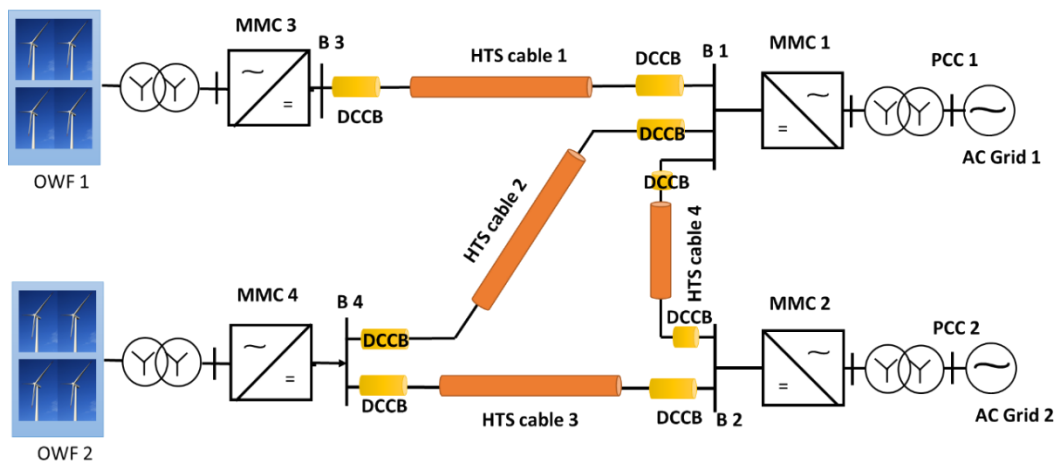


Figure 1.3 Meshed HVDC grid replotted from reference [27]

Modular multilevel converters (MMCs) play a pivotal role in contemporary HVDC transmission technologies, enhancing the efficiency of power transfer between grids operating at different frequencies. At present, the connections for European offshore wind farms (OWFs) via HVDC are point-to-point, controlled by a singular entity. However, to accommodate an increasing number of OWFs, there is a need for a comprehensive offshore HVDC network. The SuperGrid concept is designed to augment the existing European grid by promoting the distribution of renewable energy from outlying areas abundant in wind and solar power to central demand zones. This approach enhances the diversity and security of the energy supply. The envisioned structure of a European SuperGrid is outlined in Figure 1.4.
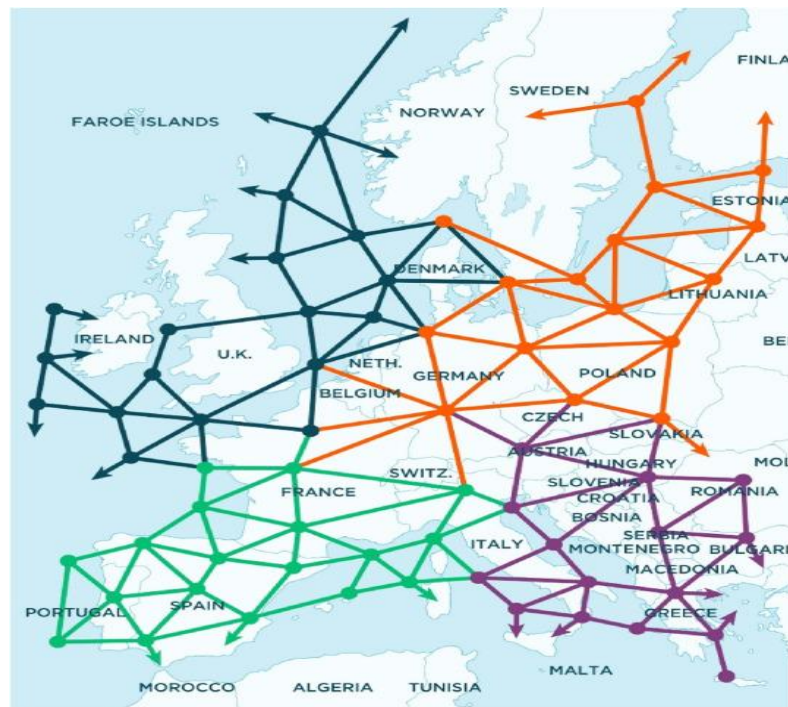
Figure 1.4 Conceptual plan for the European Centre electrical grid [28]

## 1.4. Research Problem

A long-distance subsea HTS cable for offshore wind farms has not been applied until now and there are limited studies available in this area. While designing the HTS cable model, the elements used in the simulation are non-existent. In the HTS power cable analysis, it is necessary to consider the thermal, electrical, and hydraulic characteristics together in the design of the HTS cable. The quenching of the superconductor power cable due to a grid fault may lead to damage to the superconductor cable permanently. Another reason for the quenching of the superconductor is due to temperature changes along the cable.

In the literature section of the thesis, only thermal-hydraulic and thermal-electrical models exist. The superconductor power cable behaviour depends on the current, operating temperature and magnetic field. These parameters have an impact on the superconductor power cable if they cross the critical limits, they will damage the HTS.

8

The electrical behaviour is nonlinear. There are no inbuilt components available for superconductors in the commercial simulation software. It is a key challenge to design non-linear resistance based on electrical, thermal, and hydraulic conditions. The superconductor topology and cryocooler arrangement for the superconductor power that suits the long-distance HVDC superconductor power cable best has not yet been studied. The influence of the grid fault current in the superconductor HVDC cable network means that the joule losses might lead to an increase in temperature and change its critical current behaviour along the length of the cable. This sudden inrush of current has the potential to quench the superconductor. It might recover back or lead to permanent damage. Replacing the damaged superconductor power cable is a complex process, expensive and the grid needs to go out for long hours. It is therefore necessary to protect the superconductor cable and keep its temperature below $T_c$. The study of superconductor behaviour in the fault condition and techniques to mitigate the fault current and temperature is necessary.

There is a need to identify the following:

1. Review the possible design of the superconductor and investigate its application as a subsea HVDC HTS cable.

2. The temperature distribution along the length of the cable under study relates to the arrangement of the cooling system such as the distance between the cooling stations and the quantity of the cooling stations required to keep the HTS in a superconductivity state.

3. Under fault conditions, the HTS cable generates joule heating, and this leads to the quenching of the cable by boiling the coolant. Whether quenching the cable can be withstood or degrade the cable permanently needs to be checked.

4. Need to find the best topology for the HTS cable suggested to fit in the HVDC network.

5. The need for integrating a Superconducting Fault Current Limiter (SFCL) with High-Temperature Superconductors (HTS) to limit fault currents in electrical transmission systems.

For the long-distance cable formation, there is a need to connect the developed components of a short length instead of a bulk cable consideration. This makes the system more complex and increases the simulation time.

By addressing these research problems, this thesis aims to contribute to the advancement of HTS cable technology, making it a viable and sustainable option for enhancing the efficiency and reliability of HTS power transmission systems.

## 1.5. Research Contribution

This research presents a novel modelling framework aimed at enhancing the assessment of HTS power cables within HVDC grids, specifically addressing offshore renewable energy transmission challenges. Key contributions include the innovative discrete element modelling approach for HVDC HTS power cables, as well as the development of custom SIMSCAPE superconductor elements in MATLAB. This model improves on previous work by allowing a more accurate examination of electrical and thermal dynamics along the cable's length.

The findings reveal that the distributed model provides significantly more precise insights into temperature distribution and electrical behaviour along the length of the cable's cooling system compared to traditional lumped models. This thesis identifies critical points of thermal stress and demonstrates improved methods for predicting cable performance under both steady-state and transient conditions. Through comparative analysis, it establishes that the distributed model effectively predicts electrical and thermal behaviour, including current distribution and temperature, as well as quantifies losses under harmonic conditions more accurately than conventional models.

Another breakthrough, a PbSn joint was fabricated for HTS cable joints, and its resistance was rigorously measured and used in simulations. The critical current ($I_c$) characteristics of the superconductor tapes were analysed, revealing improved joint performance metrics essential for practical deployment.

Furthermore, the research provides a comprehensive thermo-hydraulic analysis of a 10 kA/100 kV/1 GW HTS HVDC cable across multiple topologies, detailing LN2 flow dynamics in both turbulent and laminar regimes and examining different flow arrangements. Notably, the analysis demonstrates that specific flow configurations significantly impact the thermal and electrical stability of the cable, offering guidance on optimal cooling strategies for high-power HVDC applications. The 100 kV rating in this study was chosen as a practical balance for current HVDC technology, considering breaker limits. Higher voltages face challenges like increased insulation needs, higher converter station and offshore platform costs, and more complex fault protection due to limited DC circuit breaker capacity. The study concludes with a comparative assessment of HTS cables with and without a superconducting fault current limiter (SFCL), revealing that SFCL integration can mitigate fault conditions while maintaining thermal stability.

This research advances the modelling of HVDC superconducting cables, paving the way for efficient, large-scale offshore energy transmission. The outcomes offer a pathway to minimise HTS cable losses and advance the feasibility of HVDC SuperGrids, representing a substantial technical progression for future subsea energy networks.

## 1.6. Thesis Organization

Chapter 2: This chapter introduces superconductivity, superconducting materials, and their underlying theories. It provides information on the classification of superconductor power cables, discussing their advantages and disadvantages.

Chapter 3: This chapter begins with an introduction to the modelling of superconductor power cables. It presents different modelling approaches and reviews the relevant literature on various models. The chapter also reviews the current literature on various

ongoing superconductor power cable demonstrations, operational projects, and upcoming initiatives.

Chapter 4: This chapter focuses on the development of superconductor cable components in MATLAB/SIMSCAPE. It details the methodology for superconductor cable modelling, including the calculation of inductance and capacitance in HTS cables. The study examines both lumped and distributed HTS cable models for thermal-electrical-hydraulic analysis, exploring changes in electrical-thermal behaviour during PG faults in the grid and the impact of fault location on superconductor power cable performance. Chapter 4 is based on publications 1 and 4 in section 1.7.

Chapter 5: This chapter elaborates on the electrical behaviour study of 2G HTS, including the critical current for HTS applications and a comparison of quench characteristics through experiments and simulations for validation. A joint on the 2G HTS tape for the superconductor power cable was fabricated, and its resistance behaviour was studied. The resistance achieved in this joint was used in the HTS power cable Simscape blocks implemented.

Chapter 6: This chapter introduces the FEM model of the superconductor power cable and studies its electromagnetic behaviour. It addresses the impact of harmonic losses in HTS power cables.

Chapter 7: This chapter explores the temperature and pressure studies of superconductor power cables based on LN2 mass flow and hydraulic diameter, as well as the roughness of the cryopath wall. It examines the thermal behaviour of CORC HTS cables with different LN2 cooling arrangements. Additionally, the chapter discusses the integration of SFCL in the grid with HTS power cables and demonstrates fault current limiting behaviour during faults.

Chapter 8: This chapter concludes the present study and outlines the plans and necessary steps for implementing superconductor power cables for long-distance energy transmission.

# 1.7. Publications

[1] Chaganti, Pavan, Weijia Yuan, Lie Xu, Min Zhang, Eoin Hodge, John Fitzgerald, and Paul McKeever. "Transient Analysis of HVDC HTS Cable in Power Grid Using Discretized Electrical-Thermal Model." IEEE Transactions on Applied Superconductivity (2024).

[2] Chaganti, P., Kawal, K., Hong, Q., Yuan, W., Zhang, M., Allais, A., Sau grain, J.M., Pochylski, A., West, B., Lallouet, N. and Ross, M. "HTS Cable and Protection System Study for UK's 275 kV Transmission Network," in IEEE Transactions on Applied Superconductivity, doi: 10.1109/TASC.2024.3363125.

[3] Yuan, W., Chaganti, P., Hong, Q., Kawal, K., Zhang, M., Maclennan, D., Strachan, A., Ward, K., Baxter, L., Saugrain, J.M. and Allais, A. "Design and Economic Analysis of 275 kV HTS Cable for UK Transmission Network." IEEE Transactions on Applied Superconductivity (2024)., doi: 10.1109/TASC.2024.3361869.

[4] Chaganti, Pavan, Weijia Yuan, Min Zhang, Lie Xu, Eoin Hodge, and John Fitzgerald. "Modelling of a high-temperature superconductor HVDC cable under transient conditions." IEEE Transactions on Applied Superconductivity 33, no. 5 (2023): 1-5.

# Chapter 2

# Superconductivity Overview

## 2.1. Introduction to superconductivity

In 1908, Heike Kamerlingh Onnes discovered the superconductivity principle in mercury at a temperature of 4.2 K. He discovered that mercury resistance exponentially drops to zero when the temperature reaches 4.2 K or below [29], [30]. This phenomenon was named superconductivity and for this discovery, Onnes received the Nobel Prize in 1911. The superconductor maintains the superconductivity region until the three interdependent parameters of current density, temperature, and magnetic field are below critical values. If any of these values exceed the critical value, the superconductor loses its superconductivity and resistance increases sharply, as shown in Figure 2.1.
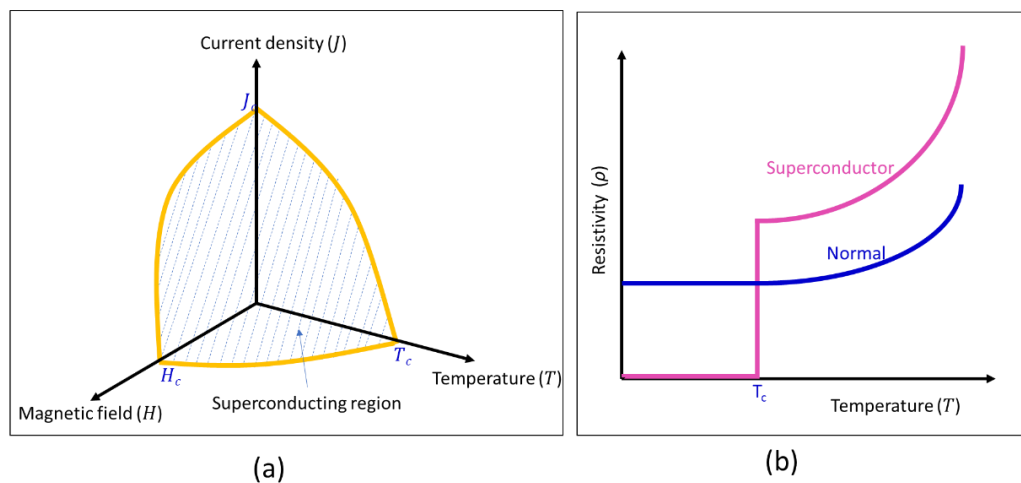
Figure 2.1 (a) Superconductivity in a 3D view defined by current density, temperature, and magnetic field and (b) resistivity behaviour with a change in temperature

In 1933, researchers Meissner and Ochsenfeld discovered that a superconductor is purely diamagnetic, hence it repels the magnetic fields irrespective of the initial conditions

[31]. As shown in Figure 2.2, when the HTS tape cooled below the critical temperature $T_c$ with and without an initial magnetic field application, the superconductor always repels the magnetic field applied. In the case of perfect or ideal conductors, the initial magnetic field conditions impact the conductor's behaviour. In an ideal conductor when there is no field, initially above $T_c$ and cooldown to below $T_c$, it will behave the same as the superconductor. The ideal conductor with an initial magnetic field application above $T_c$ and below $T_c$ means there will be no change in behaviour. The magnetic field properties will not change irrespective of the critical temperature.
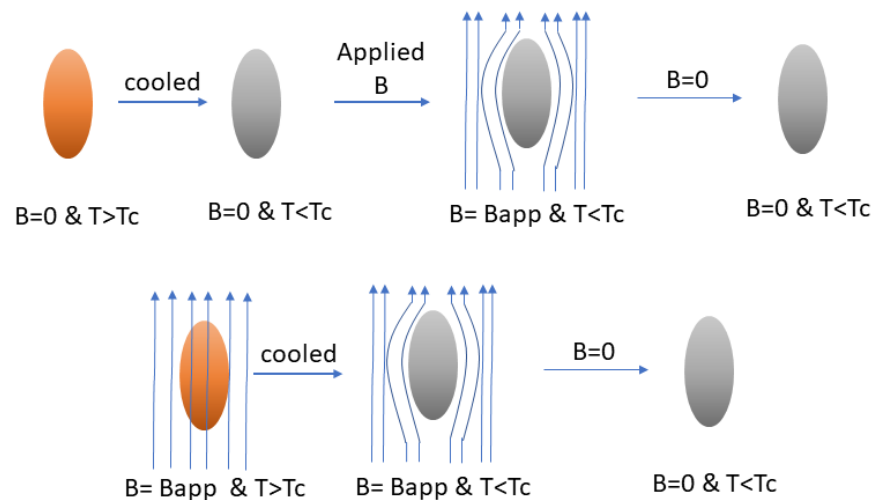


Figure 2.2 Meissner effect in superconductors replotted from reference [31].

## 2.2. Classification of superconductors

Since the discovery of superconductivity in mercury over a century ago, scientists have been on the lookout for new superconductor materials. Several superconductor materials have been discovered since then. They were categorised accordingly by the researchers.

### 2.2.1. Based on the critical temperature

Based on critical temperature, superconductors are classified as either low-temperature superconductors (LTS) or high-temperature superconductors (HTS). When

superconductivity at a high magnetic field became attainable, low-temperature superconductors were first used in electrical equipment in the early 1960s [32]. Magnetic resonance imaging (MRI), nuclear magnetic resonance (NMR), low-temperature superconducting magnets, and high-energy physics accelerators are just a few of the applications for NbTi, $Nb_3Al$ or $MgB_2$ and $Nb_3Sn$ cables [33]. However, the widespread use of LTS was marred by issues from the usage of liquid helium for cooling purposes, in terms of cost and energy efficiency. The discovery of the first HTS in 1986 with a critical temperature of around $T_c$ =35 K [34], reignited the interest in its use in electrical applications such as power cables, motors, generators, transformers, and fault current limiters [35], [36], [37], [38], [39], [40]. Superconductors with critical temperatures below 30 K are considered LTS, while those with critical temperatures above 30 K are considered HTS [41], [42]. In 1987, the YBCO was discovered which can operate at the boiling point of liquid nitrogen, followed by BSCC-2223, and $MgB_2$ [43], [44]. The evolution of superconductors is depicted in Figure 2.3.
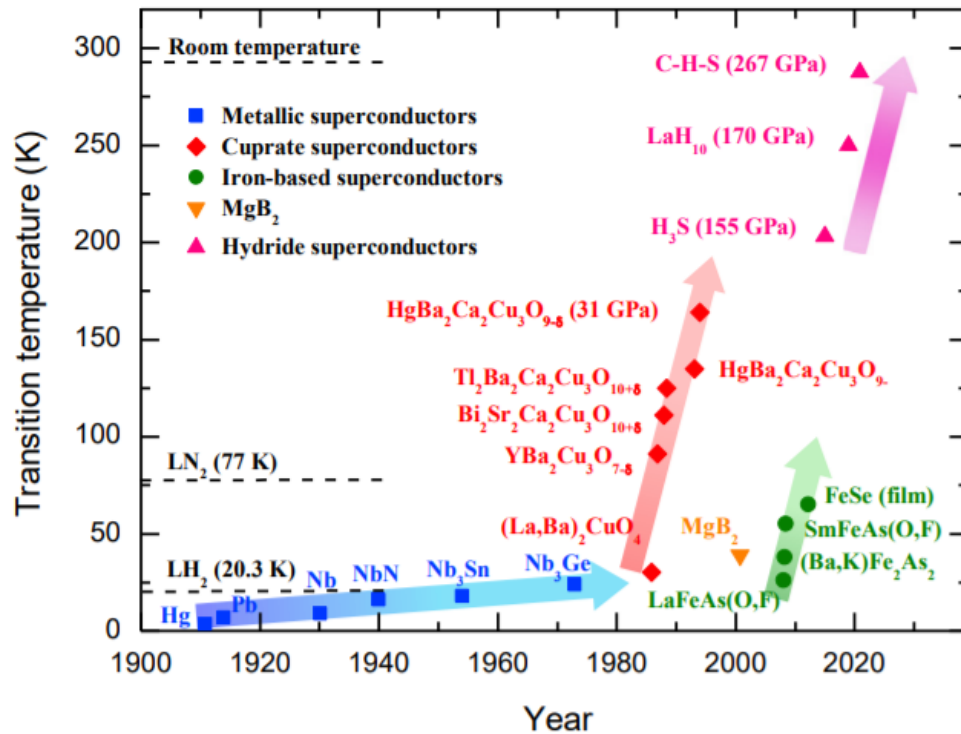


Figure 2.3 Superconductor evolution from the early 1900s to the present [45]

## 2.2.2.    Based on the reaction to the magnetic field

Superconductors can be classified into two types depending on how they respond to an external magnetic field and how rapidly they shift from a superconducting state to one that allows energy dissipation. There are type I and type II superconductors as shown in Figure 2.4.

As a result, the significant Meissner effect type I superconductor loses its superconductive properties instantly when the field $H$ surpasses the critical value $H_c$. While the type II superconductor behaves differently from Type I, it enters a total of three states capable of operating at higher magnetic fields. It has two operating critical points for the $H$ ($H_{ca}$ and $H_{cb}$). When the $H<H_{ca}$ the type II superconductor behaves as a type I superconductor which is perfectly diamagnetic.  When the field reaches $H> H_{ca}$ and $H<H_{cb}$ it starts forming vortices that allow the magnetic fields to penetrate into the superconductor, enabling larger transport currents. When $H>H_{cb}$ it will move to a dissipative state.  In type II $H_{cb}$ is much higher than the $H_{ca}$ which makes type II superior to type I superconductors. For YBCO tape, the Hca is 20 mT and the $H_{cb}$ is 100 T. Type I superconductors that are LTS, and type II are considered to be HTS with a few LTS also.
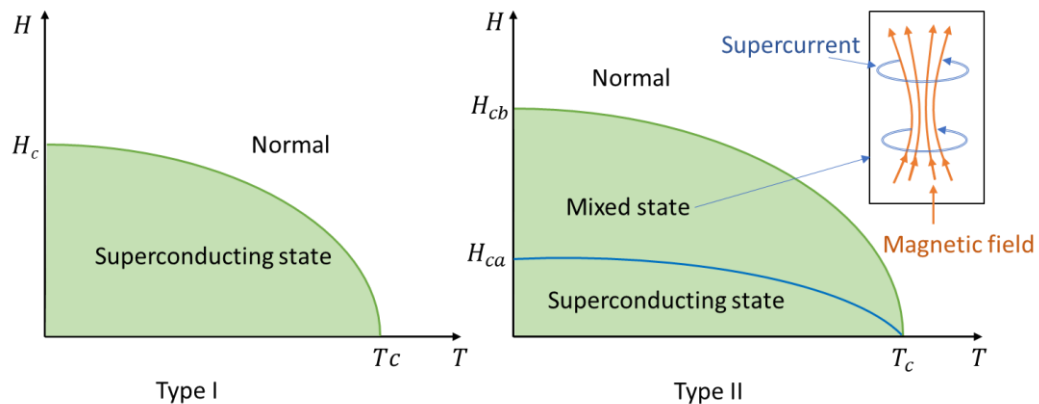


Figure 2.4 Critical field characteristics of Type I and Type II

The current, known as the screening current, on the surface of a superconductor repels the external magnetic field. This screening current in the tapes is responsible for the

Meissner effect. The remainder of the superconductor forms vortices from the residual current. These vortices permit some of the magnetic fields to penetrate them without losing superconductivity.

The vortices illustrated in Figure 2.5 depict small tubular regions, each encapsulating a single quantum of magnetic flux.

$$\varphi = \frac{h}{2e} = 2.068 \times 10^{-15} \, Tm^2 \qquad\qquad 2.1$$

Where '$e$' represents the electronic charge and '$h$' denotes Planck's constant.

The flux passing through the superconductor is referred to as pinning flux because it is immobilised by the pinning force. If the applied magnetic field $H$ begins to increase, the vortices move closer together and may overlap. As the magnetic field intensifies from $H_{ca}$ to $H_{cb}$ they start to overlap. Upon reaching $H = H_{cb}$, vortex and Cooper pairs disappear, and the applied magnetic field fully penetrates the superconductor, causing it to lose its superconducting properties.
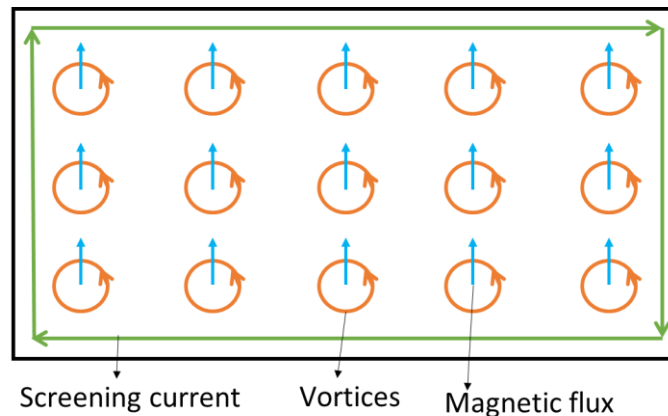


Figure 2.5 Type II superconductor mixed state.

The magnetic flux is trapped by the pinning force, requiring additional energy to alter it. While carrying DC, no additional power is needed, as the magnitude and direction remain constant. However, when carrying AC currents, its magnetic field changes in both magnitude and direction continuously.

In 1948, Fritz London solved the phenomenal London equation to give the consequence of the coherence of the quantum state. Later in 1953, Brian Pippard, motivated by the penetration experiments, modified the London equation using the new scale parameter coherence length $\lambda$.

It is necessary to define a vortex line and a flux line to comprehend the meaning of penetration depth $\lambda$ and coherence length $\xi$ as shown in Figure 2.6. As previously mentioned, a flux line can enter a type II superconductor in the form of quantised circulation, which is the primary difference between type II and type I superconductors. Superconductivity is eliminated at the centre of each flux line, meaning that the density of the superelectrons is equal to zero, and the coherence length is roughly equivalent to the diameter of a vortex's normal core. Supercurrent circulates around the vortex line; the radius of this circulation around the vortex core is measured by the penetration depth [2]. It is evident that $k < 1/\sqrt{2}$ indicates a type I superconductor and $k > 1/\sqrt{2}$ indicates a type II superconductor if $\kappa = \lambda/\xi$ is established [46], [47]. The superconducting coherence is preserved within the sample over comparatively wide distances because $\xi > \lambda$. External magnetic forces do not cause any disruption to the superelectrons' overall coherence. The $k$ values for the type I and for the YBCO (type II) are 0.48 and 95, respectively [48], [49].

The most famous among the (RE)BCO material and the first one found with a critical temperature above the boiling point of LN2 is Yttrium Barium Copper Oxide ($YBa_2Cu_3O_7$-x) or (Y123). The most known and popular rare earth materials choices are yttrium, lanthanum, samarium, neodymium, gadolinium, and europium. The number in the brackets indicates the molar ratio values of the rare-earth-barium-copper.

It is a unit cell like the structure of perovskites and its molar mass is 1:2:3 for yttrium, barium, and copper, respectively. The overlapping structure of YBCO is shown in Figure 2.7. It contains three subunit particles stacked along the axis as the barium subunits one at the top, another at the bottom, and yttrium at the centre. The copper in the lattice is at the corners which have two different coordinates concerning oxygen. The oxygen was arranged in the four possible crystallographic sites.
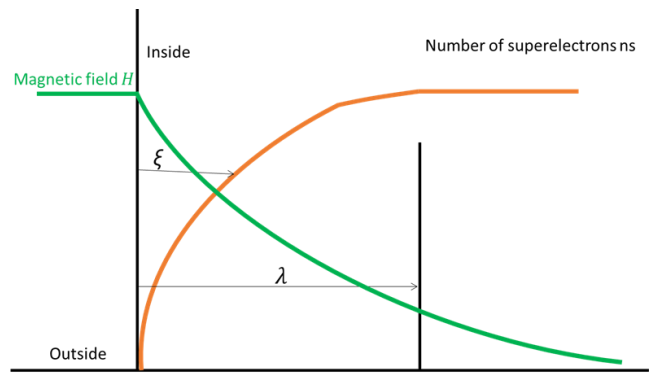
(a) Type I superconductors
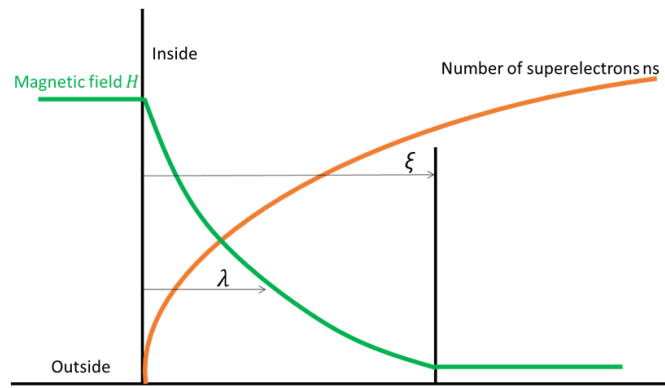


(b) Type II superconductors

Figure 2.6  Coherence length and penetration depth of the Type I and Type II relationships.
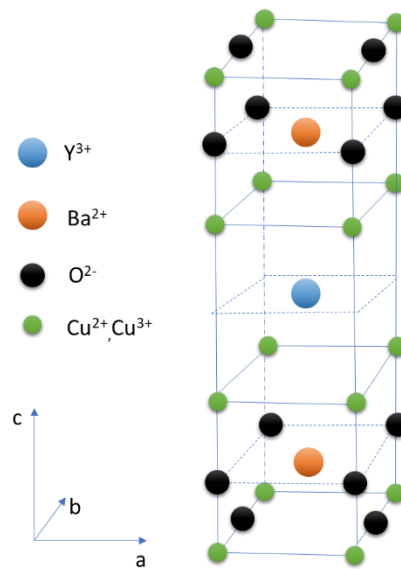


Figure 2.7 Type II superconductor YBCO single crystalline structure.

## 2.3. High-temperature Superconducting material and tapes

Several varieties of superconductor materials are depicted in Figure 2.8 below. In superconductors of the NbTi and $Nb_3Sn$ types, NbTi is more ductile, easier to fabricate, and less expensive for applications below 20 K. $Nb_3Sn$, on the other hand, is brittle and cannot be easily formed into a wire-like NbTi. With a range of 9 to 11 T for 4.2 to 1.8 K, the NbTi superconductor is employed in MRI systems, magnetic levitation trains, and superconducting magnets. The $Nb_3Sn$ superconductors are employed in high-field magnets for scientific research that can reach up to 23 T, including MRI systems, NMR equipment, particle accelerators, and tokamak fusion devices.

Copper oxide superconducting materials Bi-2223, Bi-2212, and REBCO have a critical temperature above 77 K which is the operating point for LN2. The cost of refrigeration of nitrogen is cheaper than helium and is available in abundance.  These tapes are more complex to form into wire because of the ceramic brittleness. Cuprate components are made by regulating the oxygen in the ceramic components during high-temperature heat treatment to create a superconducting phase. Because of the superior current density of REBCO tapes, Bi-2223 and Bi-2212 are 1G (1st generation) and REBCO (RE- rare earth materials) are 2G (2nd generation). The power in-the-tube (PIT) technology is used to make Bi-based 1G tapes, which have issues with grain control and low inter-grain conductivity. Increased conductivity necessitates the use of silver, which raises the cost. REBCO tapes, however, use a coated conductor (CC) that allows for grain orientation control and high current densities. The CC manufacturing process adopts either rolling-assisted biaxially textured substrates (RABiTS) or ion-beam-assisted deposition (IBAD) technology.

The $MgB_2$ tapes are not sensitive to weakly linked grains like copper oxide superconducting materials. It was prepared using the PIT method and internal Mg diffusion method. The raw material cost is economical and more compact than others. The critical current $I_c$ drops quickly as the magnetic field increases. It is used where there is a low magnetic field and high $T_c$. In iron-based superconductors, the inter-grain

conductivity across the mismatched grains is better than in REBCO tapes. The simple low-cost PIT method can be adopted for these tapes and comes with a variety of selections for the sheet materials, unlike Bi-2223 and Bi-2212 tapes.
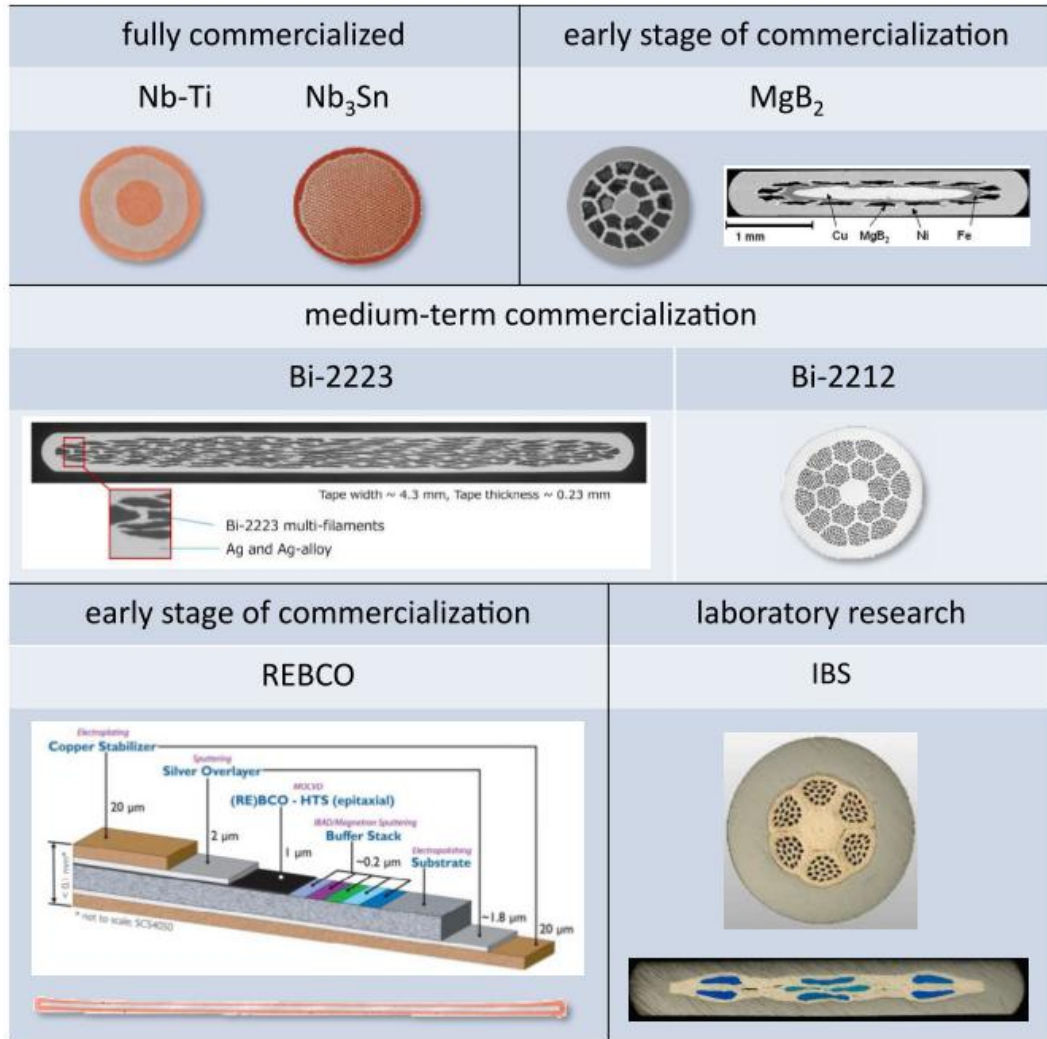


Figure 2.8 Superconducting material tapes and wires [45]

## 2.4. Superconductor model theories

Superconductors are highly anisotropic and have nonlinear electromagnetic properties. Various writers have suggested simplified theories based on certain essential assumptions to simulate the HTS. Superconductor design is expensive and making prototypes is not

economical. Numerical modelling is the best approach to identifying electromagnetic behaviour. The proposed theories that describe the HTS from the macroscopic point of view are as follows:

- Bean's model

- *E - J* Power law

- Kim-Anderson model

## 2.4.1.    Beans model

In 1962, C.P. Bean introduced Bean's critical state model to explain the macroscopic behaviour of irreversible magnetization in type II superconductors [50], [51].

Figure 2.9 (a) shows the superconductor slab with a magnetic field and current density *J* and Figure 2.9 (b) depicts the magnetization loop in the Type II hard superconductor, showing the hysteresis behaviour of the superconductor slab based on Bean's model. In Type II superconductors, the magnetization curve demonstrates a hysteresis effect due to the presence of pinning centres, which directly influences this behaviour. This hysteresis arises from the superconductor's shield current, which is at the surface. Initially, up to a certain magnetic field strength ($B_{c1}$), flux lines are prevented from entering the superconductor and are instead anchored at the surface's pinning centres, leading to almost perfect diamagnetism. Once the magnetic field exceeds $B_{c1}$, flux lines begin to infiltrate the superconductor until the magnetization completely vanishes at $B_{c2}$. When the magnetic field is subsequently reduced, the flux lines remain confined within the superconductor, continuing to do so even when the field strength returns to zero.

Current density $J_c$ is assumed to be uniform across the superconductor and its values are considered either 0 or $J_c$ based on the magnetic field or electric field as mentioned in the below equation.

The current density is expressed as a function of the electric field.

$$J = \begin{cases} 0, & E \geq E_c \\ J_c, & E < E_c \end{cases} \qquad 2.2$$

Where $E$ is the generated electric field, $E_c$ is the critical electrical field and the critical current density $J_c$ is a function of the $B_i$ (local flux density inside the superconductor).



(a)　　　　　　　　　　(b)
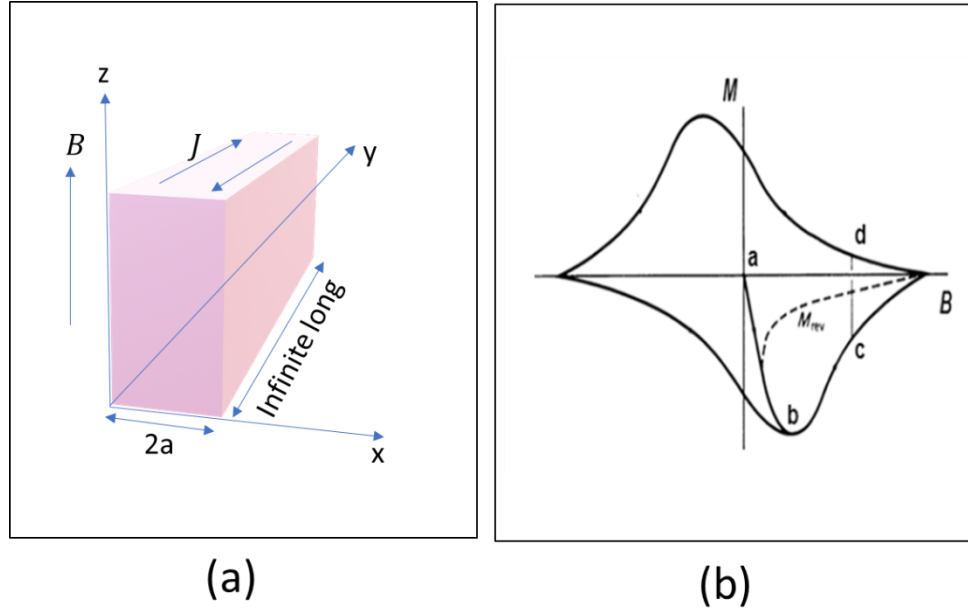
Figure 2.9 (a) Infinite long HTS slab and (b) magnetization loop of the superconductor type II, indicating the initial curve (a, b) from zero induction and a pair of magnetization values (c, d) used to extract Jc [52]

The bean model has the advantage of acting as both diamagnetic and paramagnetic and it is possible to remember the previous magnetic history data when it is used in the simulation. In this context, $a_p$ refers to the depth of penetration within the HTS material, and $H^*$ signifies the complete penetration magnetic field, meaning that the applied magnetic field penetrates fully to the centre of the superconductor shown in Figure 2.10.

The screening current is within the London penetration depth during the Meissner phase. When increase in the magnetic field above $H_{ca}$, vortices start to penetrate the superconductor and are pinned on the surface of the superconductor tapes. The current that was below this penetration depth will be $J_c$. If the field further increases above $H^*$, the vortices fully penetrate the superconductor.

When the HTS carries a transport current rather than being exposed to an external magnetic field, its magnetic and current distribution is illustrated in Figure 2.11. It is a simplified model but still faces issues with accuracy due to uniform $J_c$. assumptions and applications to thin tapes.
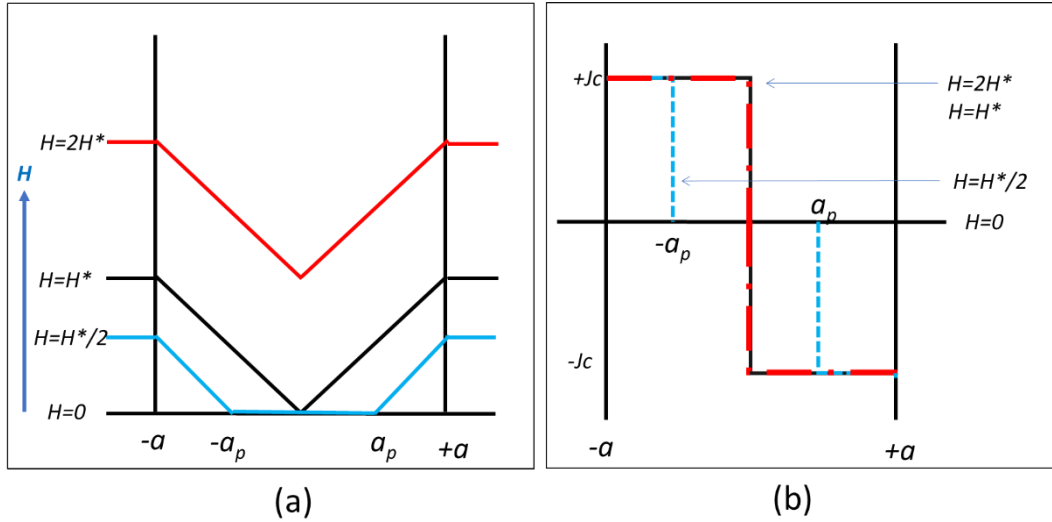


Figure 2.10 When increasing the external magnetic field on an infinite long HTS slab (a) magnetic field and (b) current distribution inside the HTS
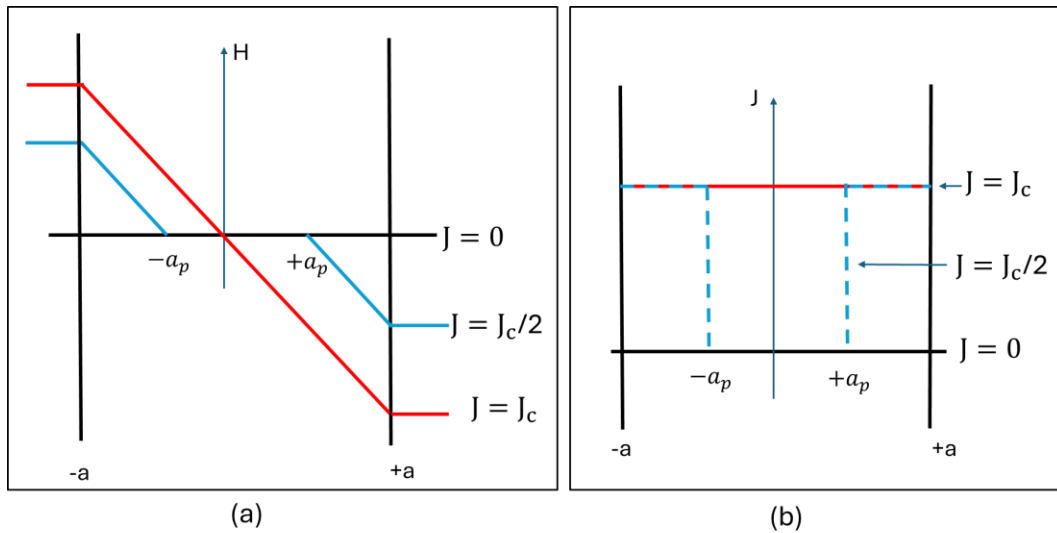


Figure 2.11 When long HTS slab carying transport current (a) magnetic field and (b) current distribution inside the HTS

## 2.4.2.    *E - J* Power law

Rhyner proposed the *E-J* power law for the non-linear behaviour of the superconductor [53]. The proposed *V-I* curve results fit well with many HTS material results conducted through experiments.

The *E-J* characteristics of the HTS are nonlinear and represented as follows:

$$E = E_c(\frac{J}{J_c})^n \qquad\qquad 2.3$$

$E_c$ is the electric field due to flux creep at $J = J_c$

The resistivity of the tape is expressed as follows using the *E-J* power law.

$$\rho_{hts}(J) = \frac{E_c}{J_c} \times (\frac{J}{J_c})^n \qquad\qquad 2.4$$

*n* is the exponential coefficient that differs from the HTS material.

Bean's model delineates a stark transition from the superconducting to the normal state as depicted in Figure 2.12. Specifically, in instances where *n*=1 and *n*=∞, this correlates with the linear Ohm's law *E=ρJ* and Bean's critical state model where the current density *J* is either zero or at the critical value $J_c$. For *n*=5, this indicates significant flux creep, while *n*=15 and *n*=50 represent weak flux creep and a demarcation between Low-Temperature Superconductors (LTS) and High-Temperature Superconductors (HTS), respectively [54]. For n values exceeding 20, Bean's model is considered a robust approximation. Notably, for Bi-2212 materials, n ranges between 5 and 15, whereas for YBCO tapes, it ranges from 20 to 30 [55], [56], [57].

The *E-J* curve is segmented into three phases: flux creep, flux flow, and normal phase. Anderson proposed the flux creep theory for hard superconductors [58]. During the flux creep phase, the transport current initiates a vortex motion within the HTS material. At this juncture, the Lorentz force acting on the superconductor equals the pinning force, causing the vortice flux lattice to move slowly. Conversely, in the flux flow state, the

Lorentz force surpasses the pinning force, leading to the unrestricted movement of the flux lattice. In this phase, n values typically range from 2 to 4 for both LTS and HTS materials. In the normal phase, the vortices dissipate, and the material loses its superconductivity. Here, the n value is typically 1. The *E-J* curve's three stages are shown in Figure 2.13.
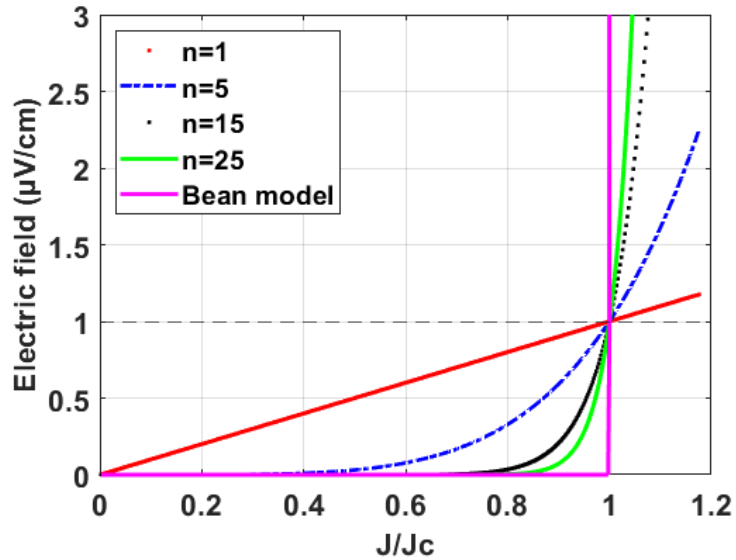


Figure 2.12 E-J power law figure based on then=1 to n=∞
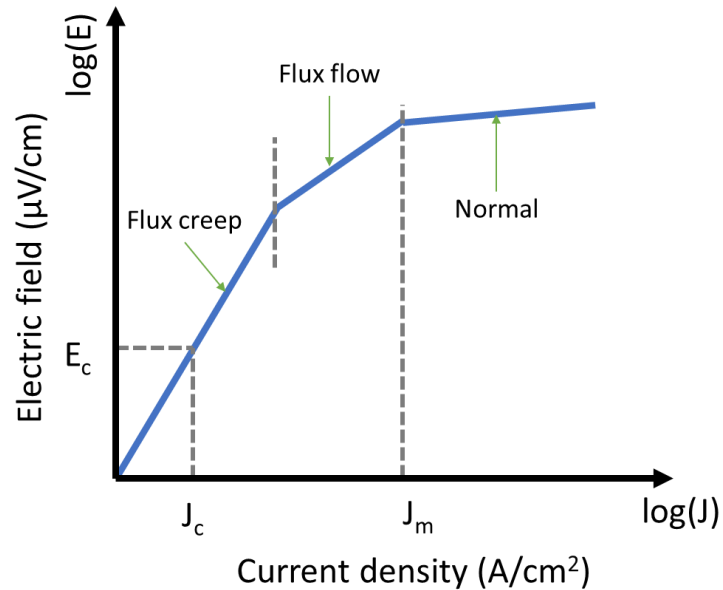


Figure 2.13 E-J power law curve showing the three stages below T$_c$ in log scale.

### 2.4.3.    Kim-Anderson model

Researchers Kim, Hempstead, Strnad, and Anderson studied the critical phenomenon in a superconductor of type II [59]. Chen and Goldfarb pointed out that the equation below is a more generalised model for the critical state model and that it is like a linear model where $B_o >> B$. Kim and Anderson showed a relationship where the critical current is dependent on the local magnetic field and temperature. It defines the $J_c$ as a function of the magnetic field $B$.

$$J_c(B,T) = \frac{J_{co}(T)}{(1+\frac{B}{B_o})}$$                    2.5

$J_{co}(T)$ is the temperature-dependent current density at zero fields and $B_o$ is constant.

This model is more efficient than the Beans model but still fails to solve the anisotropic critical current behaviour under a magnetic field in a different direction.

## 2.5. AC losses in superconductors

Transport current losses and magnetization losses are the two types of AC losses found in superconductors. The flow of electrical current through the superconducting material causes transport current losses, and the voltage across the test specimen indicates the amount of power lost. Transport current can be classified into two types: hysteresis losses and flux flow losses. Hysteresis losses result from the self-field generated by the applied transport current. On the other hand, flux flow losses occur when the transport current intensifies, generating an additional magnetic flux, which in turn begins to unpin the vortex. As the vortex starts moving, it generates heat, leading to what is known as flux flow loss. With an increase in transport current, flux flow losses become increasingly dominant.

Magnetization losses consist of hysteresis, coupling, and eddy current losses. Hysteresis losses stem from the non-reversible behaviour caused by vortex pinning. As the magnetic field increases and decreases, the magnetic flux does not replicate this behaviour due to

vortex pinning, leading to a hysteresis loop in the *B-H* curve for a single cycle. In the absence of a transport current, hysteresis losses correlate with the area enclosed by this loop. These losses manifest as heat and are significant due to the strong pinning forces, high critical current ($I_c$) values, and notable losses in type II superconductors.

Eddy current losses occur when a time-varying magnetic field penetrates a normal conductor, such as Hastelloy, copper, or silver, inducing an electric field and consequently, eddy currents occur within sections of the superconductor tapes. These currents lead to resistive energy loss, particularly when the magnetic field is perpendicular to the plane of the superconductor tape.

Coupling losses arise from ohmic losses in the metal matrix. As eddy currents flow through the layers of silver filaments, these inter-filamentary currents create a significant magnetic system, with the inherent resistance of silver opposing the current flow, leading to ohmic losses.

According to the critical state model, a superconductor experiences no losses when subjected to direct current (DC) or a DC magnetic field. Redistribution of the magnetic field within the superconductor occurs due to transport current or magnetic field variations, with Faraday's law describing the relationship between flux motion and the induced electric field in the superconductor, where the current density and electric field align. This forms the basis for understanding magnetization losses in superconductors.

$$Q = \int_S EJdS \qquad\qquad 2.6$$

Where *Q* is the total losses in the superconductors.

## 2.5.1.     Analytical techniques for AC loss

Norris and Brandt proposed the equations used to calculate transport current and AC magnetization losses in a superconductor. These two are used in the verification of the accuracy of AC losses using FEM (Finite Element Method) and other techniques.

### 2.5.1.1. Norris

The Norris model provides an approach to estimate AC losses in a self-field situation. It utilises the London model as a foundation. In this model, resistance undergoes a step change when the transport current exceeds the critical current ($I > I_c$), ensuring that the ohmic voltage drop perfectly counterbalances the driving electromotive force (emf) while maintaining a constant current density. However, the current density depends on the magnitude and direction of the magnetic field, contrary to the assumption made here that it is field-independent.

In a superconductor strip carrying a transport current $I$, the AC losses can be described as follows.

$$P_{loss} = \frac{\mu_0 I_c^2 f}{\pi} [(1 - F) \, ln(1 - F) + (1 + F) \, ln(1 + F) - F^2] \quad [\text{w/m}] \qquad 2.7$$

Where $F = \frac{I}{I_c}$, $f$ is the frequency, and $\mu_0$ is the permeability of the free space.

### 2.5.1.2. Brandt

Brandt introduced an innovative approach to evaluate the alternating current (AC) losses within the two-dimensional domain of high-temperature superconductors (HTS) by applying the $E$-$J$ power law within the context of Maxwell's equations for a HTS strip under the influence of perpendicular magnetic fields. $H_c$ represents the critical magnetic field value.

In this context, where there are AC losses in the HTS strip subject to an external magnetic field with amplitude, $H_o$, can be computed using the following equation:

$$P_{loss} = 4\pi\mu_0 a^2 H_0 H_c f [\frac{2H_c}{H_0} \, lncosh \left(\frac{H_0}{H_c}\right) - tanh \left(\frac{H_0}{H_c}\right)] \quad [\text{w/m}] \qquad 2.8$$

## 2.6. Summary of Chapter 2

In this chapter, embarked on a comprehensive journey through the evolution and conceptual framework of superconductivity. Beginning with a historical overview, we explored the incremental discoveries and theoretical advancements in superconductor materials from the $18^{th}$ century to the present. This narrative set the stage for understanding the complex landscape of superconductivity, categorizing materials into type I and type II superconductors, each with distinct properties and applications. Further, we delved into the critical state models, particularly the beam and the Kim-Anderson models, which play a pivotal role in understanding the phenomena of flux pinning, flux creep, and the nonlinear characteristics governed by the *E-J* power law. These models not only enhance our grasp of the physical mechanisms at play but also pave the way for engineering applications and innovations in superconducting technologies. Additionally, the chapter addressed the crucial aspect of AC losses in superconductors, which are significant for practical applications, especially in magnetization and transport phenomena. The analytical definitions provided by the Norris and Brandt equations offer a foundational understanding of these losses, enabling further research and development in reducing AC losses in superconductor applications.

# Chapter 3

# Review of Superconductor Modelling

# Methods and Power Cables

## 3.1. Introduction to modelling

### 3.1.1.　　Mathematical models

One of the primary challenges when modelling superconductors is the non-linearity of the *E-J* power law relationship. To address this problem and to analyse the electromagnetic and thermal behaviour of superconductors, various model formulations have been proposed, including *H, E, A-V, J-A*, and *K-ϕ*. These are based on state variables in Maxwell's equations, and each offers distinct advantages and limitations. The formulations are explained in the below section.

#### 3.1.1.1. *H*-formulation

Many research groups worldwide use the *H*-formulation for modelling the electromagnetic behaviour found in high-temperature superconductors (HTS) [60], [61], [62], [63]. The *H*-formulation is favoured across various superconductor topologies due to its good convergence, accuracy, and reasonable computational time. The first commercial finite element method (FEM) of the *H*-formulation was implemented in COMSOL Multiphysics [64] [59]. The name "*H*-formulation" originates from the single dependent variable, magnetic field intensity (*H*), which is used to calculate the macroscopic current and field distribution in the superconductor.

The *H*-formulation utilises the Finite Element Method (FEM) to solve Faraday's law through mathematical formulation [65], [66], [67], [68].

$$\nabla \times E = -\frac{\partial B}{\partial t} \qquad \text{3.1}$$

The strength of the magnetic field is determined by applying both Ampère's and Faraday's laws, along with the relationship between the electric field, current density, and resistivity. The equation is represented as follows:

$$\nabla \times \left(\rho_{hts}\nabla \times \vec{H}\right) = -\mu_0\mu_r\frac{\partial \vec{H}}{\partial t} \qquad \text{3.2}$$

where $\mu_0$ denotes the magnetic permeability of free space, $\mu_r$ is the relative permeability of the material, and $\vec{H}$ is the vector representing magnetic field strength.

The current density can be derived from the magnetic field by utilising the quasi-static approximation of Ampere's Law, as expressed in equation 3.3.

$$J = \nabla \times \vec{H} \qquad \text{3.3}$$

Not as effective when handling complex, multi-material domains, especially in mixed systems. Although effective, there is scope for improving its performance in dynamic fault scenarios involving rapid magnetic field changes, where computational efficiency becomes a challenge.

### 3.1.1.2. *J-A* formulation

Wang Sijian and his colleagues developed a formulation known as the *J-A* formulation, which enhances the accuracy and versatility of superconductor modelling [69]. In this formulation, the current density vector (*J*) and magnetic vector potential (*A*) are coupled. It utilises Maxwell's equations to solve *A* in the expression.

$$\nabla \times \left[\frac{1}{\mu}(\nabla \times A)\right] = J \qquad \text{3.4}$$

The non-linear superconducting behaviour of high-temperature superconductors (HTS) is described by the following equation, using the *J* expression. This relationship is used to explain the characteristics observed in the HTS materials.

$$E = \rho_{hts}J = -\frac{\partial A}{\partial t} - \nabla\varphi \qquad\qquad 3.5$$

Where $\varphi$ is the electrical scalar potential.

The *J-A* formulation is similar to the A-V formulation governing equation. By replacing the $J = \sigma(-\frac{\partial A}{\partial t} - \nabla\varphi)$ in the equation ($E = \rho_{hts}J$), it converts to an *A-V* formulation if we substitute this in the equation above.

The nonlinearity of the conductivity in superconductors introduces numerical complexities into simulations. The *J-A* formulation separates $E$ in Equation 3.5 from Maxwell's equation calculations to mitigate these numerical complexities. Although this approach increases the number of variables, it facilitates easier convergence of the simulation. Increases variables, leading to longer simulation times. The separation of $E$ and $J$ calculations can hinder performance in high-frequency transient studies, where the demand for real-time analysis is high.

### 3.1.1.3. *A-V* formulation

A numerical method for addressing two-dimensional and axially symmetric issues employs Maxwell's equations and the *E-J* power law within the *A-V* formulation [70].

The governing equation to solve nonlinear 2D electromagnetic behaviour using the *A-V* formulation is as follows [71], [72]:

$$\nabla\frac{1}{\mu_0}\nabla A_z + \sigma(E,B)\frac{\partial A_z}{\partial t} = -\sigma(E,B)\nabla V \qquad\qquad 3.6$$

In this equation, $A_z$ represents the magnetic vector potential, and $\nabla V$ denotes the voltage gradient. The electric field, *E*, is derived using the formula:

$$E = -\frac{\partial A_z}{\partial t} - \nabla V \qquad\qquad 3.7$$

Here $\sigma(E, B)$, the non-linear conductivity, is defined as follows:

$$\sigma(E, B) = \frac{J_c(B)}{E^{\frac{1}{n(B)}}} |E|^{\frac{1-n(B)}{n(B)}} \qquad\qquad 3.8$$

In this case, the driving source is a voltage gradient, and $J$ and $A$ are directed along the length of the HTS tapes in the $Z$-direction. The model's 2D constraint suggests that future work should focus on adapting this approach for 3D simulations in complex, heterogeneous environments.

### 3.1.1.4. $K$-$\Omega$ formulation

The numerical model for superconductors is developed using the current vector potential ($K$) and magnetic scalar potential ($\Omega$), employing the Finite Element Method (FEM), known as the $T$-$\Omega$ formulation. This approach utilises the current vector potential ($K$) to calculate the current density ($J$) in the superconducting tapes, as outlined in references [73], [74], [75], [76].

$$J = \nabla \times K \qquad\qquad 3.9$$

In superconductors, the flow of current generates a magnetic field described by:

$$\nabla \times H_s = J \qquad\qquad 3.10$$

The total magnetic field ($H$) is the cumulative effect of the magnetic field generated by the High-Temperature Superconductor (HTS) and the external magnetic field ($H_o$).

$$H = H_s + H_o \qquad\qquad 3.11$$

The magnetic scalar potential ($\Omega$) is defined by:

$$\nabla \Omega = K - H_s \qquad\qquad 3.12$$

Substituting the relevant equations, we obtain the total magnetic field:

$$H = K - \nabla\Omega + H_o \qquad\qquad 3.13$$

To determine the electromagnetic behaviour using the current distribution in the HTS cable and the resultant magnetic fields, Faraday's law and Gauss's law are employed as follows:

$$\nabla \times \sigma\nabla \times K = -\mu\partial\partial t(H_o + K - \nabla\Omega) \qquad\qquad 3.14$$

$$\nabla.\mu\partial\partial t(H_o + K - \nabla\Omega) = 0 \qquad\qquad 3.15$$

In the $K$-$\Omega$ formulation, the transport current ($I_o$) is established through a boundary condition, derived from K at the boundary by integrating $J = \nabla \times K$ across the entire domain.

$$I_o = \int (\nabla \times K).ndS = \oint K.ds \qquad\qquad 3.16$$

Effectively captures current distribution within superconductors. Suitable for large-scale FEM applications. Computationally intensive, requiring substantial processing power. Improvements in computational efficiency are needed, especially for long-duration simulations essential in energy applications.

### 3.1.1.5. Mixed formulation

When a system comprises both superconducting and nonlinear ferromagnetic materials, the classical formulations employed are not very efficient as they encounter convergence issues. By utilising the Newton-Raphson method, the power law can be easily determined in the '$H$' formulation, which relates to resistivity. The '$A$' formulation proves to be more effective than the '$H$' formulation in addressing the typical saturation law associated with ferromagnets. In choosing the most suitable methods to resolve the solution, the '$H$-$A$' formulation presents an efficient approach when addressing systems involving both materials [77], [78].

## 3.1.2. Numerical methods

Numerical methods employ techniques for solving equations numerically. By discretizing models, we can obtain solutions. This involves creating a mesh or grid within the geometry of the problem area. The dimensions of this discretization, specifically how the mesh and grid conform to the boundaries, determines the number of unknowns, referred to as the degree of freedom. This degree of freedom is crucial in determining computational time as well as matrix size and memory requirements. These numerical methods can be either the integral method, Finite difference method, volume element method, discontinuity and minimum of energy method, or another hybrid of any two methods, etc.

### 3.1.2.1. Integral methods

One benefit of integral approaches is their ability to remove boundary conditions. They are employed to define the current distribution in the superconductor field, and the integrated parameters of the magnetic vector potential and the magnetic field are used to determine the total energy within the domain. The integrator and optimised mathematical techniques are utilised to find the optimum current distribution in the HTS.

Early formulations were created by C.J. Carr, who used the transport current and an external magnetic field to study AC losses in superconductors. To characterise the penetration in the Type II superconductor, Brandt created the Brandt model. Subsequently, researchers began solving the time derivative of the current density based on basic geometric shapes such as thin tapes, rectangular bars, and cylindrical bulks using integral equations.

To avoid dealing with the integral equation, a discrete model was offered as an alternative to the original formulation of the integral method. This involved splitting the superconductor's geometry into N elements, each of which was given a uniform current density.

### 3.1.2.2.  Finite difference method

The finite difference method is a numerical technique that addresses differential equations by approximating derivatives with finite differences. This method can be segmented into finite intervals, either in the time or spatial domains, where the final values of the solution at the endpoints are approximated by solving algebraic equations derived from the finite differences at adjacent points. The finite difference approach transforms partial or ordinary differential equations, which may be nonlinear, into a system of linear equations using algebraic matrices.

### 3.1.2.3.  Finite volume method

The volume method is a technique where we use the integral of the volume in coordinate systems. It uses aspects from both the finite element and difference methods according to the partial differential equations in the physical conversion law. It can be applied to the complex geometry shapes of the superconductor.

A numerical integration method based on point-wise calculation is utilised within the volume integral formulation for each control volume, employing a predefined polynomial approximation. This involves the computation of flux integrals that traverse the boundaries of the established control volumes within the mesh, which are then linearly approximated as numerical fluxes. The finite volume approach requires only a limited number of degrees of freedom to approximate a solution closely. In the case of structured meshes, the resultant matrix is banded and sparse. Conversely, with unstructured meshes, the matrix does not exhibit a linear structure.

## 3.1.3.      Superconductor power cable modelling

In contrast to conventional power cables, high-temperature superconductors (HTS) have been rapidly designed for efficient electricity transmission due to their low losses, high transmission capability, small size, and absence of electromagnetic pollution [79]. As they are used in a transmission system, however, they are often exposed to over-currents

induced by a short circuit fault. A large amount of joule heat is generated in these situations, which can compromise the HTS cable's stability and reduce power transmission performance. To study the behaviour of any HTS system, detailed electrical and cryogenic thermal models of the device are needed. Coupled thermal and electrical models are needed because the electrical and thermal outputs of HTS devices are intertwined.

Finite-element modelling (FEM) is a sophisticated and effective computational approach for solving boundary-value problems based on the discretization of a domain into a finite number of elements. Such software can successfully replicate non-linear behaviour in superconducting cables [80]. The effect of various parameters on the steady-state and transient heat transfer phenomena in HTS power cables is frequently studied using FEM methods. However, because of the long simulation time, the computational effort needed to obtain accurate results is typically high, making FEM applications inefficient.

Modelling the complex behaviour of a superconducting magnet using a network of non-linear lumped elements and solving it with in-house or commercial network solvers such as Simulink, PSpice, SPICE, or Simscape is an alternative method. In certain cases, the electromagnetic and thermal dynamics of a superconducting magnet can be reliably replicated using only limited differential-algebraic equations.

To discover a quick and adaptable modelling technique that enables system-level parametric analyses of the electrical-thermal behaviour of HTS devices, a Thermal Network Model (TNM) was examined. The TNM, which consists of thermal resistors, thermal capacitors, heat sources, and temperature potentials comparable to an electrical circuit, is based on the analogy between thermal and electrical fields to determine the temperature distribution with the aid of Kirchhoff's Law, Ohm's Law, and the superposition principle [26].

This technique necessitates a detailed understanding of the phenomena that exist in coil strands and cables since they have a direct effect on the device dynamics. This results in

a substantial reduction in CPU time for solving the model compared to FEM when properly implemented.

A numerical approach using partial differential equations (PDEs) can model these interactions by dividing the cable into domains with specific state variables. The thermal domain models temperature changes via diffusion equations, while the hydraulic domain accounts for cooling flow dynamics through conservation equations. Lastly, the electrical domain includes circuit equations for current flow, with each domain interconnected through state variable dependencies, ensuring a consistent and comprehensive simulation of superconductor performance [81].

A critical factor when assessing the effectiveness of each cooling strategy is the maximum length of the HTS cable. Every cooling design is required to meet the established technical specifications. This compliance can be verified through a comprehensive analysis of the cable's electrical, hydraulic, and thermal characteristics, as detailed in sections 3.1.3.1 to 3.13.3. Additionally, when designing the HTS cable, it is essential to consider the parameters [4] illustrated in Figure 3.1 below.
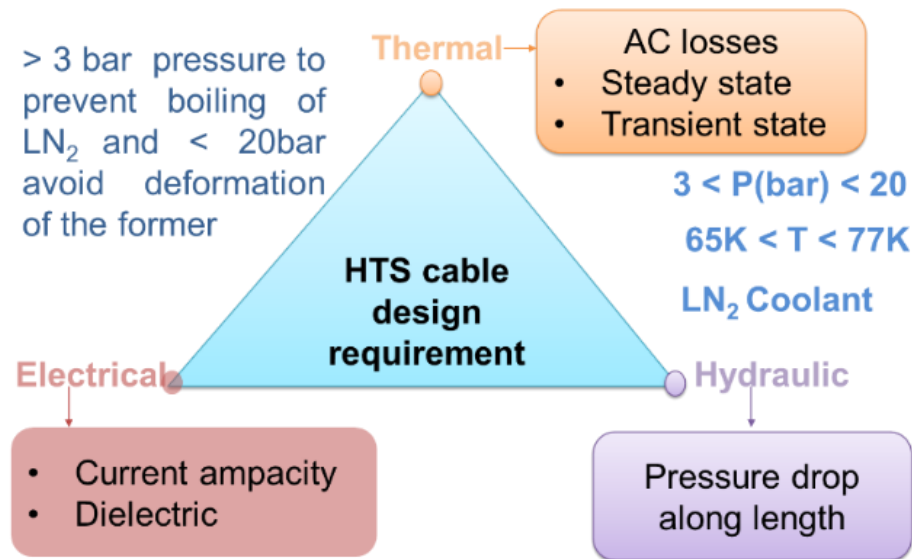


Figure 3.1 HTS cable design requirement considerations when LN2 is used in the system replotted from reference [4]

### 3.1.3.1. Hydraulic parameter formulations

The electrical characteristics of the HTS cable depend on the temperature of the coolant used, and the coolant temperature needs to be maintained below a specific limit range. The coolant or refrigerant's flow rate should be sufficient to restrict the temperature increase along the cable's length. The losses caused by resistance between the coolant and the pipe increase the pressure drop inside the cable. This pressure drop leads to an increase in the mass flow rate which disturbs the pump that circulates the coolant and also depends on the geometry of the pipe such as diameter. Especially, in long-distance transmission cables, it is essential to measure the pressure drop, mass flow, and temperature rise in the cable design [82].

The pressure drops ($\Delta P$) in the cryogenic pipe (within the former and annular gap) where the cable is installed is calculated by the Darcy-Weisbach equation [83]:

$$\Delta P = \frac{f l \rho v^2}{2 D_h}$$

3. 17

The friction factor, represented as $f$, along with the hydraulic diameter of the HTS cable, $D_h$, the density of LN2, denoted as $\rho$, and the velocity of LN2, $v$, are key parameters. The pressure drops along the cable correlates directly with its length and the mass flow rate is considered unchanged.

The hydraulic diameter is equal to

$$D_h = d_o - d_i$$

3. 18

$d_o$, and $d_i$ are the outer diameter of the pipe and the inner diameter of the hydraulic path.

When disregarding the thermal loads at the terminations, the necessary mass flow rate of LN2 to dissipate both the incoming and friction-generated heat can be calculated as follows:

$$\dot{m} = \frac{lQ}{C_p \Delta T} \qquad\qquad 3.19$$

The flow velocity is calculated as

$$v = \frac{\dot{m}}{\rho . A_f} = \frac{\dot{m}}{\rho . \left(\dfrac{\pi . (d_0^2 - d_i^2)}{4}\right)} \qquad\qquad 3.20$$

where $\dot{m}$ is the mass flow rate in kg/s, $C_p$ is the specific heat of the coolant in J/kg-K and $A_f$ is the area of the hydraulic path.

The friction factor is used to calculate the pressure loss in the pipes. For different pipe structures and coolants, the friction factors derived by researchers are given in Table 3.1.

Table 3.1 List of friction factors proposed for the cryostat.

| Year | Type of cryostat | Coolant | Friction factor | Ref. |
|---|---|---|---|---|
| 1977 | Smooth | He | $f = 0.0014 + 0.1254 R_e^{-0.32}$ | [84] |
| 1996 | - | H2O | $f = \ln{(1.05 + 0.72 \times 10^{-7} R_e + 0.74 \times 10^{-13} \times R_e{}^2)}$ | [85] |
| 2001 | Corrugated | LN2 | $f = 0.96 R_e^{-0.2}$ | [86] |
| 2004 | Corrugated | LN2 | $f = 2.60(\frac{e}{d})^{1.08}(\frac{p}{d})^{-0.57}$ | [87] |
| 2011 | Corrugated | LN2 | $f = [\frac{\varepsilon}{3.71D} + \frac{5.1286}{R_e^{0.89}}]^2$ | [88] |
| 2012 | Smooth | LN2 | $f = 0.3164 R_e^{-0.25}$ | [89] |
| 2015 | Corrugated | LN2 and LH2 | $\frac{1}{\sqrt{f}} = -\log_{10}{(\frac{5.02}{R_e\sqrt{f}})}$ | [90] |
| 2016 | Smooth | LN2 | $f = R_e/64$ | [82] |

| | | | | |
|---|---|---|---|---|
| 2017 | Corrugated | LN2 | $\frac{1}{\sqrt{f}} = 2\log\left(\frac{R_e\sqrt{f}}{2.51}\right)$ | [91] |
| 2017 | Corrugated | LN2 | $\frac{1}{\sqrt{f}} = -2\log\left(\frac{\varepsilon}{3.7D_h} + \frac{2.51}{2.51R_e\sqrt{f}}\right)$ | [92] |
| 2019 | Corrugated | LN2 | $f = \frac{2\Delta p \times D_h}{\rho l v^2}$ | [93] |
| 2019 | Corrugated | LN2 | $\frac{1}{f} = 2\log\left(\frac{R_e\sqrt{f}}{2.51}\right)$ | [94] |
| 2019,2022 | Corrugated | LN2 | $f = \frac{8\tau_{wall}}{\rho v_{avg}^2}$ | [95] |
| 2022 | Corrugated | LH2, LNG | $f = 0.032 + 0.0214R_e^{-0.237}$ | [96] |

The Reynolds number $R_e$ is as follows.

$$R_e = \frac{vD_h\rho}{\eta} \qquad 3.21$$

where $\eta$ is the viscosity of LN2.

To inhibit the bubbling of liquid nitrogen, the maximum temperature was maintained below 78 K, and a minimum pressure range of 3-5 bar was sustained to ensure that the liquid nitrogen remained in a non-boiling state. To prevent the structure deformation of the corrugated pipe and to maintain a safe operation considering bursting pressure, a maximum pressure limit of 16-20 bar was established. The lowest operational temperature for liquid nitrogen was established at 65 K to prevent it from solidifying.

To ensure the circulation of LN2 through both the inner and outer corrugated sections of the high-temperature superconducting (HTS) cable, a pump is necessary. The power needed for this pump is determined through the calculations below [93].

$$w = \Delta p . Q_v \qquad\qquad 3.22$$

The formula $Q_v = A \text{ x } v$ represents the volumetric flow rate (m3/s), where A denotes the cross-sectional area of the corrugated pipe in m$^2$.

## 3.1.3.2. Electrical parameter formulations

The electrical layout involves determining the necessary number of tapes based on the critical current. The number of tapes needed for the HTS cable has been estimated electrically [94].

$$N_{T,i} = \frac{I_{r,peak}}{K_{SI} \, I_C} = \frac{I_{r,max} \, \sqrt{2}}{K_{SI} \, I_C} \qquad\qquad 3.23$$

$N_{T,i}$ is the number of tapes in the i$^{th}$ layer, $I_{r,peak}$ is the peak current, $K_{SI}$ is the safety margin, and $I_C$ is the critical current of the HTS tape. The geometrically required number of tapes in the cable should always need to be higher than or equal to $N_{T,i}$

In the electrical distribution network, the short circuit faults lead to overcurrent in the tapes and result in quenching. To avoid quenching, a safety margin of 50% to 70% is considered [97]. Here, we consider a safety margin of 70%.

The necessary length of the 2G HTS tape for the HTS cable was determined using these formulas:

$$l_T = \frac{l_{tt}}{cos \, (\alpha t)} \qquad\qquad 3.24$$

$$l_{T,total} = \sum_{i=1}^{N_{LA}} N_T \, l_{st} \qquad\qquad 3.25$$

where $l_{st}$ is the length of the single tape, $l_{tt}$ is the length of the twisted tape on the former of the cable, $l_{T,total}$ is the total length of $N_T$ tapes in the cable, $\alpha t$ is the twisting angle, and $N_{LA}$ is the number of layers.

The electric field in the superconductor strands or cables is measured through experimental methods and fitted using a power law, as documented in the literature [81] as follows:

$$V = E_0 \left(\frac{I}{I_c}\right)^n \qquad\qquad 3.26$$

The $E_0$ is the electric field used to set the critical current $I_c$ with a range of 1 µV/m. The $n$ value gives the dependency of the $V$ on the electric current in terms of transition $I_c$.

The $E$-$J$ characteristic of the HTS tape was assumed by the following power law which gives the resistance of HTS [98]:

$$\rho = \frac{E_0}{J_c} \left(\frac{J}{J_c}\right)^{n-1} \qquad\qquad 3.27$$

$E_0$ = electric-field criterion of $1 \times 10^{-4}$ V/m, $J_c$ = critical current density and $J$ = current density.

The DC resistance of the cable former was calculated using the resistivity of the copper $\rho_{cui}$ as follows:

$$r_{dci} = \frac{\rho_{cui} l}{A_{fe}} \qquad\qquad 3.28$$

Where $A_{fe}$ is the effective area of the copper former (m$^2$), $l$ is the length of the cable (metres), and $T_i$ of the i$^{th}$ layer is the temperature.

$$A_{fe} = \pi r_f^2 \qquad\qquad 3.29$$

Where $r_f$ is the radius of the copper former.

Skin depth ($\delta_i$) is defined as the below equation and it was used to find the AC resistance of the former $r_{Aci}$ as follows [99]:

$$\delta_i = \sqrt{\frac{\rho_{cui}}{(\pi f)(\mu_o \mu_r)'}} \qquad 3.30$$

$$r_{Aci} = r_{dci} \frac{\pi r_i^2}{\pi (D - \delta_i)\delta_i'} \qquad 3.31$$

Skin depth is dependent on the resistivity of the copper. Here, $f$ is the frequency of the system, $D$ is the former diameter, and $\mu_o$ and $\mu_r$ are the permeability of free space and the relative permeability of copper.

The typical current density of the superconductor and the highest magnetic field it encounters can be calculated as follows [90].

$$J = \frac{I_{dc}}{\beta\left((r_f + t)^2 - r_f^2\right)\cos\alpha} \qquad 3.32$$

$$B_{max} = \frac{\mu_0 I_{dc}}{2\pi(r_f + t)} \qquad 3.33$$

Where $r_f$ is the cu former radius and $t$ is the thickness of the superconducting section. $\beta$ is the filling factor and it is estimated as 0.6-0.7, $t$=2 mm. The average winding angle $\alpha$ is between 10-20.

The necessary insulation thickness, represented as $\delta_{ins}$, for a given rated voltage, denoted as $v_{dc}$, can be determined through the following calculation.

$$\delta_{ins} = (R_f + t)\left(e^{\frac{v_{dc}}{\eta E_b (R_f + t)}} - 1\right) \qquad 3.34$$

$\eta$ (=0.3) is the appropriate safety margin and $E_b$ (=20 kV/mm) is the breakdown voltage of the insulation.

### 3.1.3.3. Thermal formulations

The thermal model is used to solve the temperature behaviour in HTS cables. The temperature gradient affects the cable parameters. How the temperature affects the operating conditions can be observed using this thermal study. The below-mentioned have been used in coupled studies such as electrical-thermal and hydraulic-thermal. The researchers carried out the modelling in the HTS cable either along the radial direction or along the axial direction.

- Along the radial direction

The different kinds of models developed by the researchers are discussed in the below section.

In the design of the cable, thermal distribution along the length of the cable is vital. AC losses and the heat load losses of the cryostat influence the temperature rise of LN2. The thermal distribution along the radial and axial axes is needed to focus on maintaining the cryostat temperature in a safe operating condition. The thermal distribution along the radial direction of the cable is derived from solving a layer-wise group of Laplace differential equations. The heat transfer in the solid layer between the conductor and ground layer is given by [94]

$$\frac{1}{r}\frac{\partial}{\partial r}\left(r\frac{\partial T}{\partial r}\right) = 0 \qquad\qquad 3.35$$

Where $r$ is the radius and $T$ is the temperature.

Additional heat sources with a heat-conducting coefficient are available in the solid conductor as explained by the Poisson equation with $\omega$ as the internal heat source and $\lambda$ as heat conductivity [98] [100]

$$\frac{\partial^2 T}{\partial r^2} + \frac{1}{r}\left(\frac{\partial T}{\partial r}\right) + \frac{\omega(T)}{\lambda} = 0 \qquad\qquad 3.36$$

For angularly arranged tapes, the hysteresis losses without any gaps between the tapes are as follows [101]:

$$Qac = Q_o[(1 - F) \ln(1 - F) + (2 - F)F/2] \qquad 3.37$$

$$F = \frac{I}{I_c} = \frac{I_n \sqrt{2}}{I_c.N} \qquad 3.38$$

Where $Q_o = \mu_o I_c^2/\pi$ and $\mu_o = 4\pi \times 10\text{-}7$ are the permeability of the vacuum.

The critical current at a particular temperature is as follows.

$$I_c(T) = I_c\left(\frac{T_C - T}{T_C - T_{LN}}\right)^\alpha \qquad 3.39$$

$T_c$ represents the critical temperature, while $T_{LN}$ denotes the temperature of LN2. $\alpha$ is referred to as the heat-rising coefficient.

The energy losses of the tapes are evaluated using energy loss.

$$P(T) = \sum_{i=1}^{N_{La}} Qac. N_{T,i} f_n \qquad 3.40$$

Where $f_n$ is the nominal frequency, $N_{La}$ is the number of layers.

To calculate temperature, the rise using an external cryostat is [102]

$$\Delta T(L) = T_o + \frac{q_{ext} \pi d_{in,ext}}{m C_{LN}} L \qquad 3.41$$

Here $\Delta T$ is the temperature rise, and $q_{ext}$ is the thermal loss of the external cryostat. $d_{in,ext}$ is the inner diameter of the external cryostat. $C_{LN}$ is the heat capacity of liquid nitrogen.

Guangyu and colleagues conducted transient analysis using MATLAB and ANSYS. The model was characterised by coupling electrical, thermal, and magnetic parameters under three-phase short circuit conditions. A 10 kV power system with a triaxial cable

was modelled and the current and temperature distribution under short circuit conditions was studied. A maximum of 79.4 K in temperature was observed among the three phases when a short circuit fault happened [24].

Developed a model of a second-generation HTS cable across its cross-section in MATLAB and validated the finite element method (FEM) results with the FLUX software package. This is a method tool that establishes temperature distribution among the layers of the HTS cable at normal operating conditions. The parameters used in the modelling were 138 kV and 2500 A/phase. It was observed that the dielectric thermal conductivity is four times less than HTS, leading to detectable temperature differences between consecutive nodes [103].

A numerical model was created using MATLAB/Simulink to examine electrical and thermal parameters in power systems under transient conditions. FEM models with the same parameters were developed as in MATLAB for comparison. The advantages of using Simulink are that it runs in 0.2 sec while COMSOL needs 6 minutes, that Simulink does not require software interactions to run the power system model as is required in COMSOL, and finally, it is simple to construct self-inductance and mutual inductance without a complex magnetic coupling geometry process. The simulation focuses on analysing temperature, quench resistance, and current behaviour for a 10 kV, 2 kA peak current scenario, utilising an efficient solution approach and a rapid calculation method [104].

Conducted an overcurrent analysis on a 66 kV class HTS cable, exposing it to a fault current of 31.5 kA RMS for a period of 2 s. They carried out multiple experiments and created a computer program using the 3D Finite Element Method (FEM) along with an equivalent circuit model. The current was measured using a Rogowski coil and the temperature using thermocouples. The thermal behaviour and current distribution under the fault current were measured using the above methods and only a slight variation was found between the simulation and experimental results. This minor difference can be attributed to the resistive and inductive properties of the terminals, as well as errors in

measurement. Here, two cases were studied, one with four and the other with three copper shield layers. The shield current decreases with the decrease in shield layers [105].

Wang and colleagues used the above-mentioned process to study the thermal behaviour of 275 kV/3kA class HTS cables subjected to a fault of 63 kArms with 50 and 100 µm thick cable stabilisers [106].

A new MO structure that uses a weighted sum technique and employs new indices for angular and voltage stability is introduced. The methodology was tested using the New England network, specifically the IEEE 39-bus system, to assess the optimization challenges. They confirmed the effectiveness of their solutions through root mean square and transient analysis simulations in MATLAB and PSCAD, respectively [107].

- Along Axial direction

A 3-D FEM model was built to examine the dynamic thermal properties and to determine the optimal operational parameters and setup duration for a protective system. The model ensures that the high-temperature superconducting (HTS) cables remain below their critical temperature using liquid nitrogen (LN2) in the cooling system. The two primary concerns that may affect temperature fluctuations include failures in the cooling system and fault currents. Consequently, assessing the thermal stability of HTS cables under such fault conditions is crucial. A 50 cm HTS cable is computed in an axial direction for thermal distribution using FEM. Within the LN2 environment, the heat transfer is mainly convective, influenced by the flow velocity and physical characteristics of the LN2 [108].

When the LN2 is in a steady state, the convective heat transfer is computed as follows.

$$h = \lambda_{LN2} N_{uf} d^{-1} \qquad\qquad 3.42$$

$$d = \frac{4S}{L} = 2(R_{out} - R_{in}) \qquad\qquad 3.43$$

The Gnielinski formula is an empirical method used to calculate the Nusselt number.

$$N_{uf} = (\frac{f_f}{8})(R_e - 1000)[1 + 12.7\left(\frac{f_f}{8}\right)^{0.5} (P_r^{2/3} - 1)]^{-1} \qquad 3.44$$

The coefficient of friction is represented by $f_f$, and the Prandtl number is denoted by $P_r$. These terms are defined as follows:

$$3.45$$
$$f_f = (0.79 ln R_e - 1.64)^{-2}$$

$$3.46$$
$$P_r = \eta C_{LN2} \lambda_{LN2}^{-1}$$

When there is no flow of LN2, the convective heat transfer is computed as follows.

$$3.47$$
$$h = \lambda_{LN2} N_{uf} \delta^{-1}$$

The Nusselt number can be computed as

$$3.48$$
$$N_{uf} = 0.2[(G_r P_r)]^{0.25}$$

The Grashof number denoted as $G_r$, can be calculated using the following formula: [80]

$$3.49$$
$$G_r = g\alpha(T_{in} - T_{out})\delta^3 (\eta/\rho_{LN2})^{-2}$$

To protect the HTS, it is necessary to limit the current, as the joule heating accumulates copper former temperature increases very fast. The limiting current in the system is given in equation 3.50.

$$\int_0^{\tau_{lim}} I_{lim}^2 \rho_t l A_{uc}^{-1} dt = c_{cu} \rho_{cu} l A_{cu} (T_{max} - T_0) \qquad 3.50$$

The action time necessary to protect the HTS cable, the relay protection system involving *T1*, is based on the temperature variation analysis of copper former while *T2* is based on the HTS layers.

$$\int_0^{\tau_1} I_{cu}^2 \rho_t A_{uc}^{-1} dt = c_{cu} \rho_{cu} A_{cu} (T_{max} - T_0) \qquad 3.51$$

$$\int_0^{\tau_2} V \sum_{i=1}^{m} I_i dt = c_{sc} \rho_{sc} A_{sc} (T_{max} - T_0') \qquad 3.52$$

The study was conducted along the cable's axial direction using the FEM in COMSOL. A 400 m/2.5 kA/10 kV tri-axial HTS cable was fabricated. The turbulence in the cable was solved using the Reynolds averaged Navier Stokes (RANS) equation [25]

Analysed the thermal losses of the AC HTS cable in radial and axial directions using COMSOL Multiphysics. A 2-D model was developed to determine the convective and conductive heat fluxes in the HTS cable during the transient and study state models. A coupled study was performed on the fluid and thermal zones. The simulation was performed on 100 m and 1000 m cables to discern temperature distribution. For 1000 m, the total thermal non-load leak power flow is 5.632e$^{-4}$ and 6.032 W/m respectively in the axial and radial directions [109].

Developed a detailed mathematical formulation for the thermo-electrical modelling of a long-distance DC HTS cable. The analytical mathematical formulation employs the volume element method (VEM) and finite-difference time-domain (FDTD) to solve the heat transfer equations for a two-dimensional axisymmetric cable model, determining the temperature distribution across length and time. It is also observed that cable energization increases the temperature along the cable, but it is within the safe limit. Lighting surges occur for a short period, and they have a negligible impact, and the short circuit leads to quenching and the deterioration of the equipment [110], [111].

A thermal model network (TMN) of HTS cables was presented using MATLAB, utilising helium gas as the cooling medium for the cable system. The unidirectional coupling between the thermal and electrical model equations is as follows.

The total heat flux generated by the three resistors as shown in [26] is as shown in equation 3.53.

$$Q_{hs} = R_1 I_1^2 + (R_2 + R_3) I_2^2 \qquad 3.53$$

The temperature of the heat sink is

$$T_{hs} = R_{thHS-amb} Q_{hs} + \frac{1}{C_{thHS}} \int Q_{hts}\, dt \qquad 3.54$$

The flow of electrical currents through resistors generates joule heating. This heating leads to a heat flux $Q_{hs}$, which in turn causes a temperature decrease across the heat sink's heat capacity ($C_{thHS}$) and thermal resistance ($R_{thHS-amb}$) to the surrounding ambient temperature ($T_{amb}$).

The applied current changes in a step from 0 to 3000 A, and the temperature changes from 49 to 63 K. When no current is applied, the heat flux associated with joule heating is 38 W, and the current is 3000 A. Here, the heat flux reverses its direction and changes to -65 kW due to additional joule heating. The fastest simulation time is less than 1 s. This model needs a more iterative process to converge the solutions of the thermal model, and the initial results are promising. Further research focus is required [26].

Xianhao and colleagues also focused on the thermal behaviour of the HTS cable under faults to determine recovery time. The key parameters for the HTS property are current density and temperature. Here, the model was developed using MATLAB, and individual electrical and thermal models. In the electrical model, the resistivity of the HTS was given as follows [112], [104]:

$$\rho_{YBCO} = \frac{(\rho_{PL1} + \rho_{PL2} + \rho_o)\rho_{sat}}{\rho_{PL1} + \rho_{PL2} + \rho_o + \rho_{sat}} \qquad 3.55$$

The thermal analysis effective method used is an electrical analogy. It is sufficient and the high degree of consistency of the equations reduces the computational complexity of the coupling of both electrical and thermal parameters. In the thermal model, HTS tape is expressed by an RC circuit with and without an internal heat source. Based on the HTS

structure, each layer is connected to solve the temperature of the final circuit. The thermal analysis under short circuit conditions in different locations has different thermal behaviours and recovery times [112].

In the Volume Element Method (VEM), the domain is segmented into small volume elements (VEs) along both the radial (r) and axial (z) directions. The energy equation, which represents the first law of thermodynamics, is applied to each of these VEs. Consecutive equations are then utilised to determine the heat fluxes and physical properties between adjacent VEs. There is a total of 9 layers divided into 9 VEs [113].

The thermal-hydraulic model for the Cable-in-Conduit Conductor (CICC) utilises the 4C code developed by Savoldi and colleagues [114]. The model accounts for heat transfer within the cable through two primary mechanisms: advection through the parallel hydraulic channels and conduction via the aluminium core of the CICC. These two mechanisms are compared by Peclet number $Pe$ and evaluated based on the whole cable.

$$Pe = (\frac{dm}{dt}) \times c_p \times (T_{out} - T_{in})/(k_{A1} \times A_{A1} \times (T_{out} - T_{in})/L) \qquad 3.56$$
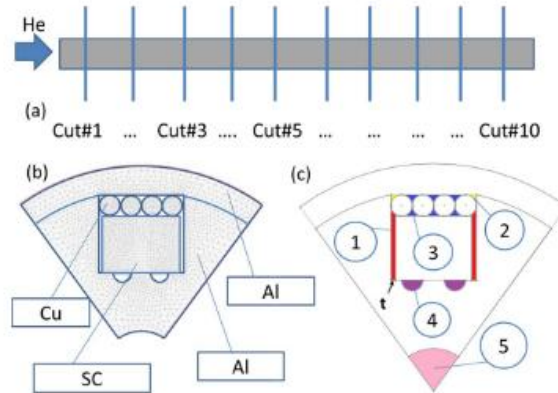


Figure 3.2 (a) One-dimensional model of the hydraulic channel, with the location of the longitudinal 2D cross-sections (cuts) adopted in 4C. (b) Mesh of the idealised 2D solid cross-section (reduced to 1/5 thanks to the symmetry). (c) Regions 1–5 are available for cable cooling [114]

An open-source, two-dimensional finite difference model to study the transient electro-thermal behaviour of three-phase superconducting power cables. The model, developed

54

using MATLAB and employing the alternating direction implicit method, aims to enhance computational efficiency and simulate thermal responses accurately. This tool helps predict cable performance, including temperature changes and heat distribution during operations and faults, providing valuable insights for cable design and operational safety [115], [116].

A new approach was introduced for detecting faults in high-temperature superconducting (HTS) power cables using machine learning and electromagnetic modelling. Its novelty lies in employing a machine learning model, combined with S-parameter analysis, to identify series faults non-destructively and improve the reliability of HTS power systems. This method is significant because it offers a way to predict and detect faults without interrupting cable operation, using changes in transmission characteristics. However, the approach has limitations. The need for advanced and sensitive equipment for real-time monitoring [117].

Employing sophisticated numerical models, researchers have utilised tools like MATLAB, PSCAD, ANSYS, and COMSOL to simulate and analyse these behaviours [103], [118], [119], [120], [121]. This analysis not only aids in understanding the non-linear resistance characteristics of HTS cables affected by variables such as current load, and temperature. To develop more resilient power transmission systems, improvements to the mentioned models are necessary to enhance the simulation of long-distance superconductors while minimizing the computational burden.

## 3.2. High-temperature superconductor power cables

Superconducting tapes are used in a variety of industries, such as power lines, transformers, generators, energy storage systems, and fault current limiters (FCL) [36], [37], [39]. There are currently several manufacturers of these tapes on the market. Terminations, junction boxes, and cooling systems are a must for installing superconductor power cables.

In terms of materials manufacturing, several key players dominate the scene, including AMSC, Fujikura, Sumitomo Electric, Theva, Shanghai Superconducting Technology, SuNAM, and ASG Superconductors. These manufacturers contribute to the development of superconducting tapes, exemplified by the structure displayed in Figure 2.8.

AMSC's signature product is the Amperium wire, representing their second-generation high-temperature superconducting (HTS) wire, notable for its slender ribbon-like form. This wire, encapsulated within thin metal layers such as copper or stainless steel, delivers superior power density and efficiency over traditional copper wires. In the realm of power cables, the typical width of Amperium wire is 4.4 mm, while the wire used for generators and motors stands at 12 mm. Recently, AMSC has initiated the transition to manufacturing strips that are 100 mm wide, promising an expansion in production capacity and a reduction in costs. Additionally, the company produces Amperium wires tailored for various applications, including high-current cables and fault current limiters, each distinguished by their lamination materials and dimensions.

Fujikura is recognised for its YBCO (2G) superconductor wires, designed for use in extensive applications. These tapes, which can be manufactured at lengths exceeding half a kilometre, leverage Ion Beam Assisted Deposition and Pulsed Laser Deposition techniques. They are available with different stabilisers, catering to various operational demands.

Sumitomo Electric Industries, Ltd. offers a range of HTS wires suitable for magnets, cables, and current leads, primarily based on the Bi-2223 superconducting material. These wires are integral to numerous projects and are distinguished by their mechanical and electrical properties.

Shanghai Superconductor Technology Co., Ltd. excels at producing high-temperature superconducting tapes on a large scale, utilising physical vapour deposition to achieve superior electrical properties at low temperatures and high fields.

THEVA, another key player, produces the THEVA Pro-Line HTS wire using the PVD method, offering tapes with different stabilisers to meet varied application needs. SuNam offers four types of REBCO HTS tape, catering to diverse requirements with options available in different widths, made using the IBAD process.

ASG superconductors, utilising the PIT method, focus on $MgB_2$ materials for their wires, catering to applications requiring high current intensity.

In the cable manufacturing domain, companies like Nexans and LS Cable & System have advanced the deployment of superconductor cables for AC and DC grid systems. Nexans, for instance, has been instrumental in projects like the AmpaCity project in Germany, while LS Cable & System specialises in cables that maintain superconductivity at extremely low temperatures, which is significant for both demonstration and commercial projects. Each of these entities plays a pivotal role in advancing the infrastructure for superconducting applications, contributing to the development of more efficient and robust power transmission and storage solutions.

The critical temperature, coolant type, critical temperature, wire form, and final suitability for what kind of transmission are given in Table 3.2.

Table 3.2 HTS material properties [45]

| Material | Coolant | $T_c$ (K) | Wire technology | Wire forms | Suitable for |
|----------|---------|-----------|-----------------|------------|--------------|
| YBCO | LN2 | 93.15 | CC | Flat tape | AC or DC |
| BSCCO (Bi-2223 & Bi-2212) | LN2 | 113.15 | PIT | Flat tape | AC or DC |
| $MgB_2$ | Liquid He | 38.15 | PIT internal Mg diffusion | Wire or tape | DC |

## 3.2.1. High-temperature superconductor compactness

In the manufacturing of superconductor cables, superconducting tapes are stranded around the former made out of copper or aluminium which in turn acts as a fault current limiter. The number of tapes needed is based on the current rating and derating factor ($\frac{I_{op}}{I_c}$=70-75%$I_c$). The superconductors are 25 times lighter and take up 12 times less space than conventional cables [90]. The XLPE and HTS footprint is shown in Figure 3.3 below.
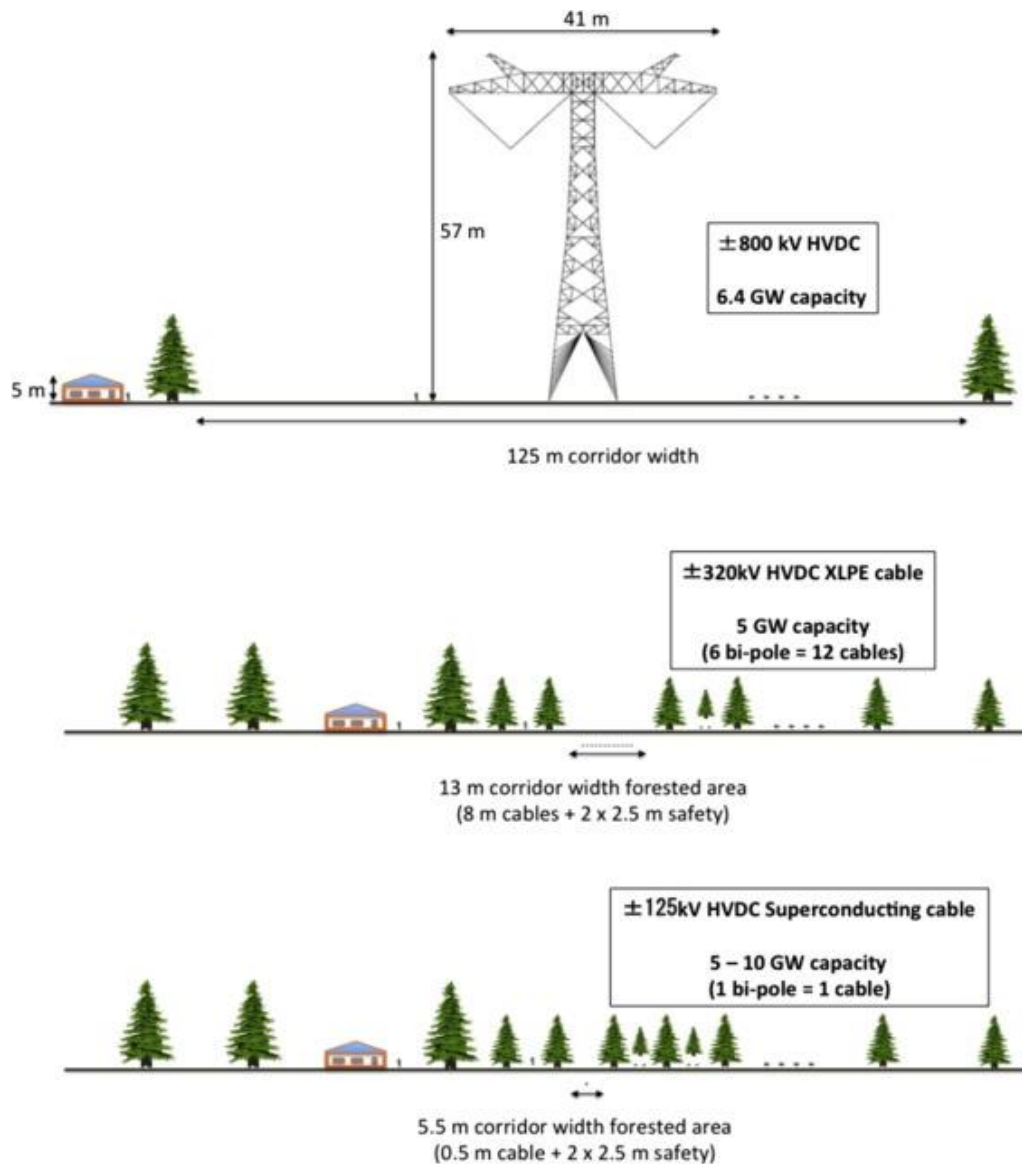


Figure 3.3 Comparison of the overhead, XLPE, and HTS footprints from reference [90]

## 3.2.2.  Cable structure based on HTS arrangement

Various designs of HTS cable are structured based on the tapes wound around them. These include coaxial cables, twisted stacking tape cables, Roebel assembled coated conductor (RACC) cables, Rutherford cables, and CRPP cables. These designs are further categorised according to the operating temperature of their insulation, distinguishing them as warm dielectric and cold dielectric cables.

### 3.2.2.1.  Coaxial cable

The structure of the coaxial cable is depicted in Figure 3.4. This cable serves both forward and reversed superconducting paths, effectively nullifying external magnetic fields. It is categorised into two types based on its core structure: cable-in-conduit conductor (CICC) and conductor-on-round-core (CORC) cable. The CICC variant features a hollow core, facilitating coolant flow in both inner and outer regions, thereby enhancing cooling efficiency. It increases the cooling efficiency, and it is used in fault current limiting cables because it doesn't have any alternative path and triaxial cables. Triaxial cables house all three cores within the same cryostat, optimizing the superconducting material usage compared to individual coaxial cables. On the other hand, CORC cables exhibit high resistance during transient and quenching scenarios, safeguarding the tapes from damage.
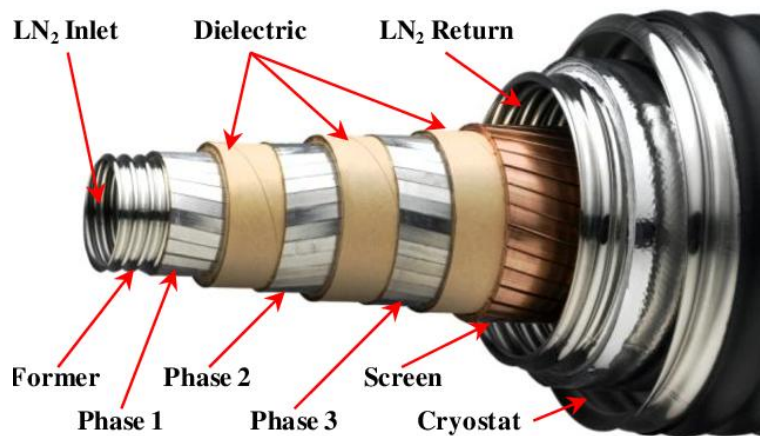
Figure 3.4  Coaxial HTS power cable [122]

- CORC cable

Advanced Conductor Technologies LLC has developed CORC cables, which are designed to be compact and are primarily used for power transmission and magnet applications. The Round Core cabling technique entails helically wrapping REBCO conductors around a cylindrical core. These cables are created by winding High-Temperature Superconductor (HTS) tapes around thin cores, each less than 6 mm in diameter, resulting in a total cable diameter of less than 8 mm. Their unique design, characterised by a short twist pitch and a smaller diameter compared to the other cable types depicted in Figure 3.5, facilitates a flexible bending radius of 100 mm without substantially affecting the superconducting properties [123].



Figure 3.5 CORC cable 7 mm in diameter with 30 tapes [123]

- CICC cable

In the CICC cable, the HTS tapes or strands are encased in a conduit, usually composed of composite or metal materials (copper or aluminium), soldered to form a single sub-cable structure. The CICC cable structure is shown in Figure 3.6. This design offers mechanical stability, and protection from external environmental variables, and increases the cooling efficiency of the superconducting materials. CICCs are particularly common in applications like the coils of fusion reactors and high-energy particle accelerators that require both robustness and high current capacity.
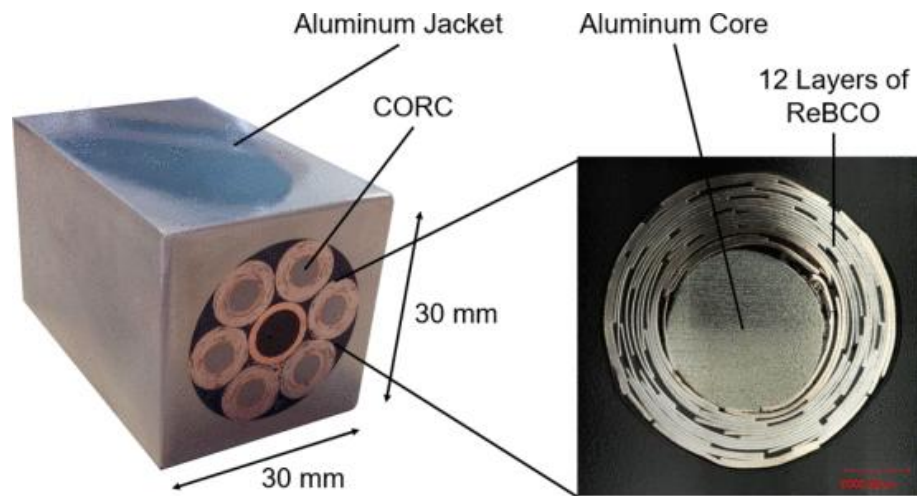
Figure 3.6 CORC-based cable-in-conduit conductor CICC zoomed view of the CORC strand [124]

### 3.2.2.2.  Twisted Stack Tape Cable (TSTC)

The twisted stack tape cable (TSTC) concept was introduced by MIT in 2012. In the cable process, several tapes are stacked and twisted periodically to obtain transposition. The TSTP cables used are stranded tapes and it is shown in Figure 3.7 [125].
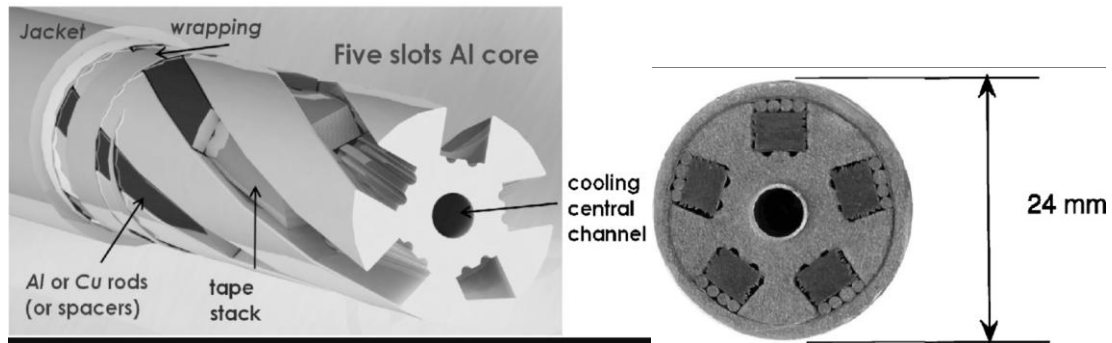


Figure 3.7 TSTC cable view  [126]

### 3.2.2.3.  Roebel cables

Roebel cables are patented by Ludwig Roebel and are made with a round-shaped wire as shown in Figure 3.8. In Robel bars, the strands are transposed i.e. the strands are not rotated during the cable process. In other cables, transposition is obtained by twisting the strands [125]. The Roble concept was adopted for the coated conductors using the KIT

(tapes are stacked in two stacks) meandered strand tapes manufactured by punching wide tapes to avoid tape bending. The drawback of the punching is that it causes the delamination of the tapes at the edges, which can be overcome using copper electroplating, and there is no limitation on length. This is controlled using the computer feedback system for punching the tapes [125],[127].
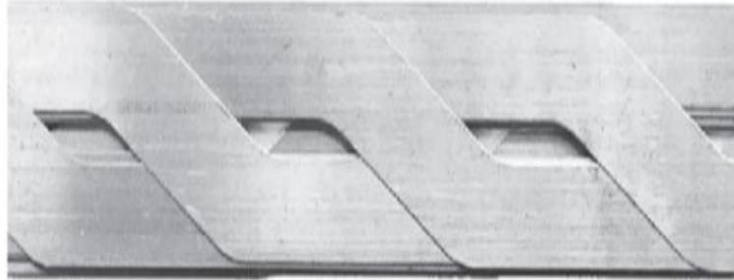


Figure 3.8 Robel cable [125]

### 3.2.2.4.   CRPP cables

The CRPP (Centre de Recherche's en Physique des Plasmas) cable of EPFL employs REBCO tapes in the CRPP cable design illustrated in Figure 3.9. The cabling technique uses the TSTC technique, reinforced by copper to achieve a circular shape [128].  The cable performance of the CRPP and other types above are discussed in Table 3.3.
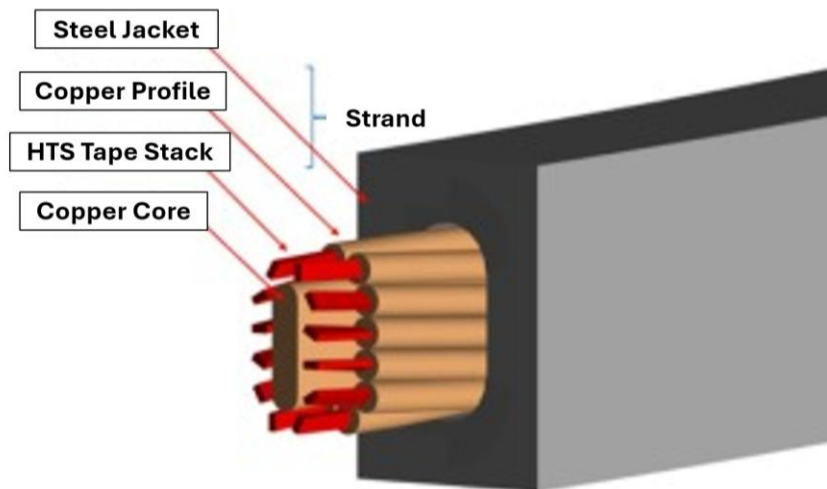


Figure 3.9  CRPP cable [129]

Table 3.3 Various cable performance metrics

|  | Coaxial [122] | TSTP [126] | Robel [125] | CRPP [129] |
|---|---|---|---|---|
| AC losses | Low | High | Low | Medium |
| Flexibility | High | Low | Medium | Medium |
| Ic reduction upon cabling | Low | Medium | High | Medium |
| Cooling design | Easy | Intermediate | Intermediate | Difficult |
| Power density | Low | Medium | High | Medium |

## 3.2.3. Based on the operation temperature of the dielectric material in power cables

Superconductor power cables are classified into two types based on the operation temperature of the dielectric material. These are warm dielectric and cold dielectric superconductors as shown in Figure 3.10. A warm dielectric superconductor consists of the stranded HTS tapes which are cooled by the flow of liquid nitrogen using coaxial stainless-steel pipes. This is covered with dielectric and outer cable sheets at room temperature. In a cold dielectric cable, the dielectric is at cryogenic temperature and the insulation is shielded with the screen layer which prevents stray electromagnetic creation. In the warm dielectric cable, there is no shielding present to prevent electromagnetic activity while in operation. In the design of the superconductor cable, the superconductor tapes required depend on the current and critical current of the cable. The triaxial cable consists of three cables arranged concentrically in a single cable separated by dielectric insulation between each phase. The dielectric thickness depends on the voltage rating and the dielectric material is wrapped in layers impregnated in LN2. The critical challenging

part of the HTS cable is the cooling system, as along the length of the cable, the losses should not lead to the boiling of the liquid nitrogen, and it should be in a liquid state.
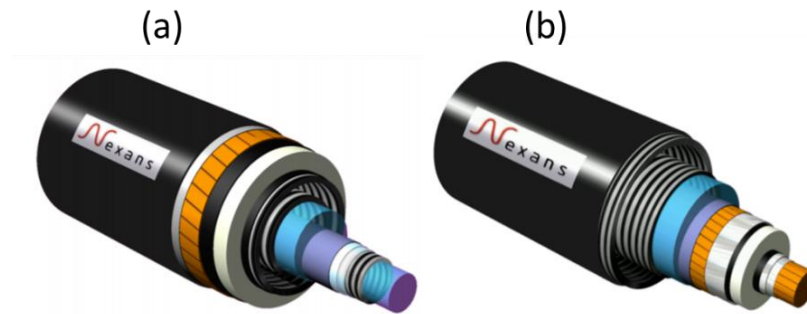


Figure 3.10 Schematic views of HTS (a) warm dielectric cable and (b) cold dielectric cable [4]

## 3.2.4.       Cables suitable for AC application

The three types of commercial AC power cables are shown in Figure 3.11. These cables are commercially available and used in demonstration projects. HTS cables consist of HTS tapes, dielectric material, cryostat wall, coolant, copper and hollow former, a polyethylene sheet, and cable joints and terminations. Superconducting HVDC power cables are designed similarly to HVAC HTS power cables. The dielectric separates the inner HTS layers from a screen made up of only copper wires.
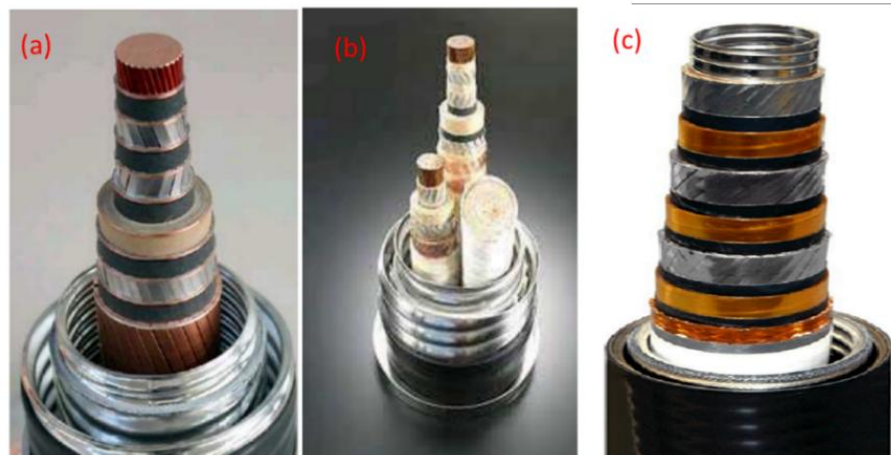


Figure 3.11  (a) Single-core, (b) three-core, and (c) three-core concentric cable [130]

## 3.2.5. Cables suitable for DC application

HTS power cable designs for use in a DC transmission and distribution system are dependent on the voltage rating. These are elaborated on in Table 3.4.

Table 3.4 HTS Cable designs for the DC power transmission

| Cable system | Two coaxial poles [131] | Two twisted poles in one envelope [132] | One pole per envelope [133] |
|---|---|---|---|
| Conception |  |  |  |
| Voltage rating | For low voltage <20 kV | For medium <90 kV | For high voltage >90 kV |
| Benefits | Compact cables | | Bulk power cables used to transfer higher power |
| Benefits | It has common termination and joints for both poles and no magnetic impact | Similar to a two coaxial pole cable | Maximum unit length |
| Benefits | No thermal impact | | |
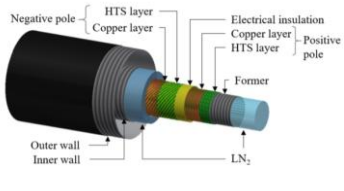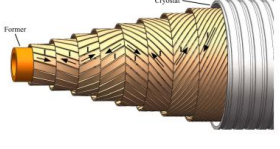
## 3.3. Superconductor power cable accessories

The main components required for a superconductor power cable application are terminations, a joint box, and a cooling system. The former is used to wind the HTS tapes,

to carry current when the superconductor quenches and holds pulling tension. The core of the cable consists of former, HTS tapes, insulation, and a shield layer. The three major parameters that need to be taken into account when selecting insulation are breakdown strength, lightning impulse voltage, and partial discharge. After the cable is manufactured, it undergoes electrical tests, pressure tests, critical current tests, AC loss tests, and handover tests.

The HTS cable is also undergoing different testing according to the grid standards. Some maintenance and tests are similar to those for conventional cables and some special care is necessary due to the ceramic nature of the superconductor material. The standards for superconductors are mentioned in the CIGRE TB538 [130]. Cable projects using the superconductor power cables are shown in Table 3.5 with the current ranges being from 0.8 to 3.5 kA. The length of the cable varies from 30 metres to 2.5 km long.

Table 3.5 HTS power cable projects

| Year | Location | Cable Company | Type | kV/kA/MW | Length [m] | HTS material | Ref. |
|------|----------|---------------|------|----------|------------|--------------|------|
| 2001 | Georgia (US) | Southwire | AC | 12.4/1.2/15 | 30 | Bi2223 | [134] |
| 2002 | Copenhagen (Denmark) | NKT | AC | 30/3.5/104 | 30 | Bi2223 | [135] |
| 2004 | Shenzhen, Puji (China) | Innopower | AC | 35/3.4/120 | 33 | Bi2223 | [18] |
| 2006 | Albany (US) | SEI | AC | 34.5/0.8/48 | 350 | Bi2223 | [13] |

| 2006 | Gochang (South Korea) | LS cable | AC | 22.9/1.3/50 | 100 | Bi2223 | [136] |
|------|-----------------------|----------|----|-------------|-----|--------|-------|
| 2006 | Columbus, Ohio (US) | NKT | AC | 13.2/3.0/69 | 200 | Bi2223 | [137] |
| 2007 | Long Island (USA) | LIPA I and II Project (Nexans) | AC | 138/2.40/574 | 600 | BSCCO and YBCO | [138] |
| 2011 | Icheon (South Korea) | LS cable | AC | 22,9/1.3/50 | 410 | Bi2223 | [136] |
| 2014 | Essen (Germany) | Nexans | DC | 10/2.3/40 | 1000 | Bi2223 | [139] |
| 2016 | Saint Petersburg (Russia) | VNIIKP | DC | 20/1.25/50 | 2500 | Bi2223 | [140] |
| 2018 | Yongin (South Korea) | LS cable | AC | 23/1.3/50 | 1000 | YBCO | [136] |
| 2021 | Shanghai (China) | Shanghai Superconductor & Shang Chuang Superconductor | AC | 35/2.2/77 | 1200 | YBCO | [19] |
| 2021 | Chicago (US) | AMSC | AC | 12/3.0/62 | 200 | YBCO | [141] |

| 2021 | Shenzhen, (China) | China Southern Grid Co. | AC | 10 kV/2.5 kA | 400 | YBCO | [18] |
|---|---|---|---|---|---|---|---|
| 2024 | Montparnasse project, France | Nexans | DC | 1.5/3.5/5.3 | 60 | YBCO | [142] |

The cable parameters are indicated in Table 3.6. The resistance of the HTS cable is negligible compared to the conventional XLPE cable and overhead lines. The following are the key benefits of HTS cables over conventional cables.

a. Visual impact is reduced, land utilisation is reduced, and the environmental footprint is reduced.
b. Loss-free transmission of high-carrying-power capacities.
c. Low-voltage operation is simpler, requires less equipment, and is less expensive.
d. Lower electromagnetic fields impact the environment.
e. Fault current limiting functions integrated with cables.

Table 3.6 Comparison of conventional and HTS cable lines [143]

| Type of cable | Resistance (Ω/km) | Inductance (mH/km) | Capacitance (MVAR/km) |
|---|---|---|---|
| Cold dielectric HTS | 0.0001 | 0.06 | 1.08 |
| XLPE cable | 0.03 | 0.36 | 1.4 |
| Overhead conductor | 0.08 | 1.26 | 0.05 |

The composition of the entire HTS cable is shown in Figure 3.12. The system contains a superconductor cable, two joints, two terminations, and a refrigeration unit. The temperature was maintained below 77 K, below the boiling point of the LN2.
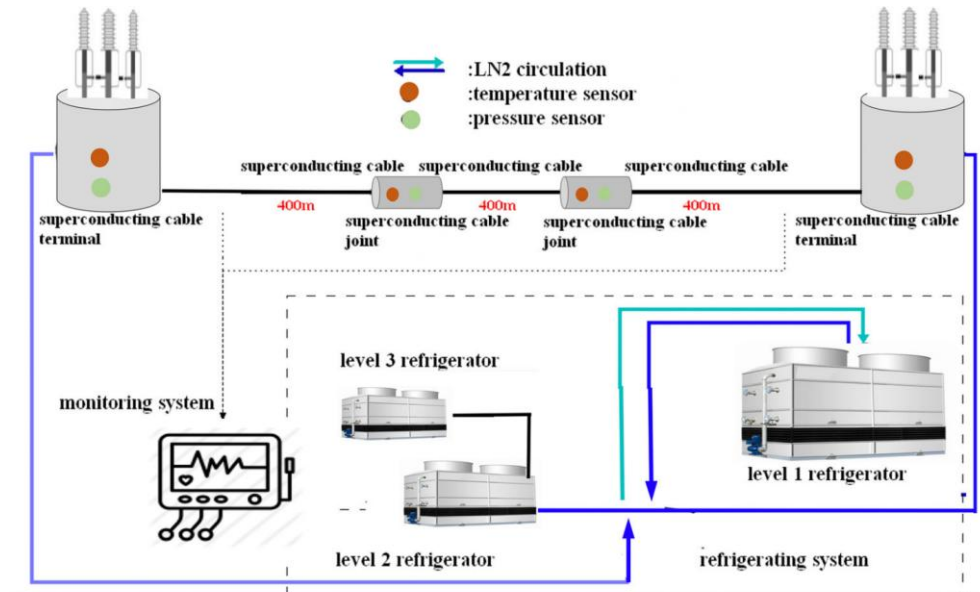


Figure 3.12 HTS power cable system [144]

## 3.3.1.      Cable Fabrication

After preparing the tapes, the tapes are wound around the core of the cable based on the structure required by CICC or CORC. The quantity of the tapes required is determined by the cable's current rating. As illustrated in Figure 3.13, the advancement of CORC cables towards commercial viability involves the capability to wind extended CORC cables using a specially designed winding machine. The machine is capable of winding high-quality CORC conductors in lengths reaching up to 25 metres, maintaining precise control over both winding tension and the spacing between the tapes. It can handle winding CORC cables that are 5–8 mm thick using tapes that are 3–4 mm wide with substrates that are 30–50 micrometres thick. Additionally, it can wind CORC wires that are 2.5–5 mm thick from tapes that are 2–3 mm wide, featuring substrates that are 30 micrometres thick.
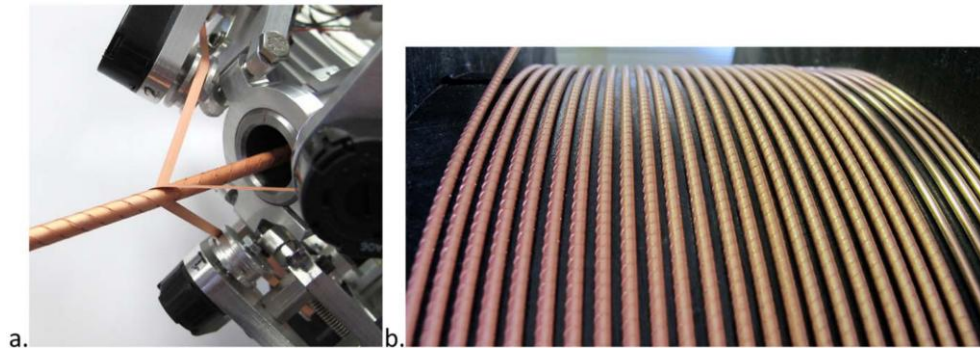
Figure 3.13 (a) CORC cable winding machine and (b) 25 m long CORC wire after winding [145]



Figure 3.14 Fabrication of the HTS cable core [146], [147]

The cable core was wound using a stranding machine in accordance with the specified design parameters. Figure 3.14 illustrates the HTS tape winding machine. The tapes are attached to the copper terminals by soldering them with a low-melting-point alloy.

The production of the HTS cable should be done in the following order as shown in Figure 3.15. The former chosen for the supporting HTS tapes are stranded, then followed by a dielectric material (laminated polypropylene paper). Then, after the installation of the inner aluminium cryostat for the liquid coolant flow, the MLI spacer is installed for thermal insulation. The outer aluminium cryostat to maintain a high vacuum is installed. The outer jacket is then installed to protect it from the outside environment.

The number of tapes and dielectric thickness depends on the cable power ratings. For the three-core and three-core concentric cables, it uses a similar process with a change in the order and repetition of the procedure according to the configuration of the cable.



Figure 3.15  Fabrication of HTS DC cable by the manufacturer, LSC [148]

## 3.3.2.    Terminations and Joints

The termination of the HTS plays two major roles. The first role involves establishing an electrical connection between the high-temperature superconductors (HTS) operating at cryogenic temperatures and the conventional equipment at room temperature. The second role pertains to creating a circulation link with the transfer line of the refrigeration system.

The superconductor tapes wounded around the core of the superconductor core are enclosed in the cryostat. The design and fabrication of superconducting cable terminations are critical to the whole superconducting cable system's long-term operating reliability, and superconducting cable terminations have more complex requirements than conventional cable terminations. It compensates for the thermal shrinkage of the cable during cool-down.

The superconductor cable terminations can carry a few kA currents by providing cryogenic paths, insulating in both electrical and thermal ways, and also managing the thermal gradient from a cryogenic to an ambient state. There are different termination designs available based on the superconductor cable design. The terminations available are single-core terminations and three-in-one core terminations.

The terminations for the YBCO and $MgB_2$ cables, which are schematically represented in Figure 3.16 (a), also contribute to the overall heat load. An intermediate section made of either 1G or 2G HTS materials is placed between the copper lead and cable core to prevent heat ingress at low temperatures. Heat is conducted from the copper lead to the HTS section, which runs at 77 K and is cooled using a closed-loop liquid nitrogen circulation. From 300 K to 77 K, the heat load of a single termination is typically around $50WkA^{-1}$ and $0.5WkA^{-1}$ from 77 K to 20 K.

Single-core and three-core terminations are shown in Figures 3.16 (b), and 3.16 (c). The three-core cable can adopt three individual single-core terminations using a splitter or it can use a three-in-one termination. The three cores in one termination are provided with three fibre reinforcement plastic bushings and epoxy units to connect the cable core shown in Figure 3.16(d). The three-in-one is more compact than three individual terminations. Due to its direct exposure to the ambient temperature and the high thermal conductivity of copper, the current lead plays a crucial role in heat conduction. The shape and design of the current lead greatly influence the amount of heat loss and the distribution of temperature.

The bellows in the inner cryostat are used in terminations to reduce thermal stress during the cool downstage. Also, between cable and termination, the vacuum space and coolant circulation path were isolated to prevent potential leaks and to accurately measure the thermal loss of each system.
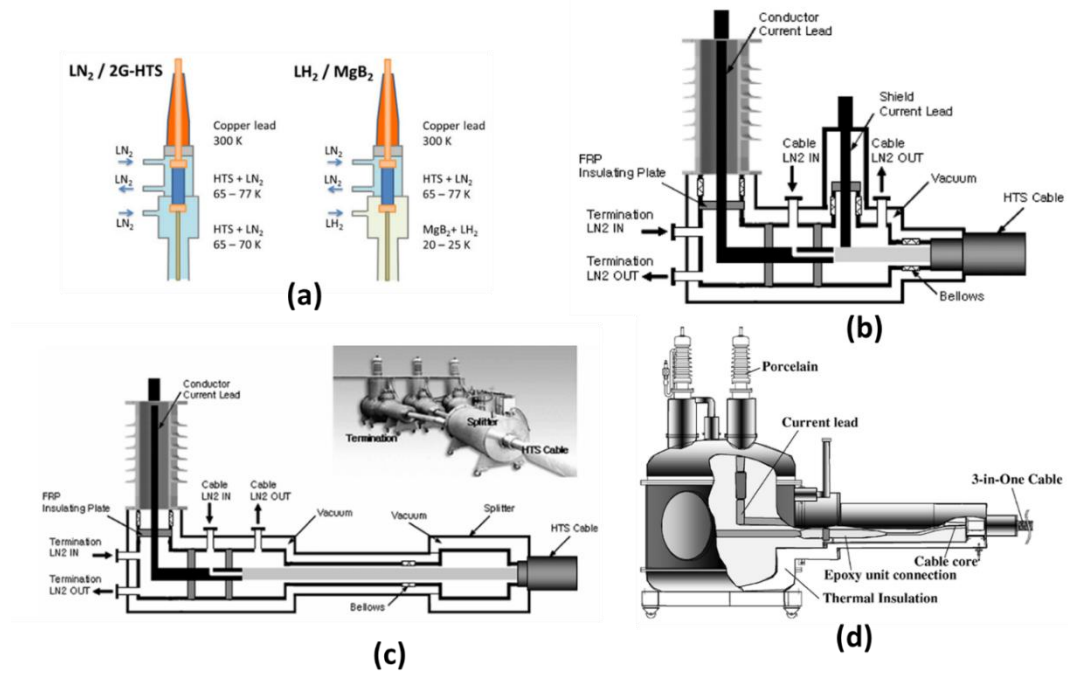
Figure 3.16 Schematic view of the terminations (a) of the YBCO and the MgB$_2$ cable [90], (b) single-core HTS cable [149], (c) 3 core HTS cable [149] and (d) three cores in one termination [150]

To establish a connection between the HTS conductor and the current lead, as well as between the former and transfer line within a termination, appropriate insulation techniques are essential. This involves the use of a stress relief cone and the application of extra insulating layers. These measures help mitigate the high electric field at the terminal end [149]. The terminations used in the demonstration projects are shown in Figure 3.17. The joint box is based on the conventional joint box where the corresponding individual cable cores from both ends are separated and connected at the centre.

This discussion explores various superconducting joints, and the technologies used to produce them. Due to technical constraints, the most common method used for joining the HTS tapes together is soldering. Joints are usually between the terminal and cable, and cable to cable.

Low-temperature superconductors like niobium-titanium (Nb-Ti) and niobium-tin (Nb$_3$Sn) in industrial applications commonly use lead-bismuth (Pb-Bi) solder. HTS

joining methods have been proposed by many researchers. Further research is underway on joining high-temperature superconductors for high-quality superconductor joints.

Hai Liang and colleagues developed superconducting joints made of $MgB_2$. The process begins by etching the material surrounding the conductor using either nitric acid or mechanical polishing. Subsequent heat treatment then creates an interface between the $MgB_2$ conductors. The joints are classified into several types, including in-situ, ex-situ, or IMD, depending on whether they were reacted or unreacted in the state before being joined [151]. The resistance of joints achieved using the superconducting joints is elaborated on below.

The development of a direct joint between the copper layer in REBCO tapes by achieving a resistivity of 44-53 $n\Omega/cm^2$ with high reproducibility. To make a direct joint between the cupper stabiliser, citric acid is used to remove the oxide layer on the copper surface [152]. Another approach developed an Indium joint for HTS DC feeder cable using Bi-2223 tapes. He proposed press welding indium joint at room temperature and with heat treatment at 90-120 °C [153]. To effectively reduce the joint resistance, a pickling process using flux and 10% HCL was adopted from the reference [154]. The resistivity of these Indium joints is in the range of 25-60 $n\Omega cm^2$ at 77 K self-filed [155], [156], [157].

Ultrasonic welding (UW) has been applied to joints as part of a quick process to finish HTS joints. The UW joints for the coated conductor tapes are joined either by lap or butt joints using REBCO tapes. The resistivity achieved for 4 mm with multiple bridges was 152 $n\Omega cm^2$ and the 12 mm wide single bridge joint was 154 $n\Omega cm^2$ [158]. A minimum resistivity achieved for silver-sheathed BSSCO tapes, and copper-stabilised REBCO tapes are 14 $n\Omega cm^2$ and 36.1 $n\Omega cm^2$ respectively [159]. The $I_c$ of the cable is not significantly affected by the joint [152]. The joint resistance is not significantly influenced by the pre-joining process, and spiral joints [153].

The joint consists of the cryostat, conductor insulation and copper in the joint to provide electrical continuity. A high cross-sectional area of copper should be chosen to reduce the

quantity of heat generated by the copper conductor. The copper-to-superconductor tape transition requires the superconductor tape to be soldered to the copper connection. The cryostat junction allows liquid nitrogen to flow freely between two separated superconducting cables. There is also a cryostat vacuum to reduce heat loss through the joint. The dielectric insulator insulates the connection, which works similarly to a traditional cable joint. The schematic and the real cable joint are shown in Figure 3.18.



Figure 3.17 (a) Cable system with a single termination [147]. (b) Current leads are connected to cryostats [146].
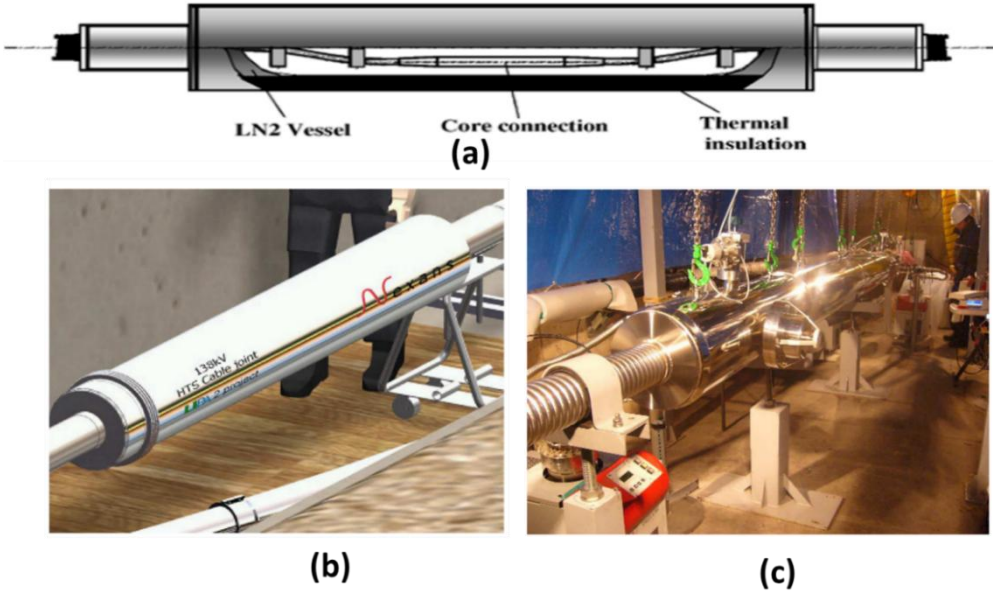


Figure 3.18 (a) Schematic view of three cores in one joint [150]. (b) Image of a joint in the joint pit [10]. (c) Joint box in the vault before covering it with waterproof tapes [13]

### 3.3.3.　Insulation system for HTS cables

Understanding the cooling system, high voltage insulation, and cryogenic materials is necessary for developing high-temperature superconducting (HTS) cables. For the system's long life, dependability, and compactness, the basic qualities of the insulating materials must be solved and understood.

The electrical and mechanical characteristics of polypropylene laminated paper (PPLP) are studied when immersed in liquid nitrogen (LN2). In LN2, the volume resistivity of the PPLP sheet is around $10^{16}$ $\Omega$cm. The volume resistivity decreases as the temperature rises. In DC and impulse breakdown voltage, they observed that the negative polarity slightly exceeds the positive polarity, whereas the impulse breakdown voltage is marginally lower than the DC breakdown voltage. The mechanical parameters of PPLP, including elastic modulus, yield, and fracture strength, improved at 77 K. in comparison to those at 300 K. However, when comparing 77 K to 300 K, the displacement indicated a substantial reduction. Furthermore, the mechanical characteristics of PPLP at machine direction (MD) were significantly higher in strength and elastic modulus than in a cross direction (CD). This study also noted that the size and shape of any frost formations are influenced by the applied voltage, duration, and polarity, with purity factors like moisture content and corona charge playing a crucial role [160].

The primary challenge in practical insulation termination is the surface flashover characteristics of solid insulators at cryogenic temperatures. Consequently, it is essential to understand the DC surface flashover properties of solid insulators in liquid nitrogen (LN2) during the stage phase.

PPLP samples are utilised as cable insulators. The electrode configurations for the mini-model DC cable and the sheet sample used in breakdown testing are illustrated in Figures 3.19 (a) and 3.19 (b). The mini-model DC cable has a construction that is nearly identical to the mini-model AC cable. The PPLP stress cone at the cable's end prevents surface flashover on the cable terminal.

Glass fibre-reinforced plastics (GFRP) were employed as the termination insulator. As an insulation material, it has outstanding mechanical qualities and negligible thermal contraction at cryogenic temperatures. The electrode arrangement for surface flashover is shown in Figure 3.19 (c). A non-uniform electrode system with a stainless-steel triangle and a planar design (tip radius: 60 degrees). The breakdown voltage rises somewhat as the LN2 pressure rises, eventually saturating at around 0.3 MPa. In DC, the saturation pressure is comparable to that of AC. The maximum electric field strength (Emax) was measured to be 120 kV/mm under direct current (DC) voltage and 112 kV/mm under impulse voltage with positive polarity. Notably, Emax for DC is considerably higher than that for alternating current (AC). Additionally, the degradation of polypropylene laminated paper (PPLP) in liquid nitrogen (LN2) shows less sensitivity to DC voltage compared to AC voltage. The deterioration coefficient for DC cables is 1.03. Finally, the breakdown properties of DC appear to be superior to those of AC. A 9 mm thickness is required for a 220 kV class cable and the negative flashover of the GFRP is higher than the positive [161].
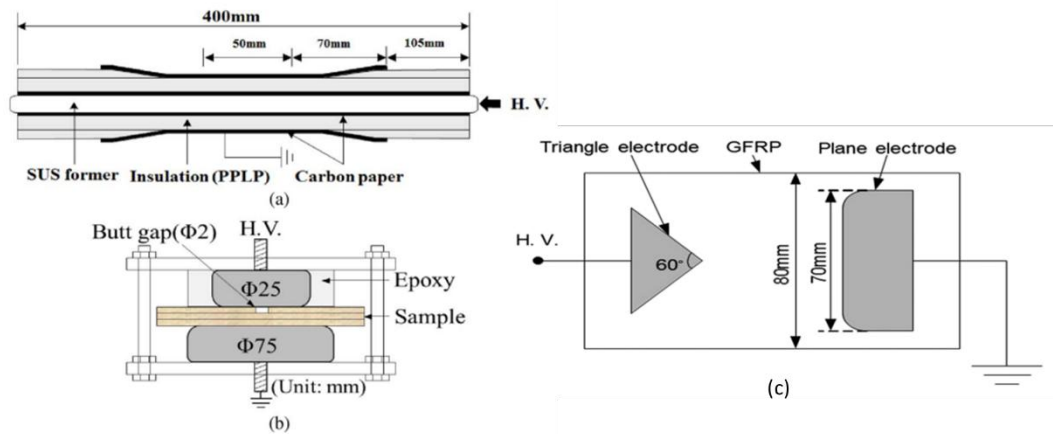


Figure 3.19 Electrode systems for a breakdown test. (a) Mini-model cable; (b) sheet sample and (c) for surface discharge [161].

The polymers mentioned below, and the polymers mentioned in the above conventional cable system of epoxy resin, varnish, and Micro-multilayer Multifunctional Electrical Insulation (MMEI), are used for the insulation of the HTS cables.

### 3.3.3.1. Polyimide tape

Kapton is the most recognised insulating material for superconducting applications, including superconducting transformers, fault current limiters (FCLs), and magnets. Kapton tape is available in a variety of widths and thicknesses, both adhesive and non-adhesive. In most low-power, small-scale prototypes, Kapton is typically used to cover the surface of tape or wire between turns. However, for higher-power applications, it is essential to wrap Kapton tape around the superconductors with appropriate tension. Kapton tape is effective as insulation for low-voltage and low-power scenarios, and it does not require curing once applied to the superconductor surface. At high power, the adhesive tapes deteriorate due to thermal cycling, local hotspot heating, and so on.

### 3.3.3.2. Nylon

Nylon is a thermoplastic material known for its exceptional wear resistance, high compressive strength, and ability to withstand chemicals and high voltages. Because it is so easy to process, it is frequently utilised to make electro-mechanical components. Extruded and cast nylon can be enhanced by incorporating various materials to increase impact resistance, reduce the coefficient of friction, boost stiffness, and improve other characteristics. Nylon has the problem of being highly vulnerable to moisture absorption. It is suitable for dry cryostat.

### 3.3.3.3. Liquid and gaseous insulation

Liquid nitrogen (LN2) is extensively utilised in superconducting applications, serving both as a cryogenic coolant and an insulating medium. Key benefits of LN2 include its simplicity of use, cost-effective production, suitable breakdown voltage strength, and high thermal capacity.

However, since LN2 has a minimum operating temperature of 64 K under subcooled conditions—below which it solidifies—its application is generally restricted to terrestrial or ground-based uses of REBCO superconductors.

Compared to liquid nitrogen (LN2), gaseous helium (GHe) can operate at lower cryogenic temperatures and pose a reduced risk of asphyxiation. However, when compared to LN2, GHe's low breakdown voltage is a limiting factor. One method to increase the breakdown voltage of GHe in superconducting applications at medium and low voltage levels is by raising the pressure. As a result, increasing the gas pressure to 1.5 MPa allows for sufficient electrical strength as well as other helium benefits at a greater cryogenic temperature [57]. As a result, high-pressure GHe is used as a cryogen in superconducting devices such as cables [58]. The electrical strength improves by using a gas mixture combination.

## 3.3.4.     Cooling system

The superconductor power cables' cooling system encompasses terminations, a cryostat, and a cryocooler station. This system, which can be either open or closed loop, employs a circulation pump to distribute the coolant through the cables, reducing their temperature to cryogenic levels. As the coolant begins at the inlet, it absorbs the heat generated within the cable, leading to a rise in temperature by the time it reaches the outlet. The system is designed to ensure that the temperature difference between the inlet and outlet does not exceed 12 K. To reset the coolant's temperature to its original state, a heat exchanger is employed before reintroducing liquid nitrogen at the inlet. Additionally, it is noted that the DC cable does not incur losses from the DC aspect itself but primarily from frictional losses.

The maintenance of a superconductor power cable primarily involves keeping the cooling system operational, and this can be done without halting the cryocooler's function. There's no need to attend to the HTS (High-Temperature Superconductor) material itself. Additionally, for cable applications over short distances, a closed-loop system is employed, whereas an open-loop system is recommended for long-distance usage.

### 3.3.5.    Cable installation

The cable installation includes cable laying, the connection of the superconductor to terminals, the terminal to the power grid, and cryogenic system connections. The HTS cables are directly buried or can be placed in the cable trench along with the conventional cables. There are no specific recommendations for laying due to low EMF, and the absence of thermal and magnetic fields.

Certain precautions that need to be considered while laying the HTS cable are as follows: to avoid excessive tension, adopt a synchronised method to use a winch and caterpillar simultaneously. The cable pulling speed is limited and maintained at 4m/min. The tension and bending radius of the cable should be maintained below 300 kg and 5 m. The cooling is carried out in stages to avoid thermal shock [59].

The joints are connected using a superconductor cable to another HTS using prefabricated joints. First, the former is connected using a copper sleeve, then the HTS tapes are soldered, dielectric paper is wounded around the tapes, shielding layers are connected with soldering and copper wires are used to make press-in contact for the shield layer then finished with winding protective layer. Finally, the LN2 and vacuum tank are assembled.  The termination connects the superconductor to the power grid at ambient temperature and HTS at cryogenic. A soft transition cable is used to connect the HTS and copper leads of the HTS. The integration of the cryogenic tube and vacuum is done. Both the joint and termination are complex, and no standard is available for the installation procedure. They are recommended to be installed by the manufacturer.

The superconductor power cable technology for overland applications is a proven technology yet there are still questions regarding its cost-effectiveness. For offshore use, the deployment of subsea High-Temperature Superconducting (HTS) cables over long distances requires expertise from the subsea engineering community, traditionally associated with oil and gas pipeline engineering [28].

Despite the advancements in high-temperature superconducting (HTS) cables, significant research gaps remain, particularly in addressing the impact of joint resistance on the overall efficiency and reliability of the cable system. Current HTS cable technologies primarily focus on enhancing the material properties and optimising the cryogenic cooling systems. However, the electrical joints, essential for connecting discrete cable segments over long distances, often introduce additional resistance, which can compromise the superconducting state. This joint resistance not only contributes to energy losses but also exacerbates thermal challenges, increasing the risk of quenching and subsequent damage. Accurately incorporating joint resistance into modelling and design is crucial for predicting and mitigating its impact under both steady-state and transient conditions, which has been lacking in existing models. Furthermore, the development of low-resistance joint technologies is imperative to ensure seamless integration of cable segments, minimise losses, and maintain the superconducting state throughout the cable length. Addressing these challenges is vital for the deployment of HTS cables in large-scale applications, such as offshore wind power transmission, where reliability, efficiency, and fault tolerance are paramount.

## 3.4.  Summary of Chapter 3

In Chapter 3 of this thesis, which delves into superconductor modelling methods and power cables, a variety of key points and findings have been addressed. As we draw this chapter to a close, it is essential to consolidate these insights and underscore the significance of the research conducted.

The exploration of modelling methods for high-temperature superconductors (HTS) has revealed the critical role these methods play in advancing our understanding of HTS behaviour under varying conditions. The chapter highlights the complex interplay between thermal, electrical, and hydraulic dynamics within HTS systems and underscores the necessity of sophisticated modelling techniques such as Finite Element Modelling (FEM), Thermal Network Modelling (TNM), and the use of coupled partial differential

equations. Each modelling approach offers distinct advantages but also presents unique challenges, reflecting the intricate nature of superconductor technology.

Furthermore, this chapter has successfully delineated various HTS power cable configurations and their corresponding cooling systems, illustrating how these components are vital for the practical application and efficiency of HTS technologies in real-world scenarios.

The assessment of different cooling concepts and their impact on maximum cable length provides valuable insights for the design and operation of HTS cables, ensuring they meet technical requirements while maintaining operational stability.

This comprehensive review not only enhances our comprehension of the current state of HTS modelling and cable systems but also sets the stage for future innovations in the field. The ongoing development of more accurate and efficient modelling techniques will undoubtedly contribute to overcoming the existing limitations and expanding the applicability of HTS technologies in the energy sector and beyond.

In conclusion, Chapter 3 underscores the importance of continued research and development in superconductor modelling methods and power cables. As this field evolves, it holds the promise of revolutionizing power transmission systems with higher efficiency and lower environmental impact. The insights gained from this chapter lay a solid foundation for the subsequent sections of the thesis, which will build upon these concepts to explore new horizons in superconductor technology.

# Chapter 4

# Lumped and Distributed High-Temperature Superconductor Cable Modelling

## 4.1. Introduction

The high current density and low electrical transmission losses of HTS power lines are widely recognised. Maintaining the temperature of the HTS cable under specified circumstances, as described in Chapter 3 section 3.1.3, is one of the challenging aspects of using this technology. Superconductor technology still faces numerous difficulties in terms of reliability and cost, and large-scale commercial applications are not yet feasible. The large-scale commercial application of HTS cables still faces some obstacles [7].

To achieve net-zero carbon emissions, the electricity supply industry has transitioned from non-renewable to renewable sources. The electricity production has grown, particularly from offshore wind farms (OWF). Offshore wind farms currently generate about 40 GW of electricity globally. By 2050 that amount is expected to rise to 640 GW. These days, offshore wind farms can be built up to 100 km offshore. Because DC cables have no length restrictions and have minimal power loss, they are a better option for power transfer than AC cables [22], [23].

The HVDC system's power rating is in the GW range due to the increasing number of OWFs. Extra- or ultra-high voltage direct current (EHVDC or UHVDC) cables were created to transfer high power in situations when the voltage is above 500 kV in order to minimise transmission losses. Raising power transfer capacity in HVDC lines by increasing voltage to ultra-high levels (above 500 kV) significantly raises costs and

footprint due to the need for enhanced insulation and larger converter stations. This is particularly impactful for offshore installations. Increasing voltage is more complex and costly than simply boosting current-carrying capacity, as it demands extensive modifications to insulation, converter and other infrastructure.

High current density is a benefit of superconductors, and coolants such as LN2 are utilised for insulating as well as cooling. The advantages of superconductors include their compact footprint, minimal losses, and absence of electromagnetic interference. The HTS is appropriate for OWF energy transmission applications because of these benefits. In order to fully use HTS cables in the electrical grid, a number of initiatives utilising HTS cables have been tested and run in the past two decades [9], [15], [164].

The cooling system's dependability, the HTS's cost, and its overall complexity are some of the constraints of the large-scale application of HTS in the power grid [165]. Predicting cable performance requires modelling and simulation work before long-distance cable tests or lab prototypes are installed. Moreover, improving cable performance and design requires simulating the HTS power cable.

A time-dependent thermal and electromagnetic model in MATLAB [104], [110], ANSYS [166], PSCAD [99], [167], and COMSOL [168] has served as the foundation for a number of recent numerical models that have been created. These suggested numerical models primarily use time-frequency domain reflectometry (TFDR), finite element analysis (FEA), and finite-difference time-domain (FDTD) analysis to compute the cable's local electromagnetic behaviours, such as local hot spots and AC losses. By keeping the LN2 temperature constant at 77 K under both steady state and transient situations, a recent cable model created by Wang explores the HTS model using single-element and single-layer cable models [169]. The LN2 layer temperature must be taken into account in the circuit model for the long-distance and fault scenario condition simulations.

In this chapter, the long-distance cable electrical-thermal model by discretised volume element method is developed in MATLAB/Simscape by dividing the 100 km cable into different cable element sizes connected in series by considering the copper former and

coolant layers along with the HTS tapes in each section. This model's advantage is its ability to realistically show the thermal model at various cable sites by including several cryocoolers and joint resistances along the length of the cable. When simulating the HTS cable under transient conditions, we concentrated on the lumped and distributed LC models as well as element size simulation models. This discusses the long-distance superconductor power cable inductance behaviour and fault location behaviour.

## 4.2. Methodology

The long-distance superconductor power cable is very complex when it comes to studying its parameters. This section considers lumped and distributed models for the superconductor power cables. In the lumped model, the model temperature is considered constant and there is no thermal conduction along the axial direction not considered in the model. As in the real scenario, there is a change in the superconductor cable temperature variation along the length of the cable and its impact on the critical current behaviour of the superconductor power cable and hydraulic parameters. The superconductor power cable lumped model is sufficient or do we need a distributed electrical network for the superconductor power cable modelling? This chapter discusses the methodology of the superconductor power cable SIMSCAPE components in the model and how we interconnected the lumped and distributed components developed in the simple HVDC network to study the grid fault in order to look at scenarios for the superconductor power cable. The superconductor will quench and increase the joule losses in the superconductor power cable and sometimes it permanently damages the superconductor tapes.

One of the most crucial aspects that results from a grid failure is the superconducting power cable's quench detection and recovery time. The temperature, $n$, and $I_c$ values from the experimental findings reported in the reference are used to compute the superconductor's resistance. [170]. The following lists the hydraulic, thermal, and electrical calculations required for the HTS cable.

The resistance of HTS was determined using the *E-J* characteristic of the HTS tape, where the electric field was coupled with critical current density [98]:

$$R_{hts} = \frac{E_0}{J_{c(T)}} \left(\frac{J}{J_c(T)}\right)^{n(T)-1} \frac{l}{A} \qquad 4.1$$

$E_0$ = electric-field criterion of $1\times10^{-4}$ V/m, $J_c(T)$ = critical current density dependent on temperature, and $J$ = current density. The n is the exponent that describes how quickly resistance rises as current density exceeds $I_c$, and $l$ is the length of the tape.

Temperature and geometric structure have an impact on the copper layer's resistance. Equation 4.2 is used to determine the resistance of the copper stabiliser ($R_{stabilizer}$) and the copper former ($R_{cu}$) for a temperature range of 65 to 600 K [99].

$$R_{stabilizer} = R_{cu} = (0.0635T_i - 2.4641)10^{-9} \frac{l}{A} \qquad 4.2$$

Where *A* is the cross-sectional area of the respective layer.

The resistance of the HTS cable is determined by equation 4.3.

$$\frac{1}{R_{hts,tape}} = \frac{1}{R_{stabilizer}} + \frac{1}{R_{hts}} + \frac{1}{R_{silver}} + \frac{1}{R_{allostey}} \qquad 4.3$$

$$R_{cable} = \frac{R_{cu} \times R_{hts,tape}}{R_{cu} + R_{hts,tape}} \qquad 4.4$$

The transient analysis requires a thorough examination of the key parameters: temperature, resistance, critical current, and network current. Table 4.1 and 4.2 contains a list of the cable parameters used in the network model simulation. Every element in the cable has four layers separated by the *r* direction. The resistance of the superconductor tape determined using Equation 4.3 is shown in Figure 4.1.

86

Table 4.1 HTS cable details

| Layer | Radius (mm) | Parameter | Value |
|---|---|---|---|
| Copper former | 20.5 | Cable length | 100 km |
| | | Joint resistance | 90 nΩ |
| HTS tapes | 27 | Critical current (Ic) | 13900 A |
| PPLP | 37 | Capacitance (C) | 0.076 µF/km |
| LN2 | 90 | Inductance (L) | 1.43 mH/km |
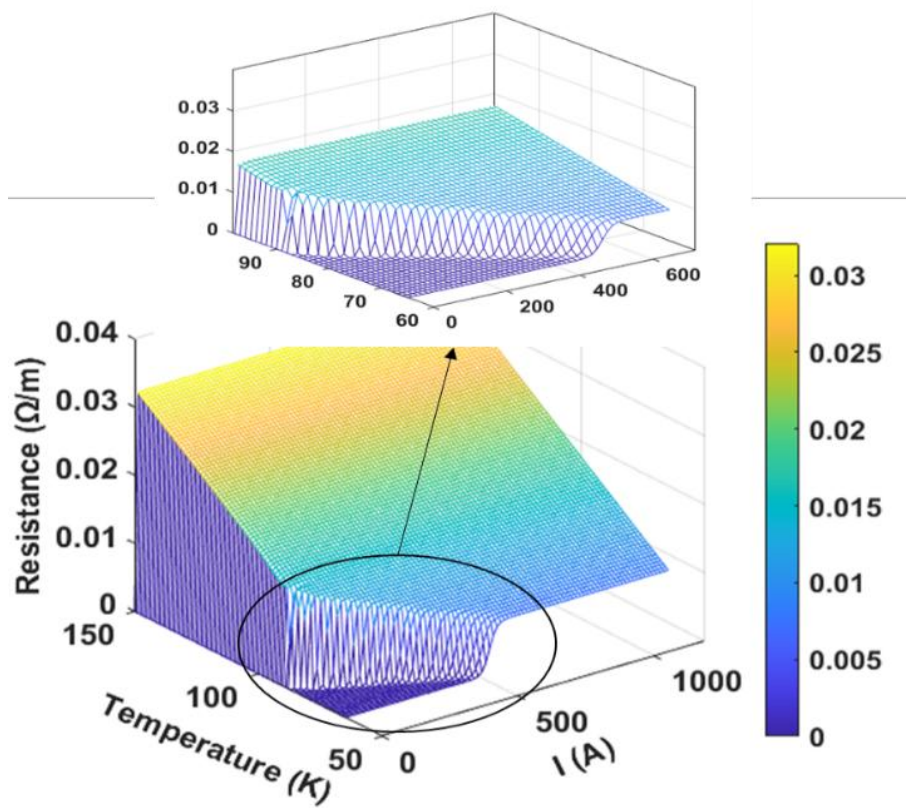


Figure 4.1 Resistance characteristics of a single HTS tape with temperature and current ramp.

Table 4.2 HTS cable material properties

| Layer | Material | Parameters | |
|---|---|---|---|
| HTS material | GdBCO | Tape Width | 12 mm |
| | | HTS layer | 1 µm |
| | | Density | 7039 kg/m$^3$ |
| | | Critical temperature $T_c$ | 92 K |
| | | Tape critical current at 77K | 282 A |
| Stabiliser layer | Copper | Layer thickness | 40 µm |
| | | Density | 8940 kg/m$^3$ |
| | | Heat capacity | 185(J/ kg-K) |
| Substrate layer | Hastelloy | Layer thickness | 60 µm |
| | | Density | 8910 kg/m$^3$ |
| Insulation | PPLP | Density | 946 kg/m$^3$ |
| | | Heat capacity | 1930 (J/ kg-K) |
| | | Thermal conductivity | 0.05 W/mK |
| | | Specific heat | 600 J/kg-K |
| Cooling liquid | Liquid Nitrogen | Density | 808 kg/m$^3$ |
| | | Thermal conductivity | 0.026W/mK |
| | | Volume Specific heat | 742 J/kg-K |
| | | Specific heat | 1930 (J/ kg-K) |

In the cryogenic pipe, the pressure drop ($\Delta P$) is determined using the Darcy-Weisbach equation [83]:

$$\Delta P = \frac{f_f l \rho v^2}{2D_h}$$

4.5

Where $f_f$ friction factor, $D_h$-inner hydraulic diameter of HTS cable and return path, $\rho$ density of LN2, and $v$ – velocity of LN2. Assuming a steady mass flow, the condition pressure decrease is proportionate to the cable's length ($l$).

The hydraulic diameter is equal to

$$D_h = d_o - d_i$$

4.6

$d_o$, and $d_i$ are the outer and inner diameters of the coolant cross-section, respectively.

The product of volume flow and pressure drop determines the heat load per unit length resulting from friction losses between the coolant and pipe surface [88]. The friction losses are presented as

$$Q_f = \frac{\Delta P}{l} \dot{V} = \frac{\Delta P . m}{l . \rho}$$

4.7

The first law of thermodynamics is applied to each layer in the cable. The physical parameters and heat fluxes between the layers in the $r$ and $z$ directions are assessed using consecutive equations. The term $\frac{dT}{dt}$ is taken to be ($T_{final} - T_{initail}$) during a steady state.

For the copper layer,

$$M_{cu} cp_{cu} \frac{dT1}{dt} = (Q_{12} + Q_{1in} - Q_{1out} + Q_{former})$$

4.8

For the superconductor layer

$$M_{hts} cp_{hts} \frac{dT2}{dt} = (Q_{hts} - Q_{12} - Q_{23} + Q_{2in} - Q_{2out})$$

4.9

$$cp_{hts} = (2T_2 d_{hts} t_{hts} + 2T_2 d_{hastelloy} t_{hastelloy} + cp_{cu} d_{cu} t_{cu}) \times w \times l \times n1 \quad \text{4.10}$$

Where $w$ is the width of the tape, n1 is the number of tapes, $d_{hts}, d_{hastelloy}, d_{cu}$ are the densities of the materials in the HTS tapes and similarly, $t_{hts}, t_{hastelloy}, t_{cu}$ are the thicknesses.

For the dielectric layer,

$$M_{pplp} cp_{pplp} \frac{dT3}{dt} = (Q_{23} + Q_{3in} - Q_{3out} - Q_{34} + Q_{pplp}) \quad \text{4.11}$$

For the cryogenic coolant layer,

$$M_{ln2} cp_{ln2} \frac{dT4}{dt} = (Q_{34} + Q_{4in} - Q_{4out} + Q_f + Q_o) \quad \text{4.12}$$

The losses in the copper, HTS and PPLP are measured as follows.

$$Q_{fomer} = i_{former}^2 R_{cu} \quad \text{4.13}$$

$$Q_{hts} = i_{hts}^2 * R_{hts} + i_{cu}^2 R_{stabilizer} \quad \text{4.14}$$

$$Q_{pplp} = 2\pi f tan(\delta)\varepsilon(10^{-11}) \frac{v^2}{2log \left(\frac{r_3}{r_2}\right)^2} \quad \text{4.15}$$

Using the Norris equation from reference [171], the $Q_{hts}$ was computed. The heat through conduction, convection and radiation in the cable $(Q_{12}, Q_{23}, Q_{34}, Q_{1in}, Q_{1out}, Q_{2in}, Q_{2out}, Q_{3in}, Q_{3out}, Q_{4in}, Q_{4out}$, and $Q_o)$ is computed as mentioned in reference [110]. Where $M$ and $c_p$ stands for mass in [Kg] and specific heat at constant volume in [J/KgK] with the subscript indicating the specific cable layer.

Within the solid layers, heat conduction occurs in both axial and radial directions. Heat transfer by conduction within the same material layer is expressed in Equation 4.16 in the axial direction, and heat transfer between different materials is expressed in Equation 4.17 in the radial direction.

$$Q_{cond,i,i+1} = \frac{k_r A_r (T_r^{i+1} - 2T_r^i + T_r^{i-1})}{\Delta l} \tag{4.16}$$

$$Q_{cond,r2,r3} = (T_{r3}^i - T_{r2}^i)(\frac{\ln(\frac{2r_2}{r_1 + r_2})}{2\pi k_{r2} \Delta l} + \frac{\ln(\frac{r_2 + r_3}{2r_2})}{2\pi k_{r3} \Delta l})^{-1} \tag{4.17}$$

Convection heat transmission can occur between liquid and solid materials or inside a liquid medium. Equation 4.18 provides the convection heat transmission in the radial direction, and equation 4.19 provides the heat transfer in the axial direction.

$$Q_{conv,r4,r5} = -hA_{r4,r5}(T_{r5}^i - T_{r4}^i) \tag{4.18}$$

$$Q_{conv,i,i+1} = mc_p(T_r^{i+1} - T_r^i) \tag{4.19}$$

The heat through the radiation between the layers is given in Equation 4.20:

$$Q_{radiation} = -\frac{\varepsilon_1}{1 - \varepsilon_1} A_{r6}(B_1 - \sigma(T_{r6}^i)^4) + \frac{\varepsilon_2}{1 - \varepsilon_2} A_{r7}(\sigma(T_{r7}^i)^4 - B_2) \tag{4.20}$$

Where $h$ is the heat transfer coefficient $A_r$ is the cross-section area, $k_r$ is thermal conductivity, $\Delta l$ is the element size, $m$ is mass flow in kg/s, and $c_p$ is the specific heat (J/kg-K).

The specific processes from resistor component design to network modelling are shown in detail in the flowchart in Figure 4.3(a). The aforementioned equations were used in MATLAB/Simscape to construct the component R. The HTS HVDC Subsea cable structure is depicted in Figure 4.3(b).

Figure 4.2 displays the schematic view of the MATLAB simulation model. The lumped network model of the cable with L, C, and R values for a 100 km length is displayed in Figure 4.2(a). The distributed network model with L, C, and R values for a 1-kilometre length is shown in Figure 4.2 (c), while the lumped L, C with a distributed R model is shown in Figure 4.2 (b). Each $\pi$ segment is made up of R, L, and C. R elements including the cable's four layers. It is considered that the superconducting tape resistance is homogeneous which describes all of the tape layers. The initial temperature of all layers in the cable is considered 70 K.

The 100 km long HTS power cable operates at 10 kA/ 100 kV. In the simulation, a transient Pole to Ground fault is started at time=10 sec and lasts for 20 ms near the end point of the cable. The sample time of $10^{-3}$ seconds and consistency tolerance of $10^{-9}$ is maintained throughout the simulation. Sampling time is the interval between each calculation step when running a model simulation. Using a smaller time step improves the accuracy of the simulation, as it enables the solver to capture quick changes in the system more effectively. In Simscape simulations, the tolerance setting controls how precise the numerical solutions are, especially for solvers handling differential equations. This tolerance represents the maximum allowed error for the state variables.



(a)

(b)

(c)
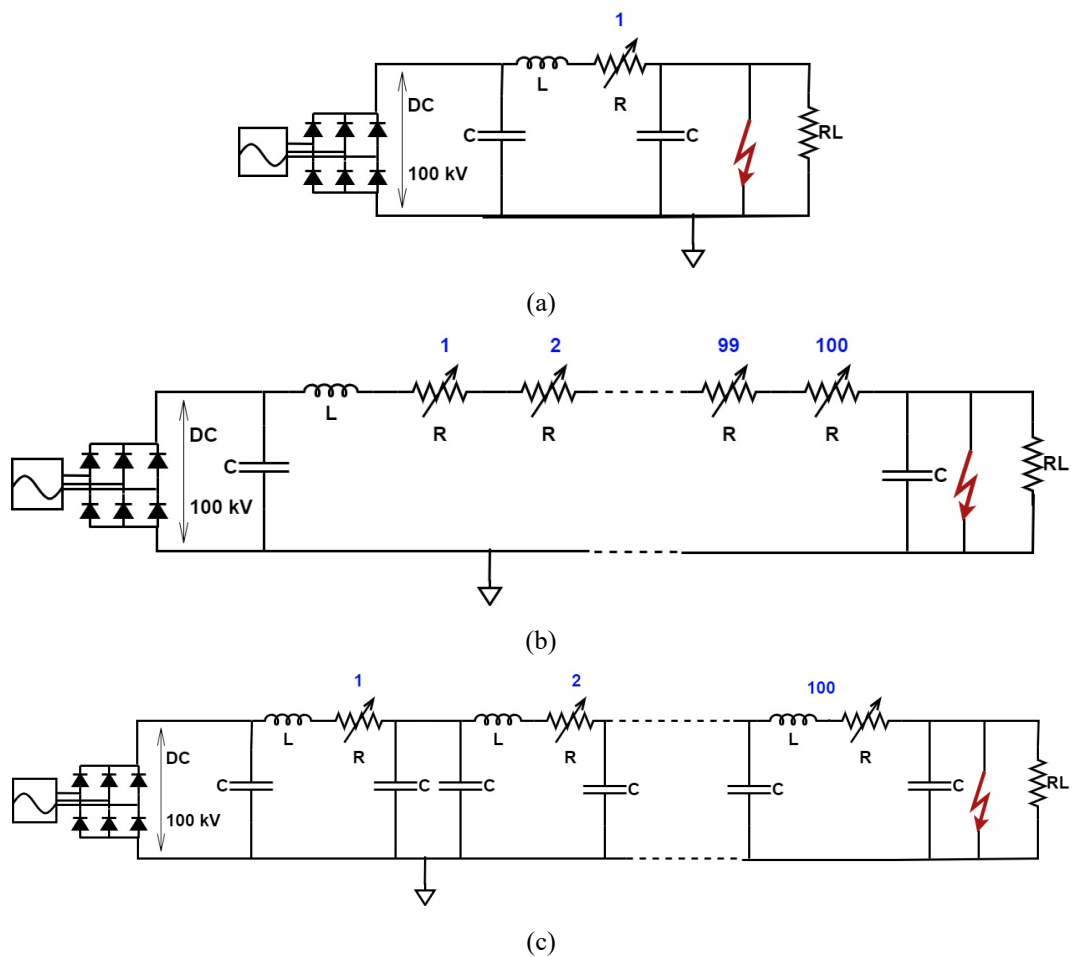
Figure 4.2 Simulation circuit schematic view (a) lumped cable model, (b) lumped L, C and distributed R and (c) distributed L, C, and R cable model with 100 cable blocks.
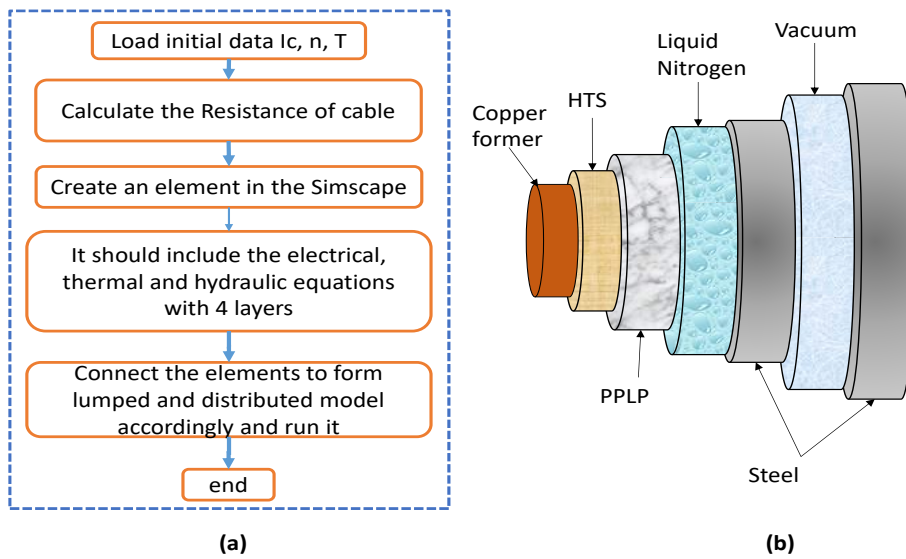
Figure 4.3 (a) Flow chart explaining the step-by-step simulation procedure in MATLAB and (b) the HTS HVDC subsea cable structure

The cable structure utilised in the R component is shown in Figure 4.4(a). Layers of liquid nitrogen (LN2), polypropylene laminated paper (PPLP), copper, and HTS make up this structure. The discretization of the HTS's volume elements and the heat transfer across the layers in the r and z directions are depicted in Figure 4.4(b).
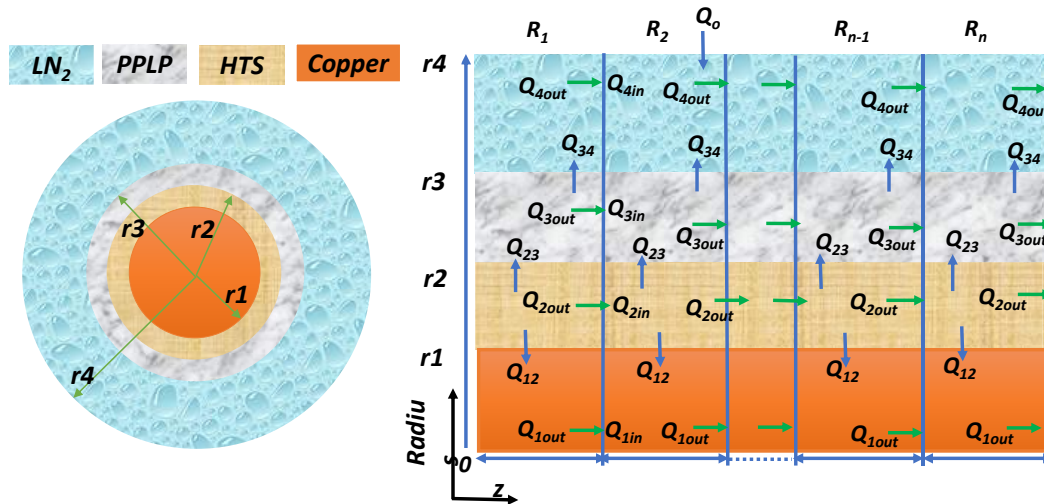


Figure 4.4 (a) Cross-section view and (b) volume element discretization of the HTS cable.

Since the vacuum space is devoid of matter, no energy equation is defined for this layer. Radiation heat transfer occurs across the vacuum, transferring heat between the outer and

inner layers of the vacuum in the cable is taken into account. The computational burden for the distributed LC model with 100 components is 4.5 hours when utilising an Intel(R) Core (TM) i7-7700 CPU running at 3.60 GHz with 32 GB of RAM installed.

## 4.3. Lumped and distributed model analysis

The AC/DC converter circuit, which provides an output of 100 kV DC voltage, is used to power the HTS cable with a DC voltage. In a steady-state scenario, the superconductor's temperature is constant throughout the cable's length in a lumped model. The receiving end of the cable is short-circuited to the ground while under temporary circumstances. The lumped LC model in Figure 4.2(a) takes 2 minutes to run, while the distributed RLC model in Figures 4.2(b) and 4.2(c) requires 4.5 hours to run.

The temperature of the copper former and HTS is shown in Figure. 4.5. The copper former reaches 234.6 K, while the HTS tapes reach 230.5 K. Figure. 4.6 displays the cable's resistance. At 0.93 $\Omega$, the cable's resistance achieves its maximum value. It takes approximately 227 seconds for the lumped model to attain $T<T_c$ (critical temperature ($T_c$)=87.5 K) during the superconductor's quench recovery time. The current increases to 22 kA during the fault.
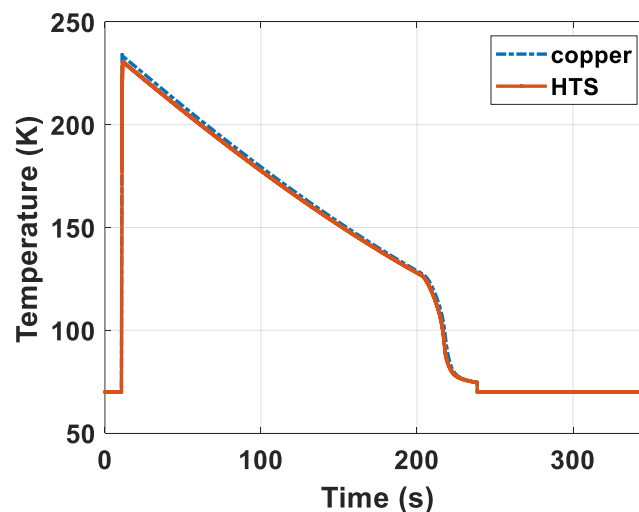


Figure 4.5  The temperature of the superconductor and copper former layers in the HTS cable.

94
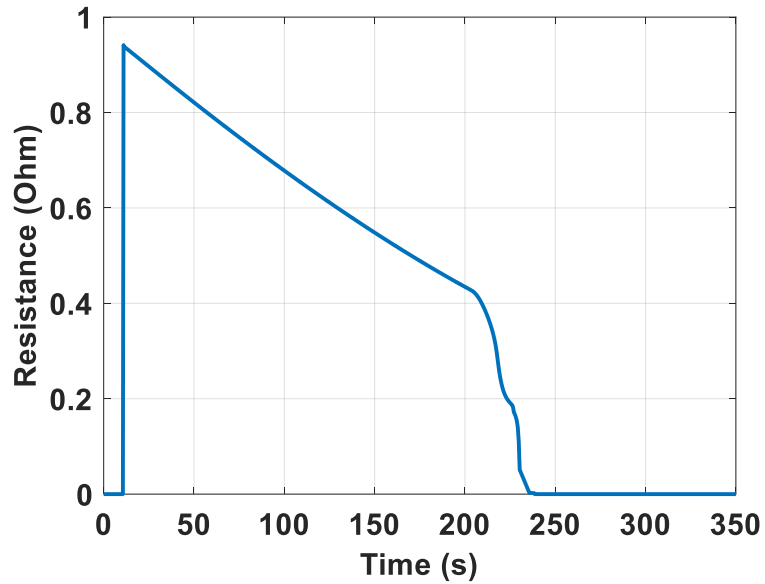
Figure 4.6 Resistance of the superconductor cable.

Once it reaches the critical current value of 13.9 kA, as the temperature rises, the resistance of the HTS increases $R_{hts} > R_{cu}$ and, as shown in Figure 4.7 the current shifts from the HTS to the copper former, preventing damage to the HTS layers. Figure 4.8 shows the total current in the HTS cable.
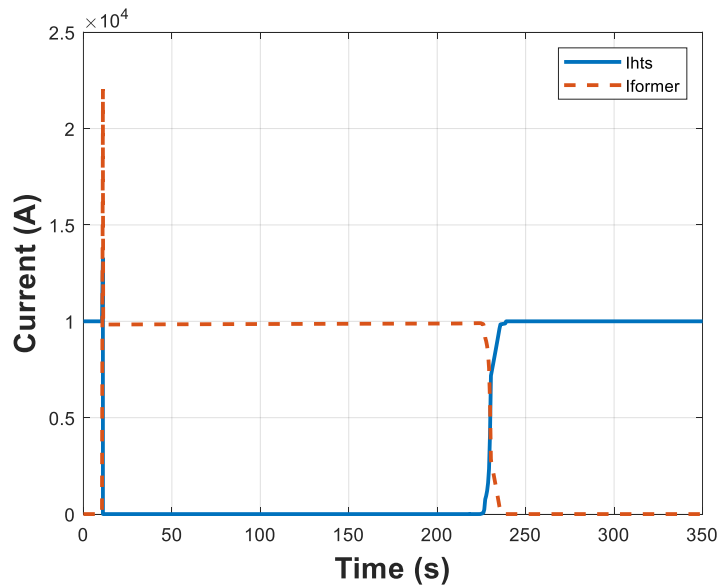


Figure 4.7 Current flow in the HTS and copper former layers.

95
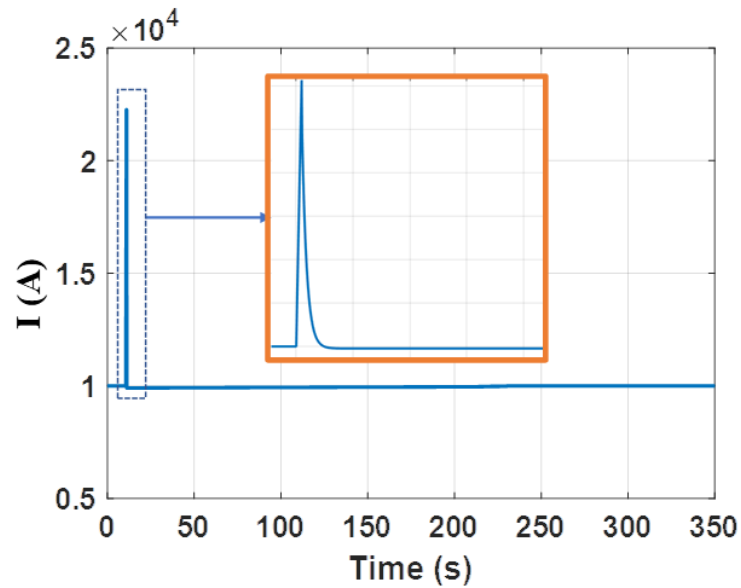
Figure 4.8 Current in the HTS power cable.

As seen in Figure 4.8 and Figure 4.9, the cable behaves the same whether it is a lumped LC with dispersed R or distributed LC. This is because in both cases, the overall LC values of the cable are identical. Compared to the lumped L, C, and R models, the distributed model has a greater temperature and current limiting differential of roughly 1 kA during the fault, as shown in Figure 4.10.
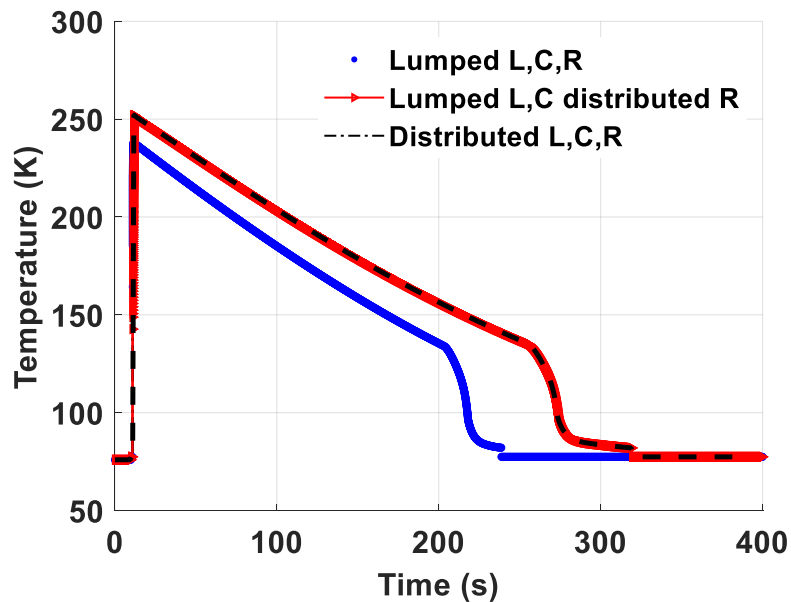


Figure 4.9 HTS temperature when the distributed elements used are 50 at 2 km long each.
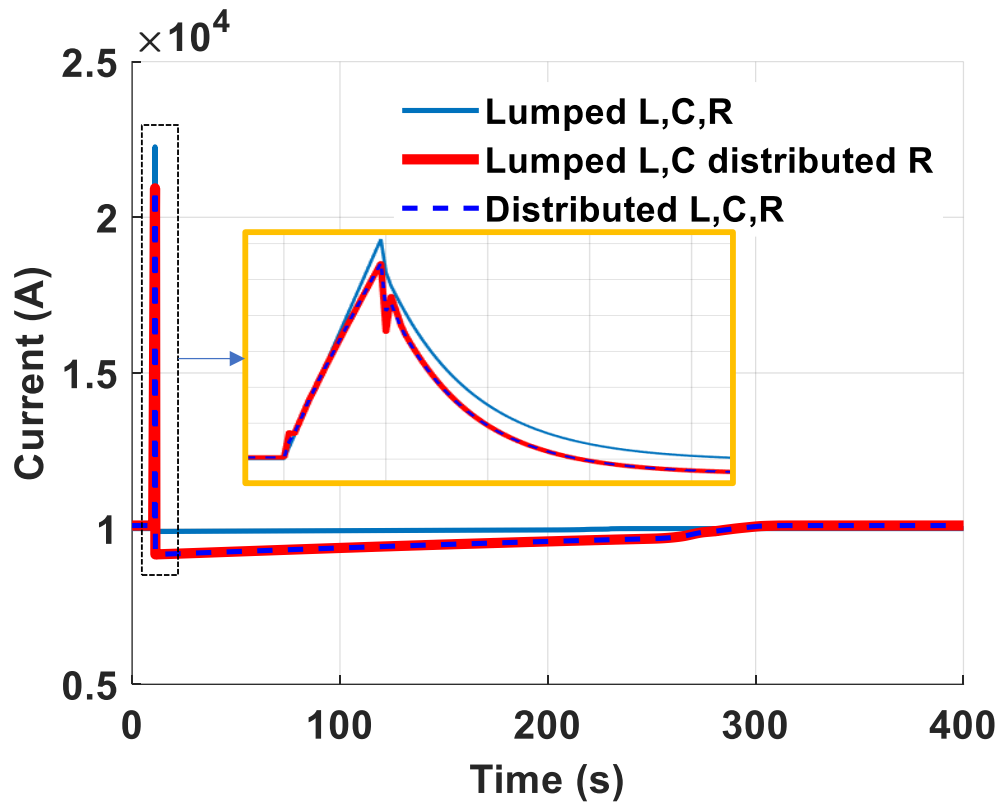
Figure 4.10 Current through the cable when the distributed elements used total 50, with elements being 2 km long each.

Figure 4.11 displays the HTS temperature and pressure at several points throughout the cable's length in a steady state. The pressure of LN2 is kept between 3 and 20 bar in HTS power cables to prevent it from boiling and to ensure stable cooling. Pressures above 20 bar can deform the cable structure. Maintaining pressure above 3 bar prevents phase changes in LN2, which could compromise the cooling efficiency and stability required for superconducting performance. The LN2 was kept at a temperature between 65 and 77 K to avoid quenching the HTS cable. To meet these needs, 10 cryocoolers were considered for a 100 km long cable. The cable has a pressure decrease of 1.5 bar/km under normal conditions. The heat transfer from the external environment to LN2 and the friction losses in the hydraulic path are causes of the temperature rise; the AC losses are negligible.

The cable's critical current is displayed along its whole length in Figure 4.12. At 70 K, the $I_c$ is 13.9 kA. As the temperature rises, it falls until it reaches 76.4 K, where it is 12.1

kA. The tape number is increased for each 1 km long section, thus the $I_c$ drop variation is not much for a 10 km long cable section.
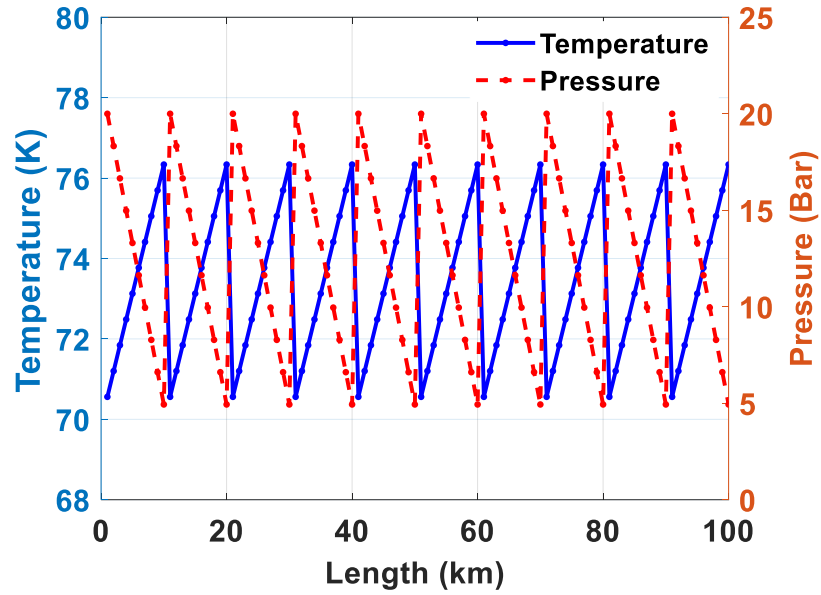


Figure 4.11 Cable with 100 elements with an element size of 1 km (a) Temperature and pressure of LN2 for m=4 kg/s
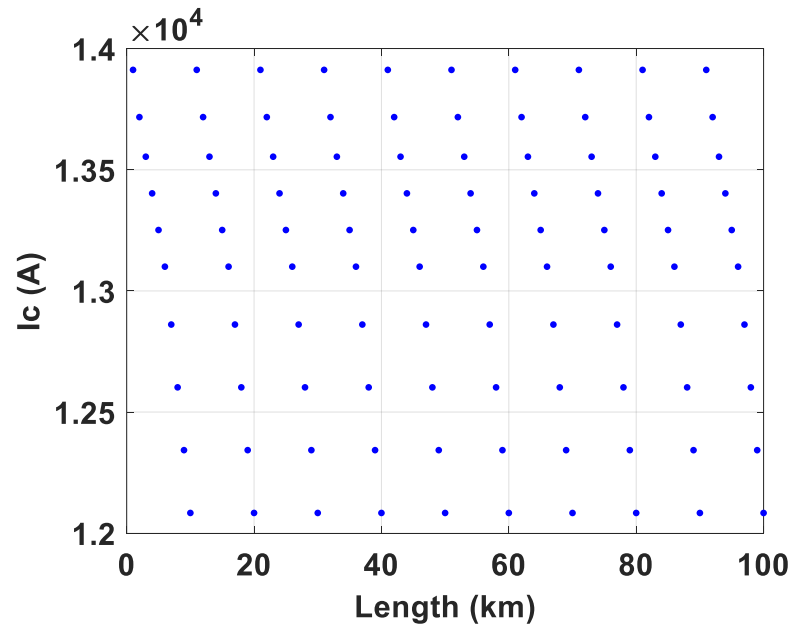


Figure 4.12 100 km long HTS cable critical current.

The behaviour of the cable transitioning from a normal to a quenched state and return is depicted in Figure 4.13. It shows the temperature of the HTS power cable at locations 2 km, 4 km, 6 km, 8 km, and 10 km.
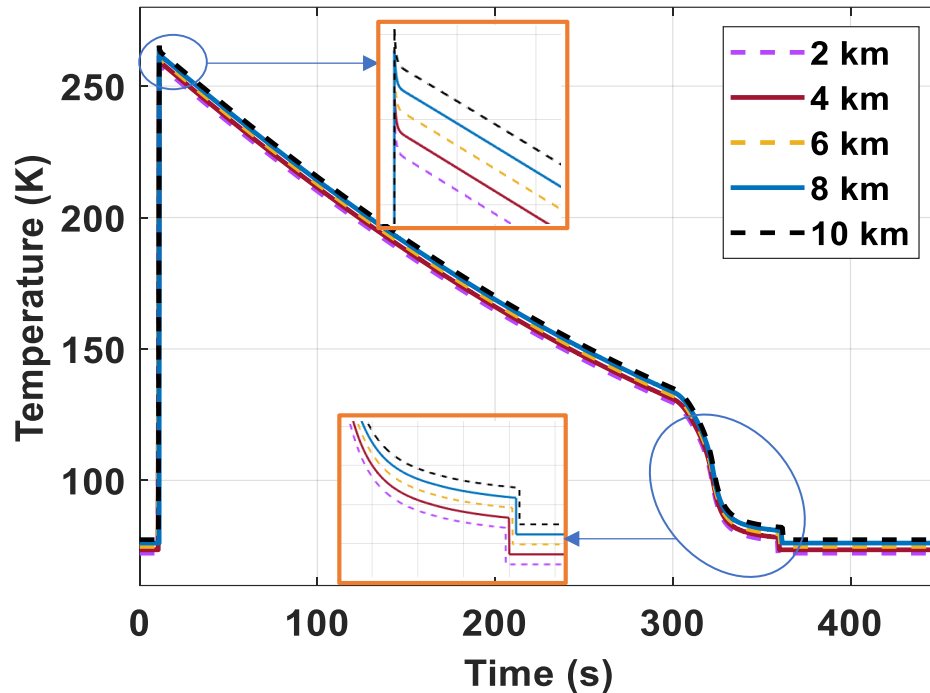


Figure 4.13 100 elements 1 km long each (a) HTS temperature.

Figure 4.14's segment on a 10-kilometre cable demonstrates that the temperature of the cable is slightly lower at the beginning than it is at the end. There is a 6.3 K temperature difference. The temperature of the LN2 on a 10-kilometre cable segment is shown along its length vs time in Figure 4.14. The LN2 may reach a maximum temperature of 91.8 K. A second peak appears at 200 s due to the heat transfer coefficient.

When the temperature differential between the HTS and LN2 is between 5 and 50 K, the reference [172] demonstrates that the h value fluctuates significantly. For a distance of 0–2 km along the fault, the LN2 temperature is below the boiling point, or 77 K. Along the remaining 2–10 km of cable, the LN2 starts to boil as a result of joule heating. During this condition, we need to take precautions and increase the mass flow of LN2 based on the temperature rise.
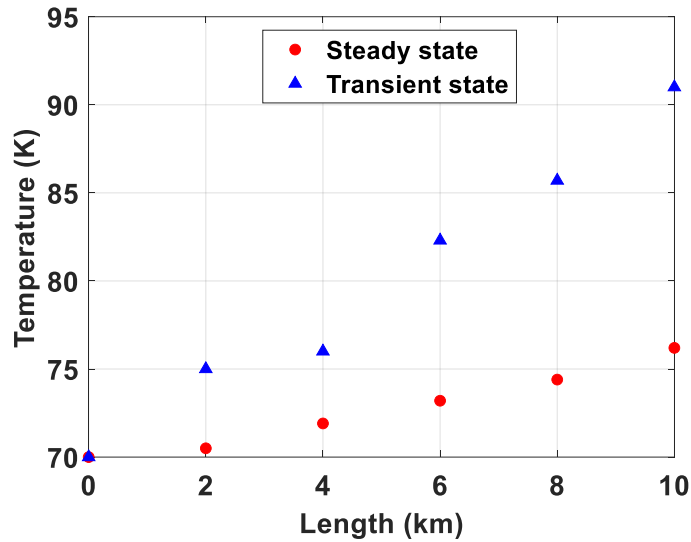
Figure 4.14 100 elements at 1 km long each, showing the maximum temperature of LN2 during the steady and transient condition

The resistance of the copper former and superconductor layer is displayed in Figure 4.15. The HTS layer has little resistance under typical circumstances. However, during the time of the fault, the $R_{hts}$ exceeds 1.4 Ω/km. Under normal circumstances, $R_{hts} <<$ $R_{cu}$, but during a transient, $R_{hts} >> R_{cu}$ rises sharply. The losses in the HTS and previous layers are 0.175 W/km in a steady state.
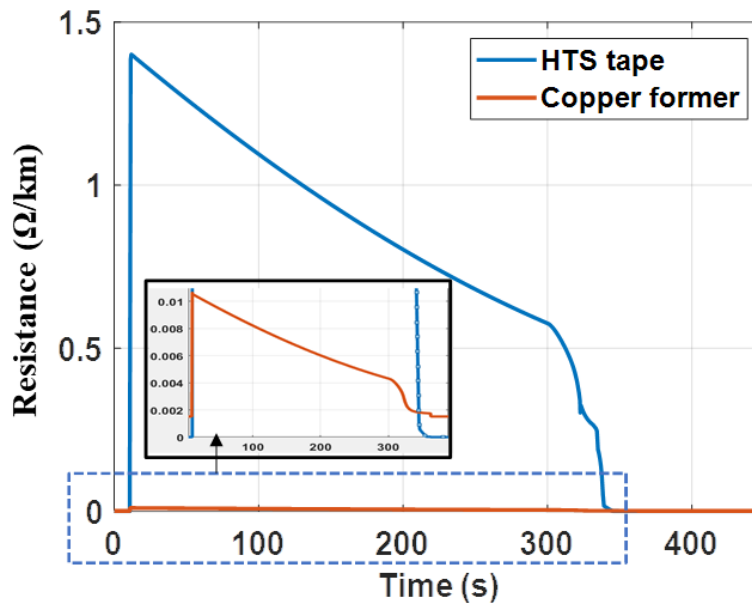


Figure 4.15 Resistance of the HTS and copper former of 1 km long.

On the other hand, as Figure 4.16 shows, it reaches $2.7\times10^4$ W/m during a fault condition. The temperature difference between the 50-element distributed model and the lumped model is approximately 14 K under the transient condition. On the other hand, as Figure 4.17 illustrates, the difference between the distributed model with 50 and 100 elements is less than 7 K.
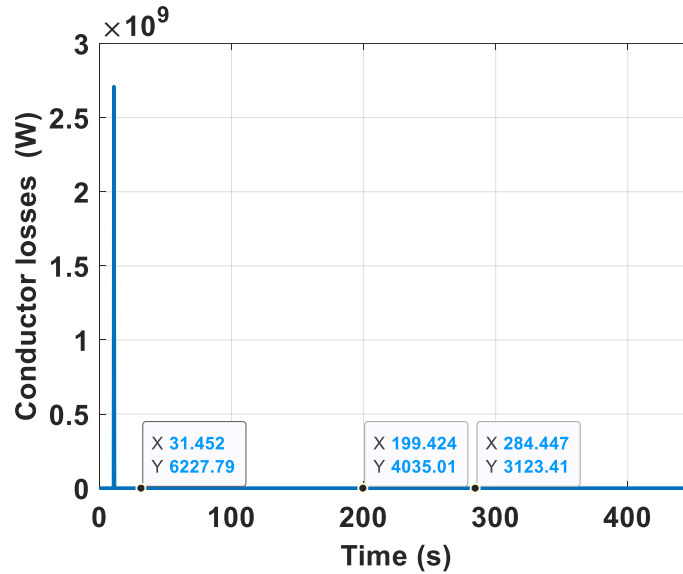


Figure 4.16 HTS cable losses for 100 elements at 1 km long each.
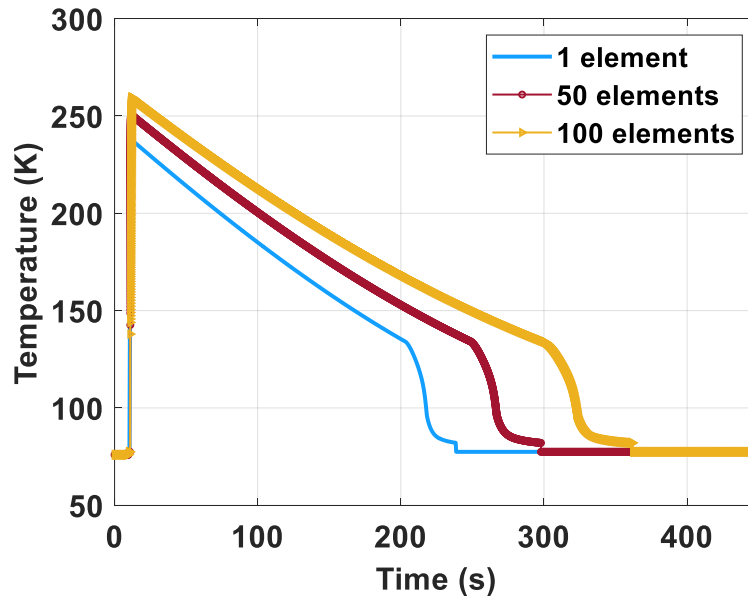


Figure 4.17 The superconductor cables are of different lengths according to element size.

The distribution LC model with 100 components is sufficient for the cable model to analyse the thermal behaviour over the length of the cable because the temperature deviation is small, and the other properties are similar. With this 7 K temperature difference, it takes 55 seconds longer to reach the pre-fault condition. In every case, the former temperature is higher than HTS in the quenched state condition.

Over the cable's length, the superconductor quench recovery varies. The beginning of the cable, which is closest to the voltage source, recovers from the quench more quickly than the end closest to the fault. This is because the cable section is initially low temperature than end part, and the second reason is that LN2 cools the cable by flowing through it first. According to Figure 4.18, the first segment of each 10 km cable section recovers from the quench and functions as a pre-fault condition (same condition before fault occurrence) 6 seconds before the 10 km cable section's endpoint. Since the model makes use of 10 cryocoolers, the thermal behaviour of the cable repeats every 10 kilometres under both stable and transient settings. Figure 4.18 illustrates the 3D temperature profile of an HTS cable.
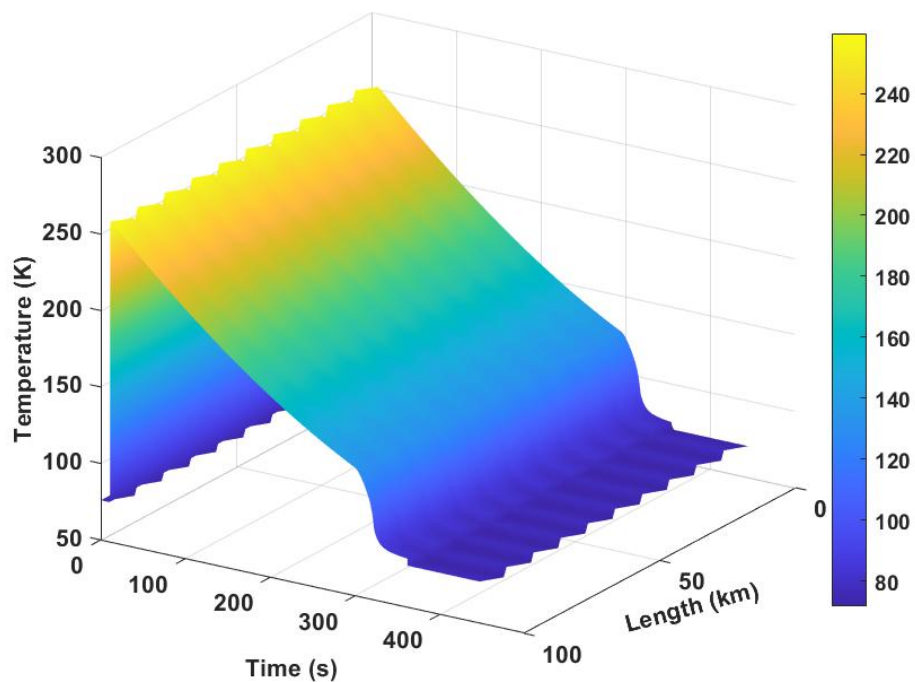


Figure 4.18 3D view of the temperature of the HTS cable.

Conducting experimental studies on long-distance power cables is impractical; hence, initial validations were performed by comparing the lumped model with simulation results. These results were further corroborated by matching the simulation outputs with experimental data obtained from shorter sections of HTS tapes, as detailed in Chapter 5.

## 4.4. Inductance and capacitance of the cable

Inductance and capacitance are crucial characteristics of a cable that significantly influence its performance. Alterations in these parameters can modify how the cable stores energy. Specifically, increases in inductance and capacitance enhance the cable's capacity for energy storage. The cross-section view of HTS is shown in Figure 4.19.
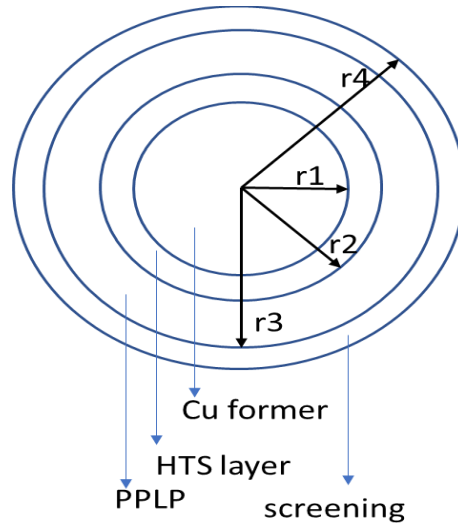


Figure 4.19 Cable cross-section view with radius.

The magnetic flux density can be calculated through Ampere's Law, which also facilitates the determination of the energy stored within the system as follows:

$$w = \frac{1}{2\mu_o} \int_0^{r1} (\frac{\mu_o I_i}{2\pi r})^2 2\pi r dr + \frac{1}{2\mu_o} \int_{r1}^{r2} (\frac{\mu_o I_i}{2\pi r} + \frac{\mu_o I_i}{l_p})^2 2\pi r dr \qquad 4.21$$

$$+ \frac{1}{2\mu_o} \int_{r2}^{r3} (0) 2\pi r dr + \frac{1}{2\mu_o} \int_{r1}^{r2} (\frac{\mu_o (I_i + I_j)}{2\pi r})^2 2\pi r dr$$

The general expression is

$$w = \frac{1}{2}L_{self\_hts}I_i^2 + \frac{1}{2}L_{self\_cu}I_j^2 + MI_iI_j$$

4. 22

Solving equation 4.21 and comparing equations 4.21 and 4.22, we get the self and mutual inductance of the copper former and HTS layer. Where $l_p$ is the pitch angle of the tapes. The superconducting tape used for the twist around the copper former top and side view is shown in Figure 4.20. A schematic view of the twisted HTS tape on the copper former is shown in Figure 4.21.
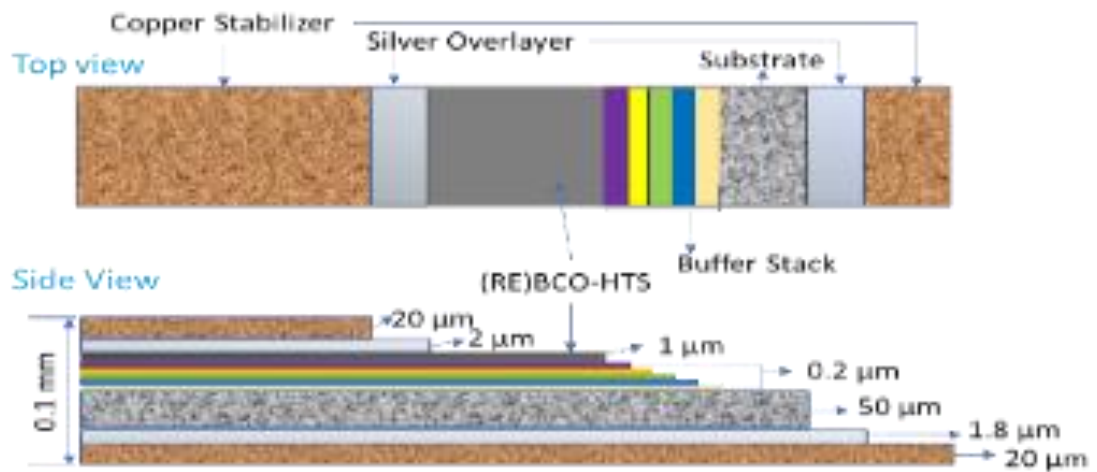


Figure 4.20  Top and side view of the 2G HTS tape.
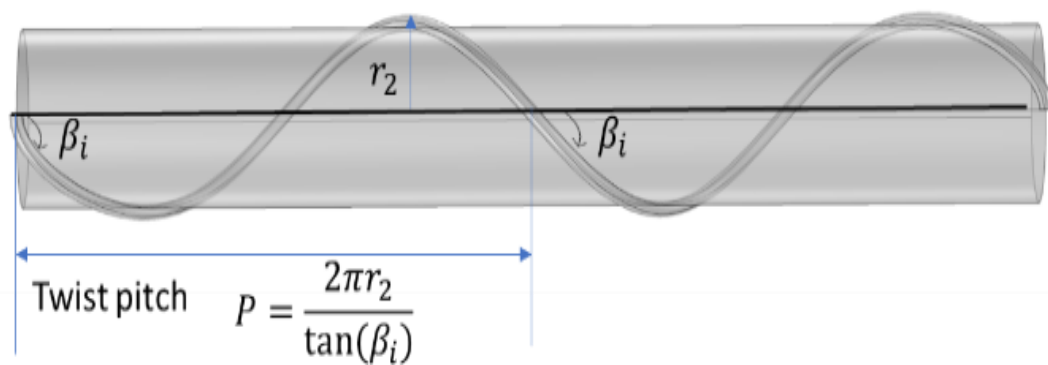


Figure 4.21 2G HTS tape twist pitch schematic view.

The inductance of a superconducting cable is influenced by several factors, including the twist pitch of the tapes, as well as the HTS cable's layer radius. Specifically, the self-inductance of an HTS cable can be determined based on the pitch angle, denoted as $\beta_i$ [173], [174]

$$L_{self\_hts} = \frac{\mu_0}{4\pi} tan^2(\beta_i) + \frac{\mu_0}{2\pi} ln\left(\frac{r_4}{r_2}\right)$$ 4.23

The mutual inductance between the HTS layer and copper former was determined using Ampere's Law and calculating the total magnetic energy enclosed.

$$M = \frac{\mu_0}{\pi} log\left(\frac{r_4}{r_3}\right) + \frac{\mu_0}{\pi}(r_2 - r_1)$$ 4.24

The capacitance of the superconducting power cable is determined using the following methodology:

$$C = \varepsilon_0 \varepsilon_s 2\pi / ln\left(\frac{r_4}{r_2}\right)[mF/km]$$ 4.25

Where $\varepsilon_0 = 8.854 \times 10^{-12}$ [F/m] and $\varepsilon_s$ are the dielectric constant of the free space and insulation material, respectively.

The inductance characteristics of a superconducting cable vary with the orientation of the tape that is wrapped around a copper core, as illustrated in Figure 4.22. An increase in the wrapping angle results in higher self-inductance and mutual inductance values. Specifically, the self-inductance of the HTS layer can vary from 0.09 mH/km to 0.14 mH/km as the pitch angle ranges from 0 to 60 degrees.

Concurrently, the mutual inductance, reflecting the interaction between the HTS tapes and copper core, ranges from 0.05 mH/km to 0.121 mH/km. In contrast, for a solid copper core without any pitch angle variation, the self-inductance remains constant at 0.18 mH/km, demonstrating that it is unaffected by changes in the twist or pitch angle of the tape.
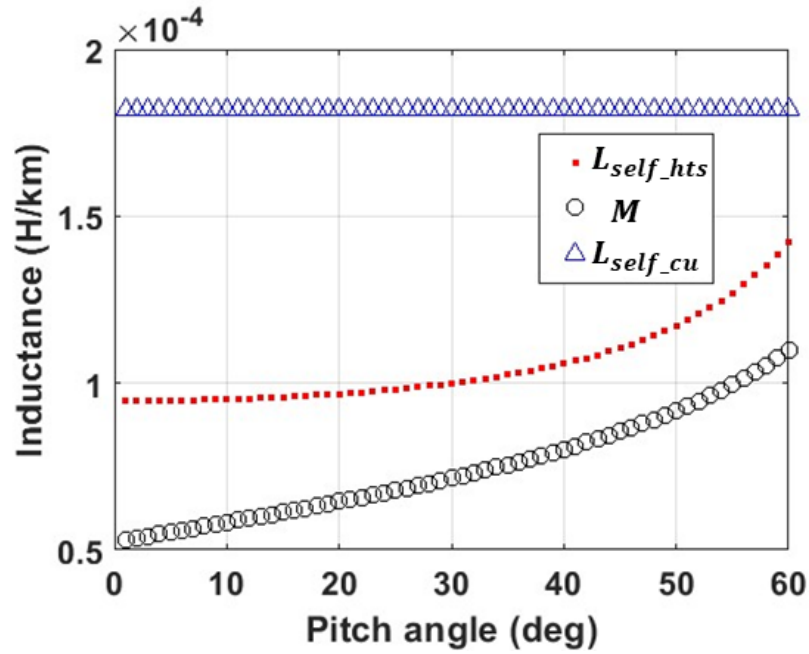
Figure 4.22  Self-inductance of the superconductor layer and former layer, and the mutual inductance between them.

# 4.5. Comparison of equivalent and distributed inductance cable model

Section 4.2 focuses on the lumped and distributed RLC along the axial directions. Here, while modelling the superconductor power cable, we considered two models to understand the electrical and thermal behaviour with a radial direction, R and L consideration for both the HTS and copper former. In case 1, the equivalent inductance ($L_{self\_hts}||L_{self\_cu}=L_{self\_hts}$) is used in the equivalent circuit and the other is not an equivalent circuit. For the cable model, we used Figure 4.23 in the previous model and now compare it with the model shown in Figure 4.24. The simulation results of these models are discussed below.

The equations provided below describe the voltage-current relationship for both the superconducting layer and copper former.

For case 1

$$V = i(R_{cu}||R_{hts}) + L_{self\_hts}\frac{di}{dt}$$

4. 26

$$i = i_{hts} + i_{cu}$$

4. 27

For case 2

$$V_{hts} = i_{hts}R_{hts} + L_{self\_hts}\frac{di_{hts}}{dt} + M\frac{di_{cu}}{dt}$$

4. 28

$$V_{cu} = i_{cu}R_{cu} + L_{self\_cu}\frac{di_{cu}}{dt} + M\frac{di_{hts}}{dt}$$

4. 29

$$i_{hts} = \frac{V_{hts} - \left(L_{self\_hts}\frac{di_{hts}}{dt} + M\frac{di_{cu}}{dt}\right)}{R_{hts}}$$

4. 30

$$i_{cu} = \frac{V_{cu} - \left(L_{self\_cu}\frac{di_{cu}}{dt} + M\frac{di_{hts}}{dt}\right)}{R_{cu}}$$

4. 31
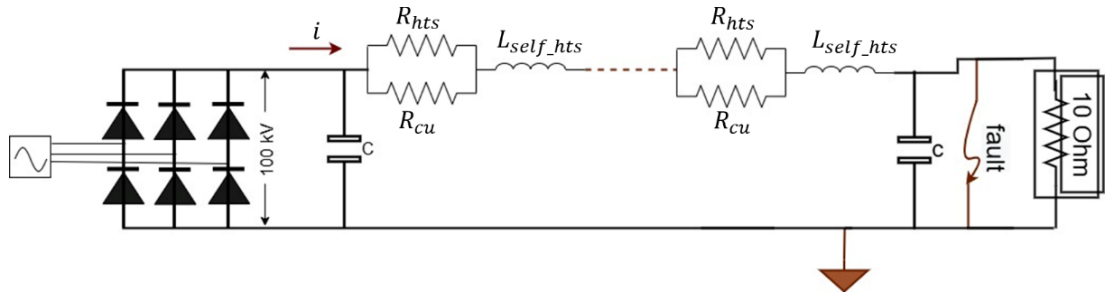


Figure 4.23 Case 1: $R_{hts}$ parallel with $R_{cu}$ and series with L.
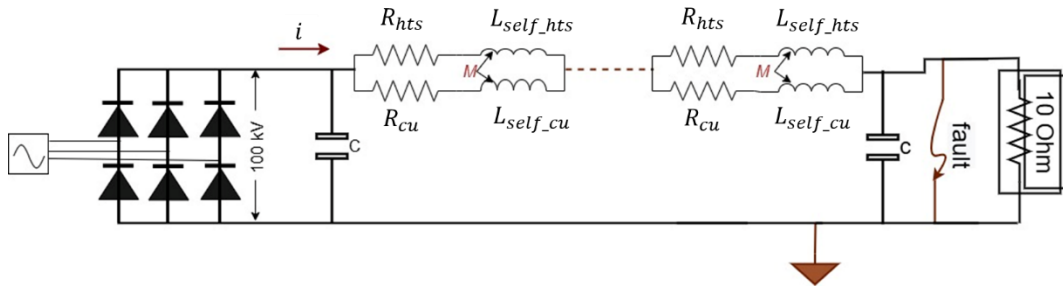


Figure 4.24 Case 2: $R_{hts}$-$L_{self\_hts}$ parallel with $R_{cu}$-$L_{self\_cu}$ including M

The influence of circuit design on the temperature characteristics of superconductors and copper is evident when comparing cases 1 and 2. Specifically, the temperatures observed in case 2 are consistently higher than those in case 1 for both high-temperature superconductors (HTS) and copper formers. This pattern is depicted in Figures 4.25 and 4.26. The suffix self indicates self-inductance of the HTS, or copper former layer and M indicates the mutual inductance between the layers.
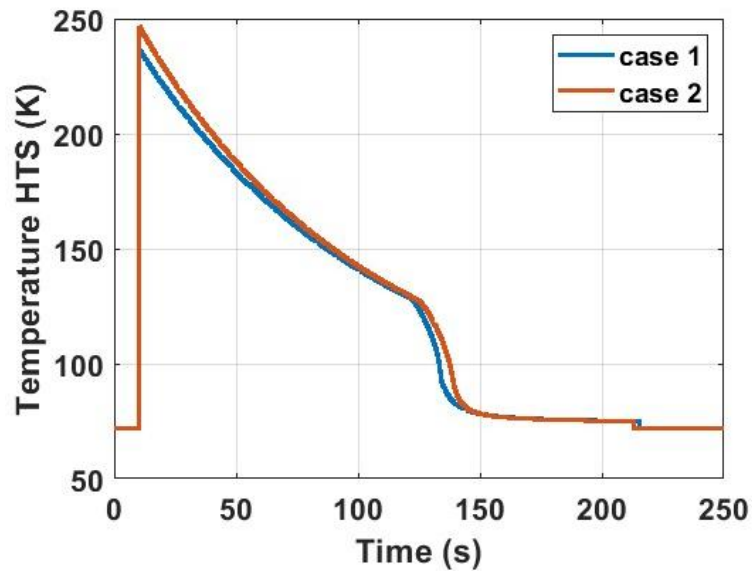


Figure 4.25  Temperature of the HTS in cases 1 and 2.
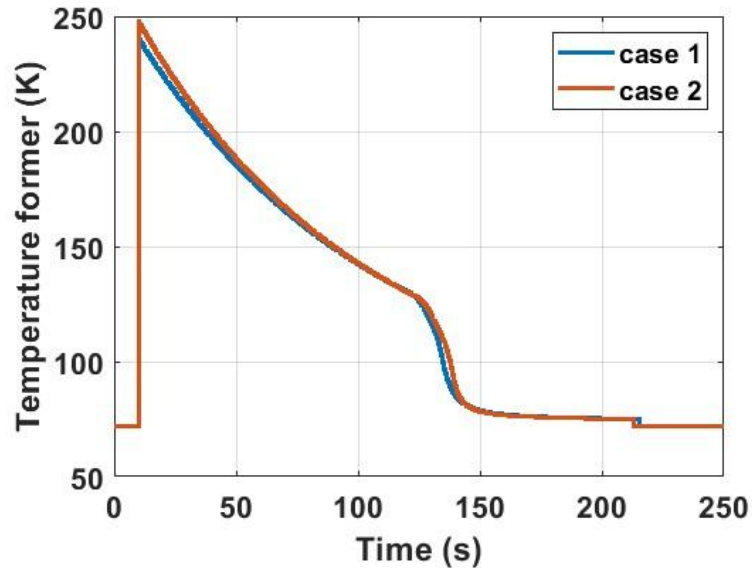


Figure 4.26 Temperature of the copper former in cases 1 and 2.

Figures 4.27 and 4.28 illustrate the current sharing between the high-temperature superconductor (HTS) layers and the copper former layers in two electrical circuit scenarios, referred to as Case 1 and Case 2, for the HTS cable.
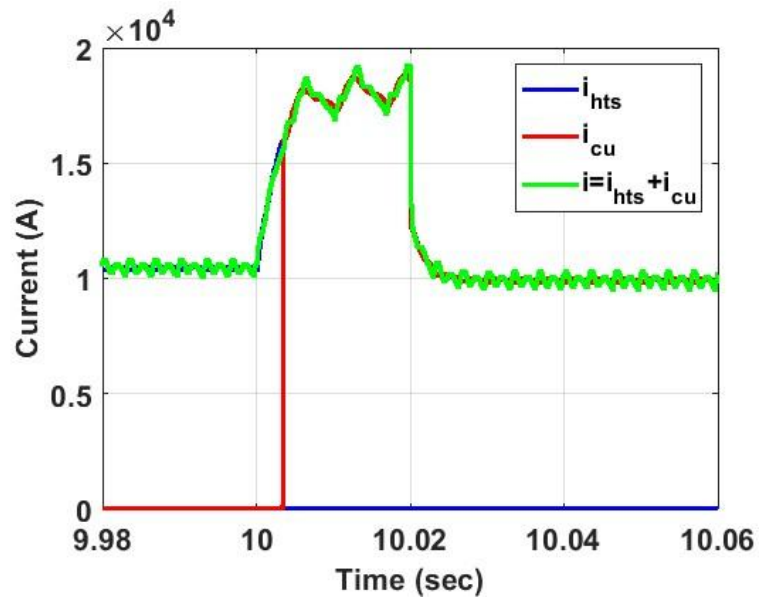


Figure 4.27  The current in the HTS Power cable layer during a fault with the case 1 condition.
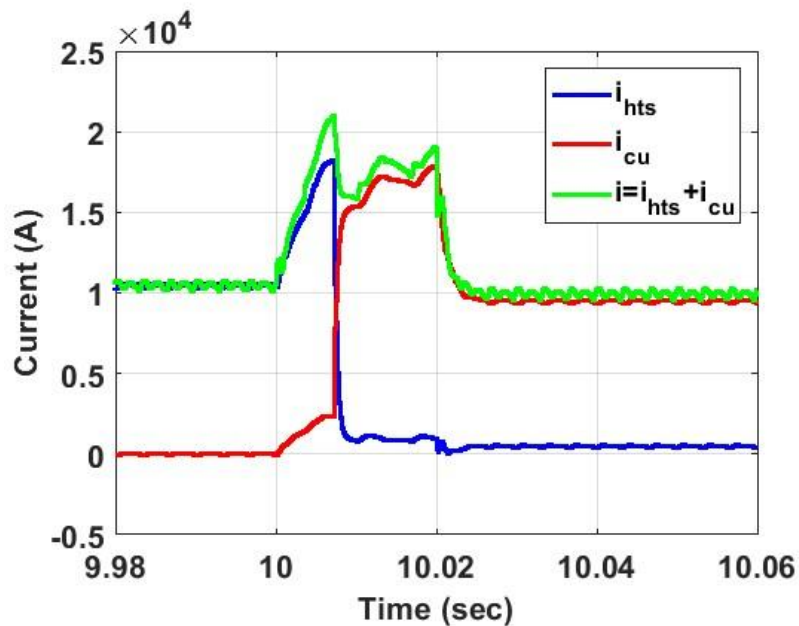


Figure 4.28  The current in the HTS power cable layer during a fault with the case 2 condition.

109

In Case 1, equivalent resistance and inductance values are assigned to both the HTS and copper layers. The inductance of the HTS is notably lower than that of the copper former, thus the overall equivalent inductance closely aligns with the HTS's inductance. This results in noticeable shifts in current distribution between the HTS and copper layers, which subsequently affects the cable's temperature, as demonstrated in Figures 4.25 and 4.26.

Conversely, Case 2 presents a more detailed comparison and closer current values in both the copper former and HTS layers during the quenching phase of the superconductor power cable, offering a contrast to the results seen in Case 1. The inductance values are critical in influencing current behaviour; a notable dip in current observed in Case 2 may impact circuit breaker operations. This dip is attributed to the differences in inductance value between the two layers, where the HTS layer has a pitch angle of 20 degrees. In Case 1, the HTS layer exhibits a lower peak current than in Case 2, while the opposite is true for the copper former as shown in Figures 4.29, 4.30 and 4.31.
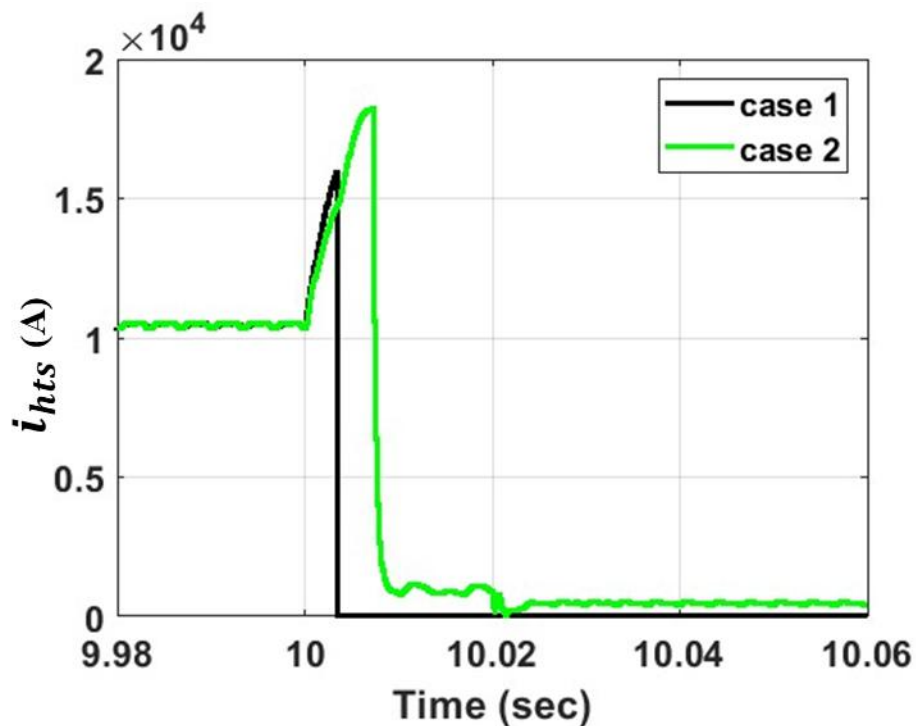


Figure 4.29 Current in the HTS layer.
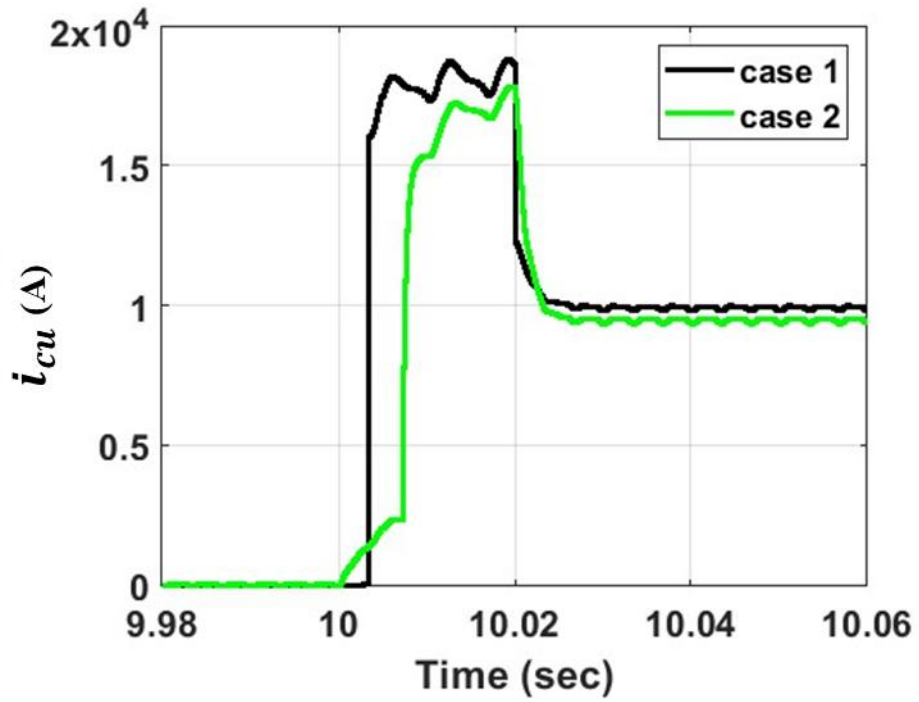
Figure 4.30  Current in the copper former layer.
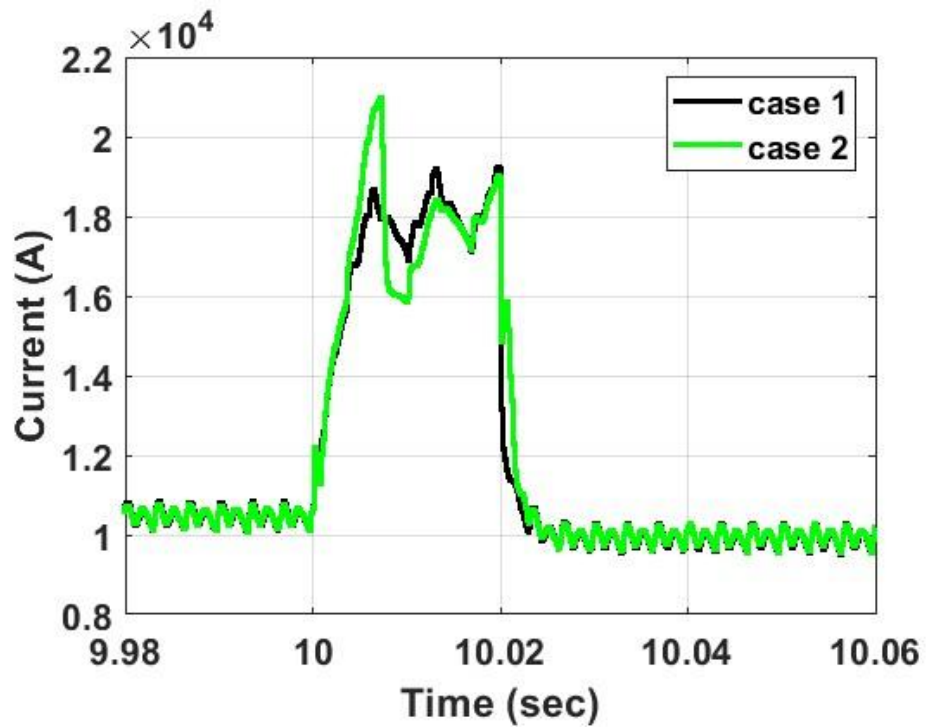


Figure 4.31 Total current in the cable.

The response to faults also differs between cases. Case 1 shows a marked increase in current in both former layers during a fault, more so than in Case 2 and for the HTS current, it is vice versa. In Case 2, the copper former layer displays a lower fault current with a slower rise time, attributed to its higher inductance. The behaviour of the inductors prevents rapid changes in current due to the energy stored within them. Using equivalent inductance values in Case 1, $L_{equ} = \frac{(L_{self\_hts} \times L_{self\_cu})}{(L_{self_{hts}} + L_{self\_cu})}$ contrasts with Case 2, where the actual inductance values of each layer are considered. This results in a more gradual change in current in Case 2 for both HTS and copper layers, with a less pronounced deviation in current amplitude compared to Case 1. Consequently, the cable temperature is higher in Case 2, where the initial peak current exceeds that of Case 1. This analysis supports the adoption of the Case 2 circuit for subsequent cable modelling sections.

## 4.6. Impact of the Pitch Angle of HTS Tapes on Electrical Parameters

The inductance of the superconductor power cable varies with the pitch angle, as illustrated in Figure 4.22. A greater pitch angle results in the higher inductance of the superconductor layer. Due to the nature of inductance, which restricts abrupt changes in current, an increase in pitch angle prolongs the rise time of the high-temperature superconductor (HTS) current during faults, as indicated in Figure 4.32. Consequently, this delay extends the transfer of current to the copper former, as shown in Figure 4.33.

As the pitch angle of the cable twist increases, both the self and mutual inductance values also increase. A cable designed with more inductance needs to wrap the HTS with more of a pitch angle and increase the turns and length of the HTS tape, which subsequently raises the overall cost of the cable. The increase in inductance leads to a delayed rise time of the current in the high-temperature superconductor (HTS) and copper former. These changes in the cable's electrical characteristics are directly related to the

112

pitch angle of the tape. Consequently, as the pitch angle widens, the time required for the fault current to rise is extended. Furthermore, the diversion of fault current from the HTS to the copper former is also delayed. Despite these delays, during a fault duration of 20 milliseconds, the currents ultimately converge to the same level.
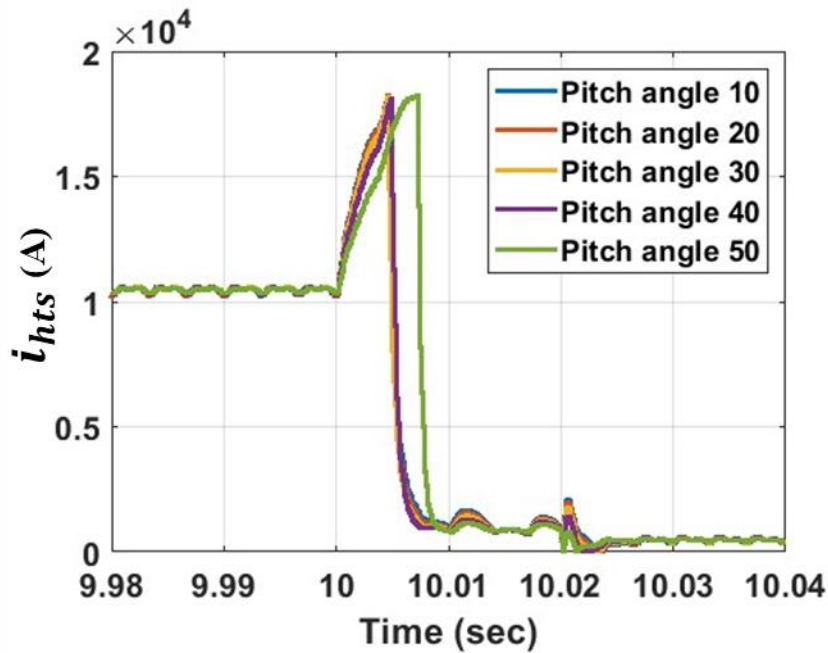


Figure 4.32 Current in the HTS layer with a change in pitch angle.
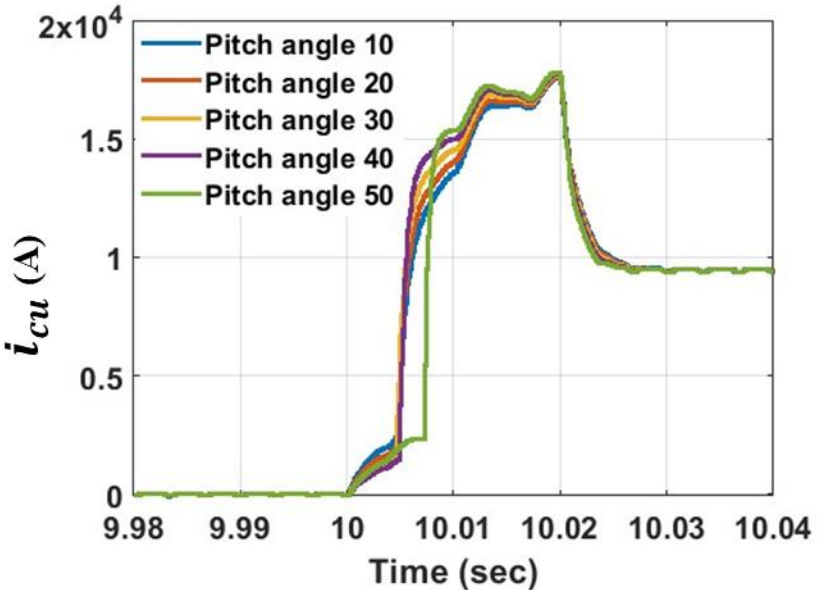


Figure 4.33 Current in the copper former layer with a change in pitch angle.

At this 50-degree pitch, the increased inductance strongly opposes sudden changes in current, explaining the observed shift in behaviour. For a 1 km cable, the tape length increases gradually with pitch angles, starting from 0 degrees at 1 km, then to 1.015 km, 1.064 km, 1.15 km, 1.3 km, and reaching 1.55 km at 50 degrees. This added length heightens both resistance and inductance, slowing down the surge of fault currents.

## 4.7. Grid Faults at Different Locations - Superconductor Study

As global energy demands escalate and the pursuit of sustainable solutions intensifies, superconductor technology emerges as a pivotal advancement in offshore power transmission. Superconductor cables, with their unparalleled current capacity and minimal electrical resistance, present a transformative approach to handling substantial power loads across vast distances. This chapter delves into the specific impact of fault locations on the performance and reliability of High Voltage Direct Current (HVDC) superconductor cables.

Faults in superconductor cables can lead to significant operational challenges, including intense joule heating which might cause the cable to quench or suffer permanent damage. This section explores the crucial role of fault location in influencing quench behaviour and current distribution within a superconductor cable system.

We considered the grid's different location on the superconductor power cable. Here we updated the cable inductance and capacitance based on the pitch angle of the cable. The shielding layer was considered in the cable structure and the cable model shown in Figure 4.34 is used in the simulation.

Where $r_1$ to $r_9$ is the radius of the superconductor cable layers as shown in Figure 4.34. where $\mu_0$ (vacuum permeability coefficient) $= 4\pi 10^{-7} \text{N/A}^2$ and $V_{hts}$, $i_{hts}$, and $R_{hts}$ are the voltage, current, and resistance of the HTS layer. Similarly, for the copper former with subscript cu.
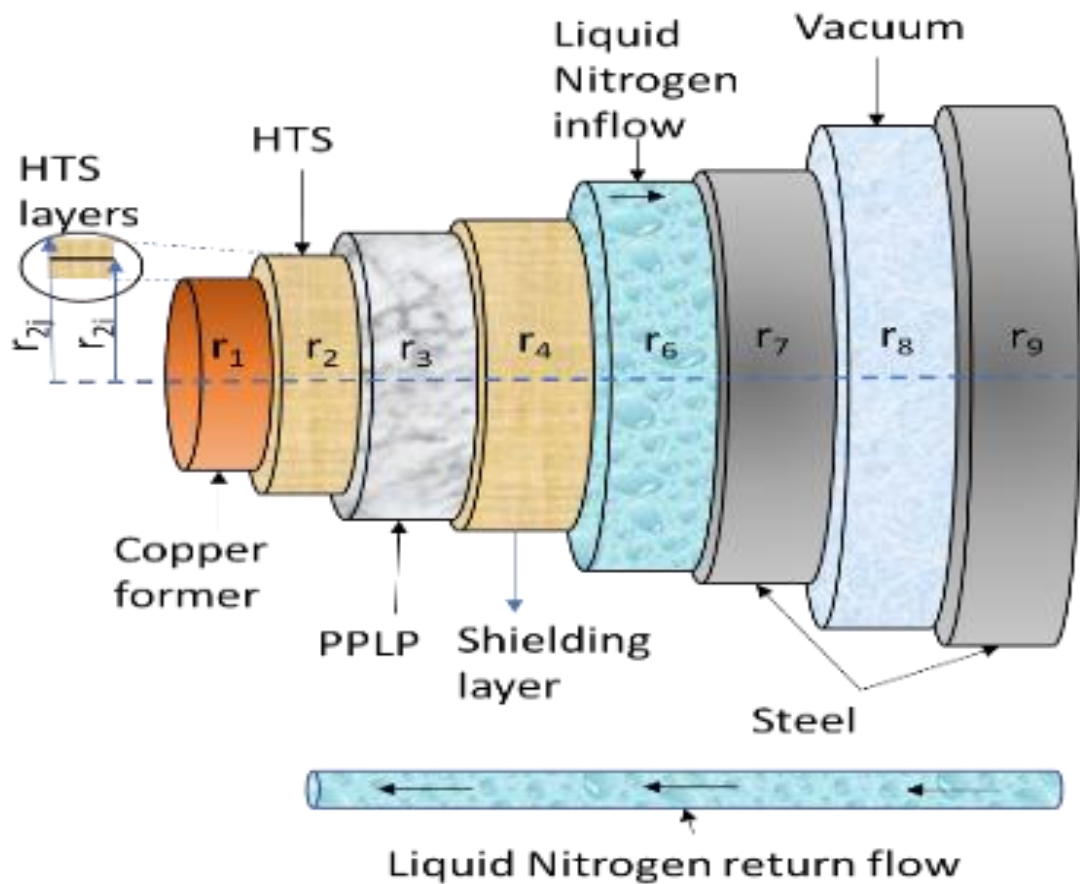
Figure 4.34 HTS cable structure view.

The starting temperature for $T_{r1}^0$ to $T_{r5}^0$ is maintained at 70 K, which is also the temperature of the LN2 inlet. The material emissivity's are $\varepsilon_1$ and $\varepsilon_2$, the material emissivity and the Stefan-Boltzmann constant is $\sigma$, and the values for $B_1$ and $B_2$ are from reference [175].

The cable parameters used for the modelling are shown in Table 4.3. The flow chart of the cable modelling is shown in Figure 4.35. The cable components are discretised both radially and axially, as illustrated in Figure 4.36.
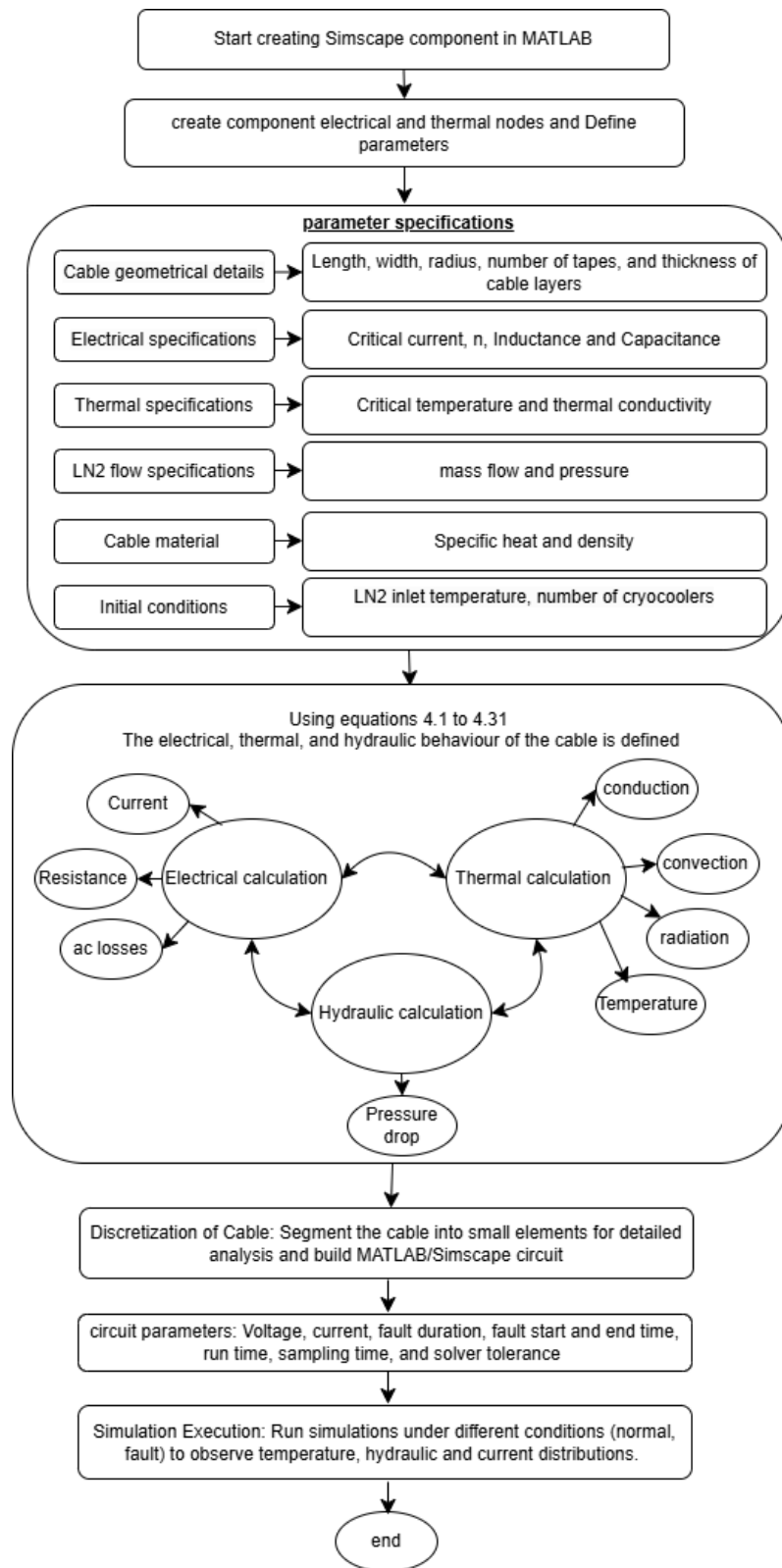
Figure 4.35 Flow chart of the cable component design in MATLAB/SIMSCAPE

Table 4.3 HTS cable parameters when the pitch angle is 20.

| Parameter | Value |
|---|---|
| Critical current (Ic) | 22 kA@70K |
| Capacitance (C) | 0.191 µF/km |
| Self-inductance of HTS ($L_{self\_hts}$) | 0.0579 mH/km |
| Self-inductance of former ($L_{self\_cu}$) | 0.188 mH/km |
| Mutual inductance ($M$) | 0.0455 mH/km |
| Number of tapes | 74 |
| Cable length | 100 km |
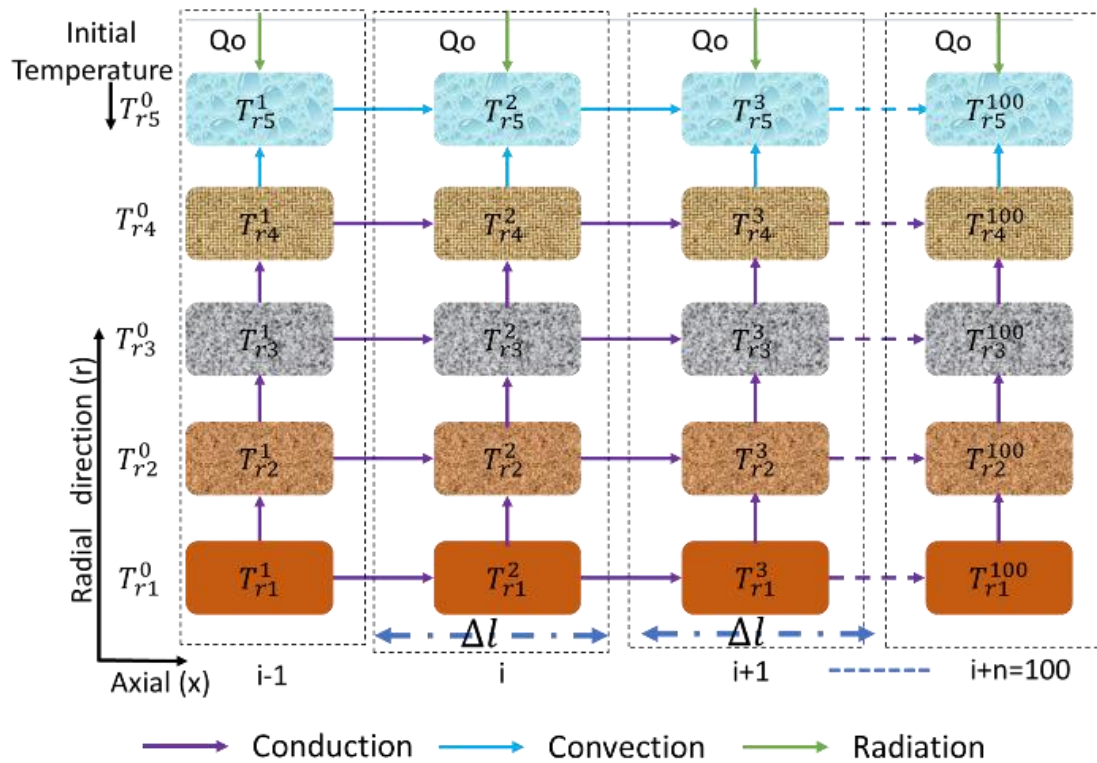
Figure 4.36 Discretised electrical-thermal model of the HTS cable.

The HTS cable model is segmented into 100 parts, each resembling a pi section and measuring 1 km in length, as illustrated in Figure 4.37(a). This model accounts for heat transfer across the layers through conduction and convection within each segment. These factors are integral to determining the electrical and thermal properties of the DC HTS cable under various fault conditions. For thermal management, a cryocooler is installed every 5 km along the length of the HVDC superconducting cable. Additionally, joint connections between cable sections are made at every 1 km interval.
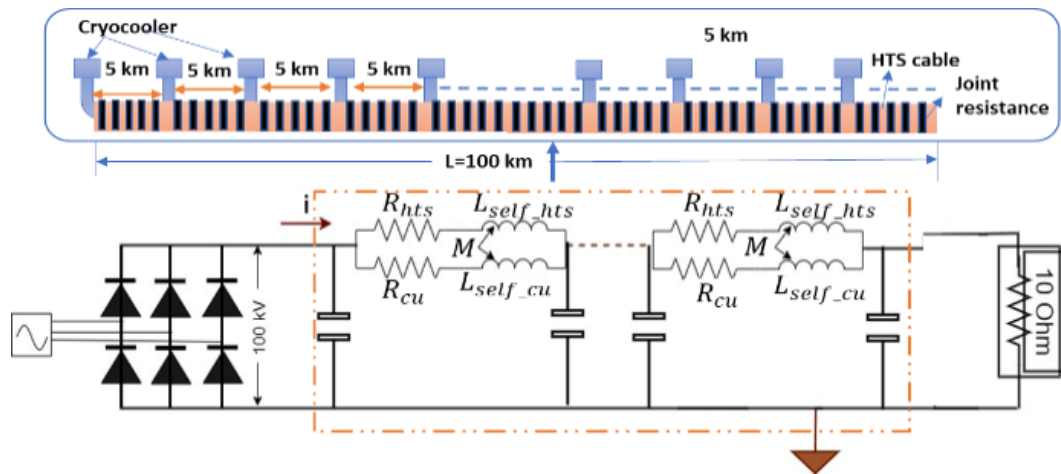


(a)
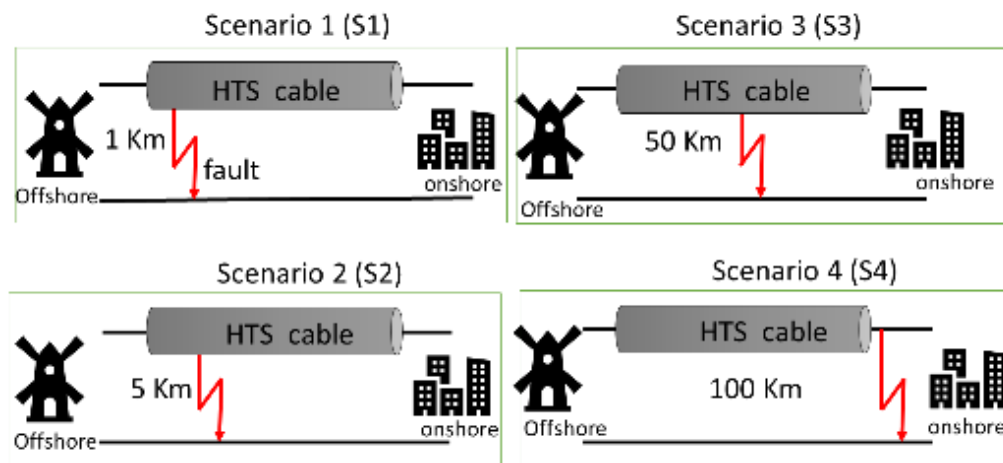


(b)

Figure 4.37 (a) The electrical equivalent circuit used in the Discretised MATLAB/SIMSCAPE model shows the cooling system arrangement and (b) fault location in the cable scenarios.

## 4.8. Steady-state condition

The simulation findings illustrate that the temperature along the superconducting cable fluctuates between 70 K and 73.8 K across each 5 km segment. This variation in temperature impacts the critical current ($I_c$) of the superconductor. Starting at 22.2 kA, the $I_c$ diminishes to 18 kA at the termination of each 5 km section within the 100 km stretch of cable. Initially set at 70 K, the system employs 20 cryocoolers to manage the temperature throughout the 100 km cable. The thermal and electrical properties of the superconductor exhibit consistent patterns every 5 km, as shown in Figures 4.38(a) and (b), which respectively display the temperature and $I_c$. In terms of resistance, the copper former registers 1.5 mΩ per km, whereas the HTS resistance is significantly lower, almost negligible in comparison. Under steady-state conditions, the HTS layers conduct a current of 10 kA, whereas no current flows through the copper former due to its high resistance.



(a)                                    (b)
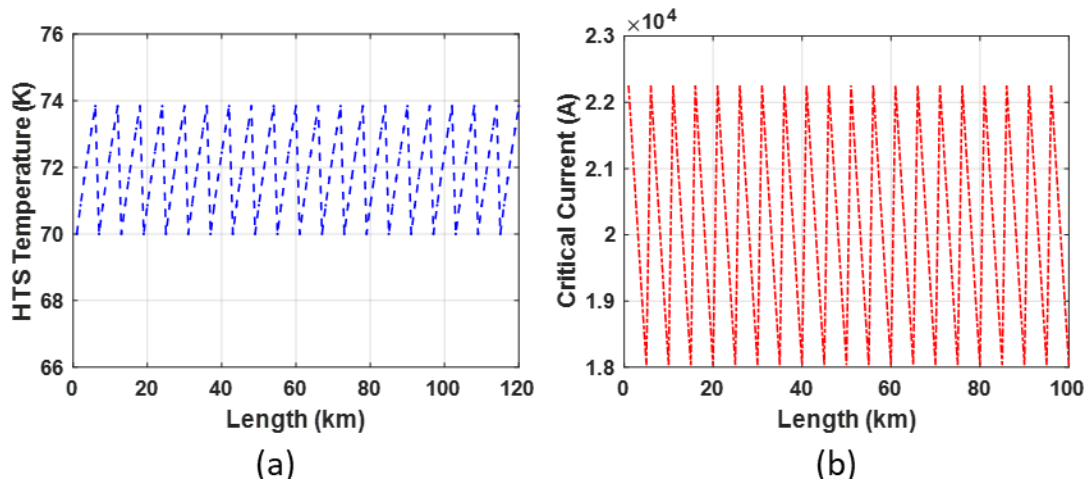
Figure 4.38 Under normal operating conditions (m=1 kg/s) (a) HTS temperature, (b) critical current of the cable.

## 4.9. Transient condition analysis

Faults in superconductors often stem from irregularities in the dielectric material [176] and the inherent limitations in the length of the 2G HTS tapes, which necessitate joints and terminations to integrate them into the power distribution network. This situation has

been observed in grids such as those centred in Europe [28]. Our research involved conducting fault tests at various locations on the superconductor power grid to examine how fault location affects the superconductor's thermal and electrical responses. When a fault occurs, the current in the superconductor surges beyond its critical threshold. This excessive current elevates the resistance in the HTS tapes, leading to joule heating. The subsequent temperature increase in the superconductor causes it to quench. During quenching, the resistance of the superconductor surpasses that of its copper former, redirecting the current from the superconductor to the copper.

The electrical properties of a cable change when the location of a fault varies. If a fault occurs further away from the power source, the resulting fault current in the cable is typically lower than if the fault is near the generation side. This effect is demonstrated in Figure 4.39, which shows that a fault 1 km from the source (Scenario S1) produces the highest fault current amplitude. As the fault location moves farther from the source, as seen in Scenarios S2, S3, and S4, the amplitude of the fault current diminishes. When the fault is closer to the power generation side, the cable's current increases more sharply, leading to a higher rise in temperature within the superconductor.
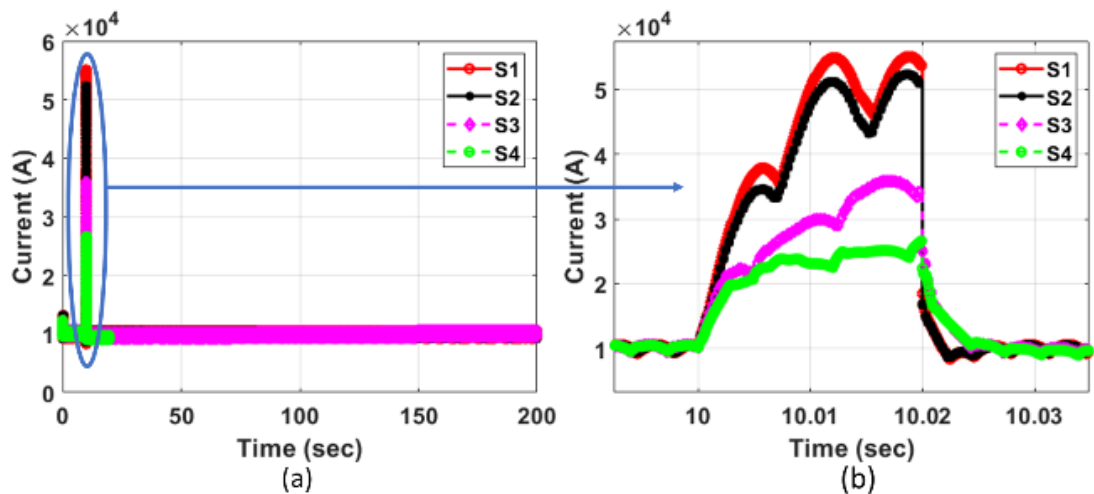


Figure 4.39 The current in the cable during a fault in different scenarios, S1 to S4.

The source we used is an AC three-phase source with a short circuit power level of 10 G VA and X/R ratio of 1, This AC was converted to DC for HVDC transmission by HTS

120

cable. The effect of the resistance is shown in Figure 4.42. After the HTS quenches during the fault, the resistance of the HTS is around 20 times higher than the copper former. As the resistance of the HTS increases, the current drifts its path and will flow in the copper former instead of HTS.

Our investigation into the behaviour of current flow in the circuit when a fault occurs at various cable segments yielded interesting findings. It was observed that the pattern of the cable repeated every five kilometres up to the location of the fault in our simulation. For instance, a fault at the 5 km mark is depicted in Figure 4.40, which also shows the resulting variations in current flow through the high-temperature superconductor (HTS) and outer layers along the cable's length.
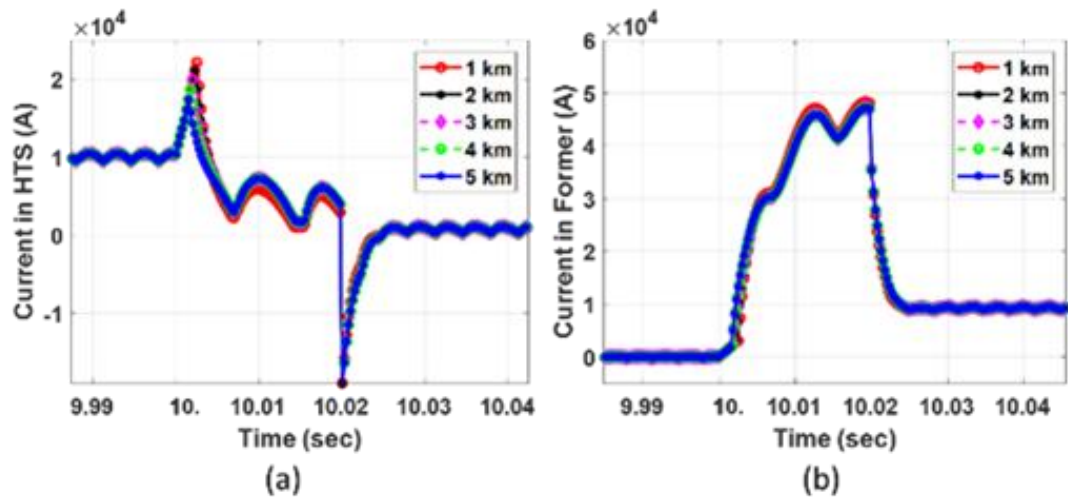


Figure 4.40 Current in the HTS and copper former during scenario 2.

When a fault occurs at the 5 km mark (S2), the current within the High-Temperature Superconductor (HTS) begins to increase, ultimately surpassing 18 kA. This leads to quenching in the cable's 4-5 km section, prompted by a rise in $R_{hts}$ and a subsequent decrease in $i_{hts}$. As the current exceeds 19 kA, similar quenching events occur sequentially in the 3-4 km, 2-3 km, 1-2 km, and 0-1 km sections of the cable as the current levels exceed the critical currents ($I_c$) of these sections. In our simulations, a temporary fault lasting 20 milliseconds was introduced. After the fault is resolved, the current shifts from the short circuit path back to the HTS cable. This transition results in a negative peak

in the HTS layer's current, triggered by rapid changes in ($M \frac{di_{cu}}{dt}$), as outlined in equation 4.28. Even once the fault is cleared, the temperature of the HTS cable remains above the critical temperature ($T_c$), and the current continues to flow through the copper former layer until it eventually cools to below $T_c$.

When a fault happens at 100 km (S4), the current distribution in the layers is illustrated in Figures 4.41(a) and (b). This pattern resembles the fault observed at 5 km in Figure 4.40. During such events, the pathway becomes more resistant, which serves to cap the fault current at a peak of 25.6 kA.



(b)
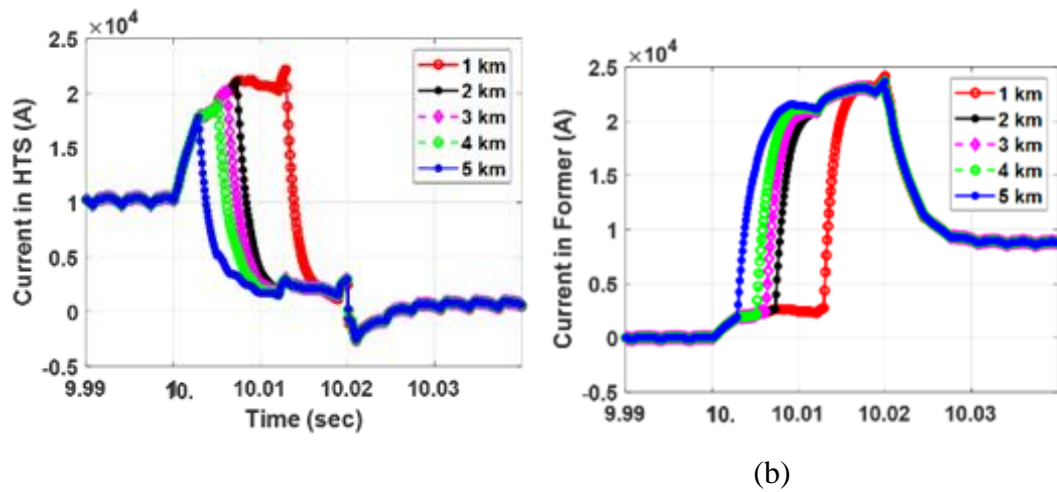
Figure 4.41 Current in the (a) HTS and (b) copper former during scenario 4 (S4)

The analysis demonstrates that the electrical characteristics and thermal behaviours are closely linked to the location of faults in the system. Figure 4.42 illustrates variations in the high-temperature superconductor (HTS) temperatures, highlighting significant differences at 5 km and 50 km from the source. Specifically, faults nearer to the generation point have a greater thermal effect, resulting in an HTS temperature difference of 20.38 K between the 5 km (S2) and 50 km (S3) locations. Additionally, the HTS temperature in the S2 scenario requires about 13 seconds longer to drop below the critical temperature compared to the S3 scenario. Peak temperatures observed after quenching are approximately ($T_{r2}^{5}$ =272.78 K) at 5 km and ($T_{r2}^{50}$=252.4 K) at 50 km, with recovery times to a stable pre-fault condition of 163 seconds and 150 seconds, respectively. The increased

122

duration of recovery near the generation source can be attributed to the higher current amplitudes during faults as shown in Figure 4.39, which lead to augmented joule losses and consequent heating. The resistance and joule losses in the HTS layer and copper former are further detailed in Figure 4.42.

Figure 4.43 illustrates the temperature escalation in the copper section, which results from the current increase shown in Figure 4.41(b). The temperature begins to rise at the 5 km mark and continues progressively to the segments from 4 km to 1 km. The thermal analysis reveals that, based on fault location, the superconductor needs roughly 2.5 to 3 minutes to return to the superconducting state after a quench event following no circuit breaker operations in the circuit for 20 ms.
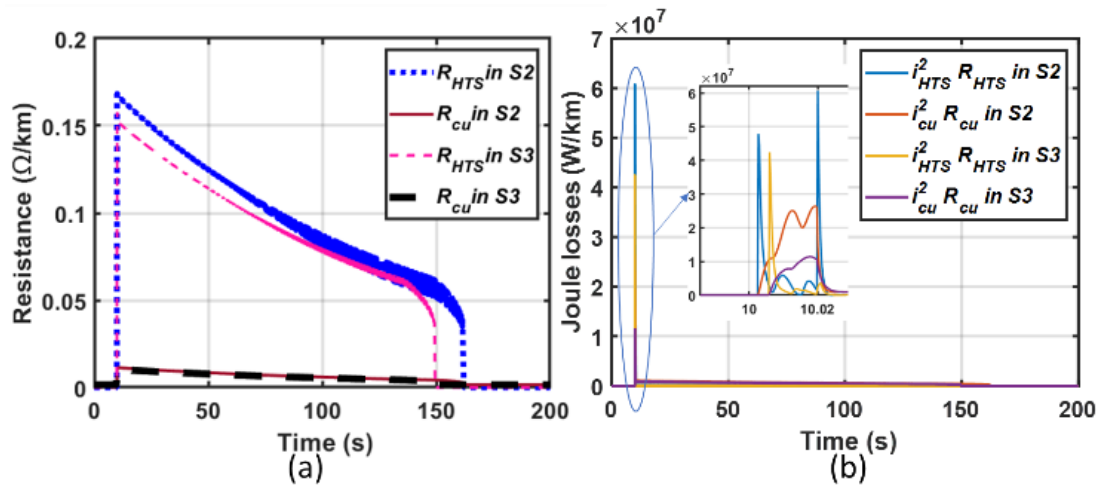


Figure 4.42 (a) Resistance and (b) Joule losses during scenarios S2 and S3.
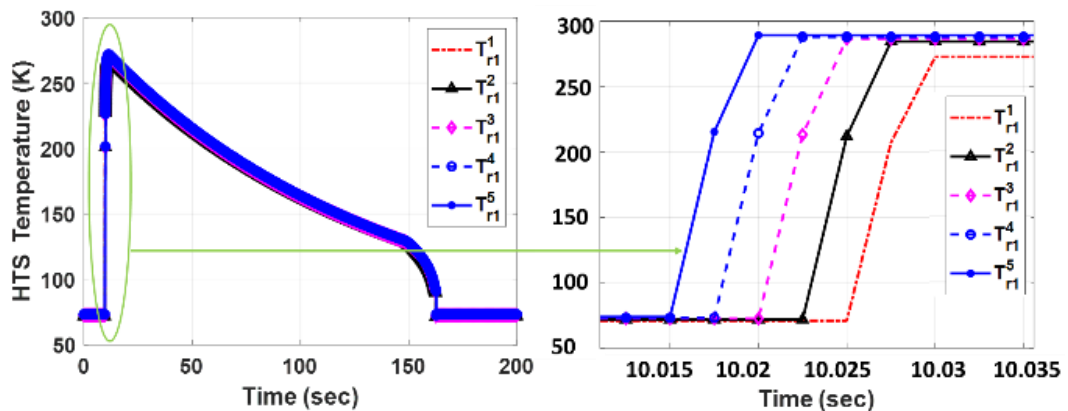


Figure 4.43  Temperature of the copper former layer during a fault occurs at 5 km.

# 4.10.      Summary of Chapter 4

This study has successfully developed and analysed a simplified distributed model of a multilayer HTS power cable for long-distance HVDC systems. The simulation outcomes have been instrumental in understanding the thermal and electrical dynamics under both normal and transient conditions. Notably, the results confirm that the thermal properties remain consistent irrespective of whether the inductance (L) and capacitance (C) are modelled as distributed or lumped, with resistance (R) distributed across the system. The investigation revealed that during a temporary PG fault, the superconductor quenches, transferring any current to the copper former for 3 minutes.

Once the fault is cleared, the current promptly reduces below operational levels, allowing the temperature to slowly decrease until it reaches below the critical temperature ($T_c$), returning the cable to its superconducting state. These findings emphasise the resilience of the HTS cable in fault conditions, showing no permanent damage to the cable structure. Further analysis highlights the necessity of employing multiple cryocoolers to maintain the temperature below the boiling point of liquid nitrogen (LN2), which is crucial for the stability of long-distance power transmission. Additionally, this study explores the impact of the twist pitch angle of the 2G HTS tapes on electrical and thermal behaviour during faults.

The study results highlight the necessity of distributed models over lumped models for HTS (high-temperature superconducting) power cables. Distributed models provide detailed information about the temperature of both the superconductor and coolant along the entire length of the cable. They also reveal the degradation of the critical current and the quenching of the superconductor during faults. For cables with a lower critical current (Ic), the superconductor quenches along the entire length of the cable, and the thermal recovery time required to return to a superconducting state is also indicated.

It was determined that variations in pitch angle significantly alter the distribution and magnitude of electrical characteristics during faults, influencing the overall performance

of the cable system. In conclusion, the insights garnered from this research provide a substantial contribution to the field, offering a detailed understanding of the operational dynamics of HTS power cables under various fault conditions. These findings not only pave the way for optimizing the design and functionality of superconducting power cables but also enhance their application in real-world grid interconnections, ensuring efficient and stable power transmission across extensive distances.

# Chapter 5

# Joint Performance and Quench Behaviour Analysis in Superconductors

## 5.1. Introduction Superconductor joints

Superconducting materials lose their electrical resistance when cooled below a specific threshold, known as the critical temperature ($T_c$). These materials exhibit the unique ability to transmit direct current (DC) power without electrical dissipation. As a result, high-temperature superconductors have become a sought-after technology for applications like power cables and superconducting fault current limiters (SFCLs) within electric grids. They are also employed in magnetic applications such as particle accelerators, MRI scanners, and various machines. The fabrication of superconducting tape involves producing limited lengths, which are connected at terminations using superconducting joints. These joints are essential for the persistent-mode operation of superconductors. The production of single-piece, long-length HTS tapes and the creation of high-quality HTS joints are essential for the application of superconductors in long-distance power transmission systems. Nowadays, 1 km long 2G HTS tapes with CC technology are possible with excellent transport current properties [177]. Unbound joint interferences, defects, and cracks lead to higher resistance, resulting in excessive Joule heating due to increased energy dissipation [178].

## 5.2. Joint Fabrication

The joint in the superconductor power cable is crucial in superconductor tapes. As they are made with non-superconductors, their resistance is higher, and improper joints lead to an increase in resistance, joule losses and thus quench the superconductor. The material used in the fabrication of the superconductor joint is PbSn (Lead and Tin) solder.

In this, a heating and pressing technique is used to create a joint. First, select the required tapes for the joints and then cut in and mark the length of the joint to prepare. Use the soldering pot and maintain the temperature around 300-350 °C, after which the solder reaches a liquid state. Apply the flux to the HTS tape area where we need a joint. Dip the HTS tapes where the flux is applied for 10 sec and remove the tape from it. In the preparation of the soldering, the tapes are first coated with flux to enhance the soldering quality before arranging the tapes according to how the joint should be as shown in Figure 5.1(d). The soldering machine as shown in Figure 5.1 (e) consists of two stainless steel plates with embedded heaters. The upper plate is hydraulically connected to a jockey handle that allows for the control of the pressure between the plates. A display monitor is used to display the temperature of the plates. The temperature of the plates is set at 230 °C.

Once it reaches the set temperature, the plates are brought close together and the tapes for soldering are carefully positioned between them. We apply the press until both the plates on top and bottom touch the joint area and leave it for 90 sec. After 90 seconds, the solder heats up and distributes the solder evenly between the tapes. After 90 sec, we then apply the full press and set the temperature to 220 °C. Now we switch on the cooling system (fan). Once the temperature comes to 165 °C, take out the joint from the hydraulic press and clean it. This process is shown in Figure 5.1. The superconductor tape joint fabricated is shown in Figure 5.2.
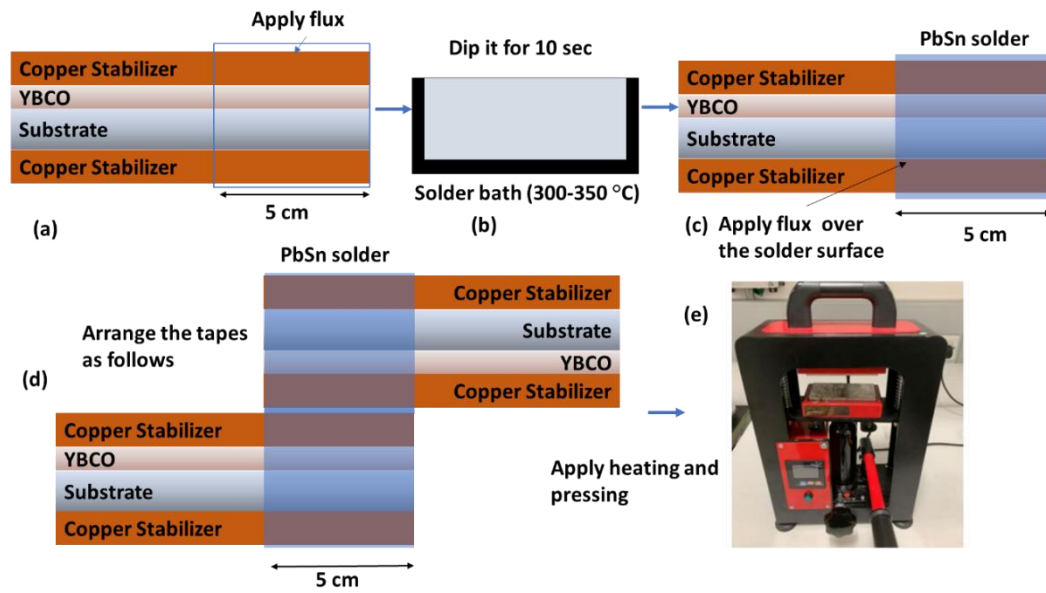
Figure 5.1 Solder joint fabrication heating and pressing technique.
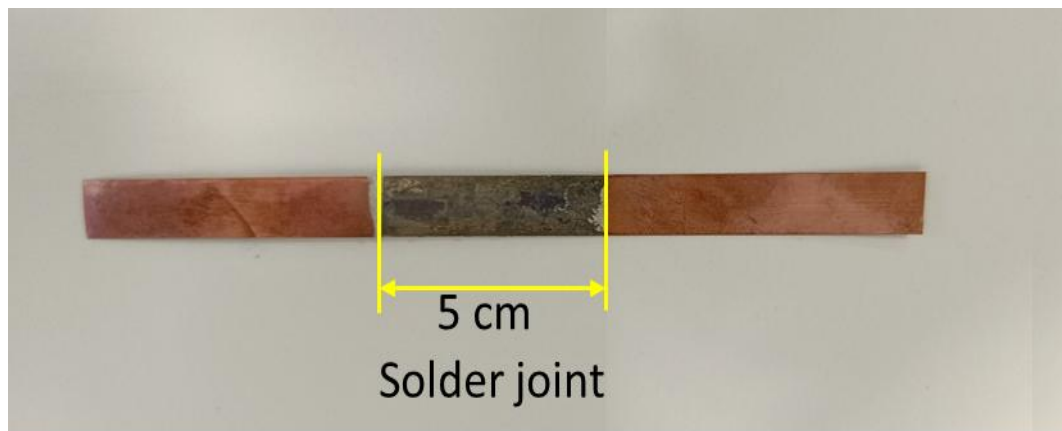


Figure 5.2 Fabricated 12 mm wide 2G HTS tape lap joint using PbSn solder.

## 5.3. Joint resistance measurement

The resistance measurement schematic diagram is shown in Figure 5.3. The 2G HTS tape was cooled to LN2 temperature by placing the superconductor in the LN2 bath. A current was applied to the HTS tape using the power source (TDK-Lambda GSP 10-100 0-10V/0-1000A DC power supply). The data was recorded using the National Instruments

(NI cDAQ-9178 and NI 9239 data card) and a computer with LabVIEW programming. The current flowing in the circuit was determined using the equation below.

$$I = \frac{V_s}{R_s}$$

5. 1

Where $V_s$ and $R_s$ are shunt voltage and resistance across the shunt.

The resistance of the HTS tape $R_j$ is calculated by a similar equation $I$ through HTS tape with voltage $V$ across it.

$$R_j = \frac{V}{I}$$

5. 2
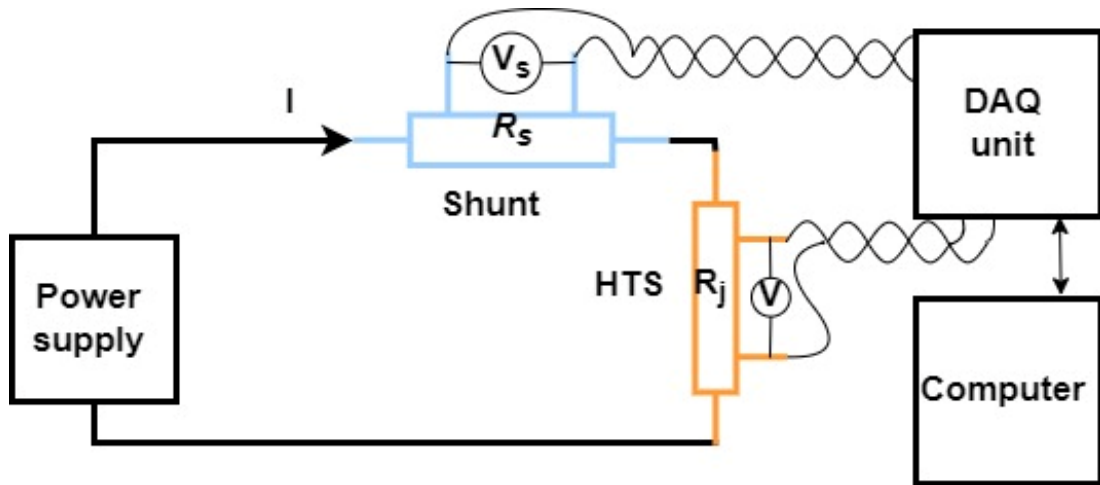


Figure 5.3 Schematic view of the resistance measurement circuit.

By using the LabVIEW software, we controlled the current flow from the power supply in the circuit. The HTS tape was fabricated with a PbSn joint of 5 cm long. The current and voltage signal is shown in Figure 5.4. The resistance signal from the data calculated is shown in Figure 5.5. The smoothed value of the joint resistance curve shows a joint resistance of around 7 nΩ.

The NI-9238 can detect voltage changes as small as 59.6 nV, which is well below one microvolt (1 μV = 1,000 nV). However, practical measurement accuracy is influenced by

factors such as noise, offset errors, and temperature drift. According to the NI-9238 specifications, the typical input noise is 3.9 µV RMS, and the offset drift is 1.3 µV/°C.
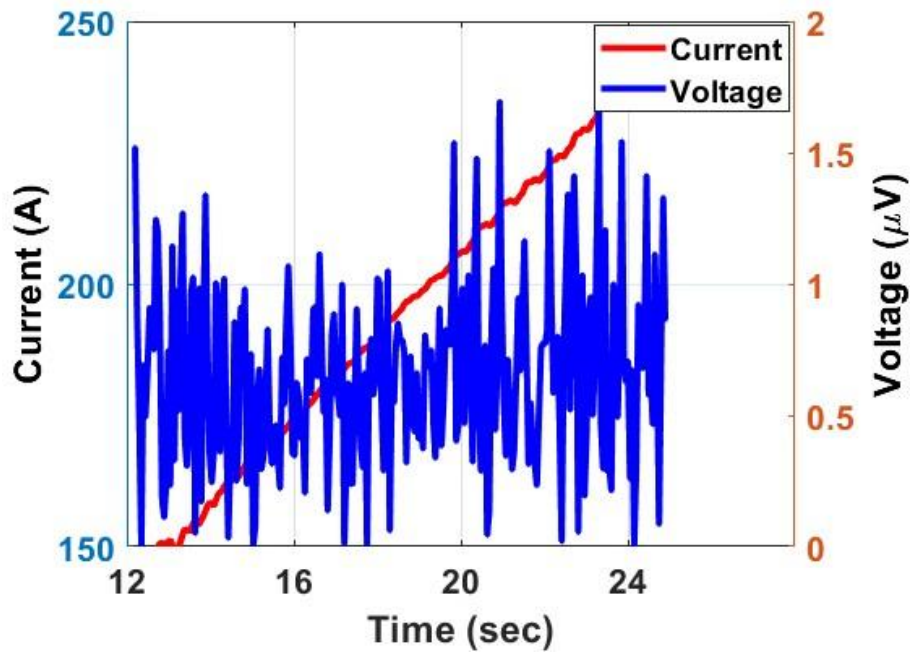


Figure 5.4 Current and voltage of the 2G HTS tape with a PbSn solder joint.
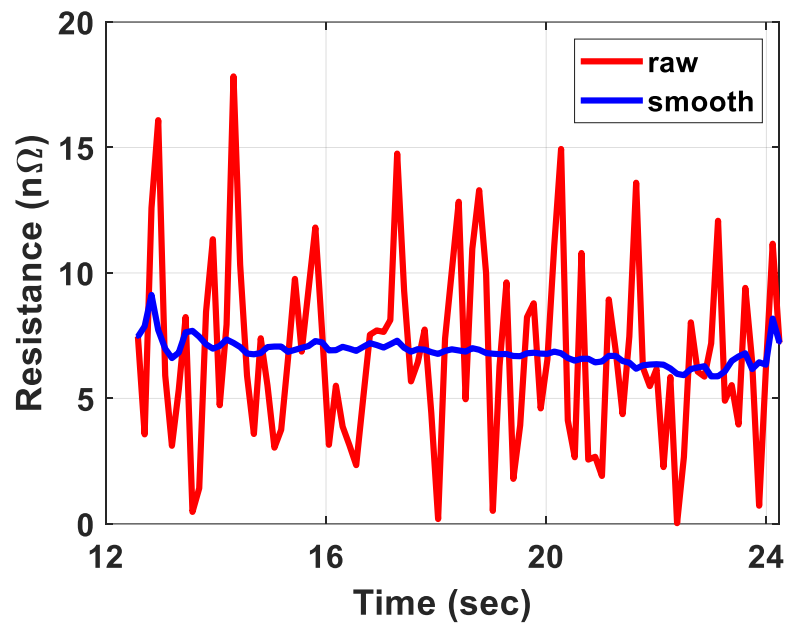


Figure 5.5 Resistance of the 2G HTS tape with a solder joint.

## 5.4. Critical current measurement

The critical current measurement schematic diagram is shown in Figure 5.6. The $I_c$ is the key parameter explaining YBCO HTS tape performance for use in the superconductor cable application. The superconductor tape is connected to the DC power supply (TDK-Lambda GSP10-1000 0-10V/0-1000A) with a shunt in series. The 2G HTS tape was placed in a tub filled with LN2 to cool to increase the superconductor to 77 K. The measurement was done using the NI 9238 Data acquisition (DAQ) unit and LabVIEW programming. To measure the voltage across the HTS tapes, a pair of voltage taps were soldered with a separation of 8 cm between voltage taps.
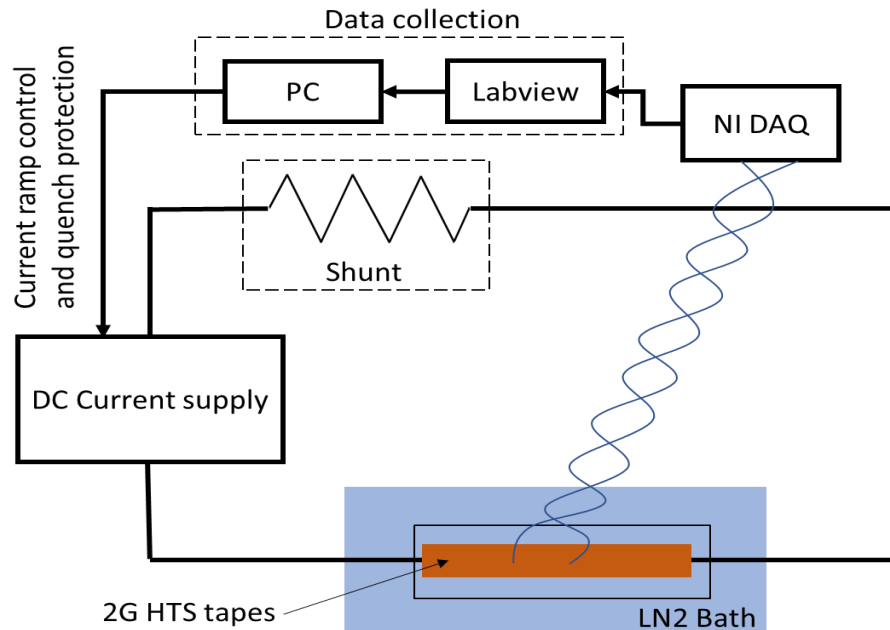


Figure 5.6  Critical current of the HTS tape.

The current ramp rate of 0.0099 A/ms was chosen to carefully control the current increase in HTS tape resistance measurements, reducing thermal and electromagnetic impacts. This rate minimises overheating risks by allowing gradual current application, helping maintain stable superconducting conditions. Additionally, it enhances measurement accuracy by avoiding sudden changes that could add noise or distort data, thus providing a clear, reliable response to the tape's resistance under testing. Using the

131

LabVIEW program, we set the limit to the maximum current flow. Here, the S-innovation superconductor 2G HTS tape (12 mm wide, 2 µm Ag, and 20 µm copper stabiliser) per side was used in the experiments. All measurements were carried out in a self-filed condition with no external field.

A current ramp was applied to the 2G HTS tapes. Under the voltage criterion (1 µv/cm), the $I_c$ of the tape measured is around 427 A as shown in Figure 5.7.
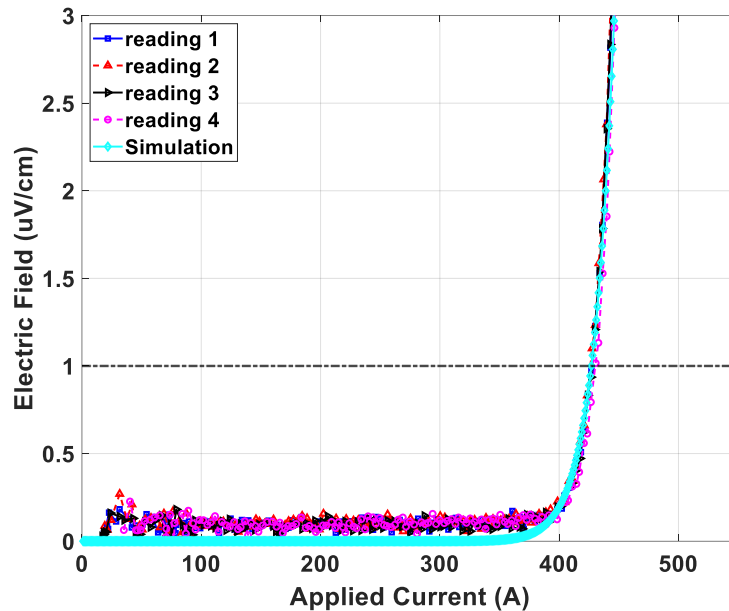


Figure 5.7. E-I characteristics of 12 mm wide HTS tape for critical current determination

The $I_c$ used in the simulation equations is validated by this experimental data. The simulation $I_c$ as in Chapter 4 calculated replicates the same as the experiment results.

## 5.5. Quench Behaviour Analysis

The main factors that are the root cause of the quench in the superconductor are a transport current higher than critical, temperature rise, conductor motion, and failure or cracks in the insulation [179]. The common quench detection methods of the superconductor are temperature sensor thermometry, the optical temperature detection method, the Hall temperature detection method, fluorescence thermal imaging

thermometry, the acoustic temperature detection method, the capacitive method, radiofrequency wave technology quench detection, and the voltage method [180].

In order to protect the superconductor from the potential damage of the quench, thermal monitoring is also necessary to detect the quench and take action to avoid damage to the superconductor.

It is not economical to validate the simulation results of the long-distance superconductor power cable via experiments. Here, short-length HTS tapes are quenched under a transport current higher than the $I_c$ of the tape experimentally and the same conditions are used in the model simulation to compare and validate the simulation results.

An experiment was conducted to detect the temperature of the superconductor using the PT 103 sensor on an HTS tape during quenched conditions, and the simulation results were validated using the same simulation methodology used in Chapter 4.

The NI 9265 data card is used to control the supply current to the RTD PT 103 temperature sensor and its details are mentioned in Table 5.1 below.

Table 5.1 PT 103 RTD sensor details

| Parameter | Values |
|---|---|
| Temperature range | 14 K to  873 K |
| Thermal response | 1.75 s at 77 K 12.5 s at 273 K |
| Recommended excitation | 1 mA |
| Reproducibility | ±5mK |

For quench detection in the superconductor, a ramp current up to 445 to 460 Amps is applied with a ramp of 0.009 A/ms, measuring the temperature of the superconductor tapes using the RTD PT 103 sensor from Lakeshore. It is a resistance temperature detector (RTD) sensor made using platinum wire. In this RTD, the temperature measurement is

achieved by observing the change in the resistance of the metal conductor in relation to temperature. The relationship between temperature and resistance is described as follows:

$$R_t = R_o(1 + (T - T_o)) \hspace{4cm} 5.3$$

Where the $R_t$ and $R_o$ are the resistance values at temperature $T$ and $T_o$, respectively.

The PT 103 has four terminals: two for the current supply and two for measurement purposes. A 1 mA current is fed into the PT 103 using the DC power supply model HY3003, which connects to the NI 9265 card. The LabVIEW program on the PC controls the current supplied to the sensor. The temperature and current measurements are depicted in the schematic diagram shown in Figure 5.8. Voltage taps, soldered 8 cm apart on HTS tapes, are used for voltage measurement, and a current shunt measures the current in the superconductor tape.
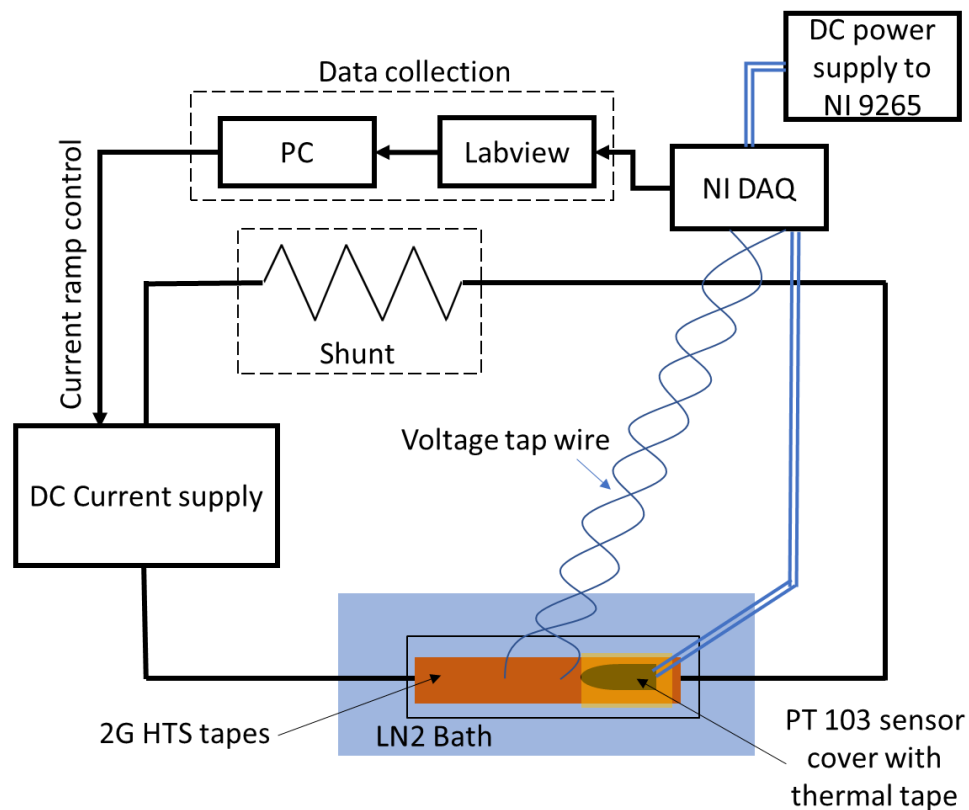


Figure 5.8 Schematic view of the temperature measurement.

To ensure uniform thermal distribution across the temperature sensor and to increase the contact area with the HTS tapes, a high thermal conductivity grease is applied over the sensor's surface. It is then wrapped with insulation tape, as illustrated in Figure 5.9.
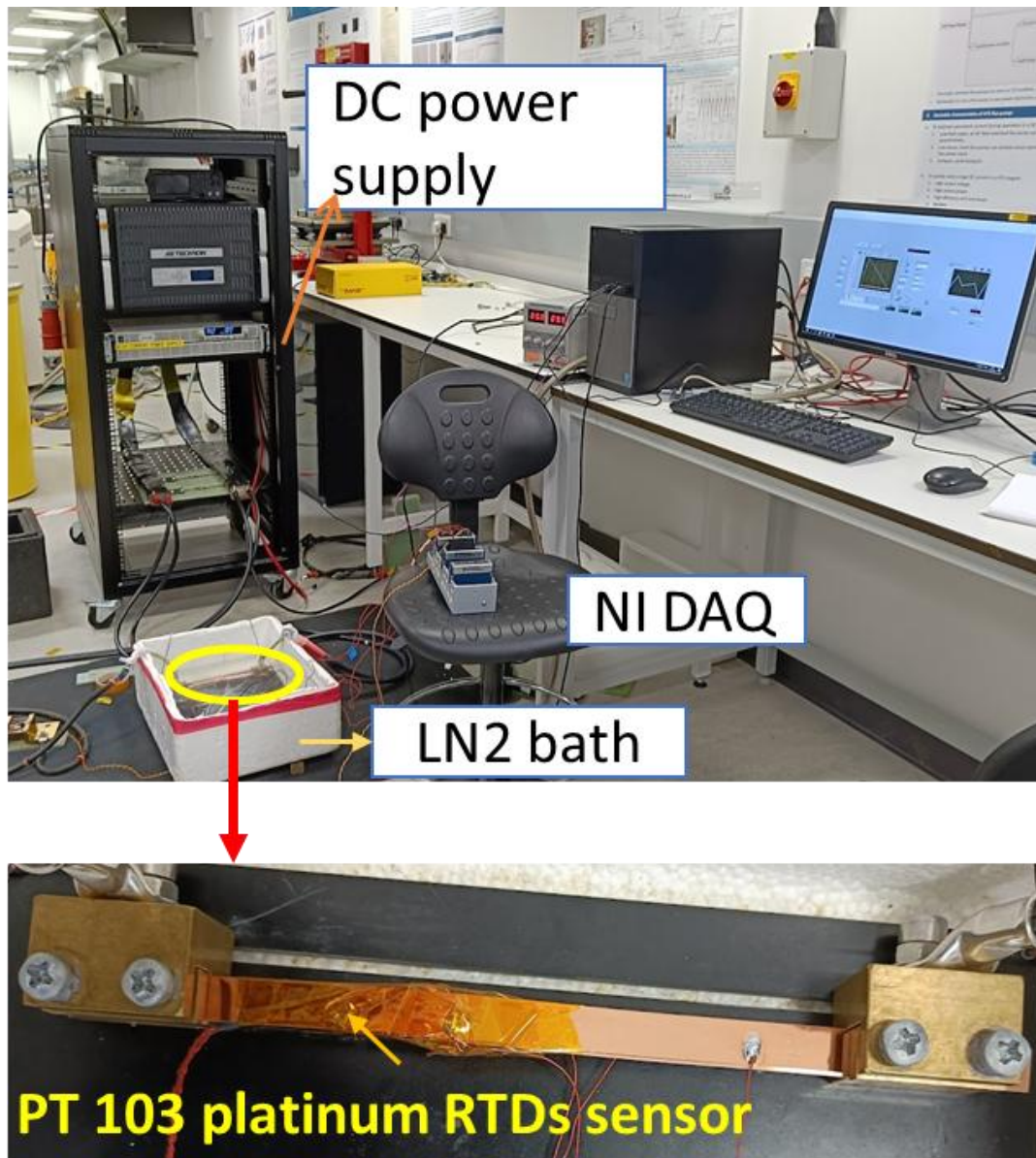


Figure 5.9. Experimental setup for quench detection using the PT 103 sensor.

As the current increases, it leads to an increase in both the resistance and temperature of the tape. These changes can be detected using thermal measurements. Initially, we used kapton tape to cover the temperature sensor. However, these tapes were very thin,

requiring multiple layers to prevent the liquid nitrogen (LN2) from entering the sensor's surroundings, which made it difficult to accurately sense the temperature of the HTS tapes. Therefore, we replaced them with insulation tape, which proved to be more effective for this measurement process.

The simulation methodology described in Chapter 4 was employed here but was applied solely to the HTS tape in the LN2 bath. The experimental results were measured and compared with those of the simulation. The current ramp is depicted in Figure 5.10(a), and the temperature of the tape is shown in Figure 5.10(b). The current pattern curves for both cases were under the same conditions. Measuring the tape temperature is complex due to its placement in the LN2 bath and because the temperature sensor's response time varies with temperature. The current ramp applied, as shown in Figure 5.10, reached up to 445 A in both the simulation and experiment during the period when the temperature was measured.

The simulation demonstrated a sharp exponential increase in the temperature of the superconductor tape when it exceeded the $I_c$. The response time of the PT 103 temperature sensor, as indicated in Table 5.1, is approximately 12.5 seconds at around 200 K. In the simulation, the temperature reached 278 K. However, the PT 103 sensor only detected 237.63 K. This discrepancy is attributed to the sensor's response time, which is slow to detect the rapid temperature changes caused by joule heating.

As the tapes are immersed in a liquid nitrogen medium, they cool quickly, as our model demonstrates. However, the experimental results indicate a slight delay in temperature rise and fall. This delay may be due to the platinum wire of the RTD being encased in a solid material, which likely slows the heat transfer from the HTS to the internal platinum resistor. It is difficult to detect short-term temperature changes in high-temperature superconductor (HTS) tapes in an LN2 bath. The temperature variations detected by the sensor experimentally are consistent with the simulation results.
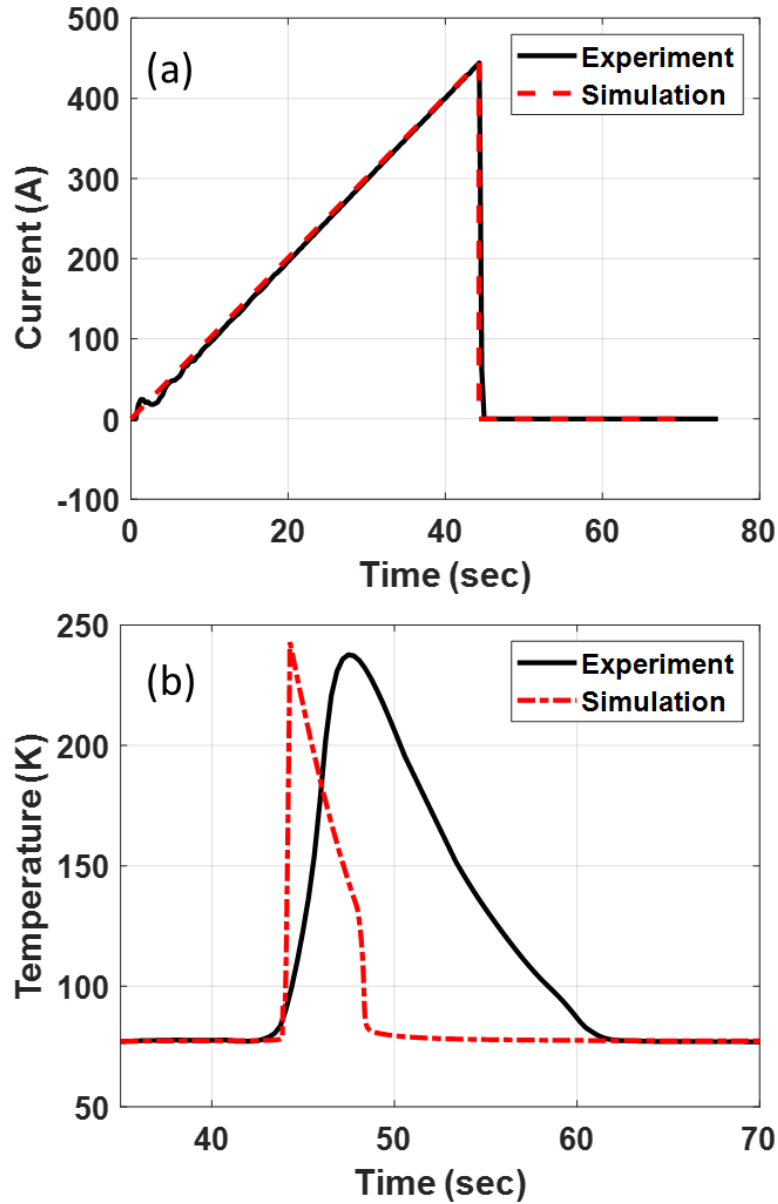
Figure 5.10 (a) Current ramp applied to the 2G HTS tapes. (b) Temperature of the 2G HTS tape.

For further clarification of the RTD sensor's temperature readings, we applied a current ramp of 460 A, after which the tapes were completely damaged and burned. At this point, the temperature sensor recorded around 370.9 K, while the model indicated 445 K. At these temperatures, the superconductor tape was completely damaged, as shown in Figures 5.11 and 5.12.
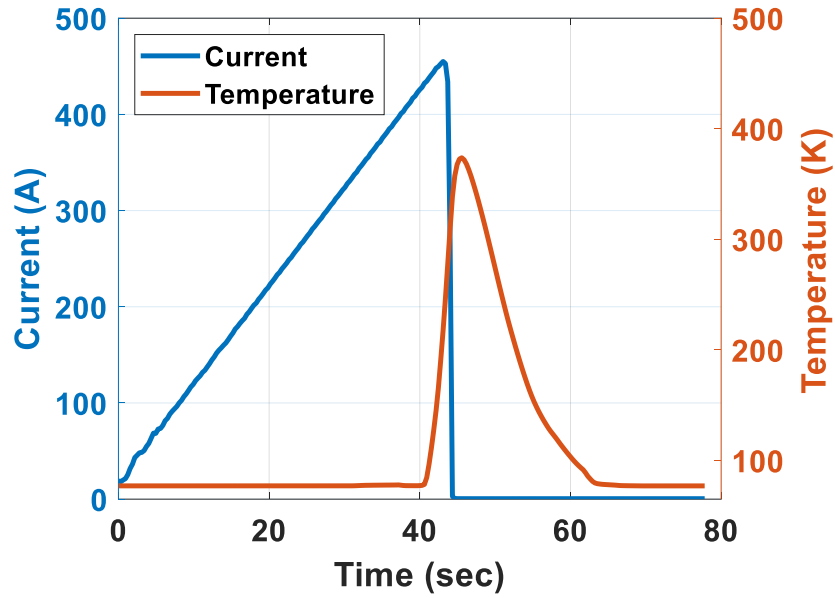
Figure 5.11 Quench detection analysis with a current ramp in 2G HTS tape using PT 103.
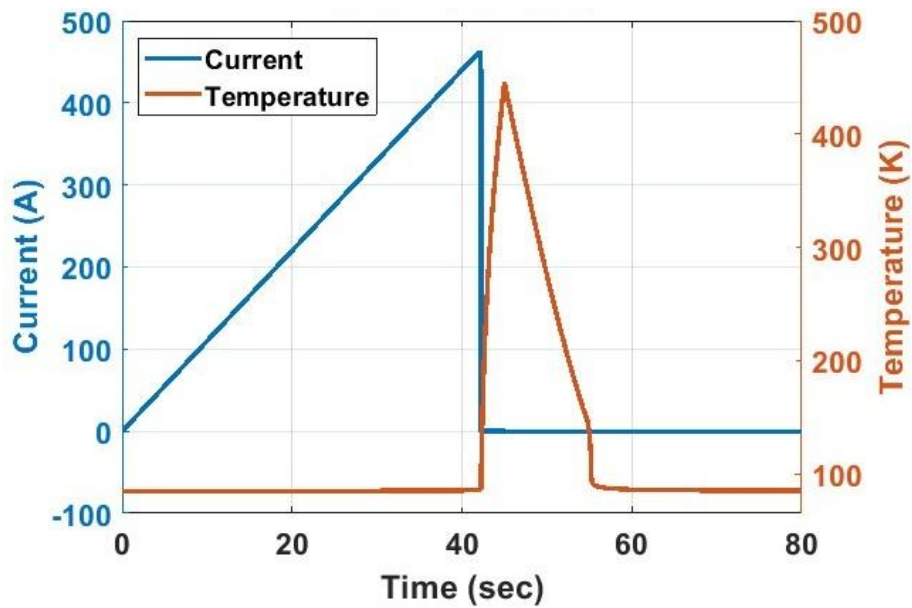


Figure 5.12 Simulation analysis for quench temperature with a current ramp in 2G HTS tape.

## 5.6. Summary of Chapter 5

This chapter presented significant findings on the electrical behaviour of 2G high-temperature superconductors (HTS), focusing on their critical current characteristics and

138

quench behaviour. Experimental measurements revealed the joint resistance of fabricated solder joints, which was instrumental in developing the SIMSCAPE model for HTS cables. The analysis underscored the nonlinear resistance properties and the distinct quench responses of HTS under varying current and temperature conditions. The findings also demonstrated that the resistance characteristics of the joints were consistent with the expected critical current performance, validating the joint's reliability for use in cable designs. The short 2G HTS tape behaviour under quench conditions was verified with the simulation. The quench analysis provided insights into the thermal limits and recovery dynamics, critical for assessing HTS performance under fault conditions.

# Chapter 6

# A Study of Ripple Effects in HVDC HTS Power Cable

## 6.1. Introduction

The power cable that transports current using converters has fluctuations known as ripples, which manifest as time-varying magnetic fields causing AC losses within the superconductor. The resulting self-field impacts the superconductor's critical current $I_c$ performance. Various methods can be utilised to estimate these losses in the superconductor.

The primary wiring techniques utilised in cable development include the Robel cable, Twisted pair stacked cable, and round core conductor cable. Among these, the round core conductor (CORC) cable stands out due to the helically wound tapes around the round core, offering benefits such as enhanced flexibility, mechanical strength, and ease of manufacturing compared to other methods. Simultaneously, refining the winding process of CORC cables can effectively diminish magnetization losses within the cable.

Analytical techniques relying on critical state models have limitations tied to the structure's geometry and underlying assumptions. In contrast, FEM modelling techniques such as the T-A formulation and H formulation prove to be more precise for intricate geometric configurations and diverse signals and fields. These methods are easily implementable within the COMSOL Multiphysics software. However, as the required number of vectors increases, the simulation runtimes become significantly longer.

The T-A formulation in the COMSOL Multiphysics software was used for the simulation of the HTS tapes in the cable superconducting power cable due to its high aspect ratio [181], [182]. The model methodology is explained in this chapter in section 6.2 followed by the experimental validation in section 6.4. The taped $I_c$ behaviour in the cable is identified by the simulation.

Using the DC superconductor power cable, we can transfer power at a rate five times greater than that of conventional copper cables. The source of ripple in the HTS power cable stems from the converter system; the use of thyristors generates harmonic components between the thyristor valves. These harmonics present issues that cannot be bypassed on either the AC or DC sides. The DC current contains ripples, and in HVDC transmission, large-scale filters are necessary to mitigate these harmonic ripples. The LCC converter in the HVDC transmission system generates harmonics of the 12th, 24th, and 36th orders of fundamental AC frequency along with DC. This is typical for Line Commutated Converters (LCC) used in HVDC systems. In contrast, Voltage Source Converters (VSC) also produce harmonics, but at higher frequencies due to their reliance on pulse width modulation (PWM) techniques. The AC signal, when converted to DC using power converters, is superimposed with ripples or harmonics on the AC signals, leading to energy losses.

In this chapter, the superconductor power cable electromagnetic behaviour was studied using the T-A formulation and the COMSOL Multiphysics FEM. This approach enabled us to calculate the AC losses in the tapes and measure the magnetic flux density. The variation in the critical current $I_c$ is attributed to the self-generated magnetic field.

## 6.2. T-A formulation

The current vector potential (T) as a state variable is for solving the current distribution in the superconducting layer only. The magnetic vector potential (A) and an additional variable were added to solve the magnetostatics problem as shown in Figure 6.1.
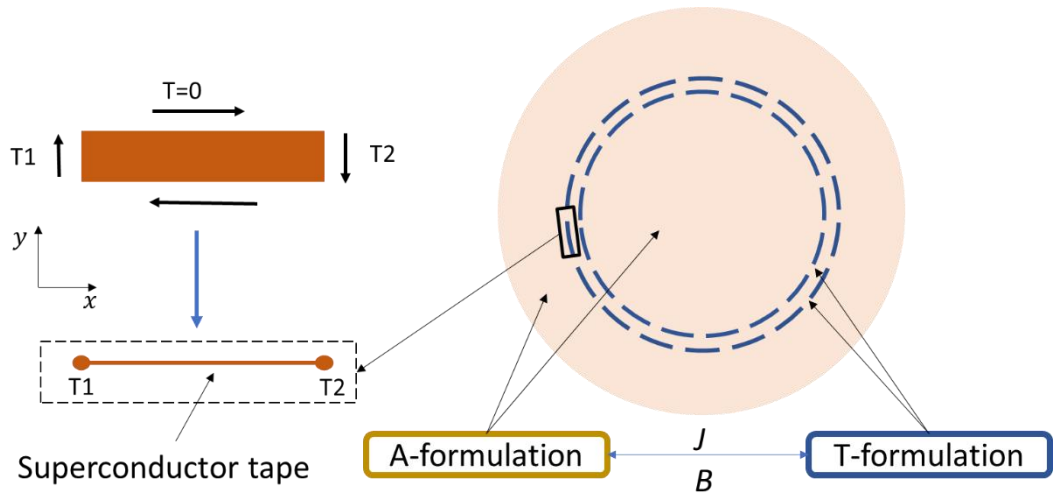
Figure 6.1 T-A formulation of the cable using 2G HTS tapes.

## 6.2.1. General formulation

The governing equation is mentioned below.

$$J = \nabla \times T \qquad\qquad 6.1$$

$$B = \nabla \times A \qquad\qquad 6.2$$

For the resistivity of the type II superconductor modelled using the *E-J* power law, the critical current density is dependent on the magnetic flux density as follows:

$$\rho_{hts} = \frac{E_c}{J_c(B)}\left(\frac{J}{J_c(B)}\right)^{n-1} \qquad\qquad 6.3$$

The electric field in the HTS tapes based on the resistivity of the HTS cable is

$$E = \rho_{hts}.J = J\frac{E_c}{J_c(J,B)}\left(\frac{J}{J_c(J,B)}\right)^{n-1} \qquad\qquad 6.4$$

Where $\rho_{hts}$ is the resistivity of the HTS tapes, $J$ is the current density, $J_c$ is the critical current density of the HTS dependent on magnetic flux density $(B)$, and $E_c$ is the characteristic electric field at 1 µV/cm.

142

Applying the Maxwell-Faradays law to the HTS domain gives

$$\nabla \times B = -\frac{\partial B}{\partial t}$$ <div style="text-align:right">6. 5</div>

In the whole domain, Maxwell- amperes laws are applied to solve the magnetic vector potential:

$$\nabla \times \nabla \times A = \mu_0 \mu_r J$$ <div style="text-align:right">6. 6</div>

Due to the non-magnetic core, the magnetic permeability depends on the magnetic flux density. The $T$ vector was calculated by solving the Faradays law and the A vector dependent on $T$ was calculated by solving Ampere's law.

The critical current density is coupled with the A formulation by application of external surface current density $J_e$

$$J_e = J.\delta$$ <div style="text-align:right">6. 7</div>

Where $\mu_0$ and $\mu_r$ are the magnetic and relative permeability of the free space, and the $\delta$ is the thickness of the superconductor tape. The external current density applied is A/m by neglecting the thickness of the HTS layer by considering a thin strip approximation.

The current flowing in the superconductor is applied at the tape terminal. It can be represented by an integral of the current density over the cross-section of the conductor.

<div style="text-align:right">6. 8</div>

$$I = \iint_S J dS = \iint_S \nabla \times T dS = \oint_{\partial S} T dS$$

Where S is the cross-section of the conductor and $\partial S$ represents the boundary edges of the cross-section.

## 6.3.  Simulation results of a single tape

First, the T-A formulation mentioned above was implemented into a single 2G HTS tape using COMSOL Multiphysics. A current of 50 A, ranging from DC offset with frequency up to 36f (where f is the fundamental frequency), with varying total harmonic

distortion (THD), was applied to the 2G HTS tape. The instantaneous AC losses are calculated using Equation 2.6 in COMSOL.

The instantaneous AC losses for a 50 A DC offset current with 5% Total Harmonic Distortion (THD) at various frequencies are presented in Figure 6.2. In cases involving DC with harmonics, the losses are measured at 0.858 µW/m, which is minimal and negligible. As the ripple frequency rises, there is a corresponding increase in the variations of the instantaneous loss signals. In most instances, the maximum peak values appear to be similar. Despite the increase in harmonic intensity, it does not impact the AC losses in the 2G HTS tapes.
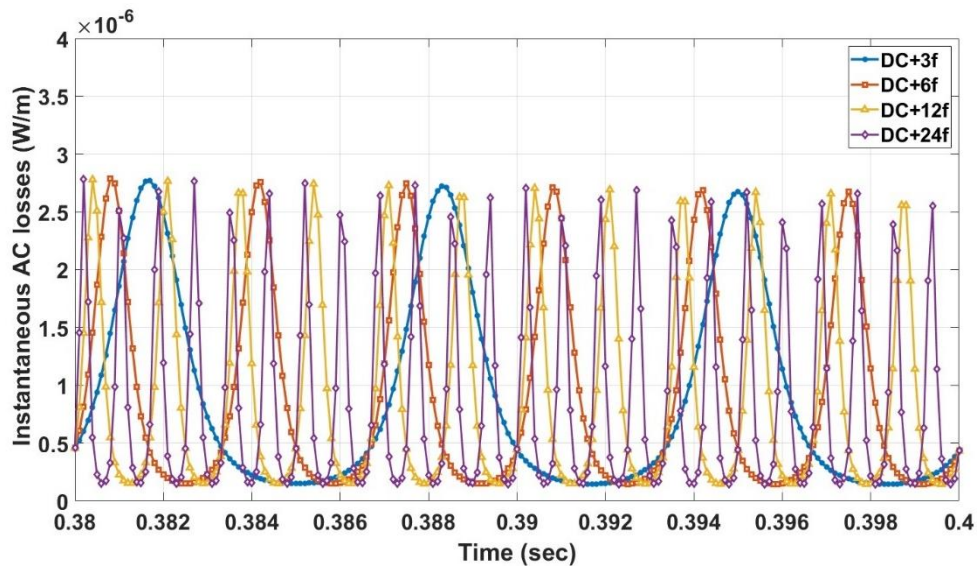


Figure 6.2 Instantaneous AC losses in the HTS tape for DC offset with 0 to 36f ripple frequencies.

The grid standards mention that the total harmonic distortion of ripples should not exceed 5% of the total current [183], [184], [185]. For the HTS DC cable, no standards are currently available regarding the safe ripple Total Harmonic Distortion (THD). In this analysis, we tested up to a maximum of 12.5% THD. Figure 6.3 shows the instantaneous AC losses under DC offset with 3f ripple with increasing ripple THD. As the THD percentage increases, the amplitude of distortion also increases, resulting in greater AC losses. Figure 6.4 depicts the average AC losses as the THD changes.
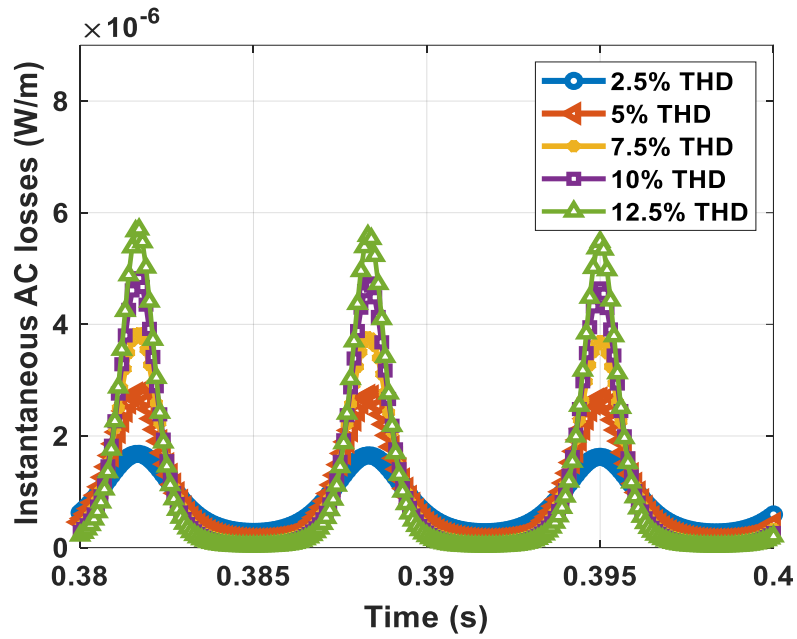
Figure 6.3 Instantaneous AC losses in the HTS tape for DC offset with 3f ripple frequency.
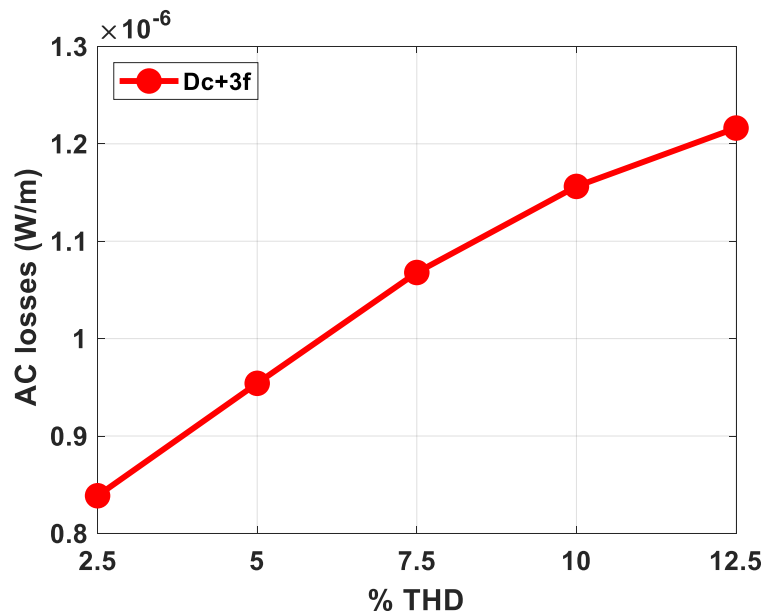


Figure 6.4  Average AC losses in the HTS tape for DC offset with 3f ripple frequency.

## 6.4. Experimental methodology

The RIGOL DG 952 function generator (50 MHz, 250 MSa/s) is utilised to generate ripples with a DC offset in the current signals. These ripples are subsequently amplified

using the AETHERON 7796 power amplifier (Maximum continuous output power= 5000 Watts and Bandwidth=DC to 100 kHz). The function generator creates the DC offset along with the AC ripple, which is then input into the TDK Lambda amplifier. This amplifier boosts the signal to 2000 times its original strength. A shunt resistor is connected in series with the HTS and power supply system to measure the current in the tape. The 2G HTS is cooled by immersing it in a liquid nitrogen (LN2) bath. Data acquisition was conducted using the National Instruments hardware, controlled through a LabVIEW interface, as depicted in Figure 6.5.
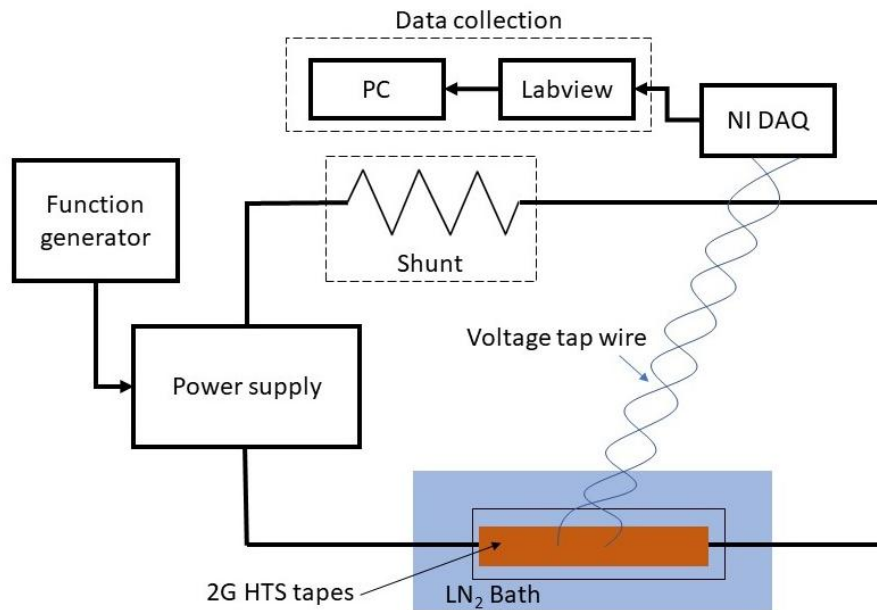


Figure 6.5 Schematic view of the ripple AC losses in the 2G HTS tape.

## 6.4.1.      Comparison of the experimental simulation results

Figures 6.6 and 6.7 display the current signals from both the simulation and experimental measurements. The AETEHRON 7796 power amplifier may face limitations regarding DC offset and AC ripples when generating high-frequency signals in the circuit. It can produce a maximum DC output current of 100 A without harmonics. The measured currents in these figures clearly show that the shunt measurement signal from the amplifier replicated the simulated harmonics up to the third harmonic (3f). However, higher harmonics experienced distorted ripple amplitudes in the experimental

measurements compared to the simulations. A DC offset of 54 A was applied to the 2G HTS tape with 5% Total Harmonic Distortion (THD). Consequently, in subsequent experiments, we utilised the ripple frequency signal up to a maximum of 3f.
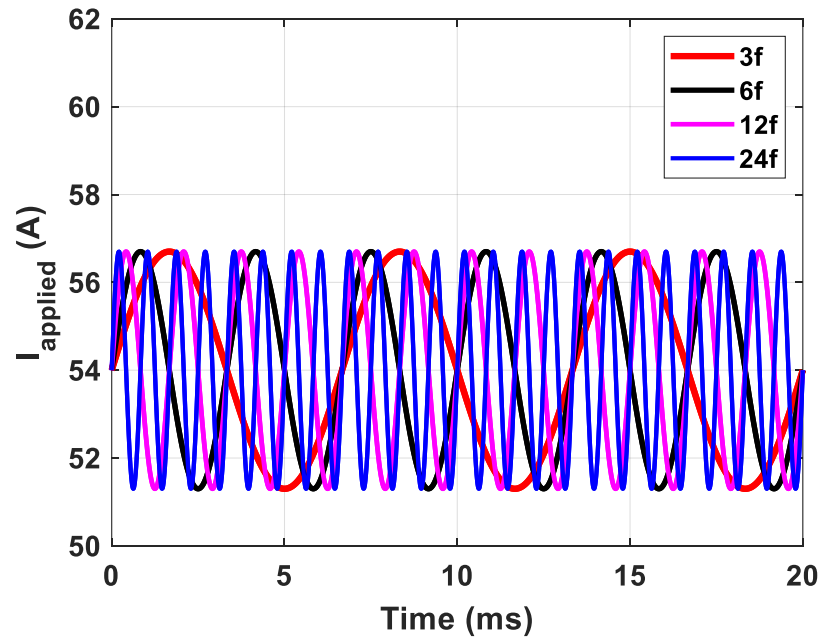


Figure 6.6 Simulation measurement of current in the 2G HTS tapes.
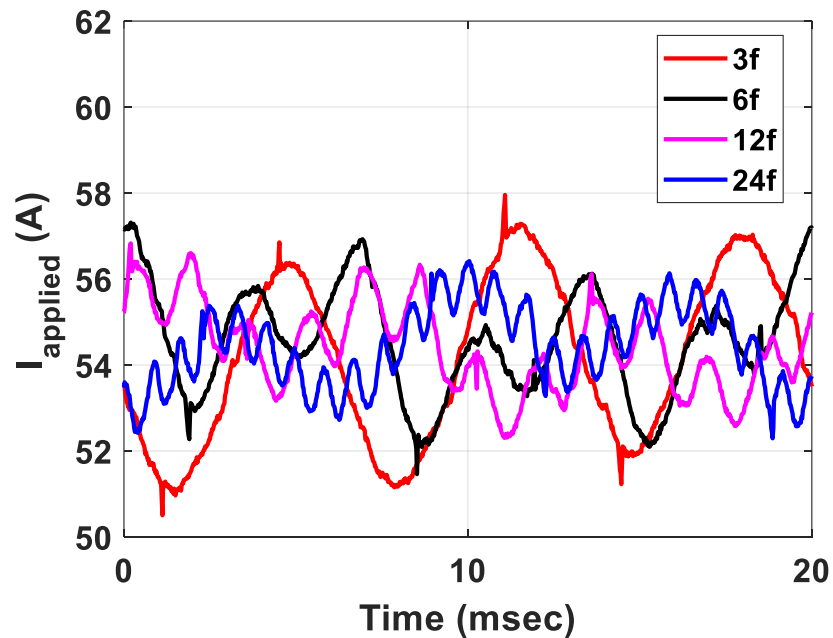


Figure 6.7 Experimental measurement of current in the 2G HTS tapes.

The comparison of the AC losses in 2G HTS tape using experimental measurements and simulation results for harmonics up to the third harmonic frequency (3f) are presented in Table 6.1. The comparison revealed a variation of approximately 15% between the experimental and simulation results, with the experimental values being higher. This discrepancy may be attributed to the extremely low values, in the micro-watt (µW) range, and to the fact that the signal detected from the amplifier includes noise along with the applied signal, contributing to the elevated experimental results. Additionally, the accuracy of the simulation results is influenced by the mesh size used in the modelling. Nevertheless, these losses are minimal, and the heat generated is negligible compared to the losses in an AC cable, where losses typically range from 0.8 to 1.2 W/m [186], [187].

Table 6.1 Experimental and simulation results comparison

| Voltage | Simulation | Experimental | % Error |
|---------|-----------|--------------|---------|
| DC+3f (5% THD) | 0.85 µW/m | ≈1 µW/m | ≈15 |

## 6.5. Electromagnetic modelling of HTS power cable

The magnetic field of the HTS power cable, which carries 10 kA with 10% Total Harmonic Distortion (THD), is depicted in Figures 6.8 and 6.9. The maximum self-generated magnetic flux density reaches 90 mT, significantly below the critical magnetic field of the REBCO superconductor. This peak magnetic field of 90 mT is primarily concentrated near the edges of the tapes. "Self-field" refers to the magnetic field created by the superconductor itself when carrying an electric current. This self-generated magnetic field, or self-field, interacts with the superconducting material and influences its behaviour, especially its critical current.
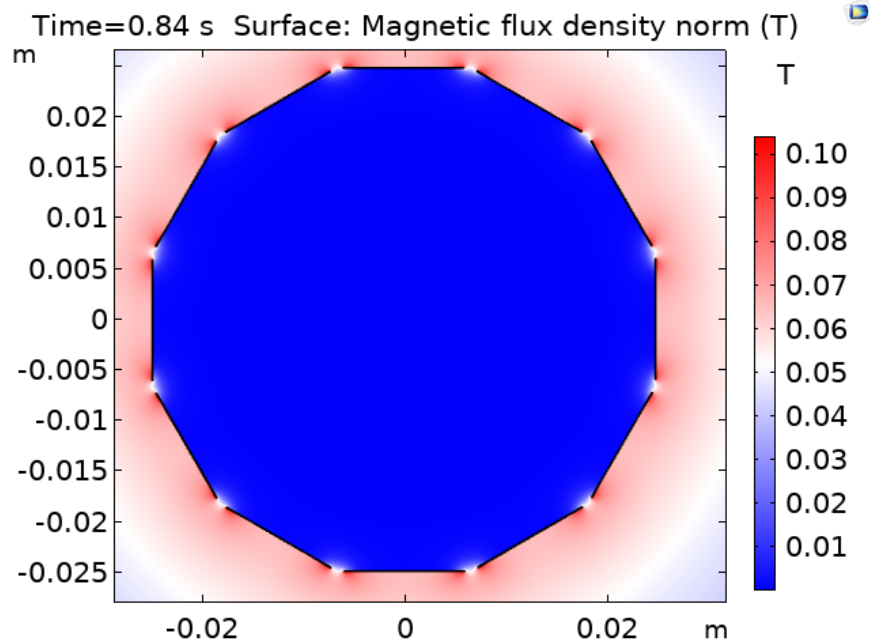
Figure 6.8 The magnetic field of the superconductor cable.
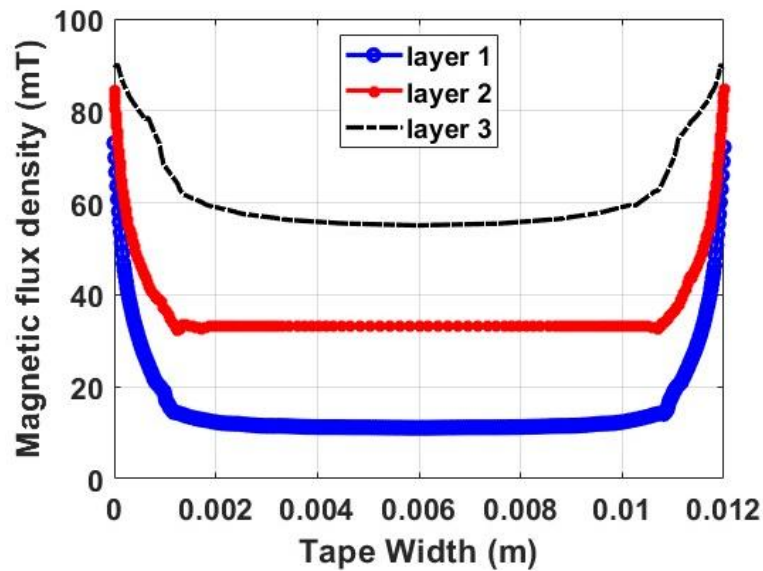


Figure 6.9 Magnetic field of the superconductor tapes for different layers.

The degradation of the critical current $I_c$ across all tapes in the cable is minimal, with reductions of less than 250 A in a 10-kA cable, except at the edges. The difference in $I_c$ between the inner layer and layer 2 is small, and it increases between layer 2 and layer 3. This degradation primarily occurs at the extremities of the tapes, as illustrated in Figure 6.10.
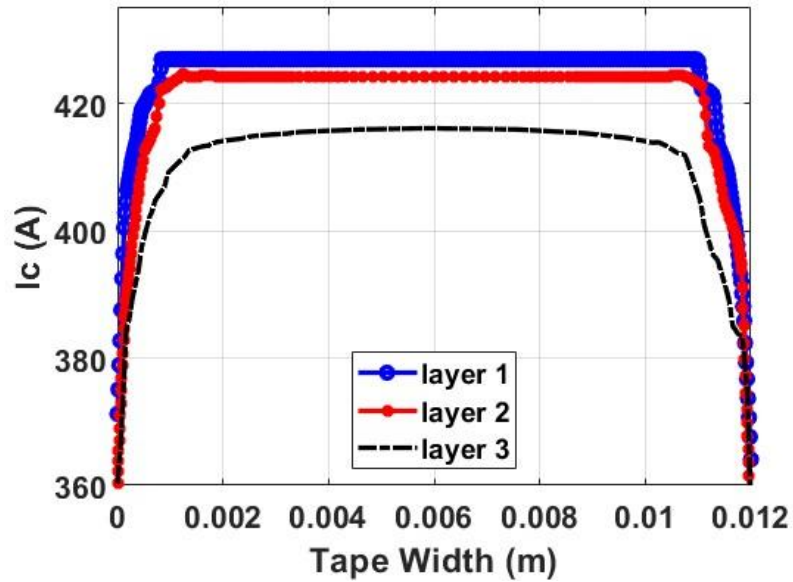
Figure 6.10 Critical current of the superconductor tapes for different layers.

The losses do not vary significantly; at 10% THD, the maximum instantaneous losses are approximately 30 mW/m, as shown in Figure 6.11.
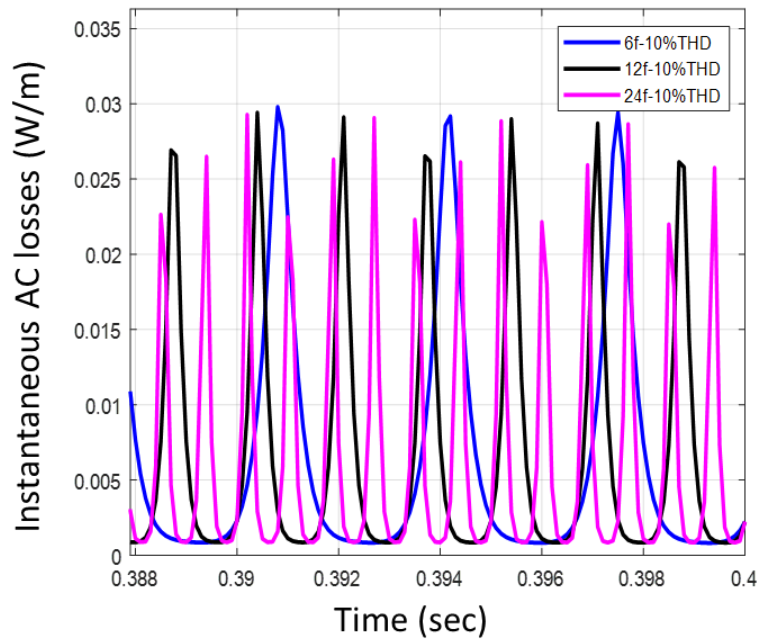


Figure 6.11 The losses in the HTS HVDC power cable with 10% THD.

Consequently, these losses do not substantially increase the Joule heating in the cable. Kim J and colleagues carried out a hardware in-loop test on the 3kA HVDC system and

the losses were 10 mW/m for the HVDC HTS cable [188]. Therefore, the losses are negligible, and ripple losses minimally impact the thermal characteristics of the HTS HVDC power cable.

## 6.6. Summary of Chapter 6

Chapter 6 delves into the analysis of ripple losses in HTS high voltage direct current (HVDC) cables. This emphasises that power cables transporting current via converters experience fluctuations, known as ripples, which lead to alternating current (AC) losses in superconductors.

Analytical techniques based on critical state models have limitations due to geometric assumptions, whereas finite element method (FEM) modelling techniques, such as the T-A and H formulations, offer greater precision. These techniques have been effectively implemented using the COMSOL Multiphysics software, despite longer simulation runtimes for complex vector fields.

This chapter outlines the use of the T-A formulation in simulating high-temperature superconductor (HTS) tapes to determine AC losses and magnetic flux density. The model methodology and experimental validation are explained, showcasing that DC superconductor power cables can transfer significantly more power than conventional copper cables. However, the use of converters introduces harmonics, necessitating large-scale filters in HVDC systems.

The experimental methodology employed a function generator and power amplifier to simulate ripple conditions. The results indicate that with an increase in ripple frequency and harmonic intensity, there is a corresponding rise in AC losses. A comparison between the simulation and experimental data highlights the significant influence of self-generated magnetic fields on the parameters of superconductor cables, particularly the degradation of the $I_c$. The chapter concludes by noting that the impact of magnetic fields on $I_c$ is minimal. However, deviations in the $I_c$ characteristics of tapes will be considered in future simulations in Chapter 7.

# Chapter 7

# Thermo-Hydraulic Study of Long-Distance Superconductor Power Cables

## 7.1. Introduction

Optimizing superconducting power cables has become a focal point in modern electrical engineering due to their potential to revolutionise power transmission and distribution. These cables, utilising high-temperature superconductors (HTS), offer remarkable advantages such as significantly reduced energy losses, higher current-carrying capacity, and enhanced efficiency compared to traditional copper or aluminium conductors. The integration of superconducting fault current limiters (SFCL) within these cables further enhances their functionality by providing rapid and effective fault current management without the need for mechanical switching mechanisms. This introduction aims to explore various optimization strategies for superconducting power cables, focusing on improving their performance and reliability in power grids. Through advanced materials science, innovative design approaches, and comprehensive system analysis, we can unlock the full potential of superconducting technology and contribute to a more sustainable and resilient electrical infrastructure.

The helical winding of second-generation high-temperature superconductors (2G HTS) around a core structure result in a magnetic field that is parallel to the cable's surface. This configuration leads to a slight decrease in the cable's critical current. These findings are detailed in Chapter 6.

As illustrated in Figure 3.1, the pressure drop and temperature change limits are $\mathit{\Delta P}$=17 bar and $\mathit{\Delta T}$=12 K, respectively. The maximum pressure and temperature values are 20 bar and 77 K.

Superconducting transmission lines require operation at cryogenic temperatures, necessitating the incorporation of cryogenic cooling systems in their design. These systems are essential to keep the superconducting cables at their ideal operational temperatures. For long-distance transmission lines, thermal losses become a critical issue that must be anticipated and controlled.

This chapter investigated the thermal and pressure changes in the HTS power cable. This study has examined the performance of the HTS power cable based on variations in mass flow, hydraulic diameter, and the surface roughness of the corrugated pipes used for liquid nitrogen (LN2) flow.

Additionally, different LN2 flow arrangements and cable topologies have been analysed. Further analysis was performed on both the steady-state and transient behaviour of the HTS power cable, with and without the integration of a Superconducting Fault Current Limiter (SFCL).

## 7.2. Cable topologies

There are two different types of cable topology configurations considered in the modelling, specifically CORC cables with solid and hollow former geometries. The CORC cable with a hollow former includes a flow of LN2 inside the hollow former and a separate return flow path. The other configuration features a solid cylinder former geometry with a distinct return flow. The cable structures are illustrated in Figures 7.1 (a) and (b). The shape of the corrugated pipe wall for coolant flow is depicted in Figure 7.2. The cable radius and layer details are provided in Table 7.1.
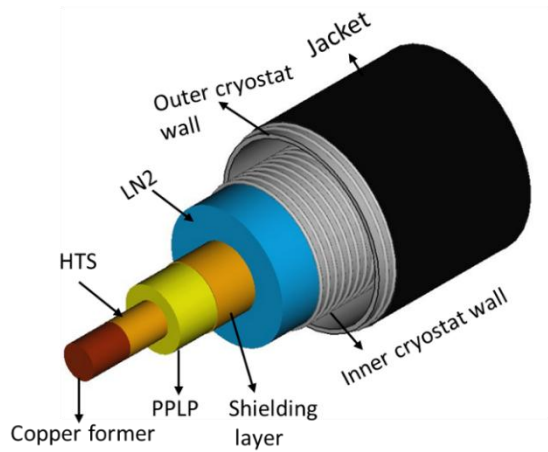
Figure 7.1 Cable topology 1: CORC cable solid former. Cable topology 2: CORC cable with the hollow former
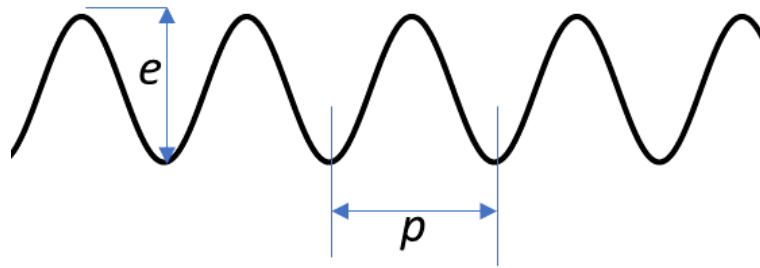


Figure 7.2  Cable corrugated pipe cryostat wall.

Table 7.1 Cable layer radius

| CORC Cable with solid former | | | CORC Cable with hollow former with the inner flow | | |
|---|---|---|---|---|---|
| Layer Radius | Radius (mm) | Material | Layer Radius | Radius (mm) | Material |
| R1 | 23 | solid former | R1 | 35 | Inner LN2 Flow |

| | | | | | |
|---|---|---|---|---|---|
| R2 | 25 | HTS layers | R2 | 45 | Copper former |
| R3 | 38 | Dielectric | R3 | 47 | HTS |
| R4 | 40 | Copper shield | R4 | 60 | Dielectric |
| R5 | 95 | Liquid nitrogen | R5 | 65 | Shielding layer shield |
| R6 | 100 | Inner cryostat | R6 | 95 | Liquid nitrogen |
| R7 | 103 | MLI | R7 | 98 | MLI |
| R8 | 143 | Vacuum | R8 | 138 | Vacuum |
| R9 | 156 | Outer cryostat | R9 | 143 | Outer cryostat |
| R10 | 157 | Epoxy | R10 | 144 | Epoxy |

## 7.3. Turbulent and laminar flow studies

The change in the roughness of the superconductor's corrugated cryogenic pipe results in changes in pressure drop, and temperature of the coolant flowing through it. Additionally, the hydraulic diameter of the coolant flow path also impacts the coolant characteristics.

For cable topology 1, with a mass flow variation from 0.25 kg/s to 6 kg/s, the temperature and pressure drop in the superconductor are shown in Figure 7.3. The limits for the maximum allowable pressure drop and temperature for the HTS cable are considered based on Figure 3.1. An increase in mass flow results in a decrease in the temperature of the LN2 and an increase in pressure drop. We decreased the roughness of

the corrugated pipe to transition the flow from turbulent to laminar. These changes are depicted in Figures 7.3, 7.4, and 7.7. The pressure drop was calculated using Equation 4.5, while the temperature was determined based on Equation 3.41.
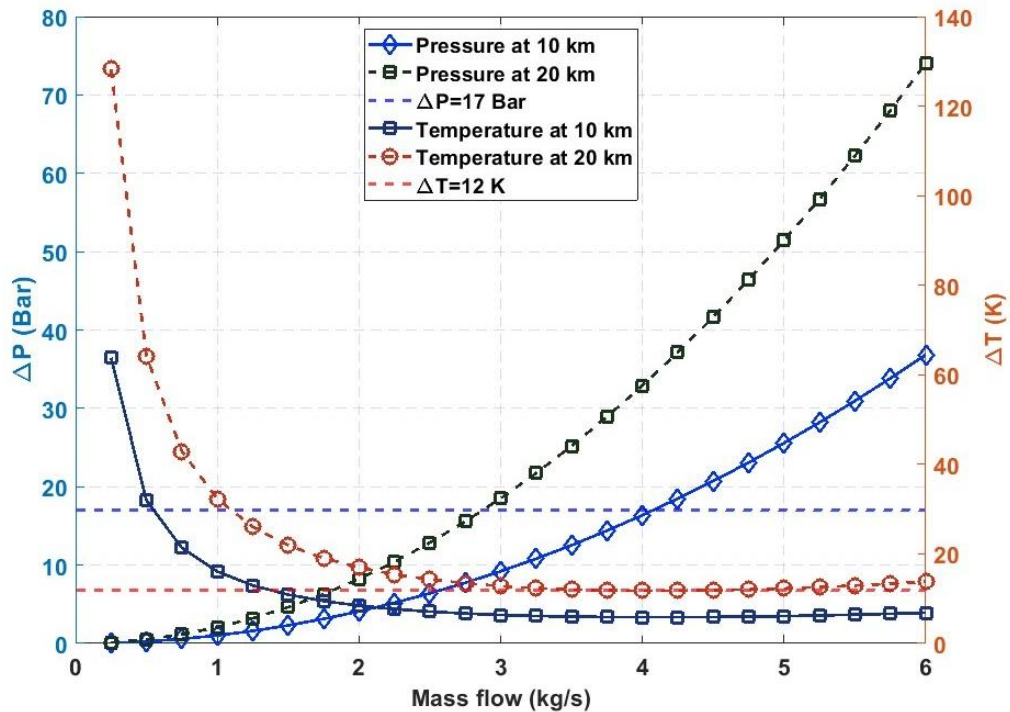


Figure 7.3 Pressure and temperature changes vs. mass flow in cable topology 1 ($D_h = 106$ mm, e = 1.25 mm, pitch = 6 mm, corrugated pipe, turbulent flow)

Corrugated pipes with a roughness of 1.25 are used in Figure 7.3, where the maximum allowable distance under the limit is around 10 km with a mass flow of 4 kg/s. The maximum distance with one cryocooler we can use is limited to 10 km. The friction factor for $e$ = 1.25 mm is 0.0842. The heat leak loss due to the radiation from the environment to inside HTS is 1.7 W/m. With the reduction in the roughness of the pipe to e=0.5 mm depicted in Figure 7.4, the temperature and pressure limits define the allowable mass flow range as 3 to 4.7 kg/s for a 20 km long cable. For a 10 km cable, the allowable range is from 1.5 kg/s to over 6 kg/s. The friction factor is 0.0313.
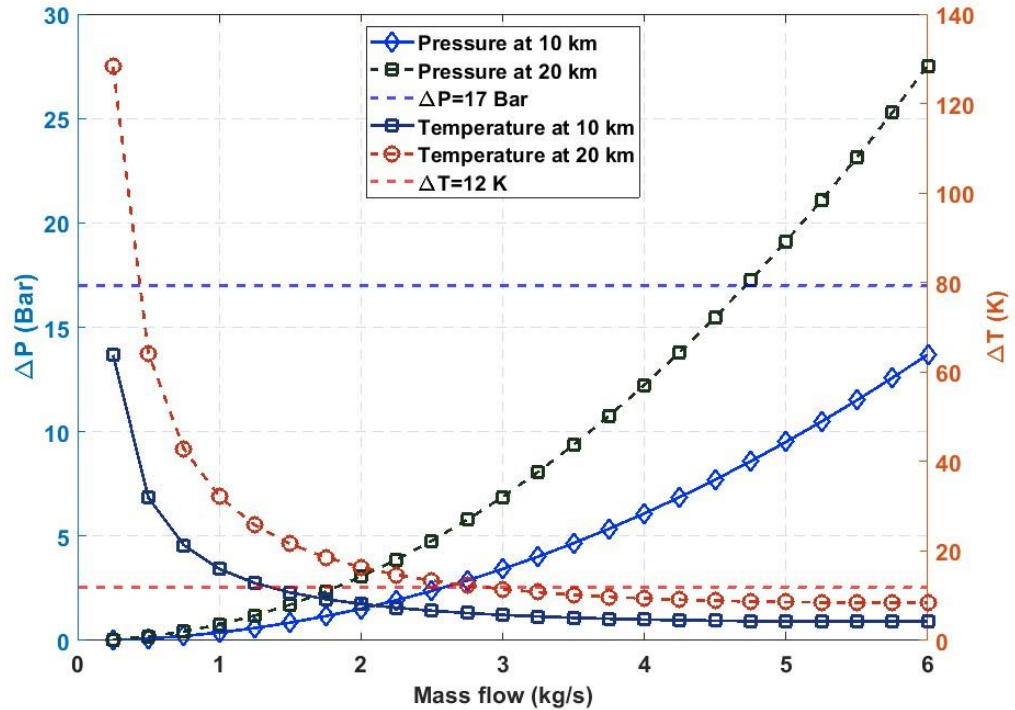
Figure 7.4 Pressure and temperature changes vs. mass flow in cable topology 1 ($D_h$ = 106 mm, e = 0.5 mm, pitch = 6 mm, corrugated pipe, turbulent flow)

Change in the diameter of the hydraulic path for the condition with roughness $e$ = 1.25 mm by altering the hydraulic diameter $D_h$ in the cable relates to the temperature rise behaviour and pressure drop as shown in Figures 7.5 and 7.6.

By increasing the hydraulic diameter, changes in both temperature and pressure decrease. The mass flow is directly proportional to the pressure drop; as the mass flow increases, we can observe the change in pressure from the initial condition. Additionally, the temperature is dependent on the $\Delta P$, which in turn depends on the mass flow. As observed, the temperature rise is higher when the mass flow is low and starts to decrease with mass flow rise. However, after a certain mass flow, it increases again due to the increase in pressure drop.
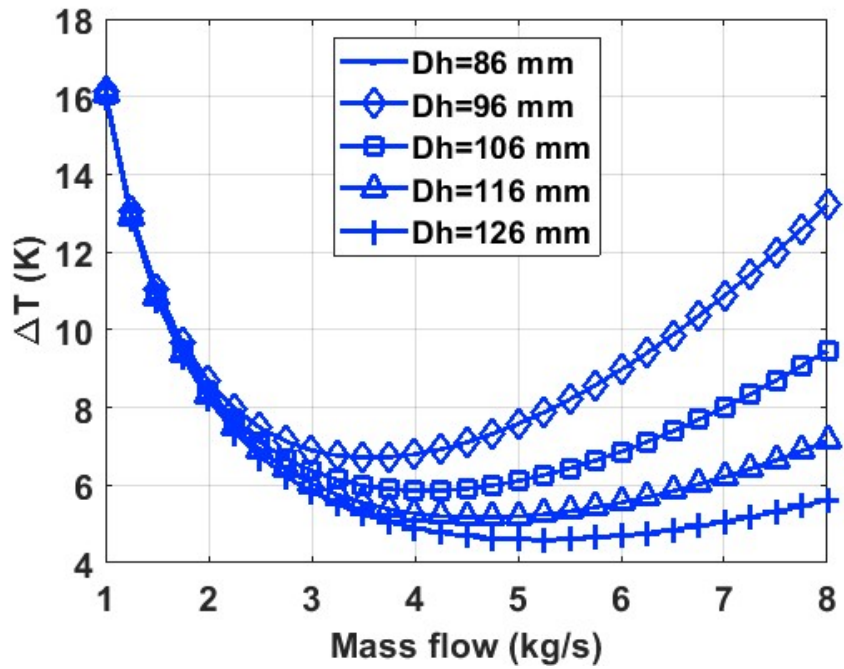
Figure 7.5 Temperature variation with the mass flow for different hydraulic diameters of LN2, with e = 1.25 mm and pitch = 6 mm under turbulent flow conditions.
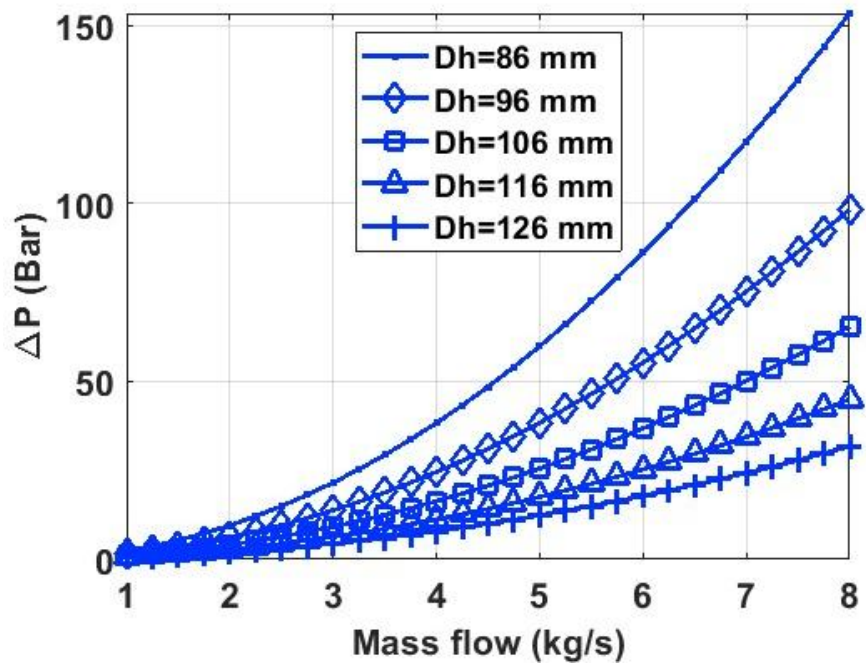


Figure 7.6 Pressure variation with mass flow rate for different hydraulic diameters of LN2 in a corrugated pipe (e = 1.25 mm, pitch = 6 mm) under turbulent flow conditions.
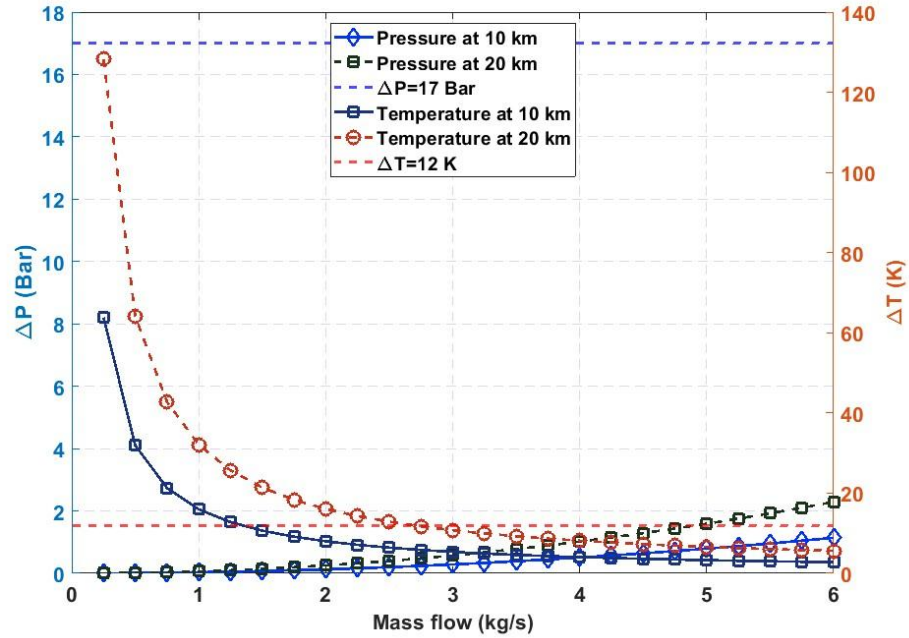
Figure 7.7 Pressure and temperature changes vs. mass flow in cable topology 1 ($D_h = 106$ mm, e = 0.05 mm, pitch = 6 mm,  laminar flow)

With the roughness of the pipe reduced to $e = 0.05$ mm, the flow of the LN2 becomes laminar. The pressure drop is very low, allowing for a mass flow range of 2.5 kg/s to above 6 kg/s over a 20 km cable length. This indicates that a single cryocooler could be sufficient for long distances if a cable with low surface roughness is used. The friction factor for $e$ = 0.05 mm is 0.0026. Furthermore, the inclusion of long, smooth pipes combined with short sections of corrugated joints enhances flexibility, absorbs vibrations, and minimises stress during the cooling transition from room temperature to cryogenic levels.

Figure 7.8 illustrates the relationship between mass flow rate (kg/s) and pressure drop ($\Delta P$ in bar) for liquid nitrogen (LN2) flowing through a smooth pipe under laminar flow conditions. The data is presented for various hydraulic diameters ($D_h$), specifically 86 mm, 96 mm, 106 mm, 116 mm, and 126 mm. The key observation is that as the mass flow rate increases, the pressure drop also increases for all hydraulic diameters. Notably, smaller hydraulic diameters result in higher pressure drops at a given mass flow rate, indicating more significant resistance to flow. Conversely, larger hydraulic diameters exhibit lower pressure drops, suggesting reduced flow resistance. This trend highlights the importance

of selecting an appropriate hydraulic diameter to optimise flow efficiency and minimise pressure losses in LN2 systems**.**
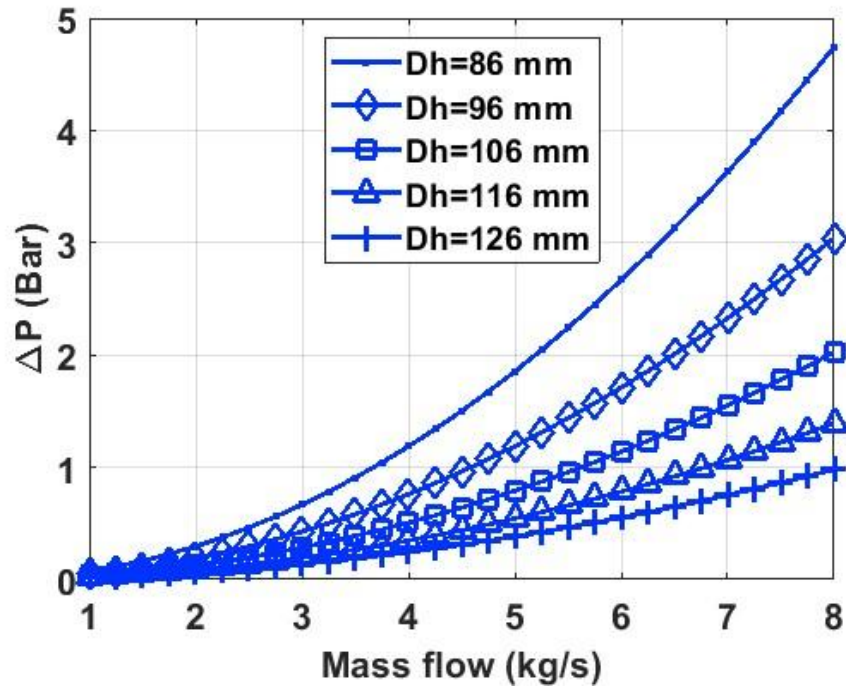


Figure 7.8 Temperature change with mass flow for a different hydraulic diameter of LN2 where $D_h$=90 and e=0.05 mm pitch =6 mm smooth pipe laminar.

Figure 7.9 depicts the relationship between the mass flow rate (kg/s) and temperature change ($\varDelta T$ in Kelvin) for the liquid nitrogen (LN2) flowing through a smooth pipe under laminar flow conditions, with various hydraulic diameters ($D_h$) ranging from 86 mm to 126 mm. As the mass flow rate increases, the temperature change decreases for all hydraulic diameters. This inverse relationship indicates that higher mass flow rates result in less temperature change, suggesting improved thermal performance due to increased convective heat transfer. Smaller hydraulic diameters exhibit slightly higher temperature changes at lower mass flow rates, while at higher mass flow rates, the differences between the diameters become less pronounced. Figure 7.9 highlights the importance of selecting an appropriate hydraulic diameter to optimise thermal performance in LN2 systems, considering that larger diameters generally promote more stable temperature conditions

across varying flow rates. Based on the above analysis, we selected a 4 kg/s mass flow for the liquid nitrogen in the corrugated pipe.
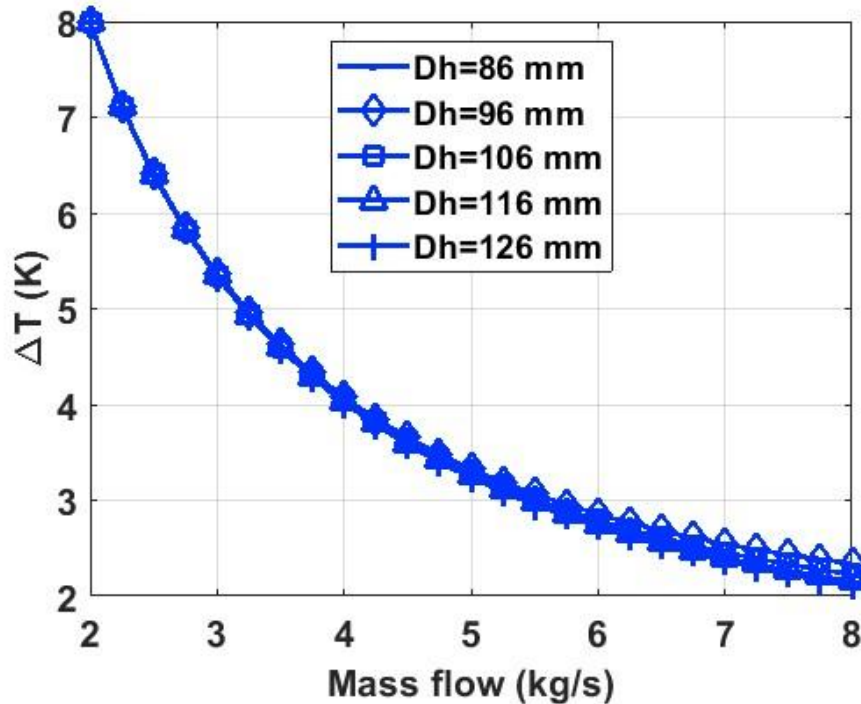


Figure 7.9  Pressure drop variation with mass flow rate for different hydraulic diameters of LN2 (e = 0.05 mm, pitch = 6 mm) in a smooth pipe under laminar flow conditions.

## 7.4. Liquid nitrogen flow arrangements in the cable

Various studies on different LN2 flow rates have been conducted to determine the most efficient solution. The initial pressure of the LN2 was set at 20 bar. Stainless steel was chosen for the cable armour and cryogenic enclosure pipe due to its suitability for low temperatures, while the outer cable pipe was constructed from regular steel.

The cooling technique applied to the HTS power cable is shown in Figure 7.10. Liquid nitrogen flows in the same direction through both cooling ducts, entering the power cable and exiting into the cryo-cooler system. The cooling fluid is circulated forcefully. Once the fluid traverses the HTS power cable, it is returned to the cryo-cooler system to be re-cooled.
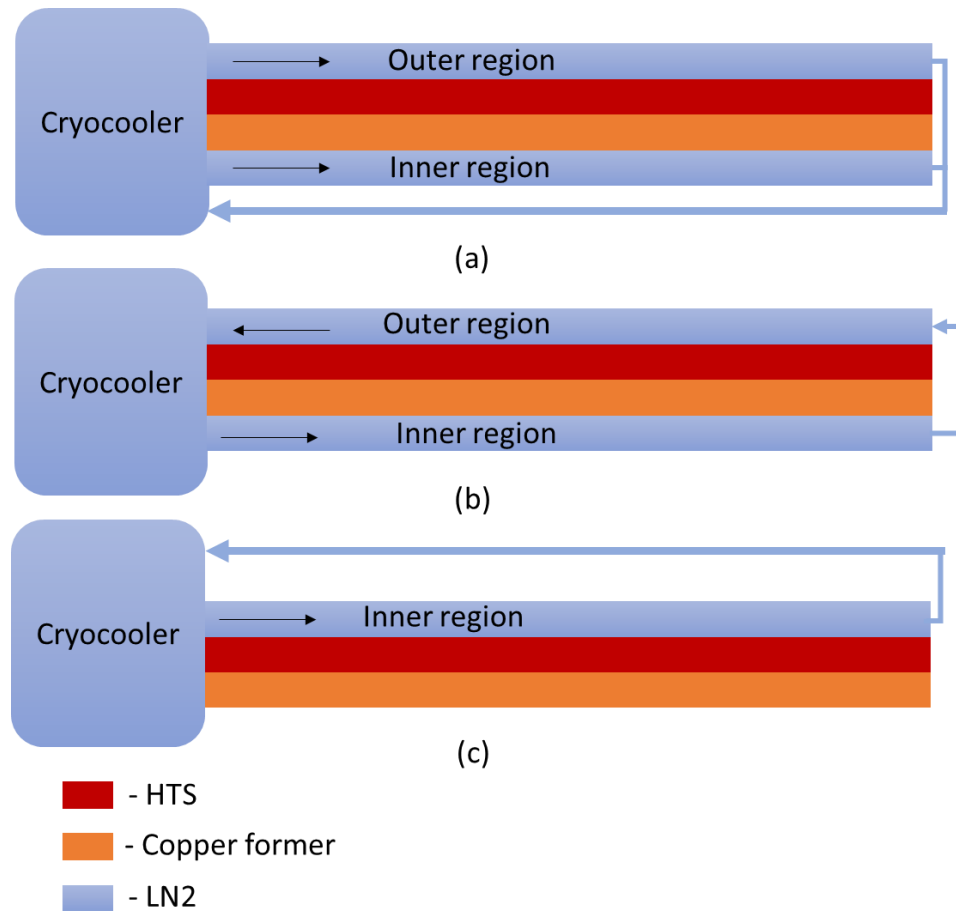
Figure 7.10 Cooling configurations of LN2 in the HTS CORC cable.

When the superconducting power cable is cooled with liquid nitrogen (LN2), and the flow direction in both the outer and inner cryopath is the same illustrated in Figure 7.10 (a), the flow in the inner pipe returns through outer pipe as depicted in Figure 7.10 (b) and the return using a speratre path as illustrated in Figure 7.10 (c). Figures 7.11 and 7.12 demonstrate the temperature and pressure changes along the length of a superconducting power cable cooled with LN2 for Figure 7.10 (a), with a mass flow rate of 4 kg/s. Figure 7.11 shows the temperature variations for both the inner and outer regions of the cable over a distance of 20 kilometres. The blue line represents the temperature in the outer region, while the red line indicates the temperature in the inner region, with both flows moving in the same direction. The data reveals that the temperature rise in the outer region is significantly higher than in the inner region. This difference is attributed to the higher

external heat load from radiation, which ranges from 1.7 to 1.9 W/m, compared to the joule losses in the superconductor.
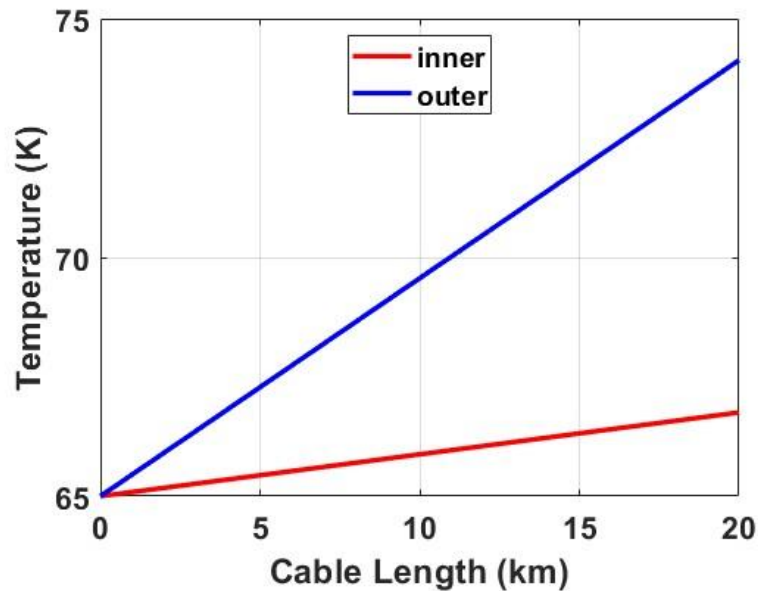


Figure 7.11 The flow of the LN2 is in the same direction from left to right with a mass flow of 4 kg/s.

In Figure 7.12, the pressure drop of LN2 along the cable length is presented. Starting at 20 bar, the pressure consistently decreases to 5 bar over 20 kilometres, indicating a pressure drop rate of approximately 0.75 bar per kilometre. This linear decrease highlights the consistent resistance to flow along the cable. The chart suggests that a single cryocooler is sufficient to maintain the necessary cooling conditions over a 20 km length of cable. However, it also indicates the need for a return path for the LN2 to ensure efficient cooling system operations. These observations are critical for designing and optimizing the cooling systems for superconducting power cables, emphasizing the need to manage both thermal loads and pressure drops effectively.

Figure 7.13 displays the temperature distribution of liquid nitrogen (LN2) along the length of high-temperature superconducting (HTS) cables, assuming the placement of a cryocooler at 20 km intervals along the cable for Figure 7.10 (b). Both inflow and outflow temperatures are plotted against the cable length. The red line represents the LN2 inflow

temperature, the black dashed line represents the HTS layer temperature, and the blue dashed-dotted line represents the LN2 return temperature.
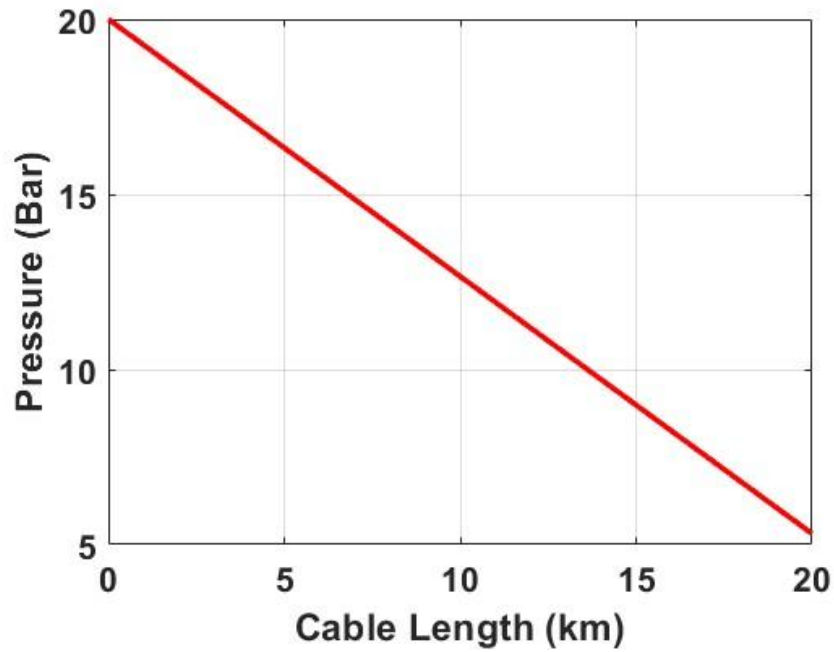


Figure 7.12 Pressure drop of LN2 with a mass flow of 4 kg/s in the outer region.
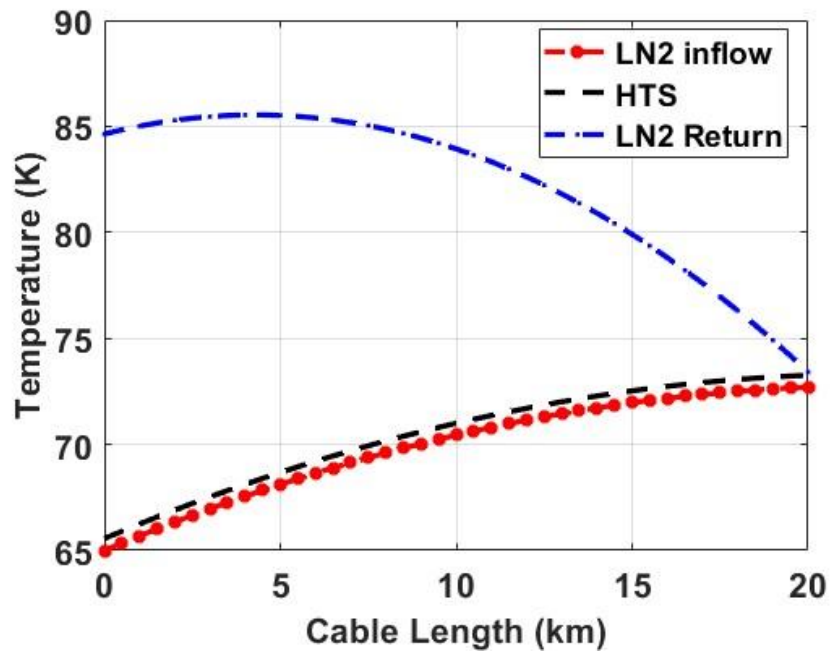


Figure 7.13  Temperature of LN2 with a return flow for 20 km long

The temperature profile shows a more significant increase. The LN2 inflow temperature starts at around 65 K and rises to approximately 72.9 K by the end of the cable. The HTS layer temperature closely follows the LN2 inflow, reaching about 72.9 K. The LN2 return path exhibits a more pronounced peak, reaching approximately 85 K. This significant temperature rise in the return path indicates that the LN2 starts to boil, suggesting that this cooling system is less suitable for cable lengths beyond 10 km due to the inefficiency and potential boiling of LN2. Overall, these temperature profiles indicate that a cooling system with a return path is effective for HTS cables up to 10 km in length, but for longer cables, the system faces challenges with maintaining optimal temperatures and preventing LN2 from boiling in the return path. This highlights the need for careful thermal management and potentially different cooling strategies for longer HTS cable installations. In the return path, the temperature of the liquid nitrogen (LN2) exceeds 77 K. To prevent boiling, it needs to be cooled down by a cryocooler before the return path to lower the temperature.

The analytical solution for the temperature of LN2 in the HTS power cable was calculated using equation 7.1 The temperature difference ($\Delta T$) between the inlet and exit of the cable system is relayed by the energy balance formula:

$$\Delta T = \frac{Q}{m c_p} \qquad\qquad 7.1$$

where, $m$ and $c_p$ is the mass flow rate and the specific heat of LN2.  Q is the heat load from the HTS, friction losses and environment.

The analytical solution and simulation results are compared and presented in Figure 7.14, showing excellent agreement. The analytical solution slightly overestimates the values compared to the simulation results. The simulation results demonstrate close agreement for short-distance cables. However, as the distance increases, variations between the results become evident. This variation is due to the analytical equation not considering heat transfer between the layers. There is a minimal discrepancy of less than 0.208 K, and the maximum discrepancy is around 0.411 K. The critical current of the 2G HTS tapes, estimated based on the Ico measured experimentally (as detailed in Chapter 5,

Section 5.4) and calculated using Equation 3.39, is depicted in Figure 7.15. At 65 K, the tape's critical current is 1024 A. When the temperature increases by 5 K, the critical current decreases to 780 A, a reduction of approximately 23.84%. This indicates a roughly 6% decrease in critical current for every 1 K rise in temperature, which is consistent with the decline in critical current density discussed in the referenced literature [189].
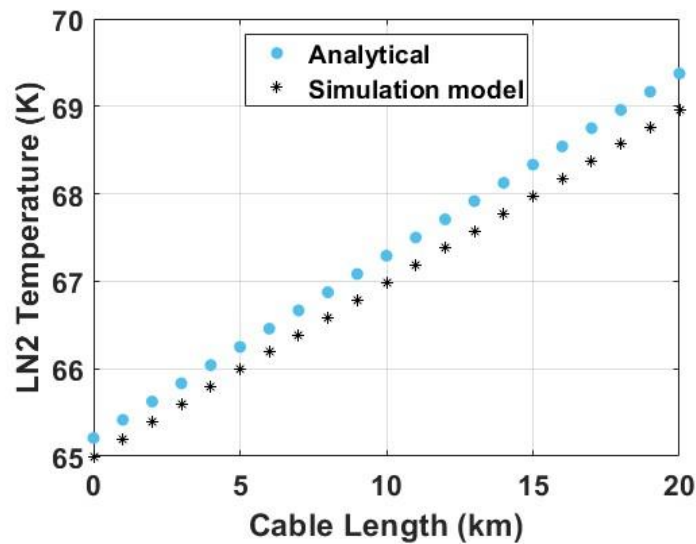


Figure 7.14  Comparison of the analytical results with the simulation model for 20 km long.
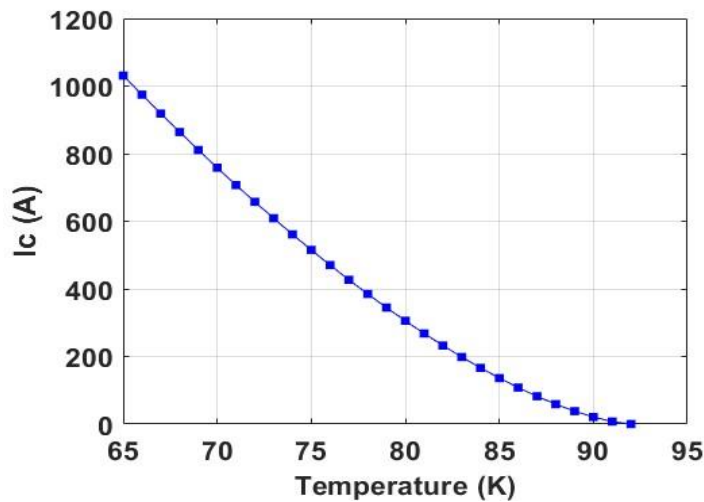


Figure 7.15 Critical current of the 2G HTS tape with respect to temperature.

## 7.5. HVDC superconductor power cable

The experimental values mentioned in Chapter 5 such as joint resistance and critical current shown in Figure 7.15 above, which are temperature dependent, are incorporated in the superconductor power cable model. The resistance of a CORC HTS power cable with a solid former is lower compared to one with a hollow former. As a result, the Joule losses and temperature increase during a fault are reduced in the CORC cable with a solid former. This type of cable exhibits a high fault withstand capability due to its larger copper area. Conversely, the CORC cable with a hollow former has higher resistance, which limits the fault current amplitude during a fault event due to its increased resistance compared to the solid former. In this study, we utilised a CORC cable with a solid former and a cryocooler, considering a 20 km cable section. Additionally, in the latter part of the study, a CORC cable with an SFCL was used to limit the fault current.

Figures 7.16 and 7.17 illustrate the steady-state behaviour of temperature and critical current along the length of a high-temperature superconducting (HTS) cable, each with cryocoolers installed every 20 kilometres under normal operation. In Figure 7.16, the temperature profile of the HTS cable is shown along its length, with cryocoolers placed at every 20 km interval. The temperature starts at approximately 65 K and increases to around 69 K before each cryocooler brings it back down to 65 K. This cyclical pattern indicates that the cryocoolers effectively manage the thermal load, maintaining the temperature within a narrow range to ensure efficient superconducting operation. In Figure 7.17, the critical current ($I_c$) behaviour along the HTS cable length is depicted, following a similar cyclical pattern due to the placement of cryocoolers. The critical current starts at around 46 kA, decreases to approximately 34 kA, and then returns to a higher value as each cryocooler is encountered. This variation in critical current is a direct consequence of the temperature changes, as the critical current capacity of superconductors is highly sensitive to temperature.

The cryocoolers help maintain the critical current capacity by preventing excessive temperature rises. Together, the temperature and critical current demonstrate the

importance of strategic cryocooler placement along long HTS cables to manage temperature and maintain optimal critical current levels, ensuring the cable's stable and efficient operation over extended distances. The friction factor with cryogenic pipe roughness e=0.005 is 0.098 and the friction losses are very small and its value is 0.0774 W/m.
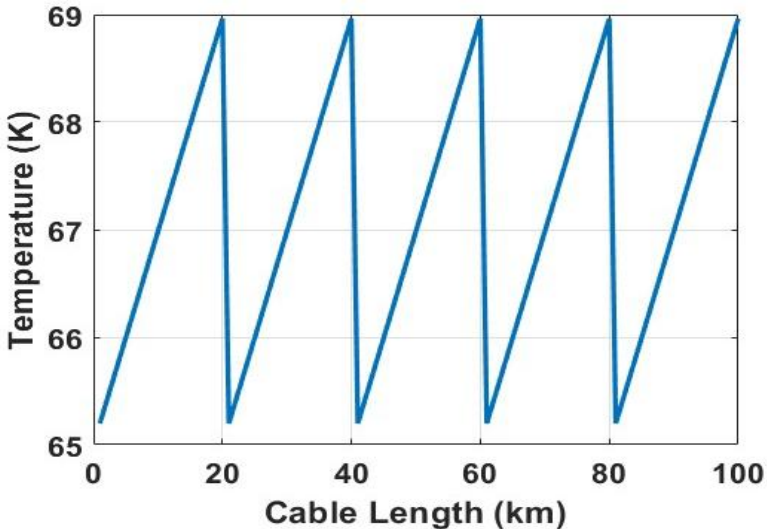


Figure 7.16 Temperature of the superconductor with a cryocooler for each 20 km long cable in a steady state.
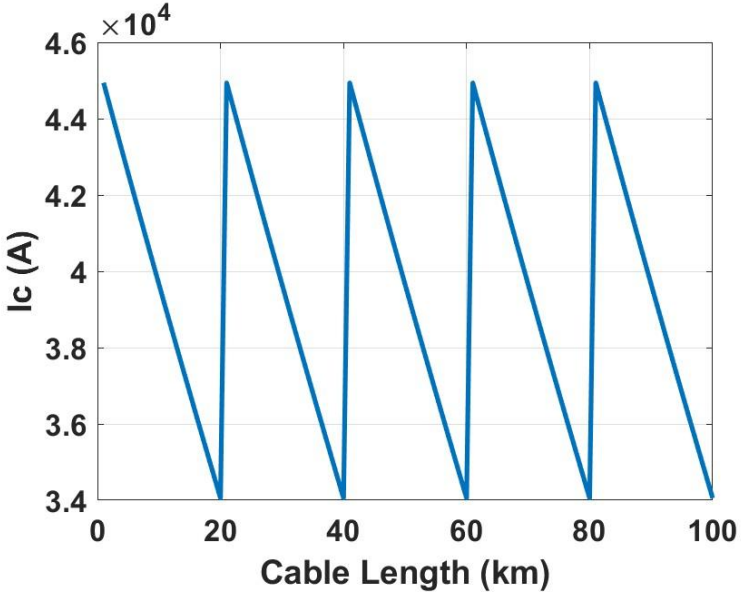


Figure 7.17  Critical current of the critical current behaviour along the length of the HTS cable in a steady state.

Figure 7.18 illustrates the current behaviour in a superconducting power cable during a fault condition. Initially, the current remains stable at around 10 kA. At 10 sec, the current spikes rapidly, peaking at around 41.5 kA due to a 20 msec temporary PG fault. This sharp increase indicates the occurrence of a fault in the system.
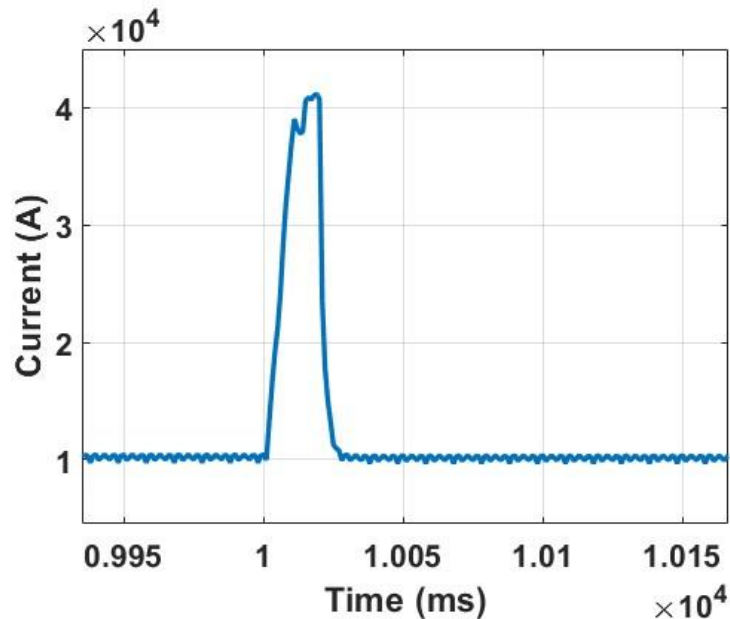


Figure 7.18 Current in the superconductor power cable during a fault.

During a temporary fault lasting a few milliseconds, the current rises and then returns to normal operating conditions. This affects the temperature of the superconductor within the power cable. The temperature profile of the HTS cable is shown in both 2D and 3D views along the length of the cable's transient response to the fault in Figures 7.19 and 7.20. As depicted, only a specific portion of the superconductor cable quenches, while the remaining section stays superconducting. In each 20 km long cryocooler, the first 15 km remain superconducting, and only the last 5 km of the superconductor cable in each cryocooled section experiences quenching. The temperature of the cable in the quenched section ranges from 121 to 123 K. It takes approximately 15 seconds for the cable to recover from the quenched state to its normal superconducting state after the fault is cleared.
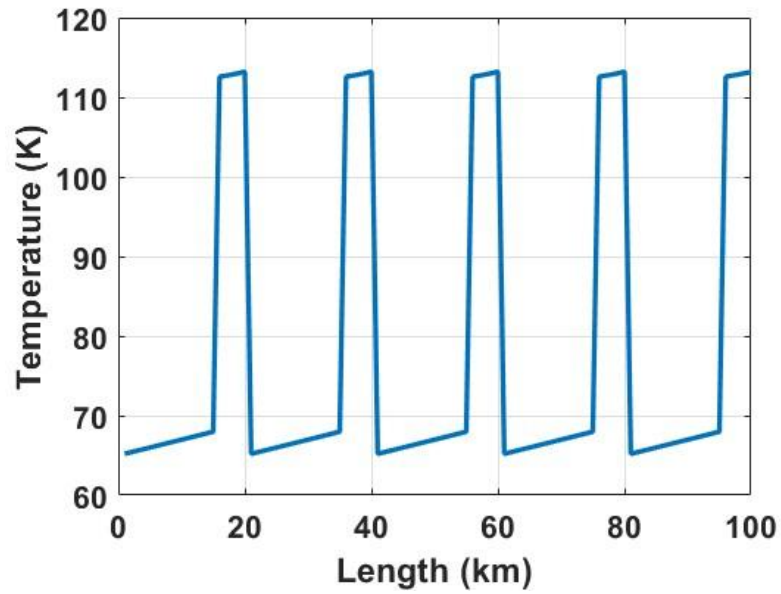
Figure 7.19 Temperature of the HTS cable along the length due to a fault.

The critical current ($I_c$) of the superconductor is shown in Figure 7.17. During a fault, the current rises to 41.5 kA. This current is higher than the $I_c$ of certain sections of the cable. The resistance values calculated from the *E-J* curve increase sharply, leading to joule heating and quenching of the superconducting power cable.
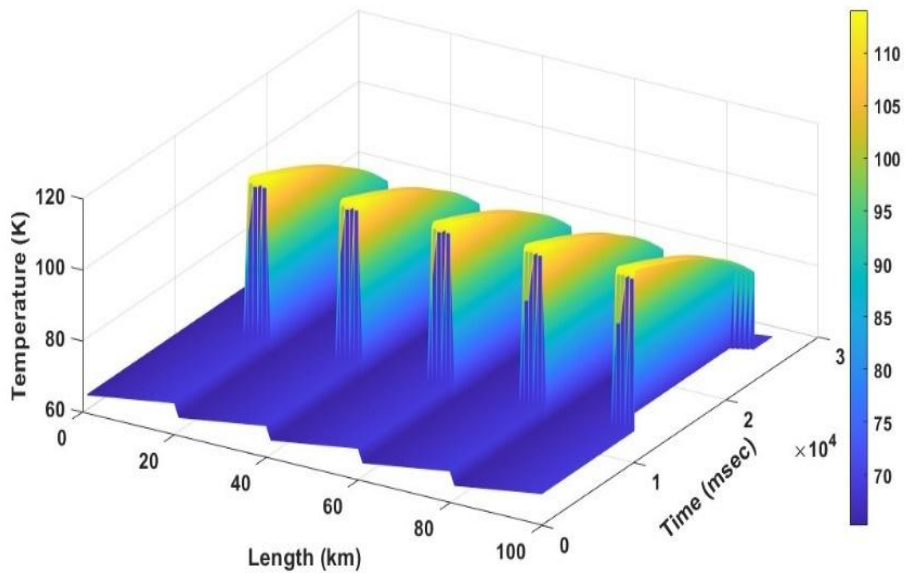


Figure 7.20  3D view of the temperature of the HTS cable along the length due to a fault.

The resistance values are depicted in Figures 7.21 and 7.22. When the current in the cable exceeds the critical current, the resistance of the cable increases. The quenched section of the cable has a resistance of approximately 4 mΩ/km. The temperature of the superconducting power cable exceeded the critical temperature ($T_c$ = 92 K) for the last 5 km of each 20 km section of the cable. For this specific length, the $I_c$ of the superconducting cable is zero, and the current in this section diverts to the copper former.

In each 20 km section, the current flows through the superconducting part in the first 15 km section (where $T<T_c$), and in the remaining section, the current flows through the copper former (where $T>T_c$). The $I_c$, which is a function of the HTS temperature, and its variation based on the temperature in Figure 7.20, is shown in Figure 7.23.
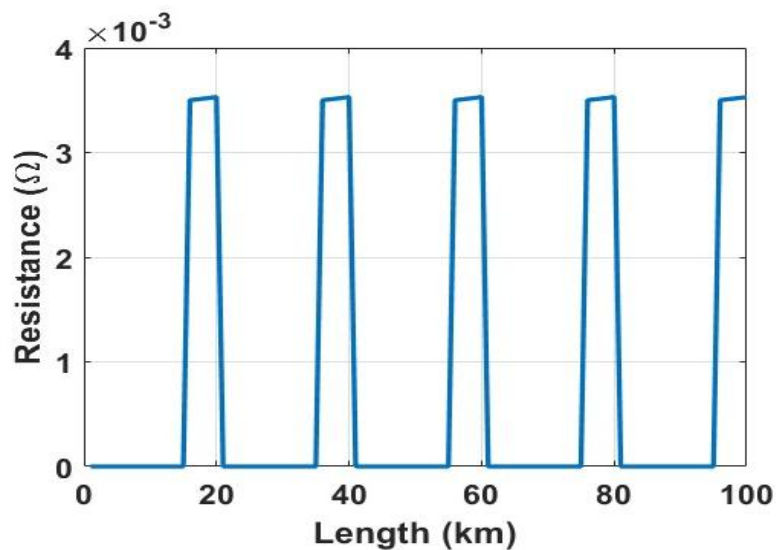


Figure 7.21 Resistance along the length of the HTS cable due to a fault.

The change in LN2 temperature due to the quenching in the superconductor as shown in Figure 7.24. The temperature of the LN2 in the quenched section, specifically the last 5 km of the cable, changed due to heat transfer from the superconductor to the LN2 layer. Despite the increase, the temperature of the LN2 remains below its boiling point.

171
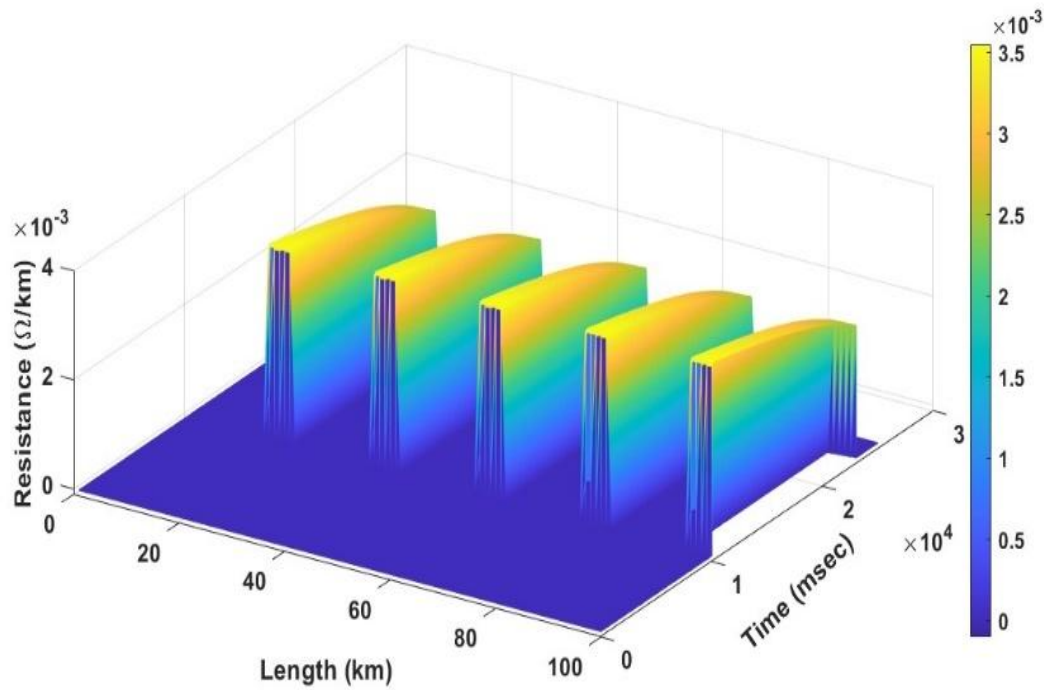
Figure 7.22 3D view of resistance along the length of the HTS cable.
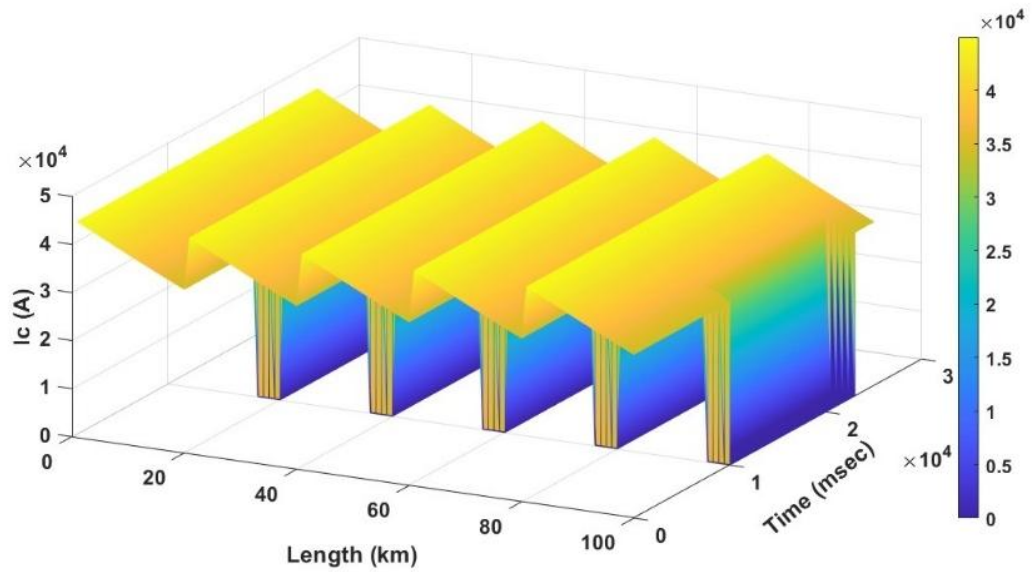


Figure 7.23 Critical current of the HTS layer along the length of the HTS cable due to a fault.
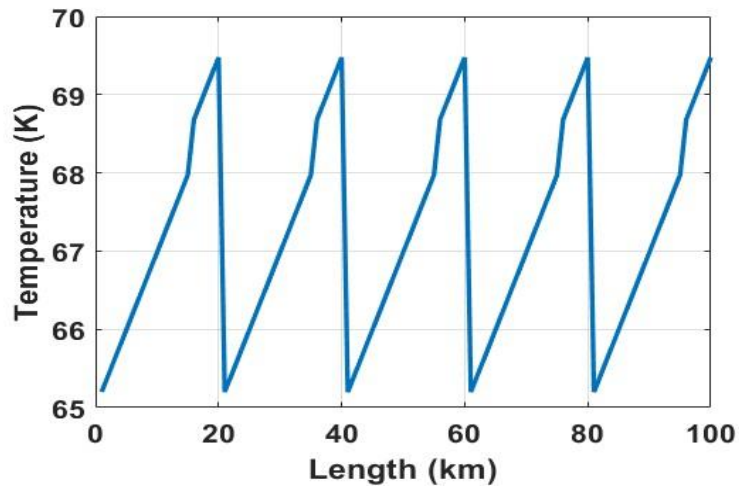
Figure 7.24 Temperature of the LN2 layer along the length of the HTS cable due to a fault.

## 7.6. HTS power cable integrated with a Superconductor Fault Current Limiter

The widespread use of low-impedance superconductor power cables enables the transfer of high current capacities, which in turn increases fault currents within the electrical grid. Traditional methods for mitigating fault currents, such as choking coils or power electronic systems, are inefficient due to their high cost, significant energy losses, and the substantial space they require in substations.

Modern electrical power systems are becoming more complicated and demanding, which calls for creative ways to manage operational issues and improve stability. The control of fault currents, which are excessive electric currents that result from short circuits or other faults, is one of the most important problems in modern power grids. These currents have the potential to seriously jeopardise safety, cause major equipment damage, and interrupt service. More effective technologies are required since traditional ways of regulating these fault currents frequently come with high infrastructure and maintenance expenses.

173

A novel approach to fault current management is the use of superconductor fault current limiters, or SFCLs. Superconductors are materials that, when cooled below a certain critical temperature, conduct electricity without resistance. SFCLs take advantage of these special qualities. When the SFCL comes into contact with a fault current, the superconducting material changes to a resistive state, which quickly and efficiently stops the excess current from flowing.

Significant benefits over traditional methods are provided by this technology, such as a smaller physical footprint, lower operating costs, and faster response times. Furthermore, SFCLs contribute to the overall reliability and resilience of power grids, accommodating fluctuations and anomalies without the extensive hardware required by traditional systems. The operational principles, forms, and effects of SFCLs on contemporary electrical networks will be covered in detail in this introduction part, highlighting their vital role in improving grid protection and management.

A superconductor power cable can achieve fault current-limiting functionality through the use of high-value alternate path resistance. This is accomplished by eliminating the copper former and minimizing the copper substrate on 2G HTS (high-temperature superconductor) tapes. During transient conditions, this approach results in increased ohmic losses, causing Joule heating that raises the temperature of the HTS material. If the temperature approaches approximately 200°C, the superconductor may suffer permanent damage, depending on the duration of the fault and the energy dissipated [190]. Therefore, when selecting the current limiting behaviour of the cable, it is crucial to ensure the circuit trips before the fault current causes the temperature to reach 200 °C.

To improve the stability of HTS power cables in the electrical grid, it is essential to ensure they can maintain safe temperatures and consistent operation, even when exposed to excessive fault currents. Integrating an SFCL is recommended to help achieve this stability. The SFCL effectively limits fault currents, providing the DC circuit breaker additional time to trip during extended fault scenarios. It features a self-activating mechanism that allows it to resume normal operations once the fault is cleared and the

superconductor's temperature drops below its critical level, eliminating the need for supplementary equipment.

The inclusion of an SFCL also protects high-temperature superconducting (HTS) cables and power electronic converters from damage by controlling excessive inrush currents. Various SFCL models are currently being explored and utilised across different power grid systems [191], [192], [193], [194], [195], [196].

The diagram presented in Figure 7.25 depicts a basic design for a resistive superconducting fault current limiter (SFCL). In this arrangement, a High-Temperature Superconductor (HTS) is connected parallel to a copper conductor, with an inductor linked in series to the combined resistive elements. This configuration aims to bolster the transient stability of the power system by effectively managing the fault currents during disturbances. A simulation was executed integrating the SFCL with the HTS cable, wherein a temporary fault lasting 20 ms was introduced to evaluate the system's response.
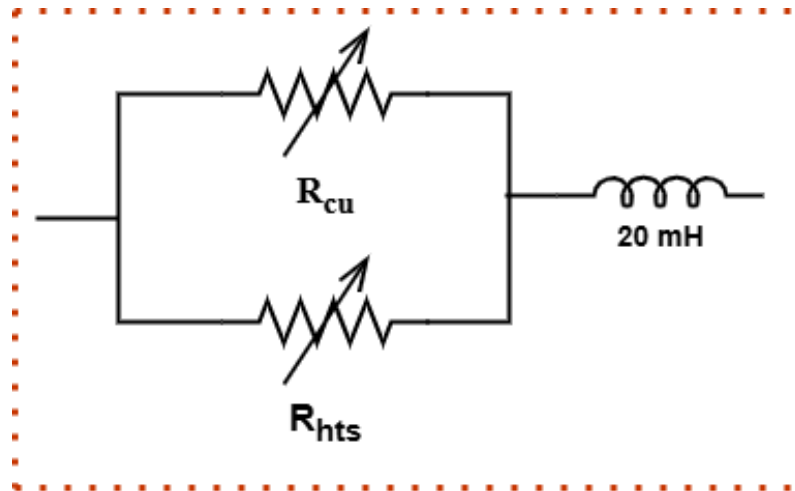


Figure 7.25 A simple resistive fault current limiter.

By integrating the SFCL with the HTS cable, the fault current for a 20 ms pole-to-ground fault, as shown in Figure 7.26, is reduced by 10 kA compared to the current shown in Figure 7.16 without integrating SFCL with HTS. The SFCL operates effectively through its superconducting properties, without the need for mechanical switching

devices. The inductance prevents sudden changes in the current, as the rise in the HTS current limits the overall current flow.
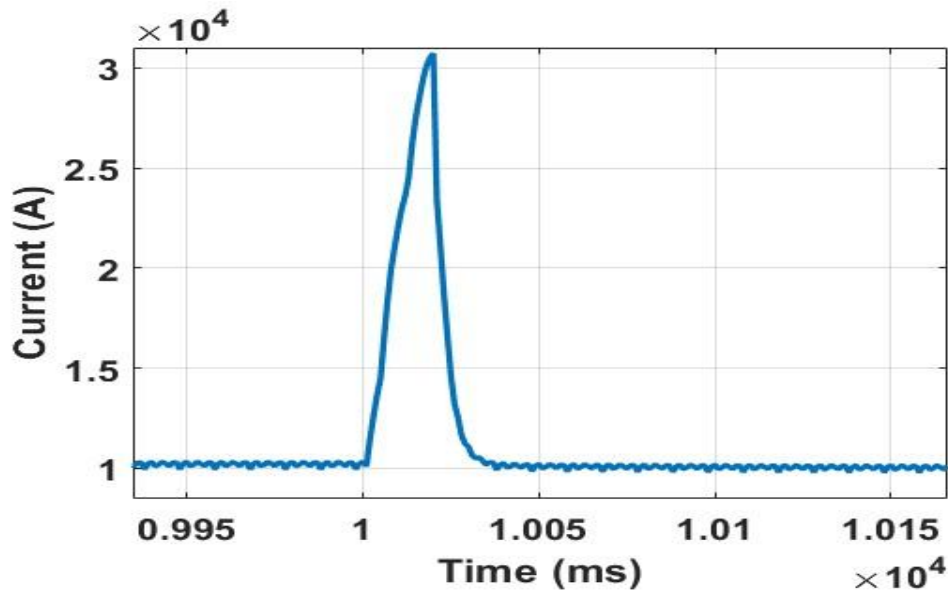


Figure 7.26  Current flow through the HTS cable during a fault.

Figures 7.27 to 7.29 illustrate the variations in temperature, critical current, and resistance of the HTS cable integrated with an SFCL. During a fault, SFCL limits the current to 31 kA, the superconductor does not quench and its critical current carrying capacity along the cable is higher than the fault current. The cable $I_c$ and temperature behave the same as the pre-fault condition. At the end of the LN2 cooling system of the superconducting power cable, the resistance of the HTS layer increases. As shown in Figure 7.29, the maximum resistance reached is 40 nΩ, which is minimal and ensures that there is no significant joule heating in the cable. Consequently, the performance of the superconductor remains unaffected when integrated with the SFCL during faults lasting up to 20 milliseconds. The integration of a superconducting power cable with a Superconducting Fault Current Limiter (SFCL) ensures that the High-Temperature Superconducting (HTS) power cable operates without sustaining permanent damage, making it a resilient and robust choice for use in the electrical grid.
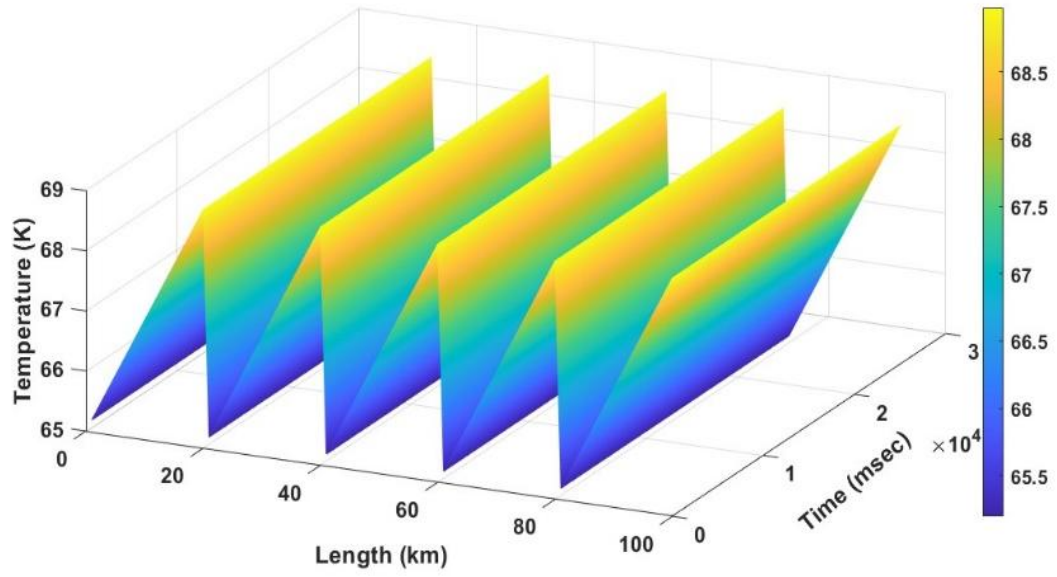
Figure 7.27  3D view of the temperature, length and time of the HTS cable during a fault.
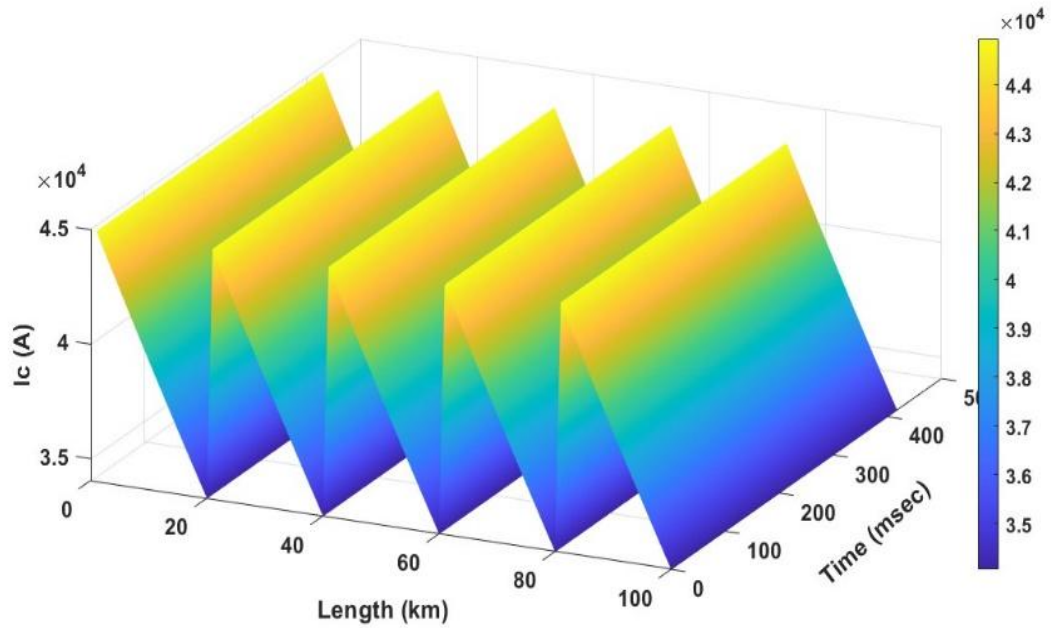


Figure 7.28  3D view of the critical current, length and time of the HTS cable during a fault
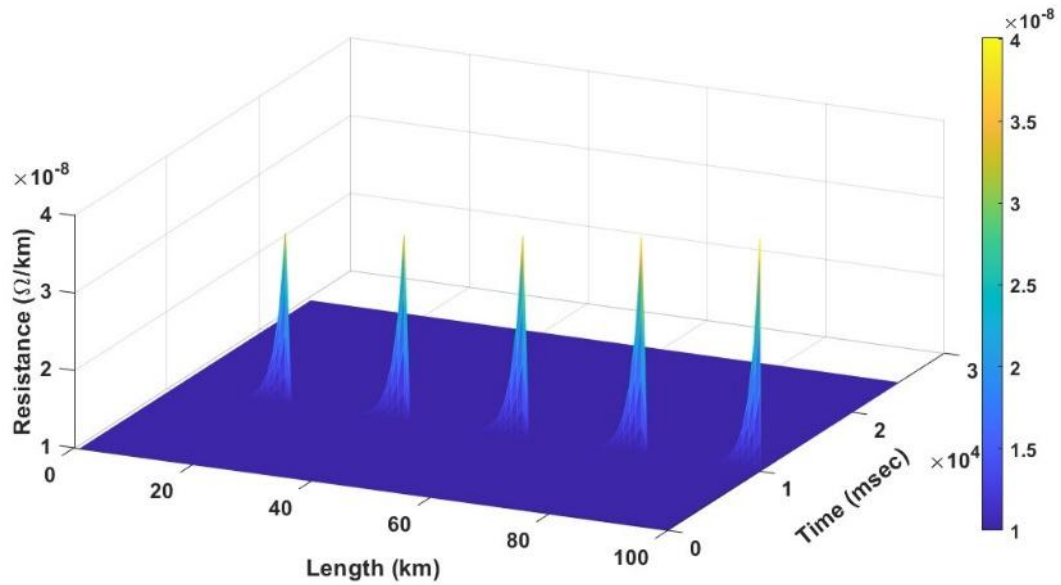
Figure 7.29  3D view of the resistance, length and time of the HTS cable during a fault.

## 7.7.  Summary of Chapter 7

This chapter outlined key findings related to the thermal and hydraulic properties of long-distance HTS power cables cooled by liquid nitrogen (LN2). The study revealed that cable topology and LN2 flow configurations greatly influence the pressure drop and temperature distribution along the cable length. Turbulent and laminar flow models indicated varying cooling efficiencies, with critical insights into optimizing flow for maintaining HTS stability. The integration of a Superconducting Fault Current Limiter (SFCL) was found to significantly mitigate fault current impacts, maintaining the cable below critical temperature, and preventing quenching. The results highlighted effective strategies for ensuring continuous operation under transient conditions, showcasing the importance of optimal cryogenic and fault management in long-distance HVDC HTS cable systems.

# Chapter 8

# Conclusion and Future Work

## 8.1. Conclusion

Chapters 2 and 3 elaborate on the basics of superconductors and the advantages of selecting coaxial cables for power transmission compared to other cable structures. Chapter 4 discusses the necessity of superconductor Simscape elements for grid studies. It provides a detailed study of the lumped and distributed models of the superconductor developed in MATLAB Simscape. Developed novel HTS Simscape components that include the electrical, thermal, and hydraulic behaviours in MATLAB.

Lumped RLC models have been compared with distributed models. This study explains the necessity of the distributed RLC model for superconductors. The results from the distributed models indicate that the thermal, electrical, and hydraulic behaviour along the length of the HTS power cable varies. The distributed model provides new insights into the cryocooler arrangement required for long-distance HTS power cables. It considers the cable's thermal behaviour, influenced by environmental heat leaks, radiation losses, pressure drop, electrical resistance, and critical current. The distributed models demonstrate, for the first time, how the current-carrying capacity of the HTS power cable diminishes due to sudden inrush currents caused by system faults. During a fault, the resistance of the superconducting power cable increases, causing the current to shift from the superconducting layer to the copper former. This variation in resistance leads to increased joule heating in the HTS power cable, resulting in significantly higher power losses. A novel discrete element model of the HTS cable has been developed in MATLAB SIMSCAPE, which includes heat transfer through conduction, convection, and radiation in both radial and axial directions.

179

This study examines the impact of PG faults and their locations for the first time on a 1GW, 100KV, 10kA superconducting power cable. Investigated how the characteristics of the cable change based on the fault location. The analysis reveals that the fault inrush current significantly affects both the electrical and thermal behaviour of the High-Temperature Superconductor (HTS) power cable. Our results show that the quenching behaviour of the superconducting cable varies with the location of the fault. Specifically, the distance from the voltage source to the fault location influences the fault inrush current; as this distance increases, the fault inrush current decreases due to increased resistance. When the fault inrush current increases, the temperature of the HTS cable also rises, leading to quenching. The temperature rise is directly proportional to the fault current and its duration. If the superconducting tape within the cable is not permanently damaged during quenching, the recovery time from the quenched state to the superconducting state is longer for higher fault currents.

Chapter 5 elaborates on joint resistance and explains the necessity of low-resistance superconductor joints. A 5 cm long PbSn joint was fabricated for the 2G HTS tape, achieving a joint resistance of 7-8 n$\Omega$. The critical current ($I_c$) of the 2G HTS tape, intended for use in a superconducting power cable model, was determined experimentally and utilised in further modelling of the power cable. The quenching behaviour of the superconducting power cable was validated experimentally. For this purpose, a short length of HTS tape was tested in a liquid nitrogen (LN2) bath at various temperatures. The behaviour was monitored with current ramps, and the HTS temperature was detected using a PT-103 RTD sensor. These experimental results were then compared with the modelling outcomes.

In Chapter 6, the ripples and electromagnetic behaviour of the 10 kA HTS cable are studied using T-A FEM formulation in COMSOL for the first time. The critical current of the superconductor depends not only on temperature but also on the magnetic field. The self-generated magnetic field can degrade the $I_c$ of the superconducting power cable. The chapter first examines the ripples generated by converters (AC/DC conversion), the impact of the DC offset with ripple signals on the behaviour of the superconducting power

cable, and the behaviour of a 10 kA/1 GW HTS power cable in relation to ripple amplitude and frequency. The results show that under normal operating conditions, the losses generated in the HTS power cable are minimal. The self-generated magnetic field is small compared to the critical field of the 2G HTS tapes, resulting in minimal degradation of $I_c$ in the HTS cable. Additionally, experimental measurements of losses under ripple conditions are conducted on short HTS tapes to validate the findings.

Chapter 7 discusses the optimization of the superconductor cable design. It studies the impact of variations in the roughness of the corrugated cryogenic path pipe on friction losses, temperature rise, and pressure drop, based on coolant mass flow. The chapter examines the effects of turbulent and laminar flow within the coolant path on temperature rise and pressure drop, which are crucial for selecting the most efficient long-distance HTS HVDC power cable cryo-cooler arrangement. A high-ampacity HTS power cable with a cryo-cooler arrangement every 20 km was chosen. The cable was integrated with the SFCL and was able to withstand 20 ms PG faults without affecting the temperature of the HTS cable, effectively limiting the fault current.

## 8.2. Future Work

**Mechanical Stress and Lorentz Force Impact:**

Future research should delve deeper into understanding the mechanical stress and Lorentz force effects during fault conditions in HTS power cables. These forces can significantly impact the cable's performance and longevity, necessitating robust design and testing methodologies to mitigate potential damages and ensure reliability.

**Vibration Impact from Tidal Waves:**

The behaviour of HTS power cables under the influence of vibrations caused by tidal waves is another critical area of study. This research should focus on the long-term effects of continuous wave-induced vibrations on cable integrity and

performance, contributing to more resilient cable designs suitable for offshore environments.

**Insulation Integrity Under High Voltage:**

Investigating the development and endurance of insulation materials capable of withstanding voltage ratings up to 100 kV is essential. Future studies should examine the propensity for cracks and other degradation forms in insulation materials, ensuring that they provide adequate protection over prolonged periods under high-stress conditions.

**Advanced Modelling Frameworks:**

While the current study uses discretised electrical-thermal-hydraulic models, further work could explore hybrid modelling techniques that integrate artificial intelligence (AI) or machine learning algorithms for real-time fault prediction and system optimisation. This could enable more adaptive designs for HTS cable networks under dynamic grid conditions.

**Focus on Cable Terminations and Joints:**

Future tasks must prioritise the development and testing of improved cable terminations, and joints. These components are crucial for maintaining the overall integrity and performance of HTS power cables. Enhancing these aspects will lead to more reliable and durable offshore power transmission systems. In summary, advancing the research on HTS power cables involves a comprehensive approach addressing mechanical stresses, environmental impacts, material integrity, and the integration of cutting-edge technologies like AI. These recommendations aim to ensure the reliability, efficiency, and longevity of HTS power cables in offshore applications.

# References

[1]     D. Gielen, F. Boshell, D. Saygin, M. D. Bazilian, N. Wagner, and R. Gorini, "The role of renewable energy in the global energy transformation," *Energy Strategy Reviews*, vol. 24, pp. 38–50, Apr. 2019, doi: 10.1016/j.esr.2019.01.006.

[2]     K. Riahi *et al.*, "Energy Pathways for Sustainable Development Convening Lead Author (CLA) Lead Authors (LA) Contributing Authors (CA) Review Editor Energy Pathways for Sustainable Development."

[3]     M. Muniappan, "A comprehensive review of DC fault protection methods in HVDC transmission systems," Dec. 01, 2021, *Springer*. doi: 10.1186/s41601-020-00173-9.

[4]     F. Schmidt and A. Allais, "Superconducting cables for power transmission applications - a review," *Workshop on Accelerator Magnet Superconductors*, p. 352, 2004.

[5]     J. G. Bednorz and K. A. Müller, "Possible high T c superconductivity in the Ba− La− Cu− O system," *Zeitschrift für Physik B Condensed Matter*, vol. 64, no. 2, pp. 189–193, 1986.

[6]     J. H. Choi, H. Park, and R. Baldick, "Transmission Investment and Expansion Planning for Systems with High-Temperature Superconducting Cables," *IEEE Transactions on Applied Superconductivity*, vol. 29, no. 8, pp. 1–9, 2019, doi: 10.1109/TASC.2019.2923589.

[7] D. I. Doukas, "Superconducting Transmission Systems: Review, Classification, and Technology Readiness Assessment," *IEEE Transactions on Applied Superconductivity*, vol. 29, no. 5, 2019, doi: 10.1109/TASC.2019.2895395.

[8] D. Miyagi, R. Sakakibara, Y. Shinozaki, M. Tsuda, and T. Hamajima, "Suitable Cable Structure of HTS Triaxial Cable Cooled by Counter Flow Cooling Method for Long-Distance Power Transmission," *IEEE Transactions on Applied Superconductivity*, vol. 28, no. 4, 2018, doi: 10.1109/TASC.2018.2810296.

[9] M. Nassi, N. Kelley, P. Ladié, P. Corsaro, G. Coletta, and D. Von Dollen, "Qualification results of a 50 m-115 kV warm dielectric cable system," *IEEE Transactions on Applied Superconductivity*, vol. 11, no. 1 II, pp. 2355–2358, 2001, doi: 10.1109/77.920334.

[10] J. F. Maguire *et al.*, "Progress and status of a 2G HTS power cable to be installed in the Long Island Power Authority (LIPA) grid," *IEEE Transactions on Applied Superconductivity*, vol. 21, no. 3 PART 2, pp. 961–966, 2011, doi: 10.1109/TASC.2010.2093108.

[11] R. Soika, X. G. Garcia, and S. C. Nogales, "ENDESA Supercable, a 3.2 kA, 138 MVA, medium voltage superconducting power cable," *IEEE Transactions on Applied Superconductivity*, vol. 21, no. 3 PART 2, pp. 972–975, 2011, doi: 10.1109/TASC.2010.2100357.

[12] M. Stemmle, F. Merschel, M. Noe, and A. Hobl, "Plenary talk - European project and application of high Tc superconducting cable," *2013 IEEE International*

*Conference on Applied Superconductivity and Electromagnetic Devices, ASEMD 2013*, p. 257, 2013, doi: 10.1109/ASEMD.2013.6780759.

[13]  T. Masuda *et al.*, "Fabrication and installation results for Albany HTS cable," *IEEE Transaction on Applied Superconductivity*, vol. 17, no. 2, pp. 1648–1651, 2007.

[14]  D. C. Superconducting and P. Cables, "Concept and Design of 500 Meter and 1000 Meter DC Superconducting Power Cables in Ishikari, Japan," *IEEE Transactions on Applied Superconductivity*, vol. 25, no. 3, pp. 3–6, 2015.

[15]  B. Yang, J. Kang, S. Lee, C. Choi, and Y. Moon, "Qualification Test of a 80 kV 500 MW HTS DC Cable for Applying into Real Grid," *IEEE Transactions on Applied Superconductivity*, vol. 25, no. 3, 2015, doi: 10.1109/TASC.2015.2396683.

[16]  J. H. Lim *et al.*, "Cryogenic system for 80-kV DC HTS cable in the KEPCO power grid," *IEEE Transactions on Applied Superconductivity*, vol. 25, no. 3, Jun. 2015, doi: 10.1109/TASC.2014.2387393.

[17]  B. Wang *et al.*, "Design, Manufacture, and Test of a 30 m 10 kV/2.5 kA Concentric HTS Cable Prototype for Urban Grid," *IEEE Access*, vol. 9, pp. 120066–120077, 2021, doi: 10.1109/ACCESS.2021.3108199.

[18]  S. Tang *et al.*, "Development and demonstration of concentric-type HTS power cable for distribution grid in Shenzhen urban," *Frontiers in Energy Efficiency*, vol. 1, p. 1160372, 2023.

[19]  X. H. Zong, Y. W. Han, and C. Q. Huang, "Introduction of 35-kV kilometer-scale high-temperature superconducting cable demonstration project in Shanghai,"

*Superconductivity*, vol. 2, p. 100008, 2022, doi: https://doi.org/10.1016/j.supcon.2022.100008.

[20]   Y. Ohki, "News From Japan Development of a 6-kV, 3,000-A Triaxial Superconducting Cable," 2022, *IEEE-INST ELECTRICAL ELECTRONICS ENGINEERS INC 445 HOES LANE, PISCATAWAY, NJ ….*

[21]   "'ComEd and AMSC Announce Successful Integration of Resilient Electric Grid System in Chicago'', AMSC, Aug. 31, 2021. https://www.amsc.com/comed-and-amsc-announce-successful-integration-of-resilient-electric-grid-system-in-chicago/ (accessed Apr. 15, 2022).'".

[22]   D. Elliott *et al.*, "A Comparison of AC and HVDC Options for the Connection of Offshore Wind Generation in Great Britain," *IEEE Transactions on Power Delivery*, vol. 31, no. 2, pp. 798–809, 2016, doi: 10.1109/TPWRD.2015.2453233.

[23]   V. E. Sytnikov *et al.*, "HTS DC Cable line project: On-Going activities in Russia," *IEEE Transactions on Applied Superconductivity*, vol. 23, no. 3, pp. 2–5, 2013, doi: 10.1109/TASC.2013.2245280.

[24]   G. Guan, K. Ding, and K. Lu, "Modeling and Transient Electric-Thermal-Magnetic Coupling Numerical Simulation of 10 kV / 1 kA Tri-Axial HTS Power Cable for Urban Application," no. 1, pp. 2020–2021, 2020.

[25]   X. Li *et al.*, "Simulation Analysis of 2D Finite Element Axial Temperature Distribution of HTS Cable," *IEEE Transactions on Applied Superconductivity*, vol. 8223, no. c, pp. 1–6, 2021, doi: 10.1109/TASC.2021.3061344.

[26] L. Graber, S. Member, J. Kim, C. H. Kim, S. V Pamidi, and S. Member, "Thermal Network Model for HTS Cable Systems and Components Cooled by Helium Gas," vol. 26, no. 4, 2016.

[27] W. Xiang, W. Yuan, L. Xu, E. Hodge, J. Fitzgerald, and P. McKeever, "Fault Transient Study of a Meshed DC Grid With High-Temperature Superconducting DC Cables," *IEEE Transactions on Power Delivery*, vol. 37, no. 6, pp. 5414–5424, 2022, doi: 10.1109/TPWRD.2022.3177406.

[28] M. Cullinane, F. Judge, M. O'Shea, K. Thandayutham, and J. Murphy, "Subsea superconductors: The future of offshore renewable energy transmission?," *Renewable and Sustainable Energy Reviews*, vol. 156, p. 111943, 2022, doi: https://doi.org/10.1016/j.rser.2021.111943.

[29] P. A. Abetti and P. Haldar, "One hundred years of superconductivity: science, technology, products, profits and industry structure," *International Journal of Technology Management*, vol. 48, no. 4, pp. 423–447, 2009.

[30] D. Van Delft, "History and significance of the discovery of superconductivity by Kamerlingh Onnes in 1911," *Physica C Supercond*, vol. 479, pp. 30–35, 2012.

[31] W. Meissner and R. Ochsenfeld, "A new effect concerning the onset of superconductivity," *Naturwissenschaften*, vol. 21, p. 787, 1933.

[32] D. U. Gubser, "Superconductivity: an emerging power-dense energy-efficient technology," *IEEE Transactions on applied superconductivity*, vol. 14, no. 4, pp. 2037–2046, 2004.

[33]    R. M. Scanlan, A. P. Malozemoff, and D. C. Larbalestier, "Superconducting materials for large scale applications," *Proceedings of the IEEE*, vol. 92, no. 10, pp. 1639–1654, 2004.

[34]    J. G. Bednorz and K. A. Müller, "Possible highTc superconductivity in the Ba−La−Cu−O system," *Zeitschrift für Physik B Condensed Matter*, vol. 64, no. 2, pp. 189–193, 1986, doi: 10.1007/BF01303701.

[35]    M. Biasion, J. F. P. Fernandes, S. Vaschetto, A. Cavagnino, and A. Tenconi, "Superconductivity and its Application in the Field of Electrical Machines," in *2021 IEEE International Electric Machines & Drives Conference (IEMDC)*, 2021, pp. 1–7. doi: 10.1109/IEMDC47953.2021.9449545.

[36]    J. Bock *et al.*, "HTS Fault Current Limiters - First commercial devices for distribution level grids in Europe," *IEEE Transactions on Applied Superconductivity*, vol. 21, no. 3 PART 2, 2011, doi: 10.1109/TASC.2010.2099636.

[37]    L. Xiao *et al.*, "Development of the World's first HTS power substation," *IEEE Transactions on Applied Superconductivity*, vol. 22, no. 3, 2012, doi: 10.1109/TASC.2011.2176089.

[38]    P. Song, T. M. Qu, L. F. Lai, M. S. Wu, X. Y. Yu, and Z. Han, "Thermal analysis for the HTS stator consisting of HTS armature windings and an iron core for a 2.5 kW HTS generator," *Supercond Sci Technol*, vol. 29, no. 5, 2016, doi: 10.1088/0953-2048/29/5/054007.

[39]  P. Song, T. M. Qu, L. F. Lai, M. S. Wu, X. Y. Yu, and Z. Han, "Thermal analysis for the HTS stator consisting of HTS armature windings and an iron core for a 2.5 kW HTS generator," *Supercond Sci Technol*, vol. 29, no. 5, Mar. 2016, doi: 10.1088/0953-2048/29/5/054007.

[40]  S. Satyanarayana, Z. Zhang, C. H. Kim, and S. Pamidi, "Models for Design and Analysis of Superconducting Power Systems Cooled with Cryocoolers," *Cryocoolers*, 2018.

[41]  N. G. Suttell, J. V. C. Vargas, J. C. Ordonez, S. V. Pamidi, and C. H. Kim, "Modeling and optimization of gaseous helium (GHe) cooled high temperature superconducting (HTS) DC cables for high power density transmission," *Appl Therm Eng*, vol. 143, pp. 922–934, Oct. 2018, doi: 10.1016/J.APPLTHERMALENG.2018.08.031.

[42]  M. J. Wolf, C. Ebner, W. H. Fietz, R. Heller, D. Nickel, and K. P. Weiss, "High temperature superconductors for fusion applications and new developments for the HTS CroCo conductor design," *Fusion Engineering and Design*, vol. 172, p. 112739, Nov. 2021, doi: 10.1016/J.FUSENGDES.2021.112739.

[43]  M.-K. Wu *et al.*, "Superconductivity at 93 K in a new mixed-phase Y-Ba-Cu-O compound system at ambient pressure," *Phys Rev Lett*, vol. 58, no. 9, p. 908, 1987.

[44]  D. Larbalestier and P. C. Canfield, "Superconductivity at 100—Where we've been and where we're going," *MRS Bull*, vol. 36, no. 8, pp. 590–593, 2011.

[45] C. Yao and Y. Ma, "Superconducting materials : Challenges and opportunities for large-scale applications," *iScience*, vol. 24, no. 6, p. 102541, 2021, doi: 10.1016/j.isci.2021.102541.

[46] F. Grilli, E. Pardo, A. Stenvall, D. N. Nguyen, W. Yuan, and F. Gomory, "Computation of losses in HTS under the action of varying magnetic fields and currents," *IEEE Transactions on Applied Superconductivity*, vol. 24, no. 1, 2014, doi: 10.1109/TASC.2013.2259827.

[47] K. Kim *et al.*, "A perspective on conducting oxide buffers for Cu-based YBCO-coated conductors," *Supercond Sci Technol*, vol. 19, no. 4, p. R23, 2006.

[48] B. Shen, *Study of Second Generation High Temperature Superconductors: Electromagnetic Characteristics and AC Loss Analysis*. Springer Nature, 2020.

[49] H. Eisaki *et al.*, "Effect of chemical inhomogeneity in bismuth-based copper oxide superconductors," *Phys Rev B*, vol. 69, no. 6, p. 064512, 2004.

[50] C. P. Bean, "Magnetization of high-field superconductors," *Rev Mod Phys*, vol. 36, no. 1, 1964, doi: 10.1103/RevModPhys.36.31.

[51] C. P. Bean, "Magnetization of hard superconductors," *Phys Rev Lett*, vol. 8, no. 6, 1962, doi: 10.1103/PhysRevLett.8.250.

[52] R. Flükiger, "Overview of superconductivity and challenges in applications," *Reviews of Accelerator Science and Technology*, vol. 5, pp. 1–23, 2012.

[53] J. Rhyner, "Magnetic properties and AC-losses of superconductors with power law current-voltage characteristics," *Physica C: Superconductivity and its applications*, vol. 212, no. 3–4, 1993, doi: 10.1016/0921-4534(93)90592-E.

[54] S. Stavrev *et al.*, "Comparison of numerical methods for modeling of superconductors," *IEEE Trans Magn*, vol. 38, no. 2 I, 2002, doi: 10.1109/20.996219.

[55] W. Paul, M. Chen, M. Lakner, J. Rhyner, D. Braun, and W. Lanz, "Fault current limiter based on high temperature superconductors - Different concepts, test results, simulations, applications," *Physica C: Superconductivity and its Applications*, vol. 354, no. 1–4, 2001, doi: 10.1016/S0921-4534(01)00018-1.

[56] J. Duron, B. Dutoit, F. Grilli, M. Decroux, L. Antognazza, and Fischer, "Computer modeling of YBCO fault current limiter strips lines in over-critical regime with temperature dependent parameters," in *IEEE Transactions on Applied Superconductivity*, 2007. doi: 10.1109/TASC.2007.898365.

[57] T. Rettelbach and G. J. Schmitz, "3D simulation of temperature, electric field and current density evolution in superconducting components," *Supercond Sci Technol*, vol. 16, no. 5, 2003, doi: 10.1088/0953-2048/16/5/318.

[58] P. W. Anderson, "Theory of flux creep in hard superconductors," *Phys Rev Lett*, vol. 9, no. 7, 1962, doi: 10.1103/PhysRevLett.9.309.

[59] Y. B. Kim, C. F. Hempstead, and A. R. Strnad, "Flux creep in hard superconductors," *Physical Review*, vol. 131, no. 6, 1963, doi: 10.1103/PhysRev.131.2486.

[60] R. Brambilla, F. Grilli, and L. Martini, "Development of an edge-element model for {AC} loss computation of high-temperature superconductors," vol. 20, no. 1, pp. 16–24, Nov. 2006, doi: 10.1088/0953-2048/20/1/004.

[61] G. G. Sotelo, M. Carrera, J. Lopez-Lopez, and X. Granados, "H-Formulation FEM Modeling of the Current Distribution in 2G HTS Tapes and Its Experimental Validation Using Hall Probe Mapping," *IEEE Transactions on Applied Superconductivity*, vol. 26, no. 8, pp. 1–10, 2016, doi: 10.1109/TASC.2016.2591825.

[62] B. Shen, T. Coombs, and F. Grilli, "Investigation of AC Loss in HTS Cross-Conductor Cables for Electrical Power Transmission," *IEEE Transactions on Applied Superconductivity*, vol. 29, no. 2, pp. 1–5, 2019, doi: 10.1109/TASC.2018.2881491.

[63] C. Kan, Y. Wang, X. Yuan, Y. Li, and Y. Hou, "AC Loss Analysis on a Quasi-Isotropic Strand Stacked by 2G Wires by Numerical Simulation in Cryogenic Temperature," *IEEE Transactions on Applied Superconductivity*, vol. 28, no. 3, pp. 1–6, 2018, doi: 10.1109/TASC.2017.2786726.

[64]    Z. Hong, A. M. Campbell, and T. A. Coombs, "Numerical solution of critical state in superconductivity by finite element software," *Supercond Sci Technol*, vol. 19, no. 12, 2006, doi: 10.1088/0953-2048/19/12/004.

[65]    B. Shen, F. Grilli, and T. Coombs, "Overview of H-Formulation: A Versatile Tool for Modeling Electromagnetics in High-Temperature Superconductor Applications," 2020, *Institute of Electrical and Electronics Engineers Inc.* doi: 10.1109/ACCESS.2020.2996177.

[66]    A. Stenvall, V. Lahtinen, and M. Lyly, "An H-formulation-based three-dimensional hysteresis loss modelling tool in a simulation including time varying applied field and transport current: the fundamental problem and its solution," *Supercond Sci Technol*, vol. 27, no. 10, p. 104004, 2014, doi: 10.1088/0953-2048/27/10/104004.

[67]    V. Lahtinen, A. Stenvall, F. Sirois, and M. Pellikka, "A finite element simulation tool for predicting hysteresis losses in superconductors using an H-oriented formulation with cohomology basis functions," *J Supercond Nov Magn*, vol. 28, pp. 2345–2354, 2015.

[68]    J. M. Brooks, M. D. Ainslie, Z. Jiang, S. C. Wimbush, R. A. Badcock, and C. W. Bumby, "Numerical Modelling of Dynamic Resistance in a Parallel-Connected Stack of HTS Coated-Conductor Tapes," *IEEE Transactions on Applied Superconductivity*, vol. 30, no. 4, pp. 1–8, 2020, doi: 10.1109/TASC.2020.2974860.

[69]  D. Ruiz-Alonso, T. Coombs, and A. M. Campbell, "Computer modelling of high-temperature superconductors using an A-V formulation," in *Superconductor Science and Technology*, 2004. doi: 10.1088/0953-2048/17/5/042.

[70]  S. Wang, H. Yong, and Y. Zhou, "Numerical calculations of high temperature superconductors with the JA formulation," *Supercond Sci Technol*, vol. 36, no. 11, p. 115020, 2023.

[71]  X. Li *et al.*, "Calculation of CORC Cable Loss Using a Coupled Electromagnetic-Thermal T-A Formulation Model," *IEEE Transactions on Applied Superconductivity*, vol. 31, no. 4, pp. 1–7, 2021, doi: 10.1109/TASC.2021.3072742.

[72]  K. Berger, C. Guérin, J. Lévêque, G. Meunier, and P. Tixador, *Comparaison de Différents Outils de Calcul pour la Modélisation des Supraconducteurs*. 2008.

[73]  N. Amemiya, S. I. Murasawa, N. Banno, and K. Miyamoto, "Numerical modelings of superconducting wires for AC loss calculations," *Physica C: Superconductivity and its Applications*, vol. 310, no. 1–4, 1998, doi: 10.1016/S0921-4534(98)00427-4.

[74]  C. J. Carpenter, "COMPARISON OF ALTERNATIVE FORMULATIONS OF 3-DIMENSIONAL MAGNETIC-FIELD AND EDDY-CURRENT PROBLEMS AT POWER FREQUENCIES.," *Proceedings of the Institution of Electrical Engineers*, vol. 124, no. 11, 1977, doi: 10.1049/piee.1977.0211.

[75] T. Nakata, N. Takahashi, K. Fujiwara, and Y. Okada, "Improvehents of the t-Ω method for 3-D eddy current analysis," *IEEE Trans Magn*, vol. 24, no. 1, 1988, doi: 10.1109/20.43864.

[76] M. Zhang and T. A. Coombs, "3D modeling of high-Tc superconductors by finite element software," *Supercond Sci Technol*, vol. 25, no. 1, p. 015009, 2012, doi: 10.1088/0953-2048/25/1/015009.

[77] J. Dular, M. Harutyunyan, L. Bortot, S. Schops, B. Vanderheyden, and C. Geuzaine, "On the Stability of Mixed Finite-Element Formulations for High-Temperature Superconductors," *IEEE Transactions on Applied Superconductivity*, vol. 31, no. 6, 2021, doi: 10.1109/TASC.2021.3098724.

[78] J. Dular, C. Geuzaine, and B. Vanderheyden, "Finite-Element Formulations for Systems with High-Temperature Superconductors," *IEEE Transactions on Applied Superconductivity*, vol. 30, no. 3, 2020, doi: 10.1109/TASC.2019.2935429.

[79] S. Kim *et al.*, "Investigation on the Stability of HTS Power Cable Under Fault Current Considering Stabilizer," vol. 17, no. 2, pp. 1676–1679, 2007.

[80] H. De Gersem, T. Weiland, and A. Time-varying, "Finite-Element Models for Superconductive Cables With Finite Interwire Resistance," vol. 40, no. 2, pp. 667–670, 2004.

[81] L. Bottura, C. Rosso, and M. Breschi, "A general model for thermal, hydraulic and electric analysis of superconducting cables," *Cryogenics (Guildf)*, vol. 40, no. 8–10, pp. 617–626, 2000, doi: 10.1016/s0011-2275(01)00019-4.

[82]   W. Hirofumi, Y. V. Ivanov, M. Hamabe, N. Chikumoto, T. Kawahara, and S. Y. Hirohisa Takano, "Circulation Test of Liquid Nitrogen for Long Superconducting DC Power Transmission Lines," *IEEE TRANSACTIONS ON APPLIED SUPERCONDUCTIVITY*, vol. 26, no. 3, pp. 1–4, 2016, doi: 10.4324/9780080549798-67.

[83]   Z. Q. Zuo, W. B. Jiang, Z. G. Yu, and Y. H. Huang, "Liquid nitrogen flow in helically corrugated pipes with insertion of high-temperature superconducting power transmission cables," *Int J Heat Mass Transf*, vol. 140, pp. 88–99, 2019, doi: 10.1016/j.ijheatmasstransfer.2019.05.078.

[84]   G. H. Morgan and J. E. Jensen, "Counter-flow cooling of a transmission line by supercritical helium," *Cryogenics (Guildf)*, vol. 17, no. 5, pp. 259–267, 1977, doi: 10.1016/0011-2275(77)90193-X.

[85]   D. M. Bernhard and C. K. Hsieh, "Pressure drop in corrugated pipes," 1996.

[86]   S. Fuchino, N. Tamada, I. Ishii, and N. Higuchi, "Hydraulic characteristics in superconducting power transmission cables," *Physica C Supercond*, vol. 354, no. 1–4, pp. 125–128, 2001.

[87]   D. Koh, H. Yeom, Y. Hong, and K. Lee, "Performance tests of high temperature superconducting power cable cooling system," *IEEE transactions on applied superconductivity*, vol. 14, no. 2, pp. 1746–1749, 2004.

[88]    B. Zajaczkowski, A. J. M. Giesbers, M. Holtrust, E. Haenen, and R. Den Heijer, "Feasibility of inline cooling in long distance HTS power line," *Cryogenics (Guildf)*, vol. 51, no. 4, pp. 180–186, 2011, doi: 10.1016/j.cryogenics.2011.01.007.

[89]    Y. Ivanov, H. Watanabe, M. Hamabe, T. Kawahara, J. Sun, and S. Yamaguchi, "Design study of LN2 circulation in a long SC power transmission lines," *Phys Procedia*, vol. 36, pp. 1372–1377, 2012, doi: 10.1016/j.phpro.2012.06.307.

[90]    A. Morandi, "HTS dc transmission and distribution: Concepts, applications and benefits," *Supercond Sci Technol*, vol. 28, no. 12, 2015, doi: 10.1088/0953-2048/28/12/123001.

[91]    E. Shabagin, C. Heidt, S. Strauß, and S. Grohmann, "Modelling of 3D temperature profiles and pressure drop in concentric three-phase HTS power cables," *Cryogenics (Guildf)*, vol. 81, pp. 24–32, 2017, doi: 10.1016/j.cryogenics.2016.11.004.

[92]    H. M. Chang, K. N. Ryu, and H. S. Yang, "Cryogenic design of liquid-nitrogen circulation system for long-length HTS cables with altitude variation," *Cryogenics (Guildf)*, vol. 83, 2017, doi: 10.1016/j.cryogenics.2017.02.004.

[93]    M. Kalsia and R. S. Dondapati, "Thermohydraulic analysis of cold dielectric high temperature superconducting cable with counter-flow cooling," *Physica C: Superconductivity and its Applications*, vol. 564, no. June, pp. 59–67, 2019, doi: 10.1016/j.physc.2019.06.006.

[94]   D. Kottonau, W. T. B. De Sousa, J. Bock, and M. Noe, "Design Comparisons of Concentric Three-Phase HTS Cables," *IEEE Transactions on Applied Superconductivity*, vol. 29, no. 6, pp. 1–8, 2019, doi: 10.1109/TASC.2019.2897893.

[95]   S. Thadela, V. V. Rao, R. Agarwal, and R. S. Dondapati, "Computational investigation on thermohydraulic characteristics of High-Temperature Superconducting (HTS) power cables," *Physica C: Superconductivity and its Applications*, vol. 559, no. December 2018, pp. 25–31, 2019, doi: 10.1016/j.physc.2019.02.003.

[96]   J. Jin, L. Wang, R. Yang, T. Zhang, S. Mu, and Q. Zhou, "A composite superconducting energy pipeline and its characteristics," *Energy Reports*, vol. 8, 2022, doi: 10.1016/j.egyr.2022.01.126.

[97]   Y. Wang, "Case study of superconductivity applications in power system-HTS Cables," *Fundamental Elements of Applied Superconductivity in Electrical Engineering*, pp. 389–420, 2013.

[98]   N. Endo, Y. Shinozaki, Y. Nagasaki, D. Miyagi, and M. Tsuda, "Configuration method of tri-axial ReBCO cable suitable for long distance power transmission," *IEEE Transactions on Applied Superconductivity*, vol. 29, no. 5, 2019, doi: 10.1109/TASC.2019.2904546.

[99]   T. Nguyen *et al.*, "A Simplified Model of Coaxial, Multilayer High-Temperature Superconducting Power Cables with Cu Formers for Transient Studies," 2019.

[100] U. Floegel-Delor *et al.*, "Long-Length Coated Conductor Copper Plating Fabrication," *IEEE Transactions on Applied Superconductivity*, vol. 23, no. 3, pp. 6602204–6602204, 2013, doi: 10.1109/tasc.2013.2244635.

[101] W. T. Norris, "Calculation of hysteresis losses in hard superconductors carrying ac: Isolated conductors and edges of thin sheets," *J Phys D Appl Phys*, vol. 3, no. 4, pp. 489–507, 1970, doi: 10.1088/0022-3727/3/4/308.

[102] C. Lee, D. Kim, S. Kim, D. Y. Won, and H. S. Yang, "Thermo-Hydraulic Analysis on Long Three-Phase Coaxial HTS Power Cable of Several Kilometers," *IEEE Transactions on Applied Superconductivity*, vol. 29, no. 5, 2019, doi: 10.1109/TASC.2019.2900710.

[103] G. Del-Rosario-Calaf, J. Lloberas-Valls, A. Sumper, X. Granados, and R. Villafafila-Robles, "Modeling of second generation HTS cables for grid fault analysis applied to power system simulation," *IEEE Transactions on Applied Superconductivity*, vol. 23, no. 3, 2013, doi: 10.1109/TASC.2012.2236673.

[104] R. Su *et al.*, "Numerical Model of HTS Cable and Its Electric-Thermal Properties," *IEEE Transactions on Applied Superconductivity*, vol. 29, no. 5, 2019, doi: 10.1109/TASC.2019.2901874.

[105] X. Wang, A. Ishiyama, M. Ohya, and N. Fujiwara, "Over-Current Characteristics of 66-kV RE123 HTS Power Cable," *IEEE Transactions on Applied Superconductivity*, vol. 21, no. 3, pp. 1013–1016, 2011.

[106] X. Wang *et al.*, "Thermal Characteristics of 275 kV / 3 kA Class YBCO Power Cable," *IEEE Transactions on Appiled Superconductivity*, vol. 20, no. 3, pp. 1268–1271, 2010.

[107] S. Alaraifi, M. S. El Moursi, and H. H. Zeineldin, "Optimal allocation of HTS-FCL for power system security and stability enhancement," *IEEE Transactions on Power Systems*, vol. 28, no. 4, pp. 4701–4711, 2013, doi: 10.1109/TPWRS.2013.2273539.

[108] J. He *et al.*, "Thermal analysis of HTS power cable using 3-D FEM model," *IEEE Transactions on Applied Superconductivity*, vol. 23, no. 3, pp. 2–5, 2013, doi: 10.1109/TASC.2013.2247651.

[109] G. Ivanov, V. Mateev, and I. Marinova, "Modeling of Cooling System for High-temperature Superconducting Cables," *2020 12th Electrical Engineering Faculty Conference, BulEF 2020*, pp. 20–23, 2020, doi: 10.1109/BulEF51036.2020.9326033.

[110] D. I. Doukas, A. I. Chrysochos, T. A. Papadopoulos, D. P. Labridis, L. Harnefors, and G. Velotto, "Coupled Electro-Thermal Transient Analysis of Superconducting DC Transmission Systems Using FDTD and VEM Modeling," *IEEE Transactions on Applied Superconductivity*, vol. 27, no. 8, 2017, doi: 10.1109/TASC.2017.2749500.

[111] D. I. Doukas *et al.*, "Volume Element Method for Thermal Analysis of Superconducting DC Transmission Cable," *Ieee Transactions on Applied Superconductivity*, vol. 27, no. 4, p. 5400608, 2017.

[112] X. Li *et al.*, "Research on Thermal Behavior of HTS Cable in Fault and Recovery," in *IEEE International Conference on Applied Superconductivity and Electromagnetic Devices*, 2020, pp. 2020–2021.

[113] D. I. Doukas, A. I. Chrysochos, T. A. Papadopoulos, D. P. Labridis, L. Harnefors, and G. Velotto, "Volume Element Method for Thermal Analysis of Superconducting DC Transmission Cable," *IEEE Transactions on Applied Superconductivity*, vol. 27, no. 4, Jun. 2017, doi: 10.1109/TASC.2017.2656785.

[114] L. Savoldi *et al.*, "Thermal-Hydraulic Modeling of a Novel HTS CICC for Nuclear Fusion Applications," *IEEE Transactions on Applied Superconductivity*, vol. 26, no. 3, 2016, doi: 10.1109/TASC.2016.2528541.

[115] W. T. B. de Sousa, D. Kottonau, and M. Noe, "Transient Simulation and Recovery Time of a Three-Phase Concentric HTS Cable," *IEEE Transactions on Applied Superconductivity*, vol. 29, no. 5, pp. 1–5, 2019, doi: 10.1109/TASC.2019.2900937.

[116] W. T. B. De Sousa, E. Shabagin, D. Kottonau, and M. Noe, "An open-source 2D finite difference based transient electro-thermal simulation model for three-phase concentric superconducting power cables," *Supercond Sci Technol*, vol. 34, no. 1, p. 015014, 2020.

[117] J. H. Choi, C. Park, P. Cheetham, C. H. Kim, S. Pamidi, and L. Graber, "Detection of Series Faults in High-Temperature Superconducting DC Power Cables Using Machine Learning," *IEEE Transactions on Applied Superconductivity*, vol. 31, no. 5, pp. 1–9, 2021, doi: 10.1109/TASC.2021.3055156.

[118] E. Tsotsopoulou *et al.*, "Modelling and fault current characterization of superconducting cable with high temperature superconducting windings and copper stabilizer layer," *Energies (Basel)*, vol. 13, no. 24, Dec. 2020, doi: 10.3390/en13246646.

[119] T. T. Nguyen *et al.*, "A simplified model of coaxial, multilayer high-temperature superconducting power cables with Cu formers for transient studies," *Energies (Basel)*, vol. 12, no. 8, Apr. 2019, doi: 10.3390/en12081514.

[120] R. Su *et al.*, "Numerical Model of HTS Cable and Its Electric-Thermal Properties," *IEEE Transactions on Applied Superconductivity*, vol. 29, no. 5, Aug. 2019, doi: 10.1109/TASC.2019.2901874.

[121] X. Li *et al.*, "Simulation Analysis of 2D Finite Element Axial Transient Temperature Distribution of HTS Cable," *IEEE Transactions on Applied Superconductivity*, vol. 31, no. 5, Aug. 2021, doi: 10.1109/TASC.2021.3061344.

[122] M. STEMMLE, "Update on world's first superconducting cable and fault current limiter installation in a German city center".

[123] D. C. Van Der Laan, J. D. Weiss, C. H. Kim, L. Graber, and S. Pamidi, "Development of CORC® cables for helium gas cooled power transmission and

fault current limiting applications," *Supercond Sci Technol*, vol. 31, no. 8, Jul. 2018, doi: 10.1088/1361-6668/aacf6b.

[124] T. Mulder *et al.*, "Design and Manufacturing of a 45 kA at 10 T REBCO-CORC Cable-in-Conduit Conductor for Large-Scale Magnets," *IEEE Transactions on Applied Superconductivity*, vol. 26, no. 4, pp. 1–5, 2016, doi: 10.1109/TASC.2016.2527241.

[125] D. Uglietti, "A review of commercial high temperature superconducting materials for large magnets: from wires and tapes to cables and conductors," *Supercond Sci Technol*, vol. 32, no. 5, p. 53001, 2019.

[126]P. Bruzzone *et al.*, "LTS and HTS high current conductor development for DEMO," *Fusion Engineering and Design*, vol. 96, pp. 77–82, 2015.

[127] W. Goldacker *et al.*, "High current DyBCO-ROEBEL assembled coated conductor (RACC)," in *Journal of Physics: Conference Series*, IOP Publishing, 2006, p. 220.

[128] D. Uglietti, N. Bykovsky, R. Wesche, and P. Bruzzone, "Development of HTS conductors for fusion magnets," *IEEE Transactions on Applied Superconductivity*, vol. 25, no. 3, pp. 1–6, 2014.

[129] R. Kang, D. Uglietti, and Y. Song, "Modelling quench of a 50 kA REBCO conductor with soldered-twisted-stacked-tape-cable strands," *Cryogenics (Guildf)*, vol. 106, p. 103037, 2020, doi: https://doi.org/10.1016/j.cryogenics.2020.103037.

[130] D. Lindsay, "Recommendations for testing of superconducting cables," *Cigré Technical Brochure*, vol. 538, 2013.

[131] G. Hajiri, K. Berger, R. Dorget, J. Leveque, and H. Caron, "Thermal and Electromagnetic Design of DC HTS Cables for the Future French Railway Network," *IEEE Transactions on Applied Superconductivity*, vol. 31, no. 5, 2021, doi: 10.1109/TASC.2021.3059598.

[132] C. E. Bruzek, A. Allais, D. Dickson, N. Lallouet, K. Allweins, and E. Marzahn, "Superconducting DC cables to improve the efficiency of electricity transmission and distribution networks: An overview," *Eco-Friendly Innovation in Electricity Transmission and Distribution Networks*, pp. 135–167, 2015.

[133] H. Zhang and Y. Wang, "A Self-Shielding DC HTS Cable Using Coaxial Configuration With Large Current Capacity," *IEEE Transactions on Applied Superconductivity*, vol. 26, no. 7, pp. 1–5, 2016, doi: 10.1109/TASC.2016.2574339.

[134] R. L. Hughey, "A Demonstration high temperature superconductor cable to power a manufacturing operation," *Proceedings of the IEEE Power Engineering Society Transmission and Distribution Conference*, vol. 1, pp. 68–72, 1999, doi: 10.1109/tdc.1999.755318.

[135] J. Ostergaard and O. Tonnesen, "Results from the Danish High Temperature Superconducting Power Cable Project," *TEION KOGAKU (Journal of Cryogenics and Superconductivity Society of Japan)*, vol. 37, no. 9, pp. 450–456, 2002.

[136] C. Lee *et al.*, "Progress of the first commercial project of high-temperature superconducting cables by KEPCO in Korea," *Supercond Sci Technol*, vol. 33, no. 4, p. 044006, 2020.

[137] D. Lindsay, "Operating experience of 13.2 kV superconducting cable system at AEP Bixby Station," *CIGRE 2008*, 2008.

[138] F. Schmidt, J. Maguire, T. Welsh, and S. Bratt, "Operation experience and further development of a high- Temperature superconducting power cable in the long island power authority grid," in *Physics Procedia*, Elsevier B.V., 2012, pp. 1137–1144. doi: 10.1016/j.phpro.2012.06.190.

[139] M. Stemmle, F. Merschel, M. Noe, and A. Hobl, "AmpaCity - Installation of advanced superconducting 10 kV system in city center replaces conventional 110 kV cables," in *2013 IEEE International Conference on Applied Superconductivity and Electromagnetic Devices, ASEMD 2013*, IEEE Computer Society, 2013, pp. 323–326. doi: 10.1109/ASEMD.2013.6780785.

[140] V. Sytnikov, A. Kashcheev, M. Dubinin, V. Karpov, and T. Ryabin, "Test Results of the Full-Scale HTS Transmission Cable Line (2.4 Km) for the St. Petersburg Project," *IEEE Transactions on Applied Superconductivity*, vol. 31, no. 5, 2021, doi: 10.1109/TASC.2021.3063067.

[141] M. Ross, "Utility applications and experience with resilient electric grid systems utilizing high temperature superconductor wires in Chicago," *Physica C: Superconductivity and its Applications*, vol. 614, p. 1354374, 2023, doi: https://doi.org/10.1016/j.physc.2023.1354374.

[142] A. Allais *et al.*, "SuperRail- World-first HTS cable to be installed on a railway network in France," *IEEE Transactions on Applied Superconductivity*, May 2024, doi: 10.1109/TASC.2024.3356450.

[143] C. S. Weber, R. Lee, S. Ringo, T. Masuda, H. Yumura, and J. Moscovic, "Testing and Demonstration Results of the 350 m Long HTS Cable System Installed in Albany , NY," *IEEE Transactions on Applied Superconductivity*, vol. 17, no. 2, pp. 2038–2042, 2007.

[144] W. Xie, B. Wei, and Z. Yao, "Introduction of 35 kV km Level Domestic Second Generation High Temperature Superconducting Power Cable Project in Shanghai , China," pp. 1927–1931, 2020.

[145] D. C. Van Der Laan and J. D. Weiss, "Status of CORC ® cables and wires for use in high- fi eld magnets and power systems a decade after their introduction," *Supercond Sci Technol*, vol. 32, no. 3, p. 33001, 2019, doi: 10.1088/1361-6668/aafc82.

[146] X. Zong, D. Wei, Y. Han, and T. Tang, "Development of 35 kV 2000 A CD HTS Cable Demonstration Project," *IEEE Transactions on Applied Superconductivity*, vol. 26, no. 7, pp. 35–38, 2016, doi: 10.1109/TASC.2016.2598490.

[147] D. Zhang *et al.*, "Testing Results for the Cable Core of a 360 m/10 kA HTS DC Power Cable Used in the Electrolytic Aluminum Industry," *IEEE Transactions on Applied Superconductivity*, vol. 25, no. 3, pp. 10–13, 2015, doi: 10.1109/TASC.2014.2374691.

[148] B. Yang, J. Kang, S. Lee, C. Choi, and Y. Moon, "Qualification Test of a 80 kV 500 MW HTS DC Cable for Applying into Real Grid," *IEEE Transactions on Applied Superconductivity*, vol. 25, no. 3, pp. 0–4, 2015, doi: 10.1109/TASC.2015.2396683.

[149] D. W. Kim *et al.*, "Development of the 22.9-kV class HTS power cable in LG cable," *IEEE Transactions on Applied Superconductivity*, vol. 15, no. 2 PART II, pp. 1723–1726, 2005, doi: 10.1109/TASC.2005.849266.

[150] T. Masuda *et al.*, "Design and experimental results for albany HTS cable," *IEEE Transactions on Applied Superconductivity*, vol. 15, no. 2 PART II, pp. 1806–1809, 2005, doi: 10.1109/TASC.2005.849296.

[151] H. Liang *et al.*, "Recent progress in MgB2 superconducting joint technology," Jul. 01, 2023, *KeAi Communications Co.* doi: 10.1016/j.jma.2023.07.010.

[152] N. Chikumoto and S. Kato, "Development of Direct Joint Process Using Cu Stabilizing Layers of REBCO Tapes," *IEEE Transactions on Applied Superconductivity*, vol. 34, no. 3, pp. 1–4, 2024, doi: 10.1109/TASC.2024.3351118.

[153] S. Ito, L. E. Aparicio, Y. Atake, H. Yamamoto, T. Onji, and M. Tomita, "Initial Study on Press Welding With Indium Applied to High-Temperature Superconducting DC Feeder Cables," *IEEE Transactions on Applied Superconductivity*, vol. 33, no. 5, 2023, doi: 10.1109/TASC.2023.3237791.

[154] R. Hayasaka, S. Ito, T. Kato, D. Yokoe, and H. Hashizume, "In-depth resistance analysis of REBCO tape joints with indium insert and solders," in *Journal of Physics: Conference Series*, IOP Publishing, 2020, p. 012034.

[155] T. Nishio, S. Ito, and H. Hashizume, "Heating and loading process improvement for indium inserted mechanical lap joint of REBCO tapes," *IEEE Transactions on Applied Superconductivity*, vol. 27, no. 4, pp. 1–5, 2017.

[156] H. Hashizume, S. Ito, N. Yanagi, H. Tamura, and A. Sagara, "Development of remountable joints and heat removable techniques for high-temperature superconducting magnets," *Nuclear Fusion*, vol. 58, no. 2, p. 026014, 2017.

[157] T. Nishio, S. Ito, N. Yusa, and H. Hashizume, "Reducing joint resistance by heat treatment during fabrication of a mechanical joint of high-temperature superconducting conductors," *IEEE Transactions on Applied Superconductivity*, vol. 26, no. 4, pp. 1–5, 2016.

[158] H.-S. Shin, C.-H. Jung, and A. R. Nisay, "Joint characteristics of ultrasonic welded CC bridge joints for HTS coil applications," *Supercond Sci Technol*, vol. 33, no. 11, 2020, doi: 10.1088/1361-6668/abb35e.

[159] S. Ito, R. Hayasaka, K. Yuki, Y. S. Sato, and H. Hashizume, "Joining condition dependency of joint resistance in ultrasonic welding of high-Temperature superconducting tapes with indium," in *Journal of Physics: Conference Series*, E. Romans, M. Ainslie, K. Berger, N. Bykovskiy, O. Kennedy, A. Palau, C. Pegrum,

L. Queval, S. Sotelo, B. de S. W. T, and M. Zhang, Eds., Institute of Physics Publishing, 2020. doi: 10.1088/1742-6596/1559/1/012065.

[160] W. J. Kim, H. J. Kim, J. W. Cho, and S. H. Kim, "The basic properties of PPLP for HTS DC cable," *Phys Procedia*, vol. 45, pp. 293–296, 2013.

[161] S. H. Kim *et al.*, "Electrical insulation characteristics of PPLP as a HTS DC cable dielectric and GFRP as insulating material for terminations," *IEEE transactions on applied superconductivity*, vol. 22, no. 3, p. 7700104, 2011.

[162] M. Yazdani-Asrami, S. M. Seyyedbarzegar, M. Zhang, and W. Yuan, "Insulation Materials and Systems for Superconducting Powertrain Devices in Future Cryo-Electrified Aircraft: Part I—Material Challenges and Specifications, and Device-Level Application," *IEEE Electrical Insulation Magazine*, vol. 38, no. 2, pp. 23–36, 2022.

[163] H. Rodrigo, D. Kwag, L. Graber, B. Trociewitz, and S. Pamidi, "AC flashover voltages along epoxy surfaces in gaseous helium compared to liquid nitrogen and transformer oil," *IEEE transactions on applied superconductivity*, vol. 24, no. 3, pp. 1–6, 2013.

[164] M. Stemmle, F. Merschel, M. Noe, and A. Hobl, "AmpaCity — Installation of advanced superconducting 10 kV system in city center replaces conventional 110 kV cables," in *2013 IEEE International Conference on Applied Superconductivity and Electromagnetic Devices*, 2013, pp. 323–326. doi: 10.1109/ASEMD.2013.6780785.

[165] D. I. Doukas, Z. D. Blatsi, A. N. Milioudis, D. P. Labridis, L. Harnefors, and G. Velotto, "Damping of electromagnetic transients in a superconducting VSC transmission system," in *2015 IEEE Eindhoven PowerTech*, IEEE, 2015, pp. 1–6.

[166] Z. Zhou *et al.*, "Magnetic-thermal coupling analysis of the cold dielectric high temperature superconducting cable," *IEEE transactions on applied superconductivity*, vol. 23, no. 3, p. 5400404, 2012.

[167] W. Xiang *et al.*, "DC Fault Study of a Point-to-Point HVDC System Integrating Offshore Wind Farm Using High-Temperature Superconductor DC Cables," *IEEE TRANSACTIONS ON ENERGY CONVERSION*, vol. 37, no. 1, pp. 377–388, 2022, doi: 10.1109/TEC.2021.3094308.

[168] W. T. B. De Sousa, D. Kottonau, and M. Noe, "Transient Simulation and Recovery Time of a Three-Phase Concentric HTS Cable," *IEEE Transactions on Applied Superconductivity*, vol. 29, no. 5, 2019, doi: 10.1109/TASC.2019.2900937.

[169] W. Xiang *et al.*, "DC Fault Study of a Point-to-Point HVDC System Integrating Offshore Wind Farm Using High-Temperature Superconductor DC Cables," *IEEE Transactions on Energy Conversion*, vol. 37, no. 1, pp. 377–388, 2022, doi: 10.1109/TEC.2021.3094308.

[170] "https://htsdb.wimbush.eu/dataset/1165595."

[171] Y. Ivanov *et al.*, "Current Imbalance and AC Losses of Long-Distance DC HTS Cable," *IEEE Transactions on Applied Superconductivity*, vol. 26, no. 7, pp. 3–6, 2016, doi: 10.1109/TASC.2016.2577600.

[172] T. Jin, J. Hong, H. Zheng, K. Tang, and Z. Gan, "Measurement of boiling heat transfer coefficient in liquid nitrogen bath by inverse heat conduction method," *Journal of Zhejiang University-SCIENCE A*, vol. 10, pp. 691–696, 2009.

[173] N. Duan, W. Xu, S. Wang, and J. Zhu, "Current Distribution Calculation of Superconducting Layer in HTS Cable Considering Magnetic Hysteresis by Using XFEM," *IEEE Trans Magn*, vol. 54, no. 3, 2018, doi: 10.1109/TMAG.2017.2751257.

[174] S. K. Olsen, C. Traeholt, A. Kuhle, O. Tonnesen, M. Daumling, and J. Ostergaard, "Loss and inductance investigations in a 4-layer superconducting prototype cable conductor," *IEEE Transactions on Applied Superconductivity*, vol. 9, no. 2, pp. 833–836, 1999, doi: 10.1109/77.783426.

[175] J. A. Souza, J. C. Ordonez, R. Hovsapian, and J. V. C. Vargas, "Thermal modeling of helium cooled high-temperature superconducting DC transmission cable," *IEEE Transactions on Applied Superconductivity*, vol. 21, no. 3 PART 2, pp. 947–952, Jun. 2011, doi: 10.1109/TASC.2010.2099196.

[176] J. Gerhold and T. Tanaka, "Cryogenic electrical insulation of superconducting power transmission lines: transfer of experience learned from metal superconductors to high critical temperature superconductors," *Cryogenics (Guildf)*, vol. 38, no. 11, pp. 1173–1188, 1998, doi: https://doi.org/10.1016/S0011-2275(98)00105-2.

[177] C. Senatore, M. Alessandrini, A. Lucarelli, R. Tediosi, D. Uglietti, and Y. Iwasa, "Progresses and challenges in the development of high-field solenoidal magnets based on RE123 coated conductors," *Supercond Sci Technol*, vol. 27, no. 10, p. 103001, 2014.

[178] S. S. Lee, T. H. Kim, S. J. Hu, W. W. Cai, and J. A. Abell, "Joining technologies for automotive lithium-ion battery manufacturing: A review," in *International manufacturing science and engineering conference*, 2010, pp. 541–549.

[179] O. Tsukamoto, J. F. Maguire, E. S. Bobrov, and Y. Iwasa, "Identification of quench origins in a superconductor with acoustic emission and voltage measurements," *Appl Phys Lett*, vol. 39, no. 2, pp. 172–174, 1981.

[180] J. Zheng, M. Wei, S. Quan, Y. Feng, and P. Wen, "Review on thermal-related measurement methods for superconducting devices and prospect for high-speed maglev transportation application," *Superconductivity*, vol. 3, p. 100020, 2022.

[181] G. Lyu, Y. Terao, and H. Ohsaki, "Electromagnetic and Thermal Analysis of HTS AC Cable using T- A Formulation," in *Journal of Physics: Conference Series*, Institute of Physics, 2023. doi: 10.1088/1742-6596/2545/1/012010.

[182] C. C. T. Chow, F. Grilli, and K. T. Chau, "Numerical modelling of HTS tapes under arbitrary external field and transport current via integral method: review and application to electrical machines," *Supercond Sci Technol*, vol. 36, no. 11, Nov. 2023, doi: 10.1088/1361-6668/ace701.

[183] S.-K. Kim *et al.*, "Harmonic Current Based Loss Characteristics Analysis of HTS DC Model Cable Using Calorimetric Method," *IEEE Transactions on Applied Superconductivity*, vol. 22, no. 3, p. 5801204, 2012, doi: 10.1109/TASC.2012.2185772.

[184] I. E. C. Standard, "61727-2004; Photovoltaic (PV) Systems—Characteristics of the Utility Interface," *International Electrotechnical Commission (IEC): Geneva, Switzerland*, 2004.

[185] D. Generation and E. Storage, "Ieee standard for interconnection and interoperability of distributed energy resources with associated electric power systems interfaces amendment 1: To provide more," *IEEE: Piscataway, NJ, USA*, 2020.

[186] M. Kalsia and R. S. Dondapati, "Thermohydraulic analysis of cold dielectric high temperature superconducting cable with counter-flow cooling," *Physica C: Superconductivity and its Applications*, vol. 564, pp. 59–67, Sep. 2019, doi: 10.1016/j.physc.2019.06.006.

[187] M. Yagi *et al.*, "Experimental Results of 275-kV 3-kA REBCO HTS Power Cable," *IEEE Transactions on Applied Superconductivity*, vol. 25, no. 3, pp. 1–5, 2015, doi: 10.1109/TASC.2014.2385960.

[188] J. G. Kim, S. K. Kim, M. Park, and I. K. Yu, "Hardware-in-the-loop simulation for superconducting dc power transmission system," *IEEE Transactions on Applied Superconductivity*, vol. 25, no. 3, Jun. 2015, doi: 10.1109/TASC.2015.2406293.

[189] S. P. Ashworth and D. W. Reagor, "A novel cooling scheme for superconducting power cables," *Cryogenics (Guildf)*, vol. 51, no. 4, pp. 161–167, Apr. 2011, doi: 10.1016/j.cryogenics.2011.01.001.

[190] S. Yazaki, A. Karasawa, T. Kotoyori, A. Ishiyama, and N. Miyahara, "Critical Current Degradation in High-Temperature Superconducting Tapes Caused by Temperature Rise," *IEEE Transactions on Applied Superconductivity*, vol. 23, no. 3, p. 4602304, 2013, doi: 10.1109/TASC.2013.2244157.

[191] D. Guillen, C. Salas, F. Trillaud, L. M. Castro, A. T. Queiroz, and G. G. Sotelo, "Impact of Resistive Superconducting Fault Current Limiter and Distributed Generation on Fault Location in Distribution Networks," *Electric Power Systems Research*, vol. 186, p. 106419, 2020, doi: https://doi.org/10.1016/j.epsr.2020.106419.

[192] G. Gonçalves Sotelo *et al.*, "A review of superconducting fault current limiters compared with other proven technologies," Sep. 01, 2022, *Elsevier B.V.* doi: 10.1016/j.supcon.2022.100018.

[193] M. Moyzykh *et al.*, "First Russian 220 kV Superconducting Fault Current Limiter (SFCL) for Application in City Grid," *IEEE Transactions on Applied Superconductivity*, vol. 31, no. 5, Aug. 2021, doi: 10.1109/TASC.2021.3066324.

[194] X. Chen *et al.*, "Superconducting fault current limiter (SFCL) for fail-safe DC-DC conversion: From power electronic device to micro grid protection," *Superconductivity*, vol. 1, Mar. 2022, doi: 10.1016/j.supcon.2022.100003.

[195] M. Song *et al.*, "Design and performance tests of a 160 kV/1.0 kA DC superconducting fault current limiter," *Physica C: Superconductivity and its Applications*, vol. 585, p. 1353871, 2021, doi: https://doi.org/10.1016/j.physc.2021.1353871.

[196] C. Liang *et al.*, "Winding Technology and Experimental Study on 500 kV Superconductive Fault Current Limiter," *IEEE Transactions on Applied Superconductivity*, vol. 28, no. 3, Apr. 2018, doi: 10.1109/TASC.2018.2805722.